VNIVERSITAT DE VALÈNCIA

Top-quark couplings in past, present and future colliders

Tesi Doctoral
Programa de Doctorat en Física

Martín Perelló Roselló

Departament de Física Atòmica, Molecular i Nuclear
IFIC (Universitat de València - CSIC)

Sota la supervisió de

Dr. Marcel Vos i Dr. Gauthier Durieux

València, Febrer 2020

El Dr. **Marcel Vos**, Científic Titular del CSIC, i el Dr. **Gauthier Durieux**, Postdoc al Departament de Física a Technion, Institut Tecnològic d'Israel,

certifiquen:

que la present memòria "Top-quark couplings in past, present and future colliders" ha sigut realitzada sota la seua direcció en l'Institut de Física Corpúscular, centre mixt de la Universitat de València i del CSIC, per **Martín Perelló Roselló** i constitueix la seva Tesi per optar al grau de Doctor en Física per la Universitat de València.

I per a que així conste, en compliment de la legislació vigent, presenten en el departament de Física Atòmica, Molecular i Nuclear de la Universitat de València la referida Tesi Doctoral, i firmen el present certificat.

València, a 11 de febrer de 2020

Dr. Marcel Vos Dr. Gauthier Durieux

Vist i plau del tutor, Dr. Santiago González de la Hoz

El treball descrit a aquesta tesi s'ha desenvolupat en el **Institut de Física Corpuscular (IFIC)** i ha sigut financiat amb l'ajuda *Severo Ochoa* SEV-2014-0398-05 concedida pel Ministeri de Ciència, Innovació i Universitats. L'IFIC és un centre mixte del Consell Superior d'Investigacions Científiques (CSIC) i de la Universitat de València.

A ma mare,
a mon pare,
a David.

A Carles, Òscar, Sònia, Julián, Ana, Iker i Clara per haver estat presents en diferents etapes. Als Haters de la Torre, als Pisiers y a Garch and Go.

A tot el grup de futurs col·lisionadors de l'IFIC: Nacho, Miguel Àngel, Pablo, Eduardo, Esteban, Juan i sobretot a Marcel per fer-me aquests anys més fàcils.

Un agraïment especial als assistents de la festa de la última compilació: Emmy, Iker, Ana, Clara, Sílvia, Joan, Julian, Anna, Flopa, Jesús, Fernando, Sara, Víctor, Núria, Mario, Paula, Andreu, Sergi i especialment a Judith per organitzar-la. Gràcies per haver fet d'aquest final de tesi un moment tan especial.

Abstract

The Standard Model (SM) is the most complete description of elementary particles and their interactions. It is composed of bosons, integer-spin particles which mediate the interactions, and fermions, spin-1/2 particles which constitute matter. However the SM is still not the final theory. It does not include gravitation as a quantum field theory, it does not offer a clear explanation of what could constitute the Dark Matter and it predicts the neutrinos to be massless. Particle physicists therefore work on different theories Beyond the Standard Model (BSM) to address these problems.

For studying deviations from the SM in top-quark physics we use an effective field theory (EFT) approach. EFTs allow us to parameterize the unknown low-energy physics effects respect to some high energy scale. We describe the top-quark couplings in terms of SM and BSM contributions of dimension-six effective operators.

In a first study we interpret the charge-asymmetry measurement for the process $pp \to t\bar{t}$ at the LHC in terms of four-quark dimension-six operators. These kind of operators have enhanced effects in the boosted regime, so we use differential measurements of the charge asymmetry for high values of the invariant mass of the $t\bar{t}$ system.

In a second study, we perform a global fit of the electroweak (EW) couplings of the top and bottom quarks. We have a total of 10 effective operators describing the left and right couplings of the top and bottom quark to the Z boson, the charged current Wtb, the EW dipole operators and the top-Yukawa coupling. We constrain these operators with existing data from SLC/LEP and from the Run 2 of the LHC.

Furthermore, we study how these bounds would improve during the remaining programme of the LHC and at a future electron-positron collider. We compare the existing bounds with the bounds that would derive from data collected at $\sqrt{s} = 250$ and $\sqrt{s} = 500$ GeV, at the International Linear Collider (ILC). We show that the bounds improve very strongly with the constraints from the $e^+e^- \to t\bar{t}$ production process. We also study the impact of adding the two-lepton-two-quark operators to the 10-parameter fit. In this case we add 7 extra operators and an extra centre-of-mass energy, $\sqrt{s} = 1$ TeV, is needed. We demonstrate that a 17-parameter fit is robust.

Contents

1.- The Standard Model

The scientific progress at the beginning of the XX century completely changed the paradigm of fundamental physics. The discovery of the electron as an explanation for the observed cathode rays radiation by J.J. Thomson, the quantization of the energy to explain the black-body radiation by M. Planck, and A. Einstein's postulation of the photoelectric effect forced physicists to develop new theories to explain all these new phenomena.

The atom was the first entity postulated as indivisible. We have learnt that it is formed by an electron and a nucleus with a balancing positive charge. Today, we know that there are several types of elementary particles. The atomic nucleus is made of quarks. Experiments have also discovered further charged leptons and neutrinos. Their interactions are beyond the scope of classical gravity and electromagnetism.

New quantum theories were needed to explain these interactions. Quantum electrodynamics (QED), the result of matching the classical theory of electromagnetism with the new quantum theory, describes the interaction of the electron and the photon. Two new interactions had to explain the atomic nucleus and the radiation observed in some isotopes; these interactions were explained with quantum chromodynamics (QCD) and the weak interaction theories respectively.

The union of these new interactions is called the Standard Model (SM) of elementary particles. It offers a precise description of the elementary particles which form matter and their interactions. It has been developed thanks to the interplay between theory and experiment.

The elementary constituents of matter are spin-1/2 particles called fermions. Examples are the electron and the up and down quarks that constitute ordinary matter. The category of which electron is part is called leptons and is completed by neutrinos. We find three families of quarks and leptons. The partners of the electron are the muon and the tau with their respective neutrinos. In the case of the quarks, the second family is formed by the charm and the strange quarks, and the third family by the bottom and top quarks.

Spin-1 bosons are responsible of the interaction of the particles: the photon mediates electromagnetism, W and Z bosons are responsible of the weak interaction while the gluon is responsible of the strong interaction. One further scalar boson is needed to give mass to elementary particles, this is the so-called Higgs boson. In Figure 1.1 we have the classification of the known elementary particles of the SM. In the following subsections we introduce the different families and their properties.

Future directions of high-energy physics are inspired by a desire to provide a natural explanation for the parameters of the SM (i.e. the Higgs boson mass) together with the necessity of giving an answer

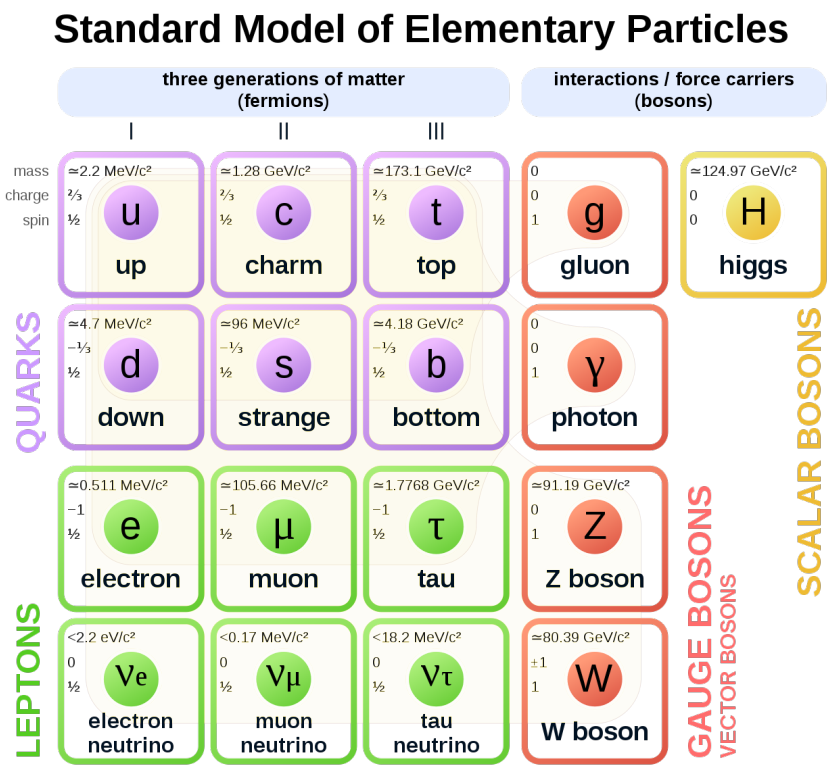

Figure 1.1: The Standard Model of elementary particles. They are classified into fermions, which form matter, and bosons, which mediate the interactions between the particles. The fermions are divided into quarks and leptons, both presenting three families. Figure reproduced from Ref. [1].

to some experimental hints for phenomena not included in the SM (dark matter), the desire to merge gravity (relativity) and quantum field theory, or an explanation for the observed neutrino masses.

This chapter presents a brief overview of the SM and is organized as follows: in sections 1.1, 1.2, 1.3 and 1.4 we introduce the formalism of the SM. We use Ref. [2] as the principal reference and point to the original bibliography where the SM is developed. In section 1.5 we classify the different elementary particles within the SM and review the current measurements of their properties. Finally, in section 1.6 we introduce the concept of effective field theory as a procedure for parameterizing the effects of physics beyond the SM.

1.1 Quantum electrodynamics

The theory of Quantum Electrodynamics (QED) was developed in the first years of the XX century by several physicists. The first formulation of a quantum theory describing the interaction of matter and radiation was made by Paul Dirac [3]. After him Shin'ichirō Tomonaga, Julian Schwinger and Richard Feynman developed the necessary tools for building an elegant quantum gauge theory which describes the interaction of the electromagnetic force [4–6]. The Nobel Prize in Physics 1965 was awarded jointly to Tomonaga, Schwinger and Feynman for their fundamental work in quantum electrodynamics, with important consequences for the physics of elementary particles.

In QED formalism a free Dirac fermion (spin-1/2 particle, such as the electron) is described by the following Lagrangian:

$$\mathcal{L}_0 = i\bar{\psi}(x)\gamma^\mu\partial_\mu\psi(x) - m\bar{\psi}(x)\psi(x), \tag{1.1}$$

where $\psi(x)$ is the wavefunction describing the particle (also known as Dirac spinor), m is its mass, γ^μ are the Dirac matrices and ∂_μ is the partial derivative. The expression for $\mathcal{L}_0$ is invariant under global $U(1)$ transformations

$$\psi(x) \xrightarrow{U(1)} \psi(x)' = e^{iQ\theta}\psi(x), \tag{1.2}$$

where $Q\theta$ is an arbitrary real constant. However if we want the phase transformation to be dependent on the space-time coordinate the free Lagrangian is no longer invariant:

$$\partial_\mu\psi(x) \xrightarrow{U(1)} \partial_\mu\psi(x)' = e^{iQ\theta}\left(\partial_\mu + iQ\partial_\mu\theta(x)\right)\psi(x). \tag{1.3}$$

The 'gauge principle' requires that the $U(1)$ phase invariance should hold locally. Physically, this gauge invariance expresses that the phase convention has to be independent of the space-time election, x. For this purpose an extra piece is required in the Lagrangian which, after transformation, cancels the $\partial_\mu\theta$ term in Equation 1.3. As $\partial_\mu\theta$ has a Lorentz index, a new spin-1 field is introduced under the transformation:

$$A_\mu \xrightarrow{U(1)} A'_\mu \equiv A_\mu - \frac{1}{e}\partial_\mu\theta, \tag{1.4}$$

defining the covariant derivative

$$D_\mu\psi(x) \equiv \left[\partial_\mu + ieQA_\mu(x)\right]\psi(x). \tag{1.5}$$

The resulting Lagrangian is then invariant under local $U(1)$ transformations:

$$\mathcal{L} \equiv i\bar{\psi}(x)\gamma^\mu D_\mu\psi(x) - m\bar{\psi}(x)\psi(x) = \mathcal{L}_0 - eQA_\mu(x)\bar{\psi(x)}\gamma^\mu\psi(x). \tag{1.6}$$

This Lagrangian describes an interaction between the Dirac fermion and the gauge field A_μ, (the QED vertex). It is common to express the QED coupling in terms of the so-called fine-structure constant, $\alpha \equiv e^2/(4\pi)$. A gauge-invariant kinematic term has to be inserted to convert A_μ in a propagating field. The QED Lagrangian is then:

$$\mathcal{L}_{\text{QED}} = \mathcal{L} + \mathcal{L}_{\text{kin}} = i\bar{\psi}(x)\gamma^\mu D_\mu\psi(x) - m\bar{\psi}(x)\psi(x) - \frac{1}{4}F_{\mu\nu}(x)F^{\mu\nu}(x), \tag{1.7}$$

where $F_{\mu\nu} \equiv \partial_\mu A_\nu - \partial_\nu A_\mu$ is the electromagnetic field strength tensor. A mass term for the gauge field of the form $\frac{1}{2}m^2A^\mu A_\mu$ is forbidden because it would violate the local $U(1)$ gauge invariance. The photon is therefore predicted to be massless, in agreement with experimental limits ($m_\gamma < 1 \times 10^{-18}$ eV [7]).

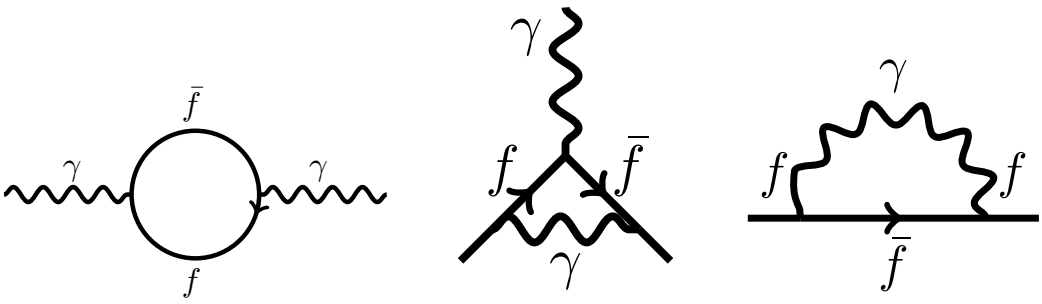

Figure 1.2: QED first-order loops.

1.1.1 Loop corrections and renormalization in QED

In QED calculations there are ultraviolet (UV, particles with unbounded energy) and infrared divergences (IR, soft and/or collinear massless particles). In such amplitude computations, our desire to integrate over loop momenta up to infinity —despite our ignorance of the physics beyond accessible energies— leads to ultraviolet divergences. Regularization procedures are deformations of ultra-high energies which render integrals finite. All the low-energy effects of these deformations can be absorbed into few constants, in a process called renormalization. The divergences can be reabosorbed in the coupling constant, α:

$$\alpha\left(Q^2\right) = \alpha_0\left[1 + \frac{\alpha_0}{3\pi} f\left(\frac{Q^2}{m_e^2}\right)\right], \tag{1.8}$$

where α_0 is the constant appearing in the Lagrangian and $\alpha\left(Q^2\right)$ the renormalized value that should agree with the measured value. The function $f\left(\frac{Q^2}{m_e^2}\right)$ is the finite correction which causes the coupling to evolve with the energy scale Q^2. The resulting QED running coupling $\alpha\left(Q^2\right)$ decreases relatively slowly at large distances (decreasing Q^2).

For $Q^2 \gg m_e^2$ the correction function can be approximated to $f\left(\frac{Q^2}{m_e^2}\right) \approx \ln\left(Q^2/m_e^2\right)$ and the running constant is then:

$$\alpha\left(Q^2\right) = \frac{\alpha_0}{1 + \beta_0\alpha_0 \ln\left(Q^2/m_e^2\right)}, \tag{1.9}$$

with $\beta_0 = -1/(3\pi)$. The higher the scale the larger the value of α and hence of the electron charge. A consequence of this effect is the charge screening by the creation of virtual electron-positron pairs popping out of the vacuum. In the first Feynman diagram of Figure 1.2 we find a representation of this screening.

The first correction is commonly named the next-to-leading-order (NLO) and higher-order corrections are labeled as N^{n}LO, with n being the number of loops or real emissions considered in the Feynman diagrams. Some corrections in QED are called radiative corrections, since they correspond to the emission and absorption of photons as shown in the last two Feynman diagrams in Figure 1.2.

One can develop the calculations as a perturbation series, where the precision is improved by adding corrections of order α, α^2, etc.:

$$\mathcal{O} = \mathcal{O}_0 + \alpha\mathcal{O}_1 + \alpha^2\mathcal{O}_2 + \alpha^3\mathcal{O}_3 + \ldots, \tag{1.10}$$

where $\mathcal{O}_0$ corresponds to the observable at tree level and $\alpha^n\mathcal{O}_n$ (with $n > 0$) is the n^{th}-order correction to the observable.

The most stringent test of QED comes from the high-precision measurement of the electron and muon anomalous magnetic moments, a_e and a_μ. The anomalous magnetic moments are quantum corrections (see Figure 1.2) to the magnetic moment (strength of a magnetic source) of the particles. The magnetic moment of a particle such as the electron is calculated through the so-called g-factor, a dimensionless quantity that characterizes the magnetic moment. Without QED corrections, it is predicted to be $g = 2$ by the Dirac equation. Then, the anomalous magnetic moment, a is calculated as the differences respect this value as $a = \frac{g-2}{2}$. The dominant corrections to the anomalous magnetic moment for the electron arise dominantly from virtual electrons and photons; these contributions are fully known to $O\left(\alpha^4\right)$ and many $O\left(\alpha^5\right)$ corrections have been already computed. The current QED prediction is [7]:

$$a_e^{\text{SM}} = (1159.65218091 \pm 0.00000026) \cdot 10^{-6}. \tag{1.11}$$

The theoretical error is dominated by the uncertainty in the input value of the QED coupling α. Turning things around, a_e provides the most accurate determination of α, also called fine structure constant:

$$\alpha^{-1} = 137.035999084 \pm 0.000000051. \tag{1.12}$$

For the muon, the corrections to the anomalous magnetic moment due to virtual heavier states are more sizeable and the calculation is not in such good agreement with the measurement as the electron. The current combination of different predictions is [7]:

$$a_\mu^{\text{SM}} = 116591823(1)(34)(26) \cdot 10^{-11}, \tag{1.13}$$

where the errors are due to the electroweak, lowest-order hadronic, and higher-order hadronic contributions, respectively.

Experimentally, these quantities are found to be [7]:

$$a_e = (1159652180.73 \pm 0.28) \cdot 10^{-12}, \qquad a_\mu = 11659209.1(5.4)(3.3) \cdot 10^{-10}. \tag{1.14}$$

1.2 Quantum chromodynamics

In the 1950s, thanks to the development of accelerators and detection techniques such as bubble chambers and spark chambers, a lot of particles were discovered. These particles were called hadrons. Murray Gell-Mann and and Yuval Ne'eman introduced in 1961 the concept of constituent quarks. They postulated that quarks were the elementary constituents of the hadrons [8, 9]. Gell-Mann was awarded the Nobel Prize in 1969 for this idea.

These studies from Gell-Mann gave rise to the development of a theory of the interaction between quarks; this theory was called Quantum Chromodynamics (QCD). To satisfy Fermi-Dirac statistics, QCD

introduces a new quantum number named *colour*. Each species of quark must have $N_C = 3$ different colours. Experimentally, no coloured particles have been observed in isolation. All observed resonances are bound states with no net colour. So to be consistent we need to assume that all asymptotic states are colourless. This is known as the *confinement hypothesis*.

The theory is very similar to QED if one replaces fermions by quarks and the photons by the new QCD mediators: the gluons. Consider a quark denoted as q_f^α, being f the flavour and α the colour. To construct the QCD Lagrangian one should start like in the QED case with the free particle Lagrangian

$$\mathcal{L}_0 = \sum_f \bar{q}_f \left(i\gamma^\mu \partial_\mu - m_f\right) q_f, \tag{1.15}$$

where to simplify we have defined $q_f^{\alpha T} \equiv \left(q_f^1, q_f^2, q_f^3\right)$. This Lagrangian is invariant under arbitrary global $SU(3)_C$ transformation in colour space:

$$q_f^\alpha \xrightarrow{SU(3)} \left(q_f^\alpha\right)' = U_\beta^\alpha q_f^\beta, \qquad UU^\dagger = U^\dagger U = 1, \qquad \det U = 1, \tag{1.16}$$

where the U matrices can be written as

$$U = e^{i\frac{\lambda_a}{2}\theta_a}, \tag{1.17}$$

where $\frac{1}{2}\lambda_a$ $(a = 1, 2, \ldots, 8)$ are the $SU(3)_C$ generators and θ_a are arbitrary parameters. The matrices λ_a are traceless and satisfy:

$$\left[\frac{\lambda^a}{2}, \frac{\lambda^b}{2}\right] = i f^{abc} \frac{\lambda^c}{2}, \tag{1.18}$$

where f^{abc} are the $SU(3)_C$ structure constants, which are real and totally antisymmetric. We have to impose as in the QED case that the Lagrangian must be invariant also under local $SU(3)_C$ transformations, $\theta_a = \theta_a(x)$. We need to add the gluons as the new spin-1 gauge bosons of the theory. In total eight different gluons have to be introduced, $G_a^\mu(x)$:

$$D^\mu q_f = \left[\partial_\mu + i g_s \frac{\lambda_a}{2} G_a^\mu(x)\right] q_f \equiv \left[\partial_\mu + i g_s G^\mu(x)\right] q_f. \tag{1.19}$$

While in QED we could assign arbitrary electromagnetic charges to the different fermions, in QCD there is a unique $SU(3)_C$ coupling, the strong coupling constant g_s. This implies that all quarks couple to the gluon fields with the same interaction strength. We can redefine the strong coupling constant as $\alpha_s \equiv g_s^2/(4\pi)$. The QCD Lagrangian becomes:

$$\mathcal{L}_{\text{QCD}} = \sum_f \bar{q}_f \left(i\gamma^\mu D_\mu - m_f\right) q_f - \frac{1}{4} G_a^{\mu\nu} G^a_{\mu\nu}, \tag{1.20}$$

where we have constructed the field strengths as:

$$\begin{aligned} G^{\mu\nu}(x) \equiv -\frac{i}{g_s}\left[D_\mu, D_\nu\right] = \partial^\mu G^\nu - \partial^\nu G^\mu + i g_s \left[G^\mu, G^\nu\right] \equiv \frac{\lambda_a}{2} G_a^{\mu\nu}(x) \\ G_a^{\mu\nu}(x) = \partial^\mu G_a^\nu - \partial^\nu G_a^\mu - g_s f^{abc} G_b^\mu G_c^\nu. \end{aligned} \tag{1.21}$$

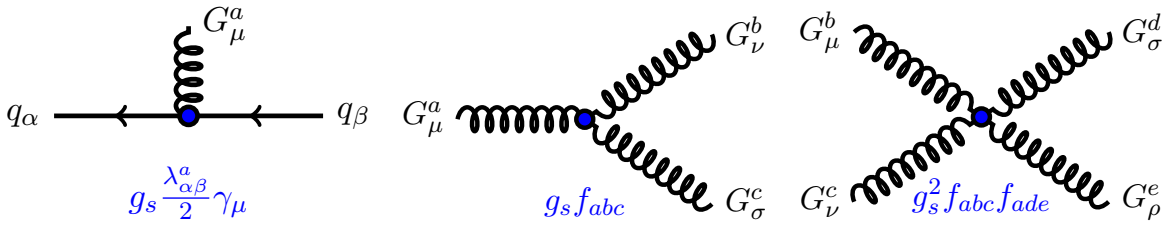

Figure 1.3: Interaction vertices of the QCD Lagrangian. The first Feynman diagram corresponds to the third term of Equation 1.22, the second and the third diagrams correspond to fourth and fifth terms respectively.

As in QED, a mass term of the form $\frac{1}{2} m_G^2 G^\mu_a G^a_\mu$ is forbidden because is not invariant under the $SU(3)_C$ gauge transformation. Therefore the gluon is theorized as a massless particle. If we expand the Lagrangian:

$$\begin{aligned}\mathcal{L}_{\text{QCD}} = &-\frac{1}{4}\left(\partial^\mu G^\nu_a - \partial^\nu G^\mu_a\right)\left(\partial_\mu G^a_\nu - \partial_\nu G^a_\mu\right) + \sum_f \bar{q}^\alpha_f \left(i\gamma^\mu \partial_\mu - m_f\right) q^\alpha_f \\ &- g_s G^\mu_a \sum_f \bar{q}^\alpha_f \gamma^\mu \left(\frac{\lambda_a}{2}\right)_{\alpha\beta} q^\beta_f \\ &+ \frac{g_s}{2} f^{abc}\left(\partial^\mu G^\nu_a - \partial^\nu G^\mu_a\right) G^b_\mu C^c_\nu - \frac{g_s^2}{4} f^{abc} f_{ade} G^\mu_b G^\nu_c G^d_\mu G^e_\nu,\end{aligned} \tag{1.22}$$

the first line corresponds to the kinetic terms of the different fields which give rise to the corresponding propagators. The second line represents the colour interaction between quarks and gluons. And finally, the third line contains the cubic and quartic gluon self-interactions. Differently from QED, this term appears in QCD due to the non-Abelian character of the theory. When a gauge theory is Abelian, the generators commute and does not exist the interaction between the gauge bosons. This is the case of QED, where the photons do not interact with themselves. See Figure 1.3 for a graphic representation of the interaction vertices of the QCD Lagrangian.

The gauge transformation of the gluon fields is more complicated than the one obtained in QED for the photon. The non-commutativity of the $SU(3)_C$ fields (see Equation 1.18) gives rise to an additional term involving the gluon fields themselves. This is a general property of non-Abelian gauge theories. The triple gauge boson interaction (and all higher point functions) is proportional to the structure constants of the gauge group, f^{abc} in QCD, where a, b, c run over vector bosons.

1.2.1 QCD loop corrections

In section 1.1 we have introduced the corrections in α to an observable in QED calculations. This kind of corrections is also present in QCD in α_s. As in QED, the corrections are labelled as N^{n}LO, with n being the number of additional loops or real emissions considered in the Feynman diagrams.

In QCD, things are more complicated due to the existence of gluon loops. An example is seen in the second diagram of Figure 1.4. These kinds of diagrams do not exist in QED with photons. Analogously

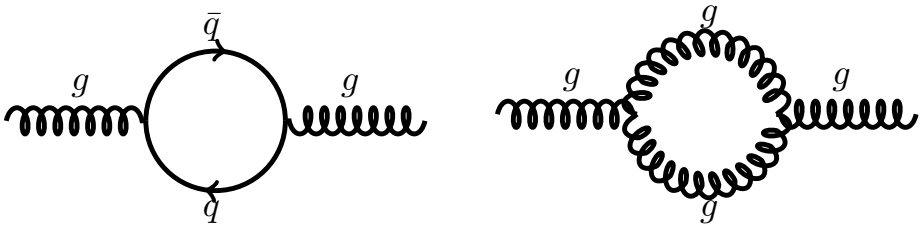

Figure 1.4: QCD first-order loops.

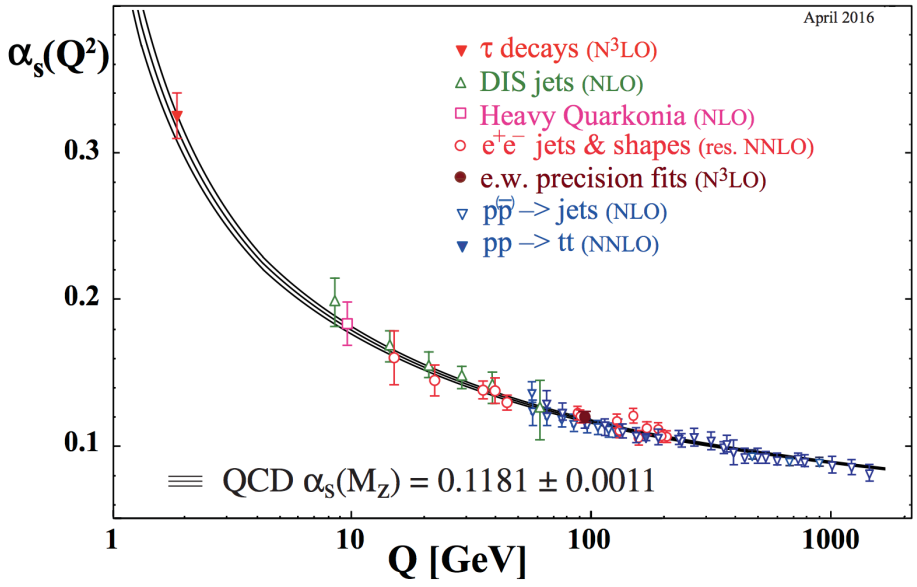

Figure 1.5: Summary of measurements of α_s as a function of the energy scale Q [7]. The respective degree of QCD perturbation theory used in the extraction of α_s is indicated in brackets (NLO: next-to-leading order; NNLO: next-to-next-to leading order; res. NNLO: NNLO matched with resummed next-to-leading logs; N^{3}LO: next-to-NNLO).

to QED, the one-loop running coupling constant in QCD is:

$$\alpha_s\left(Q^2\right) = \frac{\alpha_s\left(\mu^2\right)}{1 + \beta_0 \alpha_s\left(\mu^2\right) \ln\left(Q^2/\mu^2\right)}, \qquad \beta_0 > 0, \tag{1.23}$$

with $\beta_0 = (11N_c - 2N_f)/(2\pi)$ and μ an arbitrary reference scale known as renormalization scale. N_c is the number of colours (3 in the SM) and N_f the number of flavours (6 in the energies above m_t).

Differently to QED, Figure 1.5 shows how the strong coupling constant α_s decreases with the energy scale Q in different processes. This is due to the gluon self-coupling and it is called anti-screening. We observe that at short distances strong interactions become weaker. This is known as asymptotic freedom and explains why we can describe $q\bar{q}$ scattering as an asymptotically free process. Also, the plot shows how the strong force increases at large distances, this is known as confinement, and explain the non-observation of free quarks. These phenomena were studied by David Politzer, David Gross and Frank Wilczek in 1973 [10, 11]. They were awarded the Nobel Prize in 2004.

1.3 The weak interaction and electroweak unification

The weak interaction is responsible for the radioactive decay and decay of atoms. In 1956, Chien-Shiung Wu studied β-decay and demonstrated parity violation by the weak force [12]. This result was not expected by the physics community, which had previously regarded parity as a conserved quantity. From the Wu experiment it can be deduced that the part of the weak interaction responsible for β-decay involves only the left-handed quarks and leptons (or the right-handed antiquarks and antileptons). The right-handed particles do not feel the charged interaction.

Physicists started to develop theories in which new bosons could explain correctly the behaviour of the left- and right-handed fields. Sheldon Glashow added an unbroken symmetry to the theory. He solved it by breaking the symmetry by hand, giving rise a new particle, the Z boson [13]. In 1964, Abdus Salam and Steven Weinberg had the same idea. They predicted in their theory a photon, the neutral Z boson and the two charged bosons called $W^{\pm}$ [14,15].

In 1967, Weinberg found a set of symmetries that produced the unification of the weak force and QED, the electroweak force [16]. Furthermore, this theory was renormalizable[1]. Sheldon Glashow, Abdus Salam, and Steven Weinberg were awarded the 1979 Nobel Prize in Physics for their contributions to the unification of the weak and electromagnetic interaction.

The W and Z bosons were discovered at CERN in 1983 by the Proton-Antiproton collider (SppS) [19–22]. These bosons were found to be massive. The simplest group to include the W and Z bosons and photon in a unified theory seems to be $G \equiv SU(2)_L \otimes U(1)_Y$, where L refers to left-handed fields and Y is the hypercharge that we will define along this section.

Consider a single family of quarks with the notation:

$$\psi_1(x) = \begin{bmatrix} u \\ d' \end{bmatrix}_L, \qquad \psi_2(x) = u_R, \qquad \psi_e(x) = d_R, \tag{1.24}$$

and the same for the lepton sector:

$$\psi_1(x) = \begin{bmatrix} \nu_e \\ e^- \end{bmatrix}_L, \qquad \psi_2(x) = \nu_{eR}, \qquad \psi_3(x) = e^-_R. \tag{1.25}$$

We start with the free Lagrangian which we write here for the quarks, but which looks analogously for the leptons:

$$\mathcal{L}_0 = i\bar{u}(x)\gamma^\mu \partial_\mu u(x) + i\bar{d}(x)\gamma^\mu \partial_\mu d(x) = \sum_{j=1}^{3} i\bar{\psi}_j(x)\gamma^\mu \partial_\mu \psi_j(x), \tag{1.26}$$

[1] In 1971, Gerard 't Hooft proved that spontaneously broken gauge symmetries are renormalizable even with massive gauge bosons [17,18]

which is invariant under global G transformations in flavour space:

$$\begin{aligned} \psi_1(x) &\xrightarrow{G} \psi_1(x)' \equiv e^{iY_1\beta} U_L \psi_1(x) \\ \psi_2(x) &\xrightarrow{G} \psi_2(x)' \equiv e^{iY_2\beta} \psi_2(x) \\ \psi_3(x) &\xrightarrow{G} \psi_3(x)' \equiv e^{iY_3\beta} \psi_3(x), \end{aligned} \tag{1.27}$$

where $U_L \equiv e^{i\frac{\tau_i}{2}\alpha^i}$ is the $SU(2)_L$ transformation and only acts on the doublet field $\psi_1(x)$ (τ_i are the Pauli matrices). Since the $U(1)_Y$ phase transformation is analogous to the QED one, the parameter Y_i is called hypercharge. On the other hand, the matrix transformation U_L is non-abelian like QCD.

We now impose the Lagrangian to be also invariant under local $SU(2)_L \otimes U(1)_Y$ gauge transformations. Since we have four gauge parameters, $\alpha^i(x)$ and $\beta(x)$, four different gauge bosons are needed:

$$\begin{aligned} D_\mu\psi_1(x) &\equiv \left[\partial_\mu + ig_W \tilde{W}_\mu(x) + ig_Y Y_1 B_\mu(x)\right] \psi_1(x) \\ D_\mu\psi_2(x) &\equiv \left[\partial_\mu + ig_Y Y_2 B_\mu(x)\right] \psi_2(x) \\ D_\mu\psi_3(x) &\equiv \left[\partial_\mu + ig_Y Y_3 B_\mu(x)\right] \psi_3(x), \end{aligned} \tag{1.28}$$

where $\tilde{W}_\mu(x) \equiv \frac{\tau_i}{2} W^i_\mu(x)$ denotes a $SU(2)_L$ matrix field. The transformation of B_μ is identical to the photon in QED, while W^i_μ fields transform in an analogous way to the gluons in QCD. To construct the kinematic term we need to define the corresponding field strengths:

$$\begin{aligned} B_{\mu\nu} &\equiv \partial_\mu B_\nu - \partial_\nu B_\mu, \\ \tilde{W}_{\mu\nu} &\equiv -\frac{i}{g_W}\left[\left(\partial_\mu + ig_W\tilde{W}_\mu\right)\left(\partial_\nu + ig_W\tilde{W}_\nu\right)\right] = \partial_\mu\tilde{W}_\nu - \partial_\nu\tilde{W}_\mu + ig_W\left[\tilde{W}_\mu, \tilde{W}_\nu\right], \\ \tilde{W}_{\mu\nu} &\equiv \frac{\tau_i}{2} W^i_{\mu\nu}, \qquad W^i_{\mu\nu} = \partial_\mu W^i_\nu - \partial_\nu W^i_\mu - g_W \epsilon^{ijk} W^j_\mu W^k_\nu. \end{aligned} \tag{1.29}$$

The final Lagrangian which describes the electroweak (EW) interaction, invariant under local G transformations, is:

$$\mathcal{L}_{\text{EW}} = \sum_{j=1}^{3} i\bar{\psi}_j(x)\gamma^\mu D_\mu \psi_j(x) - \frac{1}{4} B_{\mu\nu}B^{\mu\nu} - \frac{1}{4} W^i_{\mu\nu} W_i^{\mu\nu}. \tag{1.30}$$

A remarkable fact is that the gauge symmetry forbids a mass term in the Lagrangian for the gauge bosons and for the fermions. Experimentally we know that the bosons $W^\pm$ and Z are massive, so the mass term should appear through some other mechanism (see section 1.4).

1.3.1 Charged currents and CP-violation

The three families of quarks and leptons of the SM are three identical copies of the same $SU(2)_L \otimes U(1)_Y$ structure, where the only difference is the mass of the different generations. The piece from the

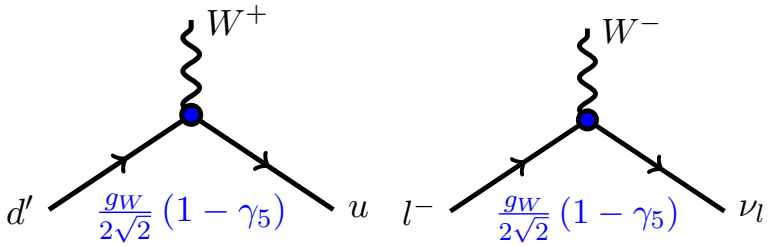

Figure 1.6: Interaction vertices of the charged-current Lagrangian. The Feynman diagram on the left corresponds to a charged-current involving quarks, while the one on the right involves leptons.

Lagrangian 1.30 which contains the $SU(2)_L$ matrix

$$\tilde{W}_\mu = \frac{\tau^i}{2} W^i_\mu = \frac{1}{2}\begin{bmatrix} W^3_\mu & \sqrt{2}W^\dagger_\mu \\ \sqrt{2}W_\mu & -W^3_\mu \end{bmatrix} \tag{1.31}$$

is the one which mediates the charged-current interactions with the boson field $W_\mu \equiv \left(W^1_\mu + iW^2_\mu\right)/\sqrt{2}$ and the complex-conjugate $W^\dagger_\mu \equiv \left(W^1_\mu - iW^2_\mu\right)/\sqrt{2}$. The charged-current Lagrangian is then:

$$\begin{aligned} \mathcal{L}_{\text{CC}} &= -\frac{g_W}{2\sqrt{2}}\left\{ W^\dagger_\mu \left[\sum_{ij} \bar{u}_i \gamma^\mu (1-\gamma_5)\, d'_j + \sum_l \bar{\nu}_l \gamma^\mu (1-\gamma_5)\, l \right] + \text{h.c.} \right\} \\ &= -\frac{g_W}{2\sqrt{2}}\left\{ W^\dagger_\mu \left[\sum_{ij} \bar{u}_i \gamma^\mu (1-\gamma_5)\, V_{ij} d_j + \sum_l \bar{\nu}_l \gamma^\mu (1-\gamma_5)\, l \right] + \text{h.c.} \right\}. \end{aligned} \tag{1.32}$$

This Lagrangian describes the interaction of the charged gauge bosons $W^\pm$ with the quarks (left diagram of Figure 1.6) and leptons (right diagram of Figure 1.6).

In the SM, only the charged current interactions can change the flavour of the fermions. The second line in Equation 1.33 changes from the weak eigenstates to the mass eigenstates in the quark sector. The unitary matrix V couples any *up-type* quark with all *down-type* quark. The mixing matrix V is called Cabibbo-Kobayashi-Maskawa (CKM) matrix [23, 24]. It is formed by three mixing angles and one phase. The standard notation for this matrix is:

$$\begin{aligned} V &= \begin{bmatrix} V_{ud} & V_{us} & V_{ub} \\ V_{cd} & V_{cs} & V_{cb} \\ V_{td} & V_{ts} & V_{tb} \end{bmatrix}. \\ &= \begin{bmatrix} c_{12}c_{13} & s_{12}c_{13} & s_{13}e^{-i\delta_{13}} \\ -s_{12}c_{23} - c_{12}s_{23}s_{13}e^{i\delta_{13}} & c_{12}c_{23} - s_{12}s_{23}s_{13}e^{i\delta_{13}} & s_{23}c_{13} \\ s_{12}s_{23} - c_{12}c_{23}s_{13}e^{i\delta_{13}} & -c_{12}s_{23} - s_{12}c_{23}s_{13}e^{i\delta_{13}} & c_{23}c_{13} \end{bmatrix}, \end{aligned} \tag{1.33}$$

where $c_{ij} \equiv \cos\theta_{ij}$ and $s_{ij} \equiv \sin\theta_{ij}$, with $i, j = 1, 2, 3$. The current experimental values of the CKM matrix elements are summarized in Table 1.1.

	Independently measured	SM global fit
$\|V_{ud}\|$	0.97420 ± 0.00021	0.97446 ± 0.00010
$\|V_{us}\|$	0.2243 ± 0.0005	0.22452 ± 0.00044
$\|V_{ub}\|$	0.00394 ± 0.00036	0.00365 ± 0.00012
$\|V_{cd}\|$	0.218 ± 0.004	0.22438 ± 0.00044
$\|V_{cs}\|$	0.997 ± 0.017	$0.97359^{+0.00010}_{-0.00011}$
$\|V_{cb}\|$	0.0422 ± 0.0008	0.04214 ± 0.00076
$\|V_{td}\|$	0.0081 ± 0.0005	$0.00896^{+0.00024}_{-0.00023}$
$\|V_{ts}\|$	0.0394 ± 0.0023	0.04133 ± 0.00074
$\|V_{tb}\|$	1.019 ± 0.025	0.999105 ± 0.000032

Table 1.1: CKM matrix elements values from independent measurements and from a global SM fit [7].

For massive neutrinos, we could add a term in the Equation 1.33 which would contain a mixing matrix for leptons. This matrix, V_{PMNS}, is called Pontecorvo-Maki-Nakagawa-Sakata matrix and was introduced in Refs. [25–27].

As demonstrated in the β-decay experiment by Chien-Shiung Wu, in the charged currents only left-handed fermions and right-handed antifermions couple to the $W^{\pm}$. Therefore there is a 100% breaking of parity (P: left $\leftrightarrow$ right) and charge conjugation (C: particle $\leftrightarrow$ antiparticle). But the combined transformation CP is still a good symmetry. However, a small violation of the CP at the level of 0.2% is observed in the neutral kaon system [28, 29] and more sizeable signals of CP violation have been observed at the B factories.

This observed violation in the K system was the motivation for assuming third generations of fermions before the discovery of the bottom quark and tau lepton. Note that δ_{13} in Equation 1.33 is the only complex phase in the SM Lagrangian, so it is the only possible source of CP-violation phenomena in the quark sector.

1.3.2 Neutral currents

Equation 1.30 also describes neutral interactions with the gauge fields W^3_μ and B_μ, so we want to relate these gauge fields with the bosons Z and γ.

However, since the photon has the same interaction with both fermion chiralities, the singlet gauge boson B_μ cannot be the electromagnetic field. That would require $Y_1 = Y_2 = Y_3$ and $g_Y Y_j = eQ_j$, which cannot be simultaneously true. Since both fields are neutral, we can try with an arbitrary combination of them:

$$\begin{bmatrix} W^3_\mu \\ B_\mu \end{bmatrix} = \begin{bmatrix} \cos\theta_W & \sin\theta_W \\ -\sin\theta_W & \cos\theta_W \end{bmatrix} \begin{bmatrix} Z_\mu \\ A_\mu \end{bmatrix}, \tag{1.34}$$

where θ_W is the so-called Weinberg angle. With this transformation, we can rewrite the Lagrangian in terms of A_μ and Z_μ:

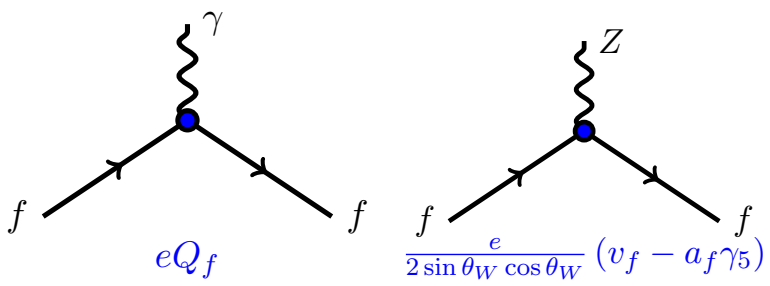

Figure 1.7: Interaction vertices of the neutral-current Lagrangian. The Feynman diagram in the left correspond to the interaction of fermions with a photon. The one on the right corresponds to the interaction of fermions with the Z boson.

$$\mathcal{L}_{\text{NC}} = -\sum_j \bar{\psi}_j(x)\gamma^\mu \Big\{ \quad A_\mu \quad \Big[g_W \frac{\tau_3}{2} \sin\theta_W + g_Y y_j \cos\theta_W \Big] + \qquad (1.35)$$
$$Z_\mu \quad \Big[g_W \frac{\tau_3}{2} \cos\theta_W - g_Y y_j \sin\theta_W \Big] \Big\} \psi_j.$$

To be consistent, we must reproduce the QED Lagrangian from the A_μ piece. For that purpose, we impose:

$$g_W \sin\theta_W = g_Y \cos\theta_W = e, \qquad Y = Q - T_3, \qquad (1.36)$$

where Q is expressed as

$$Q_1 = \begin{bmatrix} Q_{u/\nu} & 0 \\ 0 & Q_{d/e} \end{bmatrix}, \qquad Q_2 = Q_{u/\nu}, \qquad Q_3 = Q_{d/e}, \qquad (1.37)$$

and $T_3 \equiv \frac{\tau_3}{2}$ is the third component of the weak isospin. Fermions with negative chirality have $T = 1/2$ and can be grouped into doublets with $T_3 = \pm 1/2$ that behave the same way under the weak interaction. Up-type quarks (u, c, t) have $T_3 = +1/2$ and down-type quarks (d, s, b) have $T_3 = -1/2$. The same occurs with the leptons, where (e^-, μ^-, τ^-) have $T_3 = -1/2$ and the neutrinos have $T_3 = 1/2$. In all cases, the corresponding anti-fermion has reversed chirality and opposite sign for T_3.

The neutral-current Lagrangian takes the form

$$\mathcal{L}_{\text{NC}} = \mathcal{L}_{\text{QED}} + \mathcal{L}^Z_{\text{NC}}, \qquad (1.38)$$

where

$$\mathcal{L}_{\text{QED}} = -eA_\mu \sum_j \bar{\psi}_j \gamma^\mu Q_j \psi_j \equiv -eA_\mu J^\mu_{em}, \qquad (1.39)$$

for the QED part (left daigram of Figure 1.7) and

$$\mathcal{L}^Z_{\text{NC}} = -\frac{e}{2\sin\theta_W \cos\theta_W} Z_\mu \sum_f \bar{f}\gamma^\mu \left(v_f - a_f\gamma_5\right) f, \qquad (1.40)$$

	u	d	ν_e	e
$2v_f$	$1-\frac{8}{3}\sin^2\theta_W$	$-1+\frac{4}{3}\sin^2\theta_W$	1	$-1+4\sin^2\theta_W$
$2a_f$	1	-1	1	-1

Table 1.2: Fermion couplings to the Z boson.

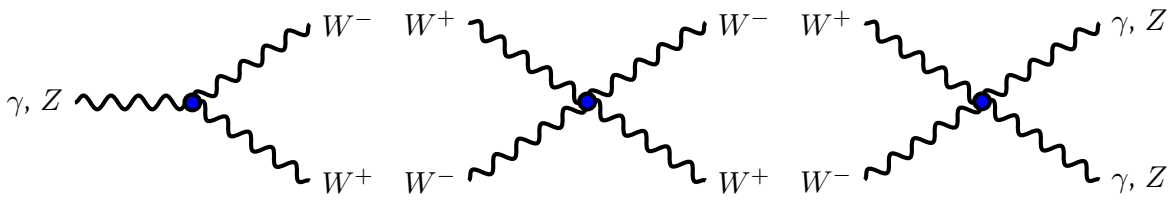

Figure 1.8: Self-interaction vertices of the gauge bosons. The first Feynman diagram corresponds to the Lagrangian of Equation 1.42 while the second and the third correspond to the Lagrangian of Equation 1.43.

for the Z-boson interaction with the neutral fermionic current (right diagram of Figure 1.7), where $a_f = T_3^f$ and $v_f = T_3^f\left(1-4|Q_f|\sin^2\theta_W\right)$. The different fermion couplings to the Z boson are given in Table 1.2. We see that each fermion interacts with the Z boson with a different strength. The pattern is the same for the second and third generation.

Thus, we have a unified description of the electromagnetic and weak interaction.

1.3.3 Gauge self-interactions

There is a piece in the Lagrangian 1.30 which generates cubic and quartic self-interactions among the gauge bosons. Expanding this term one finds:

$$\begin{aligned}\mathcal{L}_3 = ie\cot\theta_W\Big\{ &\left(\partial^\mu W^\nu - \partial^\nu W^\mu\right) W_\mu^\dagger Z_\nu \;-\; \left(\partial^\mu W^{\nu\dagger} - \partial^\nu W^{\mu\dagger}\right) W_\mu Z_\nu \\ &+\; W_\mu W_\nu^\dagger\left(\partial^\mu Z^\nu - \partial^\nu Z^\mu\right)\Big\} \\ +ie\Big\{ &\left(\partial^\mu W^\nu - \partial^\nu W^\mu\right) W_\mu^\dagger A_\nu \;-\; \left(\partial^\mu W^{\nu\dagger} - \partial^\nu W^{\mu\dagger}\right) W_\mu A_\nu \\ &+\; W_\mu W_\nu^\dagger\left(\partial^\mu A^\nu - \partial^\nu A^\mu\right)\Big\},\end{aligned} \tag{1.41}$$

$$\begin{aligned}\mathcal{L}_4 = -\frac{e^2}{2\sin^2\theta_W}&\left\{\left(W_\mu^\dagger W^\mu\right)^2 - W_\mu^\dagger W^{\mu\dagger} W_\nu W^\nu\right\} \\ -e^2\cot^2\theta_W&\left\{W_\mu^\dagger W^\mu Z_\nu Z^\nu - W_\mu^\dagger Z^\mu W_\nu Z^\nu\right\} \\ -e^2\cot\theta_W&\left\{2W_\mu^\dagger W^\mu Z_\nu A^\nu - W_\mu^\dagger Z^\mu W_\nu A^\nu - W_\mu^\dagger A^\mu W_\nu Z^\nu\right\} \\ -e^2&\left\{W_\mu^\dagger W^\mu A_\nu A^\nu - W_\mu^\dagger A^\mu W_\nu A^\nu\right\}.\end{aligned} \tag{1.42}$$

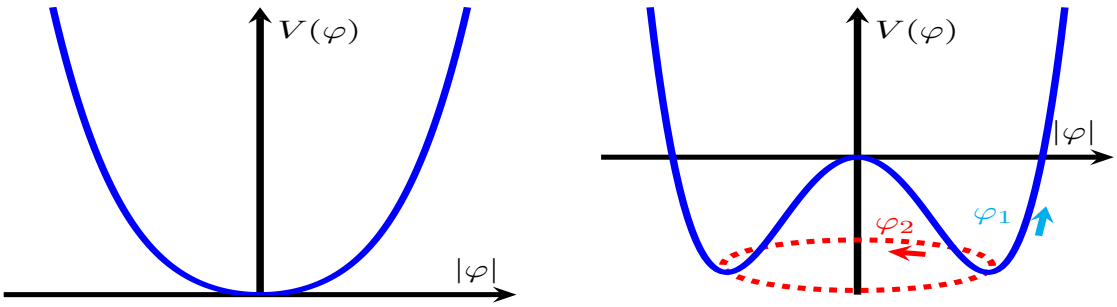

Figure 1.9: Shape of the scalar potential, $V(\varphi)$, from Equation 1.43 for $\mu^2 > 0$ (left) and $\mu^2 < 0$ (right). In the second case there is a continuous set of degenerate vacuum, corresponding to different phases θ, connected through a massless field excitation φ_2 (in red in the plot). This potential is known as mexican-hat potential.

We see that a W^+W^- pair is always involved in the gauge interactions. Furthermore, an interaction with three or four Z bosons does not exist (see Figure 1.8). The triple and quartic gauge coupling are important tests in the SM. They have been studied by several authors, see for instance Refs. [30, 31].

1.4 Spontaneous symmetry breaking

In the discussion of sections 1.1, 1.2 and 1.3 all gauge bosons must be massless. The Lagrangian does not allow for a mass term. For photons and gluons that prediction agrees with experiment to very good accuracy. The W and Z bosons are found to be massive ($m_W \approx 80$ GeV and $m_Z \approx 91$ GeV). In this section we introduce the Higgs mechanism which will generate the mass terms we need.

1.4.1 Goldstone theorem

Let's introduce the Goldstone Theorem [32, 33], which is crucial to understand the mechanism that generates the masses in the SM. We start with a complex scalar field, $\varphi(x)$, which is described in the following Lagrangian:

$$\mathcal{L} = \partial_\mu \varphi(x)^\dagger \partial^\mu \varphi(x) - V(\varphi), \qquad V(\varphi) = \mu^2 \varphi^\dagger \varphi + \lambda(\varphi^\dagger \varphi)^2, \tag{1.43}$$

which is invariant under global phase transformation of the form

$$\varphi(x) \to \varphi(x)' = e^{i\theta}\varphi(x). \tag{1.44}$$

Let's study the potential. To ensure a ground state, we need λ to be positive. However for μ^2 we have two possibilities (see Figure 1.9):

- $\mu^2 > 0$. In this case the only minimum is $\varphi = 0$. It describes a massive scalar particle with mass μ and quartic coupling λ.
- $\mu^2 < 0$. We obtain a minimum for all field configurations satisfying

$$|\varphi_0| = \sqrt{\frac{-\mu^2}{2\lambda}} \equiv \frac{v}{\sqrt{2}} > 0, \qquad V(\varphi_0) = -\frac{\lambda}{4}v^4. \tag{1.45}$$

Due to the phase invariance of the Lagrangian, fields of the form $\varphi_0(x) = \frac{v}{\sqrt{2}}e^{i\theta}$ are all valid. We can choose for instance $\theta = 0$ as the ground state, but independently of the value of θ, the symmetry gets spontaneously broken (SSB).

Parameterizing the excitations over the ground state as

$$\varphi(x) = \frac{1}{\sqrt{2}}\left(v + \varphi_1(x) + i\varphi_2(x)\right), \tag{1.46}$$

where φ_1 and φ_2 are real fields, the potential is then:

$$V(\varphi) = V(\varphi_0) - \mu^2\varphi_1^2 + \lambda v\varphi_1\left(\varphi_1^2 + \varphi_2^2\right) + \frac{\lambda}{4}\left(\varphi_1^2 + \varphi_2^2\right)^2, \tag{1.47}$$

which describes a massive state of mass $m_{\varphi 1} = -2\mu^2$ and a massless state φ_2. We see then that in the case $\mu^2 < 0$ a massless particle is generated, this means that the field φ_2 describes excitations into states with the same energy as the chosen ground state, i.e. excitations without energy cost corresponding to a massless particle.

This is a general result and is known as the Goldstone theorem: if a Lagrangian is invariant under a continuous symmetry group, G, but the vacuum is only invariant under a subgroup $H \subset G$, then there must exist as many massless spin-0 particles (Nambu-Goldstone bosons) as broken generators (i.e., generators of G which do not belong to H) [34,35].

1.4.2 Higgs mechanism

The mechanism for giving mass to the gauge bosons was independently developed by Robert Brout and François Englert [36]; by Peter Higgs [37]; and by Gerald Guralnik, C. R. Hagen, and Tom Kibble [38,39] in 1964. The mechanism uses the Goldstone theorem. We start with a $SU(2)_L$ doublet of scalar fields

$$\varphi(x) = \begin{bmatrix} \varphi^{(+)}(x) \\ \varphi^{(0)}(x) \end{bmatrix}, \tag{1.48}$$

which is described by a Lagrangian which is invariant under local $SU(2)_L \otimes U(1)_Y$ transformations:

$$\begin{aligned} \mathcal{L}_s &= (D_\mu\varphi)^\dagger D^\mu\varphi - \mu^2\varphi^\dagger\varphi - \lambda\left(\varphi^\dagger\varphi\right)^2, \qquad (\lambda > 0, \mu^2 < 0) \\ D^\mu\varphi &= \{\partial^\mu + ig_W\tilde{W}^\mu + ig_Y y_\varphi B^\mu\}\varphi, \qquad Y_\varphi = Q_\varphi - T_3 = \frac{1}{2}. \end{aligned} \tag{1.49}$$

The scalar hypercharge is fixed by requiring that the photon, A_μ, does not couple to $\varphi^{(0)}$, and $\varphi^{(+)}$ has the right electric charge. The potential is very similar to that of Goldstone Equation 1.43. Therefore, there is an infinite set of degenerate states with vacuum expectation value for $\varphi^(0)$:

$$\langle 0|\varphi^{(0)}|0\rangle = \sqrt{\frac{-\mu^2}{2\lambda}} \equiv \frac{v}{\sqrt{2}}. \tag{1.50}$$

Since the electric charge is a conserved quantity, only the neutral scalar field can acquire a vacuum expectation value. Once $\varphi^{(0)}$ gets a non-vanishing vacuum expectation value, the $SU(2)_L \otimes U(1)_Y$ symmetry gets spontaneously broken to the electromagnetic group $U(1)_{\text{QED}}$ which by construction still remains a true symmetry of the vacuum. As in the Goldstone case, we will write the scalar doublet considering excitations of the physical vacuum:

$$\varphi(x) = e^{i\frac{\tau_i}{2}\theta^i(x)} \frac{1}{\sqrt{2}} \begin{pmatrix} 0 \\ v + H(x) \end{pmatrix}, \tag{1.51}$$

in which we have four degrees of freedom (three real fields $\theta^i(x)$ and $H(x)$). Following Goldstone theorem, as $SU(2)_L \otimes U(1)_Y$ (4 generators; $\tau_i/2$ from $SU(2)_L$ and Y from $U(1)_Y$) gets broken into $U(1)_{\text{QED}}$ (1 generator; Q), there should be 3 massless Goldstone bosons. Since we have local $SU(2)_L$ invariance, we can choose a particular gauge for which $\theta^i(x) = 0$. The field $H(x)$ corresponds to massive scalar field; the Higgs boson. The doublet becomes:

$$\varphi(x) = \frac{1}{\sqrt{2}} \begin{bmatrix} 0 \\ v + H(x) \end{bmatrix}. \tag{1.52}$$

Introducing it in the Lagrangian 1.49, and expanding it in terms of the W_μ and Z_μ fields, one gets the following kinematic Lagrangian

$$\mathcal{L}_{\text{kin}} = \frac{1}{2}\left\{ (\partial_\mu H)(\partial^\mu H) + (v+H)^2 \left(\frac{g_W^2}{4} W_\mu^\dagger W_\mu + \frac{g_W^2}{8\cos^2\theta_W} Z_\mu Z^\mu \right) \right\}, \tag{1.53}$$

which contains a mass term for the bosons $W^\pm$ and Z:

$$\begin{aligned} \frac{v^2 g_W^2}{4} &= M_W^2 \to M_W = \frac{v g_W}{2}, \\ \frac{v^2 g_W^2}{8\cos^2\theta_W} &= \frac{1}{2} M_Z^2 \to M_Z = \frac{v g_W}{2\cos\theta_W}. \end{aligned} \tag{1.54}$$

We can also express the electroweak mixing angle in terms of the gauge boson masses as:

$$\sin^2\theta_W = 1 - \frac{M_W^2}{M_Z^2}. \tag{1.55}$$

Furthermore, since Q is an unbroken generator, the photon remains massless. The piece of the Lagrangian which describes the new scalar field, $H(x)$, is (see Figure 1.10):

$$\mathcal{L}_s = \frac{1}{4}\lambda v^4 + \mathcal{L}_H + \mathcal{L}_{HG^2}, \tag{1.56}$$

where we have defined:

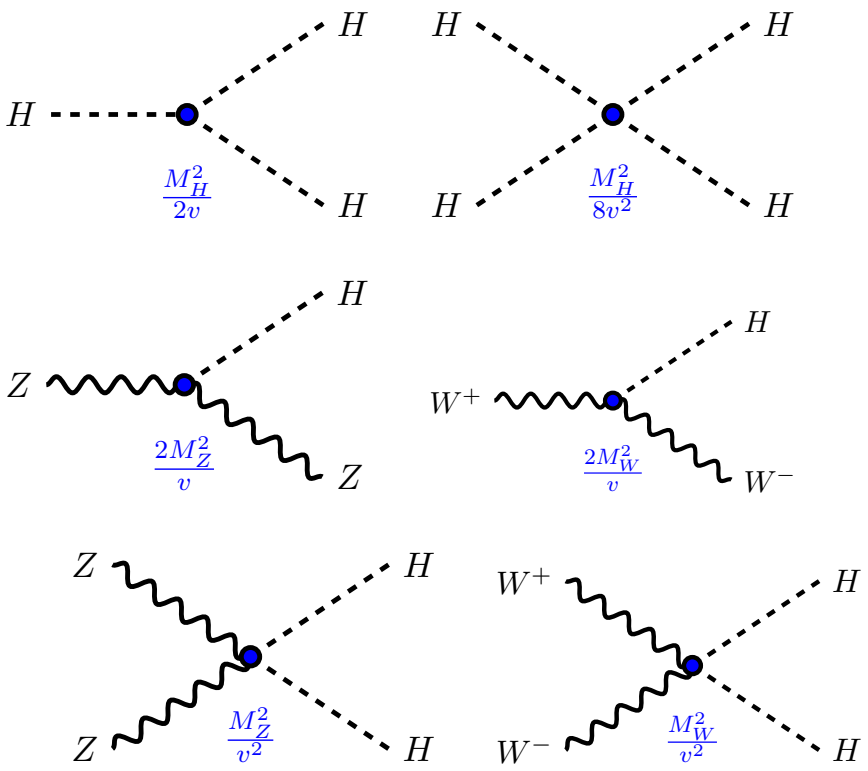

Figure 1.10: Higgs self-interaction couplings (Feynman diagram on the top) and Higgs coupling to the gauge bosons (Feyman diagram on the middle and bottom). This vertices are described in Equation 1.57.

$$\begin{aligned} \mathcal{L}_H &= \frac{1}{2}\partial_\mu H \partial^\mu H - \frac{1}{2}M_H^2 H^2 - \frac{M_H^2}{2v}H^3 - \frac{M_H^2}{8v^2}H^4, \\ \mathcal{L}_{HG^2} &= M_W^2 W_\mu^\dagger W^\mu \left\{1 + \frac{2}{v}H + \frac{H^2}{v^2}\right\} + \frac{1}{2}M_Z^2 Z_\mu Z^\mu \left\{1 + \frac{2}{v}H + \frac{H^2}{v^2}\right\}. \end{aligned} \tag{1.57}$$

From this Lagrangian, we can also extract the mass of the scalar field:

$$M_H = \sqrt{-2\mu^2} = \sqrt{2\lambda}v, \tag{1.58}$$

as a function of the vacuum expectation value, v, and the field coupling, h.

We have seen that the SSB mechanism predicts the existence of a massive scalar boson, the Higgs boson. In 2012, ATLAS and CMS announced the discovery of a new boson with a mass of 125 GeV compatible with the predicted Higgs boson [40,41]. Higgs and Englert were awarded with the Nobel Prize in 2013.

1.4.3 Yukawa sector

Since left-handed fermions are incorporated in a $SU(2)_L$ doublet, while right-handed ones form a singlet, a fermionic mass term of the form $-m\bar{\psi}\psi = -m\left(\bar{\psi}_L\psi_R + \bar{\psi}_R\psi_L\right)$ breaks the gauge symmetry and is hence forbidden in the SM.

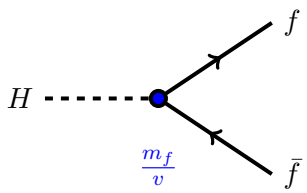

Figure 1.11: Higgs coupling to fermions from Equation 1.61.

However, since now we have a Higgs doublet the following non-violating gauge symmetry structures can be formed:

$$\mathcal{L}_Y = -\frac{1}{\sqrt{2}}(v+H)\left(y_d\bar{d}d + y_u\bar{u}u + y_e\bar{e}e\right), \tag{1.59}$$

where we have only considered the first family of fermions. Therefore, the SSB mechanism generates also fermions masses:

$$m_d = y_d\frac{v}{\sqrt{2}}, \qquad m_u = y_u\frac{v}{\sqrt{2}}, \qquad m_e = y_e\frac{v}{\sqrt{2}}. \tag{1.60}$$

The parameters y_i are called Yukawa couplings and their values are fixed by the experimental determination of the masses and v. We can rewrite the Lagrangian as (see Figure 1.11):

$$\mathcal{L}_Y = -\left(1+\frac{H}{v}\right)\left(m_d\bar{d}d + m_u\bar{u}u + m_e\bar{e}e\right). \tag{1.61}$$

Assuming a non-zero Yukawa coupling to each fermion of the SM the interaction with the Higgs field gives mass to the fermions.

1.5 The Standard Model of elementary particles

In sections 1.1 to 1.4 we have presented all the ingredients to construct the SM of the elementary particles. Thus, the SM is a relativistic quantum field gauge theory based on the symmetry group $SU(3)_C \otimes SU(2)_L \otimes U(1)_Y$ which describes strong; weak and electromagnetic interactions. This gauge symmetry is broken by the vacuum through SSB.

1.5.1 Bosons

The different interactions described by the SM are explained through the exchange of spin-1 particles. We find a massless photon for the electromagnetic interaction (section 1.1), eight different massless gluons for the strong interaction (section 1.2), and the $W^{\pm}$ and Z bosons for the weak interaction (see section 1.3 for the electroweak unification).

One further field is necessary to explain the masses of the massive bosons and fermions. This is done through the SSB mechanism (section 1.4) which, in its simple realization, gives rise an extra spin-0 particle: the Higgs boson. In Table 1.3 we list the properties of the different bosons.

Gravity is not included in the SM. A description of gravity in a gauge theory gives rise to the graviton; a spin-2 boson carrier of the gravitational interaction.

	Mass[GeV]	Q[e]
photon, γ	$< 1 \times 10^{-27}$	$< 1 \times 10^{-35}$
gluon, g	0	0
$W^{\pm}$	80.379 ± 0.012	± 1
Z	91.1876 ± 0.0021	0
higgs, H	125.18 ± 0.16	0

Table 1.3: Properties of the bosons of the SM [7]. The first column represent the current value of the measured mass, except for the gluon which we quote the theoretical value (in section 1.2 we motivate it). The second column represents the electric charge of the bosons (theoretical values except for the photon). The first four bosons are vector bosons while the Higgs boson is a scalar.

1.5.2 Fermions

Matter is formed by fermions: elementary spin-1/2 particles. There are two different type of fermions; leptons and quarks. Both are organized in three families as shown in Figure 1.1:

$$\text{I}: \begin{bmatrix} \nu_e & u \\ e^- & d \end{bmatrix}, \quad \text{II}: \begin{bmatrix} \nu_\mu & c \\ \mu^- & s \end{bmatrix}, \quad \text{III}: \begin{bmatrix} \nu_\tau & t \\ \tau^- & b \end{bmatrix}, \tag{1.62}$$

where each family is decomposed in left-handed and right-handed chirality

$$\begin{bmatrix} \nu_l & q_u \\ l^- & q_d \end{bmatrix} \equiv \begin{pmatrix} \nu_l \\ l^- \end{pmatrix}_L, \quad \begin{pmatrix} q_u \\ q_d \end{pmatrix}_L, \quad l_R^-, \quad q_{uR}, \quad q_{dR}, \tag{1.63}$$

where we have used the l and q to denote a generic lepton and quark. To this classification we also need to add the corresponding antiparticles. We see that the left-handed fields are $SU(2)_L$ doublets, while the right-handed ones are $SU(2)_L$ singlets. The three fermionic families appear to have the same properties (same quantum numbers), they only differ by their mass and their flavour quantum number (see Table 1.4). The quantum numbers for the fermions are summarized in Table 1.5.

Note then that quarks and leptons are essentially different in the way they transform under $SU(3)_C$; while the quarks are colour triplets, the leptons are colour singlets, i.e. they do not feel the strong interaction.

In the SM the neutrinos were assumed to be massless. Due to the mass generation mechanism through the SSB (see section 1.4), this implied that the existence of a right-handed neutrino was not possible. However, the experiments with solar, atmospheric, reactor and accelerator neutrinos have provided compelling evidence for oscillations of neutrinos caused by nonzero neutrino masses and neutrino mixing. This opens a new investigation area around the neutrino nature and how it can be explained within the SM. As neutrinos mix in the oscillations, the experimental mass square differences one can extract from this phenomenology are not associated to a concrete flavour.

		Mass[MeV]	Q[e]
Leptons	electron, e	$0.5109989461 \pm 0.0000000031$	-1
	electron neutrino, ν_e	-	0
	muon, μ	$105.6583745 \pm 0.0000024$	-1
	muon neutrino, ν_μ	-	0
	tau, τ	1776.86 ± 0.12	-1
	tau neutrino, ν_τ	-	0
		Mass[GeV]	Q[e]
Quarks	down, d	$\left(4.7^{+0.5}_{-0.3}\right) \cdot 10^{-3}$	-1/3
	up, u	$\left(2.2^{+0.5}_{-0.4}\right) \cdot 10^{-3}$	2/3
	strange, s	$\left(95^{+9}_{-3}\right) \cdot 10^{-3}$	-1/3
	charm, c	$1.275^{+0.025}_{-0.035}$	2/3
	bottom, b	$4.18^{+0.04}_{-0.03}$	-1/3
	top, t	173.0 ± 0.4	2/3

Table 1.4: SM leptons and quarks properties [7]. Neutrino masses are discussed in the text.

1.5.3 Hadrons: baryons and mesons

We know now that the matter we see and touch is made of atoms, which are formed by the nucleus and the electrons orbiting in different quantum states. The components of the nucleus are protons, with electric charge $Q_p = 1$, and neutrons, with $Q_n = 0$. We know today that the neutrons and protons are made of quarks. The formation of bound states is thanks to the strong force. Collectively, these bound states are called hadrons.

The hadrons are composite particles made of quarks and gluons. The hadrons are *uncoloured*, this means that the colours of the quarks that form the hadrons have to be compensated. The quarks that give the quantum properties to the hadrons are called valence quarks and give rise to a division of the hadrons into baryons and mesons.

The mesons are hadrons formed by two valence quarks with the form $q_i\bar{q_j}$, being $i, j = u, d, s, c, b$ (the top quark does not hadronize as we will explain in section 3.1). The mesons have an integer spin. On the other hand we have the baryons, which are composed by three valence quarks with the form $q_i q_j q_k$. The baryons have half-integer spin. The neutron and the proton are the most famous example of baryons, being formed by uud and udd respectively. Note that the electric charge is determined by the valence quarks, for instance for the proton $Q_p = 2 \times Q_u + Q_d = 4/3 - 1/3 = 1$. Apart from the valence quarks, the hadrons are composed by pairs of $q_i\bar{q_i}$ (sea quarks) and gluons.

With the evolution of particle colliders and the increasing centre-of-mass energy, a large number of hadrons have been discovered in the form of resonances. These resonances follow a pattern and can be classified by the spin and the electric charge. This pattern allowed physicists to predict new resonances before they were discovered.

	$SU(3)_C$	$SU(2)_L$	$U(1)_Y$
e_L	1	2	-1/2
e_R	1	1	-1
ν_{eL}	1	2	-1/2
u_L	3	2	1/6
u_R	3	1	2/3
d_L	3	2	1/6
d_R	3	1	-1/3

Table 1.5: Fermion quantum numbers. These numbers represent the dimension of each representation.

1.6 Effective field theory

The SM is the collection of all the particles and interactions explained in the previous sections. However there is evidence that the SM is still not a complete theory. It does not include gravitation as a quantum field theory and does not offer a clear explanation of what could constitute the dark matter. Furthermore, particle colliders have tested the SM until its edge giving some measurements that differ significantly from the predictions in the SM. Good examples are the anomalies found in semi-leptonic B-meson decays by the Babar, Belle and LHCb experiments [42]. All of this, together with the wish of a great theory of the unification, lead particle physicists to work on different theories Beyond the Standard Model (BSM) to address these problems.

Effective field theories (EFTs) are widely used in high energy physics to parameterize the a priori unknown effects of new physics at lower energies. The basic idea is to calculate the phenomenology of the more complete theory without knowing the exact theory that is behind the SM by systematically extending the SM with all operators compatible with the gauge structure of the theory. An EFT is a well-defined quantum field theory, with radiative corrections and regularization and renormalization scheme necessary to obtain finite matrix elements. For academic lectures of effective field theories the reader is referred to Refs. [43, 44].

1.6.1 General aspects of an effective field theory: Fermi theory

Effective field theories are the appropriate theoretical tool to describe low-energy physics with respect to some high energy scale Λ. The relevant degrees of freedom, i.e. those states with $m \ll \Lambda$ are taken into account explicitly, while the heavier excitations with $M, p \gg \Lambda$ are integrated out from the action. One gets in this way a string of non-renormalizable interactions among the light states, which can be organized as an expansion in powers of E/Λ, where E is the energy at which the interaction studied occurs. The information on the heavier degrees of freedom is then contained in the couplings of the resulting low-energy Lagrangian. Although effective field theories contain an infinite number of terms, renormalizability is not an issue since, at a given order in the energy expansion, the low-energy theory is specified by a finite number of couplings; this allows for an order-by-order renormalization [43].

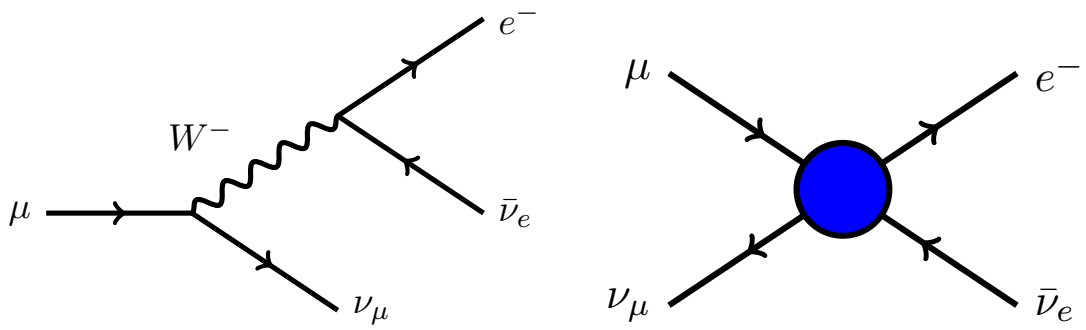

Figure 1.12: Muon decay with a W^- propagator (left) and the same decay shrinking the propagator into a point (right).

A good example of an EFT is Fermi theory. Let us consider the process $\mu^- \to e^- \bar{\nu}_e \nu_\mu$ which represents the muon decay mediated by the W boson represented in the left diagram of Figure 1.12. In a low-energy limit we can approximate the Feynman diagram on the left by the four-fermion interaction of the diagram on the right. If the W-boson mass is much larger than the energy transfer, the W boson can be integrated out:

$$\frac{g^2}{M_W^2 - q^2} \approx \frac{g^2}{M_W^2} = \frac{4\pi\alpha}{\sin^2\theta_W M_W^2} \equiv 4\sqrt{2} G_F, \tag{1.64}$$

where we have redefined the couplings of the EW theory in terms of a new constant, G_F, called Fermi's constant. Historically the reasoning was the inverse. Fermi wanted to explain β-decay and resolved the problem using the contact interaction without any propagator. The mediators of the weak interactions were unknown and the energy accessible experimentally were then insufficient to produce them. The coupling of that interaction was G_F. The Lagrangian Fermi resolved was[2]:

$$\mathcal{L} = -\frac{2G_F}{\sqrt{2}} \left[\bar{\nu}_\mu \gamma^\mu (1 - \gamma_5)\, \mu\right] \left[\bar{e} \gamma^\mu (1 - \gamma_5)\, \nu_e\right]. \tag{1.65}$$

This approximation was only valid for low energies compared with the EW scale. The current measured value of the Fermi coupling constant is [7]:

$$G_F = (1.1663787 \pm 0.0000006) \cdot 10^{-5} \text{GeV}^{-2}. \tag{1.66}$$

The Fermi constant gives also a direct determination of the EW scale, i.e., the scalar vacuum expectation value:

$$v = \left(\sqrt{2} G_F\right)^{-1/2} \approx 246 \text{ GeV}. \tag{1.67}$$

The Lagrangian in 1.65 is not renormalizable. Once the EW theory was developed, the same process was well understood through the mediation of the W boson, and the new Lagrangian (see Equation 1.33) satisfied renormalization conditions. However, Fermi's theory is very useful to understand the EFT that is used to expand the Lagrangian in terms of higher energy powers.

[2] This Lagrangian is a redefinition to the one Fermi actually employed to make it easy to compare with the one we extract from the EW theory.

1.6.2 EFT Lagrangian

The EFT Lagrangian can be constructed as:

$$\mathcal{L}_{\text{EFT}} = \sum_{\mathcal{D}\geq 0,i} \frac{c_i^{(\mathcal{D})} O_i^{(\mathcal{D})}}{\Lambda^{\mathcal{D}-4}} = \sum_{\mathcal{D}\geq 0} \frac{\mathcal{L}_{\mathcal{D}}}{\Lambda^{\mathcal{D}-4}}, \tag{1.68}$$

where $O_i^{(\mathcal{D})}$ are the allowed operators of dimension $\mathcal{D}$. All operators of dimension $\mathcal{D}$ are combined into the dimension $\mathcal{D}$ Lagrangian $\mathcal{L}_{\mathcal{D}}$. The scale Λ has been introduced so the coefficients $c_i^{(\mathcal{D})}$ (Wilson coefficients) are dimensionless. It represents the short-distance scale at which new physics occurs. Λ is a convenient device that helps to organize the EFT expansion. The SM has dimension-four operators, so for $\mathcal{D} = 4$ we reproduce the Lagrangian of the SM.

$$\mathcal{L}_{\text{EFT}} = \mathcal{L}_{\mathcal{D}\leq 4} + \frac{\mathcal{L}_5}{\Lambda} + \frac{\mathcal{L}_6}{\Lambda^2} + \dots \quad . \tag{1.69}$$

Imposing the SM gauge symmetry constraints on dimension-five operators, $O_i^{(5)}$, we get a single operator up to Hermitian conjugation and flavour assignments [45]. This operator has the form $O_{\nu\nu} \equiv \left(\tilde{\varphi}^\dagger l\right)^T C \left(\tilde{\varphi}^\dagger l\right)$, with $C = i\gamma^2\gamma^0$ in the Dirac representation. $O_{\nu\nu}$ violates the lepton number conservation (the difference between the number of leptons and the number of antileptons in an process is a conserved number) and after SSB, it generates generates a mass term for the left-handed neutrinos.

In top-quark physics, we expect the leading modification to SM processes to be at order $1/\Lambda^2$. For the analysis considered in this thesis we do not consider higher order contributions, so we will focus on operators of dimension six. Assuming baryon number conservation, the total number of dimension-six operators is 59 up to flavour assignments [45]. This is a large number of coefficients we can hope to constrain with enough data from collider experiments.

Keeping only operators of order $1/\Lambda^2$, we can expand an observable o using the EFT Lagrangian as follows:

$$o = o_{SM} + \frac{1}{\Lambda^2}\sum_i C_i o_i + \frac{1}{\Lambda^4}\sum_j \sum_k C_j C_k o_{jk}. \tag{1.70}$$

The leading EFT term proportional to Λ^{-2} reflects the interference of SM amplitudes with those featuring one dimension-six operator insertion. The terms proportional to Λ^{-4} stem from the square of the amplitudes involving one insertion of dimension-six operators, or from amplitudes involving two such insertions in interference with SM ones. As we stop at dimension-six operators, terms of order Λ^{-4} due to dimension-eight operators are ignored.

The $1/\Lambda^2$ contribution might be suppressed for a variety of reasons. For example, since all quark and lepton masses are negligible compared to the top-quark mass, a new interaction that involves a right-handed quark or lepton (except for the top quark) has a very small interference with the SM charged-current weak interactions, which only involve left-handed fermions. Some other dimension-six operators have suppressed interferences with the SM due to helicity selection rules [46]. It turns out that, although there are a large number of dimension-six operators, often only a few of them have significant effects at order $1/\Lambda^2$ in any given process.

In this thesis we will focus only on the operators of the Warsaw basis [45] affecting the top quark. In chapter 3 we introduce all the dimension-six operators we will study.

1.6.3 Validity

The use of effective field theories relies on a low-energy decoupling theorem [47]. It states that, in unbroken gauge theories, the effects of heavy fields on phenomena observed at energies scales E much smaller than their masses M are suppressed by powers of E/M. In this low-energy limit, these effects can be parameterized by a series of higher-and-higher dimensional operators suppressed by higher-and-higher powers of $1/M$. Retaining only the operators of lowest dimensions is then justified when $E/M \ll 1$.

In a bottom-up approach, that does not assume some specific heavy new physics, the operator coefficients C and mass scale Λ stand for unknown combinations of couplings and masses. They always appear as C/Λ^2 ratios (for dimension-six operators). The only model-independent information arises from the experimentally imposed constraints on C/Λ^2. The validity of the low-energy limit is then rather intangible: it requires the physical scale M of the underlying theory to be significantly higher than the energies E probed in the process described through our EFT. Without explicit model or power counting, this condition cannot be translated to bounds on either C or Λ, and no statement about the relative magnitude of different operator coefficients, of identical or different dimensions, can be made a priori either. As we will not consider the dependence on operators of higher dimensions, our results will only be interpretable in models where dimension-six operators provide the leading contributions to the observables considered. In Refs. [48–51] we find different models which receive contributions from the dimension-six operators we study in this thesis.

Under the assumption that higher-dimensional operators are subleading, one may examine what truncation of the series in powers of dimension-six operator coefficients is sensible. The expansion of an observable in dimension-six operator coefficients can be expected to contain higher-and-higher powers of CE^2/Λ^2 where, again, E is the characteristic energy scale of the process considered. For tree-level operator insertions numerical prefactors in this series can be expected to be of order one, schematically [49]:

$$\frac{o}{o^{\text{SM}}} = 1 + \mathcal{O}(1)\frac{CE^2}{\Lambda^2} + \mathcal{O}(1)\left(\frac{CE^2}{\Lambda^2}\right)^2 + \dots \quad .$$

More moderate growths with energy are also possible, especially for the linear terms which arise from interferences between EFT and SM amplitudes. This first term roughly dominates the expansion when $CE^2/\Lambda^2 \lesssim 1$. Given the experimental bound on C/Λ^2 and the energy E of the process considered, one can explicitly check whether this condition is satisfied. If it is not, higher powers of C/Λ^2 should also be included.

At lepton colliders, one can expect precision measurements at each centre-of-mass energy (which constitutes the characteristic scale of a production process) to reach the percent level. The combination of such percent-level measurements, provided they are sufficiently complementary, should be able to constrain all directions of the EFT parameter space at the $CE^2/\Lambda^2 < 10^{-2}$ level [49]. Terms beyond

the leading one are then naively expected to induce only percent-level corrections to the constraints set with a linearised EFT.

2.- Particle colliders: past, present and future

2.1 Historical overview

Modern high energy physics started in the 1960s with the advent of particle colliders. Accelerators allow to boost charged particles, mainly electrons and protons, to energies that have been increasing over the years. The first accelerator experiments used fixed targets. In order to increase the centre-of-mass energy, the concept of particle colliders was introduced, in which two particles are accelerated in opposite directions and interact in the collision points where the detectors are located.

In Figure 2.1 the progress in particle colliders is presented in terms of their year of first operation and the centre-of-mass energy at which beams are collided. We distinguish between hadron colliders (which collide protons with protons or antiprotons) and electron-positron colliders.

We see from the plot a clear log-linear trend in the increasing energy along the years. Hadron colliders lead by 15-20 years, but in that case the full energy is not available to produce new particles. This trend is first broken in the present time with the Large Hadron Collider (LHC). This log-linear trend is also present in the electron-positron colliders. The future projects also break this trend, see section 2.3. To reach higher energies at each step we need bigger colliders with a big improvement in technology. This points to a possible barrier to our exploration of the energy frontier.

2.2 Past and present colliders

Electron-positron colliders. The first electron-positron collider was AdA, built at the LNF in Frascati in 1961 which accelerated the beams up to 500 MeV. During the 1960s appeared a number of other electron-positron colliders with increasing energy: the Princeton-Stanford collider in Stanford, VEPP-II in Novosibirsk which had different upgrades in energy, the ACO accelerator at LAL laboratory in Orsay and ADONE. The maximum centre-of-mass energy in that decade did not exceed 3 GeV.

In the 1970s the new accelerators increased the collision energy up to 10 GeV. In that decade we find SPEAR and PEP at SLAC, DORIS and PETRA at DESY, and CESR at Cornell University. The accelerators started to collide particle in the range of $10-100$ GeV in the 1980s. In that decade we find the Stanford Linear Collider (SLC) at SLAC, the Large Electron-Positron collider (LEP) at CERN and TRISTAN at KEK. Consult Ref. [52] for a detailed discussion.

Hadron colliders. The first hadron collider was the Intersecting Storage Rings (ISR) at CERN. It collided protons with a maximum centre-of-mass energy of 62 GeV. It began operation in 1971 and ran until 1984.

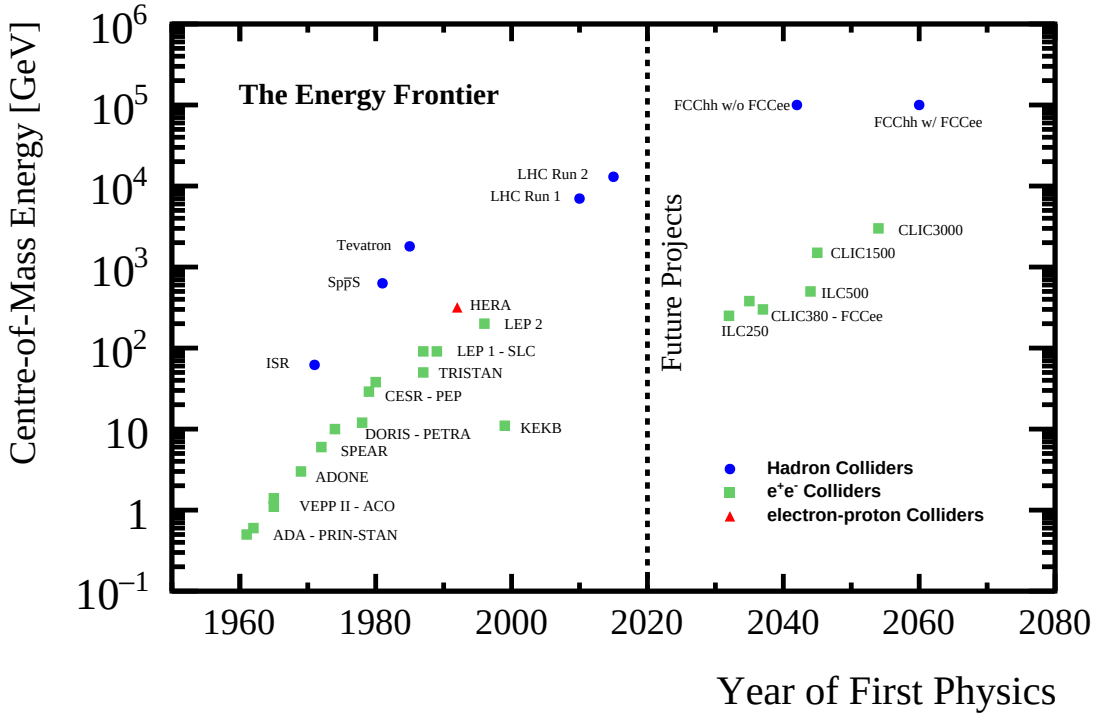

Figure 2.1: This plot shows a chart of progress in the construction of particle accelerators, which shows years on the horizontal axis and (log-scale) energy on the vertical axis. In the case of hadron colliders, the collision energy and the energy at which beams are accelerated are not the same. In the plot the energy at which beams are accelerated is shown.

It was followed by the Super Proton–Antiproton Synchrotron (SppS) also at CERN. In experiments with fixed target, the SppS could accelerate protons up to 450 GeV. When colliding protons against antiprotons, the usual centre-of-mass energy achieved was 630 GeV, i.e. 315 GeV for each beam. It began operation in 1981 and ran until 1991. The Tevatron at Fermilab was the first collider to enter the TeV regime followed by the LHC at CERN. These two colliders are discussed in more detail in the following sections.

Electron-proton collider. The Hadron-Electron Ring Accelerator (HERA) was a facility located at DESY which began operation in 1992 and closed down in 2007. At HERA, electrons or positrons were collided with protons at a centre-of-mass energy of up to 318 GeV.

2.2.1 Stanford Linear Collider (SLC)

The Stanford Linear Collider (SLC) began construction in 1983 and was completed in 1987 [53]. It was a 3-km long LINAC, being the first linear collider. It was operated from 1987 to 1998 with a constant beam energy of 45.6 GeV and up to about 80% electron-beam polarization. The beams collided in the detector called Stanford Linear Detector (SLD).

The SLD experiment accumalated a large number of Z-boson particles. The Z-boson production rate increased steadily as improvements were made to the operation of this novel machine. In the period

from 1992 to 1995, 150 thousand Z-boson events were collected. Between 1996 and 1998, 380 thousand Z-boson events were registered, including over 200 thousand events in less than 6 months of operation in 1998. Lack of funding for this program led to its termination in June of 1998. The success of the SLC machine has led to designs for the next generation of electron colliders with collision energies from 250 GeV to 3 TeV (see section 2.3).

2.2.2 Tevatron

The Tevatron was a circular particle collider hosted in Batavia (Illinois) in the United States in the laboratory of Fermilab. It consisted in a ring of 6.3 km in which protons and antiprotons were accelerated to be collided. Two experiments were installed, CDF and D0, at two different points along the Tevatron. In total it delivered more than 10 fb^{-1} of $p\bar{p}$ collisions in both experiments at a centre-of-mass energy of 1.8 and 1.96 TeV. It shut down on September 29, 2011.

Physicists observed the first $p\bar{p}$ collision produced by the Tevatron on October 13, 1985. The most important success for the Tevatron was the discovery of the top quark, announced on March 2, 1995 by both CDF and D0 [54, 55].

2.2.3 Large Electron-Positron collider (LEP)

Built in a tunnel of 27 km circumference at CERN, the Large Electron-Positron collider (LEP) was the largest circular electron-positron collider built so far [56]. It had four experiments, ALEPH, DELPHI, L3 and OPAL, which observed the collisions. It was operated from 1989 to 2000 with beam energies ranging from 45.6 to 104.5 GeV.

LEP's initial energy was chosen to be around 91 GeV on the Z-boson pole. Observing the creation and decay of the Z boson was a crucial test of the SM. In the seven years that LEP operated at the Z-pole it produced around 17 million Z boson collecting a total integrated luminosity of 200 pb^{-1} per LEP experiment approximately. In 1995 LEP was upgraded for a second operation phase doubling the energy so that the collisions could produce pairs of W bosons. The collider's energy eventually found its maximum at 209 GeV in 2000.

During 11 years of research, LEP's experiments provided a detailed study of the electroweak interaction. Measurements performed at LEP also proved that there are three generations of neutrinos to which the Z boson can decay. The main legacy of LEP is an EW precision fit at the Z-boson pole combined with data from SLC [57]. In its second stage above a centre-of-mass energy of 189 GeV, LEP searched for the Higgs boson of the SM establishing a lower bound for the Higgs boson mass [58]. LEP was closed down on 2 November 2000 to make way for the construction of the Large Hadron Collider in the same tunnel.

2.2.4 Large Hadron Collider (LHC)

The Large Hadron Collider (LHC) at CERN is the world's largest and most powerful particle accelerator. It first started up on 10 September 2008 [59]. The LHC consists of a 27-kilometre ring of superconducting dipole magnets with a number of accelerating structures to boost the energy of the particles along the way.

The LHC produces proton-proton collisions. Beams travel in opposite directions in separate beam pipes. They are guided around the accelerator ring by a strong magnetic field maintained by superconducting electromagnets with two channels with opposite-sign fields. The required temperature for the magnets is -271.3°C, very close to the absolute zero temperature. For this reason, much of the accelerator is connected to a distribution system of liquid helium, which cools the magnets, as well as to other supply services.

The beams inside the LHC are made to collide at four locations around the accelerator ring, corresponding to the positions of four particle detectors: A Toroidal LHC Apparatus (ATLAS), the Compact Muon Solenoid (CMS), A Large Ion Collider Experiment (ALICE) and the LHC-beauty (LHCb).

The LHC started its research program in 2010 with the first collisions at a centre-of-mass energy of 7 TeV (3.5 TeV per beam). In 2012 the beam energy was upgraded up to 4 TeV per beam, achieving a centre-of-mass energy of 8 TeV. After a long shutdown to prepare the collider for a higher energy and luminosity, LHC restarted activity in 2015 with a centre-of-mass energy of 13 TeV (6.5 TeV per beam). In 2018 this run finished and a second long shutdown started. The general-purpose experiments ATLAS and CMS have collected an integrated luminosity of 150 fb^{-1} at 13 TeV and will complete the nominal programme with another 150 fb^{-1} at 14 TeV.

The following stage is planned to be a high-luminosity program (HL-LHC) at a centre-of-mass energy of 14 TeV. In this run, we expect to improve the precision of several measurements.

For the studies in this thesis, we are mainly interested in the analysis performed by the ATLAS and CMS experiments. The ATLAS and CMS detectors are many-layered instruments designed to detect most of the particles produced in the collisions. They consist of different detecting subsystems arranged concentrically in layers around the collision point to record the trajectory, momentum, and energy of particles, allowing them to be individually identified and measured. A magnet system bends the paths of the charged particles so that their momenta can be measured. In Figure 2.2 the different layers of the detectors are schematically identified.

A Toroidal LHC ApparatuS, ATLAS. The largest volume detector ever constructed for a particle collider, ATLAS has the dimensions of a cylinder, 46 m long, 25 m in diameter, and sits in a cavern 100 meters below ground. The ATLAS detector weighs 7,000 tons. The four major components of the ATLAS detector are the inner detector, for measuring the momentum of each charged particle; the electromagnetic and hadronic calorimeters, which measure the energies carried by neutral and charged particles; the muon spectrometer, for identifying and measuring the momenta of muons; and the magnet system, which bends the trajectories of each charged particle to allow the measurement of its momentum. The magnet system is formed by eight big toroids that have the length of the full detector and a solenoid for the inner detector.

Compact Muon Solenoid, CMS. It is a 14,000 tons detector. It is 15 m high and 21 m long, and it really is quite compact for all the detector material it contains (it weights twice much as ATLAS with half the length). It has a powerful solenoid magnet (4T) specially motivated for a precise muon detection. Its structure is very similar to ATLAS, with a central detector, the calorimeters and the muon chambers. Because muons can penetrate several metres of iron without interacting, unlike most particles they are

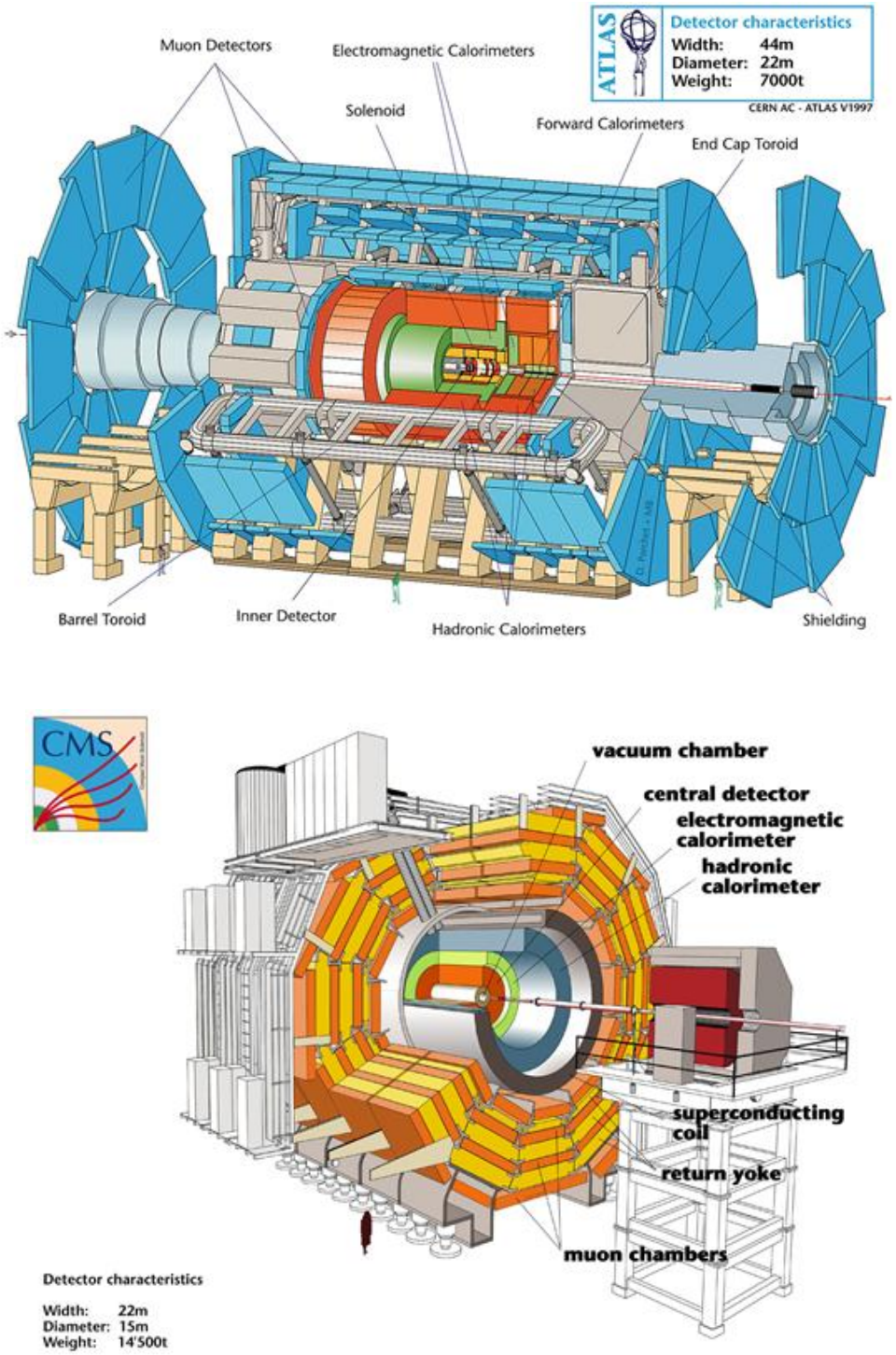

Figure 2.2: ATLAS (top) and CMS (bottom) detectors. Figures from Ref. [60].

not stopped by the calorimeters. Therefore, chambers to detect muons are placed at the very edge of the experiment where they are the only particles likely to register a signal.

2.3 Future electron-positron colliders

With the discovery of Higgs boson at the LHC in 2012, particle physics took a big step in the understanding of the particle interactions described by the SM. However there are different phenomena that cannot be explained in the SM and may point to future directions in particle physics.

Extensions of the SM predict that the Higgs boson plays an important role in the searches of new physics. The top quark is also, as the heaviest known elementary particle, a great candidate to search for deviations from the SM. Precise measurement of Higgs boson and top-quark properties and interactions are a big part of the high energy physics programme of the coming decades.

A new high-energy electron-positron collider should be built with the objective to test the EW theory with an unprecedent precision. In an e^+e^- collider there is a high control of the initial state having a well-defined, adjustable centre-of-mass energy. For instance we can perform a direct search for pair production of weakly coupled particles with masses up to half the centre-of-mass energy, without the requirement of special signatures needed for searches at hadron colliders. This allows to perform very precise threshold production scans. In Figure 2.3 we show the different SM processes accessible in an electron-positron collider.

There are four concrete proposals: the International Linear Collider (ILC), the Compact Linear Collider (CLIC), the Future Circular electron-positron Collider (FCCee), and the Circular Electron Positron Collider (CEPC).

2.3.1 International Linear Collider (ILC)

The ILC is a linear electron-positron collider with a broad physics program. In Refs. [62, 63] we find the technical design report (TDR) published in 2013. Since then, there has been a lot of progress in the physics studies and the development of the detector concept. This progress has been recently published in a report [64]. Although the project has not yet been approved, Japan is the most likely location for the ILC. In Figure 2.4 we present a schematic representation of the ILC collider. In its first stage, it will be ~ 20.5 km long.

The ILC physics program has changed since the TDR publication in 2013. In Ref. [64] the most likely stages are discussed. There is a total of three stages motivated for different physics studies for a total of 20 "real-time" years of ILC operation. There are also other stages that are not in the current baseline that are not discarded and are very interesting. The stages are:

- Stage 1 at $\sqrt{s} = 250$ GeV. Focused on the measurement of the Higgstrahlungs process, $e^+e^- \to HZ$. This is an interesting stage for studying Higgs couplings to light fermions and gauge bosons.
- Stage 2 at $\sqrt{s} = 350$ GeV. Focused on a $t\bar{t}$ threshold scan for top-quark precision measurements. A multiparameter fit in this region allows for a high precision extraction of the top-quark mass.
- Stage 3 at $\sqrt{s} = 500$ GeV or somewhat above. For studying $t\bar{t}$ production in the continuum and enabling $t\bar{t}H$ and ZHH production. This point enables studies of top-quark EW couplings and the top-Yukawa coupling. It also allows to study the Higgs self-coupling.

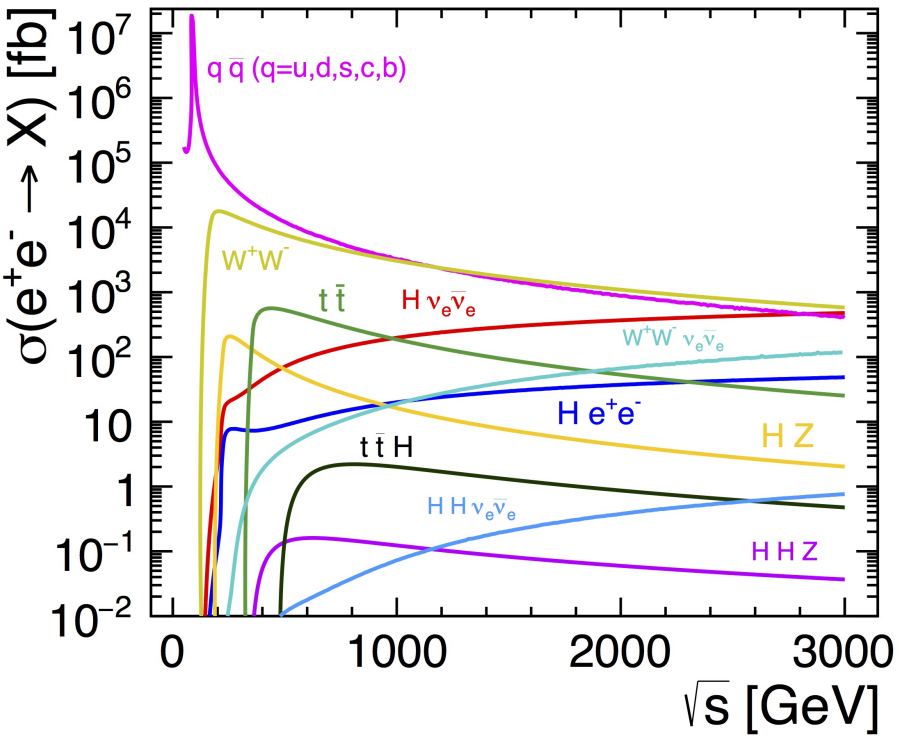

Figure 2.3: Cross-section for different SM processes as a function of the centre-of-mass energy in an electron-positron collider up to 3 TeV [61].

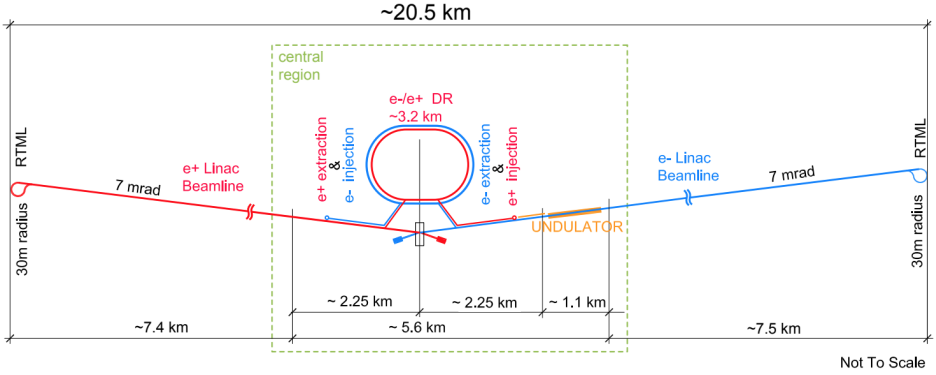

Figure 2.4: ILC accelerator layout for its first stage [64].

- Giga-Z. $\sqrt{s} = 91$ GeV for a Giga-Z program based on high precision measurements at the Z-boson resonance [65].
- High energy program at $\sqrt{s} = 1000$ GeV. This energy point allows better studies for many new physics scenarios.

The expected integrated luminosity for each stage is summarized in Table 2.1 for five nominal scenarios.

$\sqrt{s}$ [GeV]	$\mathcal{L}$ [fb^{-1}]		
	G20	H20	I20
91	100		
250	500	2000	500
350	200	200	1700
500	5000	4000	4000
1000	8000		

Table 2.1: ILC stages for three different scenarios [64, 66].

$\sqrt{s}$ [GeV]	$\mathcal{L}$ [fb^{-1}] with sgn$(P(e^-), P(e^+))$			
	$(-,+)$	$(+,-)$	$(-,-)$	$(+,+)$
91	40	40	10	10
250	900	900	100	100
350	135	45	10	10
500	1600	1600	400	400
1000	3200	3200	800	800

Table 2.2: Integrated luminosities per beam helicity configuration resulting from the fractions in Table 2.1 in scenario H20 [64]. The electron beam is 80% polarized, while the positron beam is 30%. As an example, $(-,+)$ means an helicity configuration of $(-80\%, +30\%)$.

A linear electron-positron colliders allows for beam polarization. SLC polarized its electron beams up to 80%. In the ILC program this electron polarization is kept and also the positron beam is polarized up to 30%. The integrated luminosity will be split into different polarization configurations, as summarized in Table 2.2 for the nominal H20 luminosity scenario.

2.3.2 Compact Linear Collider (CLIC)

The Compact Linear Collider (CLIC) is a multi-TeV high-luminosity linear e^+e^- collider. Its conceptual design report (CDR) was published in 2012 [67–69]. In 2018 and 2019, CLIC and CLICdp collaborations prepared some reports with an updated status of physics studies and detector and accelerator technology [51, 70–72]. The CLIC collider would be hosted at CERN. In Figure 2.5 we find a schematic layout of the CLIC accelerator at its first stage.

The CLIC physics program is split in three different centre-of-mass energies for a 25-30 years of running:

- Stage 1 at $\sqrt{s} = 380$ GeV. It gives access to Higgs-boson and top-quark physics. It also includes a run around $\sqrt{s} = 350$ GeV for a $t\bar{t}$ threshold scan.

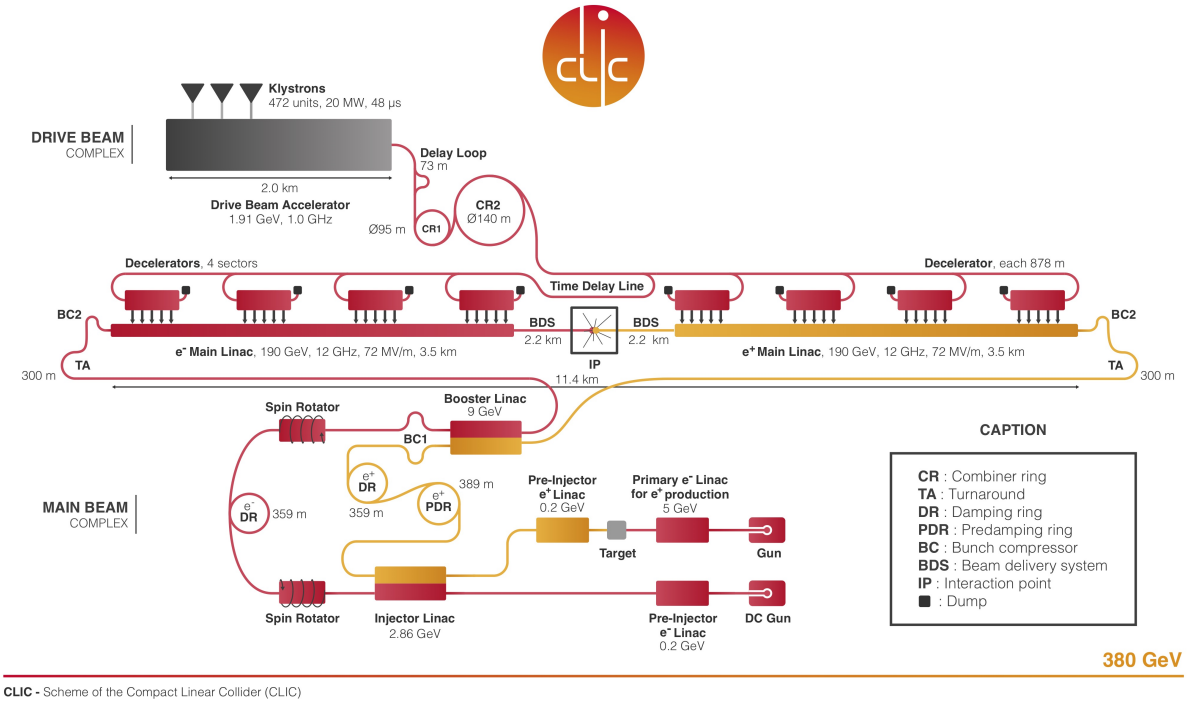

Figure 2.5: Schematic layout of the CLIC complex at 380 GeV (image credit: CLIC [61]).

Stage	$\sqrt{s}$ [GeV]	$\mathcal{L}$ [fb^{-1}]		
		total	$(-80\%, 0)$	$(+80\%, 0)$
1	380 (+350)	1000	500	500
2	1500	2500	2000	500
3	3000	5000	4000	1000

Table 2.3: CLIC stages [70].

- Stage 2 at $\sqrt{s} = 1500$ GeV[1]. This energy opens more Higgs production channels including $t\bar{t}H$, double-Higgs production. It also allows direct sensitivity to many BSM models.
- Stage 3 at $\sqrt{s} = 3000$ GeV. This energy gives the best sensitivity to many new physics scenarios and to the Higgs self-coupling.

Due to the high energy points at 1.5 and 3 TeV, CLIC has the potential to make discoveries of new states, including the possible discovery of dark matter.

In the CLIC accelerator, only the electron beam will be polarized up to 80%. In Table 2.3 we summarize the three stages with the total planned integrated luminosity and the split into the two possible polarization configurations.

[1]For the different simulation studies of this thesis, a centre-of-mass energy of 1.4 TeV is adopted, which was the previously planned stage.

2.3.3 Detector concepts for ILC and CLIC

ILC detectors: ILD and SiD. The ILC collider is planned with one interaction region, equipped with two experiments: the International Large Detector, ILD [73] and the Silicon Detector, SiD [63]. The idea is that the two experiments are changed into the interaction point within the so-called "push-pull" scheme.

SiD is a compact detector with a 5T magnetic field and silicon tracking that provides spatial resolutions of the order of microns. The ILD is a larger detector with robust and stable performance over a wide range of energies with a 3.5T magnetic field. The concept is based on a tracking system formed by a Time Projection Chamber (TPC) combined with silicon tracking for excellent efficiency and robust pattern-recognition performance. A granular calorimeter system provides very good particle-flow reconstruction in both concepts.

CLIC detector. The CLIC accelerator will have only one detector. The ILD and SiD detector concepts were a good starting point for developing the CLIC detector concept. After several R&D activities, a detector model called CLICdet has been designed. Recently, all the capabilities of CLIC detector technologies have been published in Ref. [72].

The main changes with respect to the ILC detectors are modifications of vertex detectors, an increased calorimeter depth and very forward detector regions to mitigate the impact of background. The beam and background conditions are not favorable for a TPC and a silicon tracker is planned[2]. The background suppression is based on time-stamping capabilities assumed to be 10 ns for all silicon tracking elements and a hit time resolution of 1 ns for all calorimeter hits.

In Figure 2.6 we show the CLIC detector layout with all the parts labelled. The detector layout is very similar for ILD and SiD.

2.3.4 Future circular electron-positron colliders: FCC-ee and CEPC

During the last years two new projects have been proposed.

Future Circular Collider, FCC-ee. The FCC is a 100km long ring collider to be hosted at CERN for colliding electrons against positrons (FCC-ee) in a first stage and hadrons (FCC-hh) in a second stage, as it was done with LEP and LHC. Its CDR was published in 2019 [74–77]. The CDR also includes the program for the hadron collider. The physics program of the FCC-ee includes a running plan of 15 years summarized in Table 2.4.

The program includes 5 ab^{-1} at the optimal energy for ZH production, high-luminosity Z-pole and WW threshold runs, and an energy upgrade to reach the $t\bar{t}$ threshold.

Circular Electron-Positron Collider, CEPC. The CEPC is an electron-positron circular collider of 100km long, to be hosted in China. Its CDR was published in 2018 [78,79]. The physics program of the FCC-ee includes a running plan of 10 years summarized in Table 2.4.

[2] In the CLIC CDR in 2012 [68], the detector concept was planned with a TPC for the tracking system. This detector model was called CLIC_ILD as it used the ILD concept as baseline.

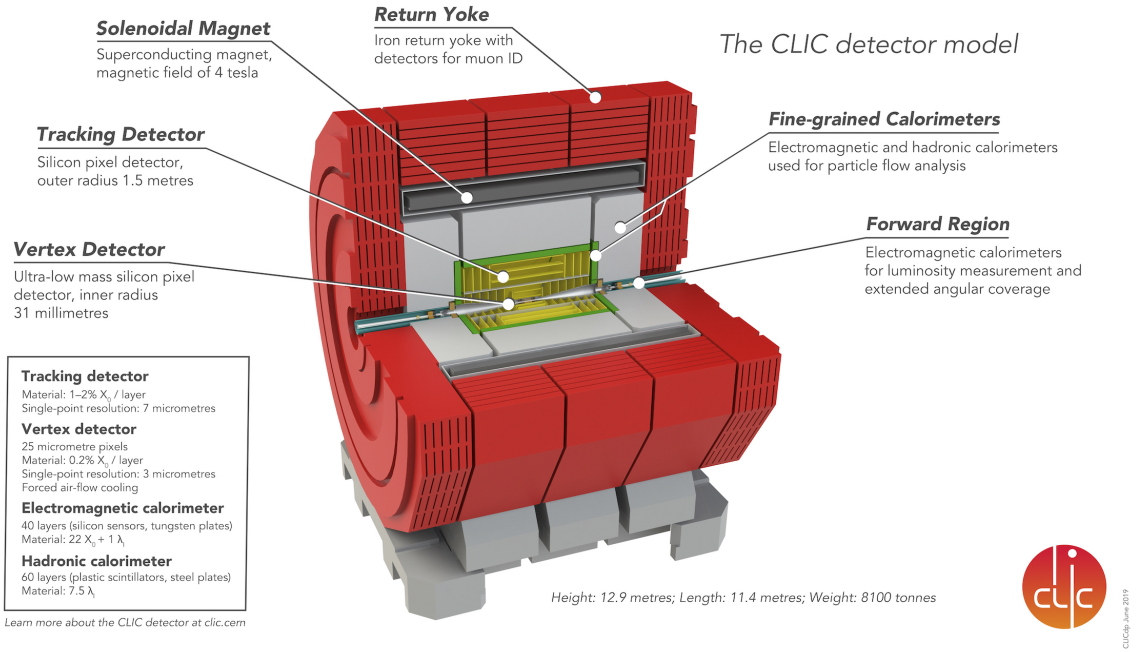

Figure 2.6: CLIC dectector layout (image credit: CLIC [61]).

The CEPC program is very similar to that at FCC-ee. The most significant differences are the absence of the top-quark physics and the much reduced time and integrated luminosity.

Stage	$\sqrt{s}$ [GeV]	Physics	$\mathcal{L}$ [ab^{-1}]	
			FCC-ee	CEPC
Z-pole	91	Precision measurements at Z-pole	150	16
W-thr.	160	Threshold scan at W^+W^- production	10	2.6
Higgs	240	Study of HZ process	5	5.6
top	350 - 365	Threshold scan at $t\bar{t}$ production	1.7	-

Table 2.4: Stages for FCC-ee and CEPC colliders. In the case of CEPC theres is no plan for running at the $t\bar{t}$ production threshold.

3.- The Top quark

The top quark is the heaviest known elementary particle. It was discovered at the Tevatron collider by the CDF and D0 experiments in 1995 [54,55]. The top quark is an up-type quark with electric charge $Q_t = +2/3$ and as the fundamental fermions of the SM it has spin $1/2$. Its left-handed component has the left-handed bottom quark as weak isospin partner.

As the heaviest particle of the SM, the top quark has a special role in many theories of physics BSM. New particles could couple preferably to the top quark. So far the top quark has been produced only in hadron colliders, and many of its properties and interactions are known to $O(10\%)$ precision. The production in electron-positron colliders would bring improved precision measurements known to $O(1\%)$. A scan of the top-quark pair production threshold would provide a measurement of the top-quark mass below 0.1%. Measurements of top-quark production and decay observables with an uncertainty below 1% could for instance give sensitivity to new physics effects; and improved measurements of the top-Yukawa coupling is important to better test the Higgs mechanism. This thesis is centered on the development of such precision measurements and their interpretation in an EFT.

In section 3.1 we discuss the properties of the top quark; its mass, decay and production at colliders. In section 3.4 we introduce the set of effective operators we will use to study the top-quark couplings.

3.1 Top-quark properties

3.1.1 Top-quark mass

The most studied property of the top quark is its mass. Using different approaches and techniques it has been studied by CDF, D0, ATLAS and CMS. The first combination of different direct measurements of the top-quark mass by the four experiments was done in 2014 [80] giving a value of $m_t = 173.34 \pm 0.36(\text{stat.}) \pm 0.67(\text{syst.})$. At that moment the LHC only had run up to a centre-of-mass energy of 7 TeV. Since then, the LHC has run at 8 and 13 TeV, and ATLAS and CMS have provided new results. We can see the evolution of these measurements in Figure 3.1.

The top-quark mass one obtains from direct measurements is the MonteCarlo mass (m_t^{MC}), which represents the mass parameter of the MonteCarlo generators. The interpretation of this parameter in terms of a renormalization scheme is subtle [81]. One very well known scheme is the top-quark pole mass, m_t^{pole}, where all UV and finite contributions of the self energy are absorbed into the mass in the on-shell limit $q^2 = \left(m_t^{\text{pole}}\right)^2$. There are other frequently used mass schemes where the top-quark mass

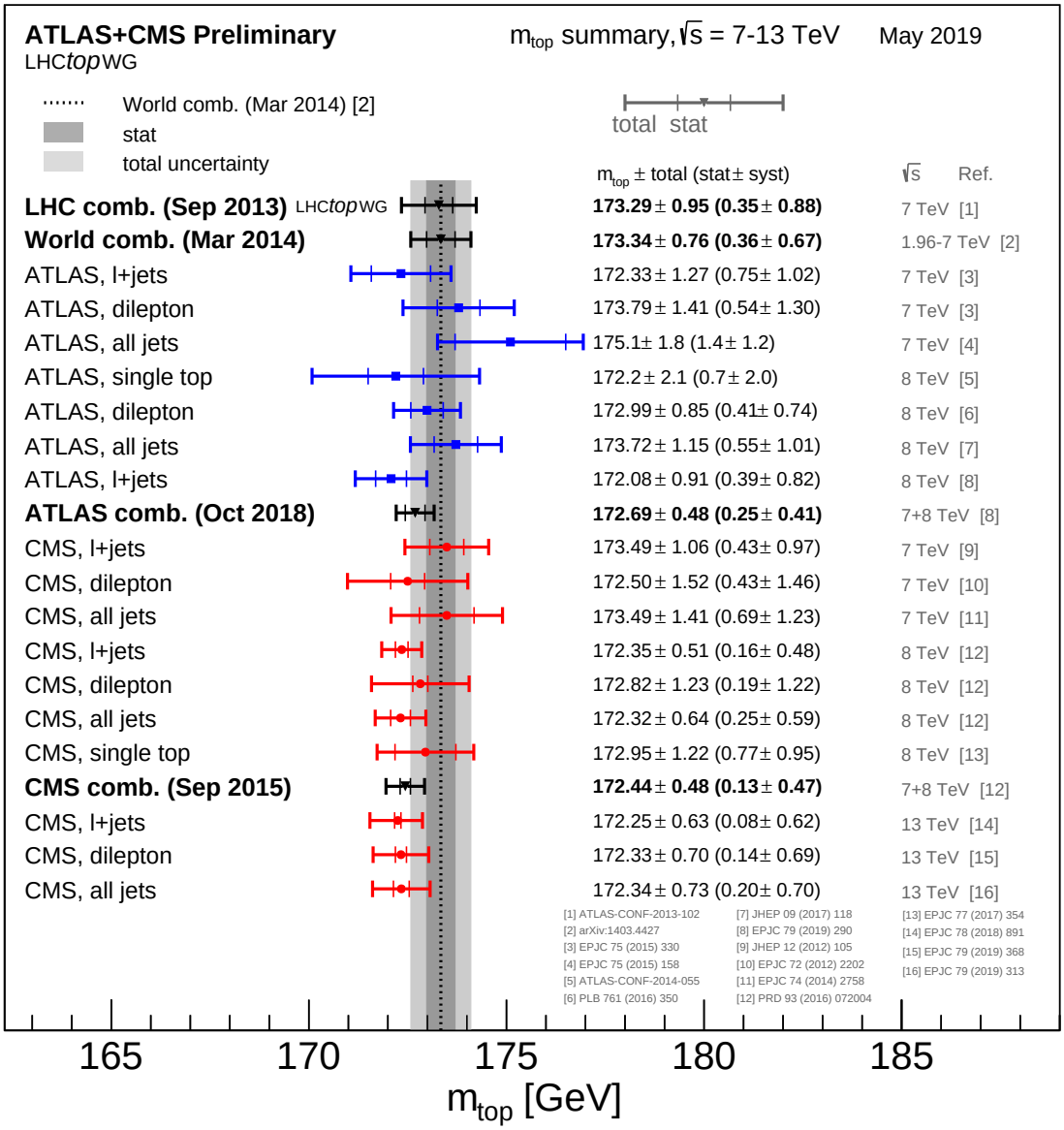

Figure 3.1: Summary of the ATLAS and CMS direct m_{top} measurements. The results are compared with the LHC and Tevatron+LHC m_{top} combinations [83].

can be defined, apart of the pole scheme, two of the most common are the $\overline{MS}$ scheme and the $1S$ scheme. For a detailed overview one can consult Ref. [82].

There are also indirect methods for measuring the top-quark mass. The most common method extracts the top-quark mass from the $t\bar{t}$ production cross-section through the theoretical dependence of the cross-section on the mass. These measurements use predictions calculated at high orders, where the top-quark mass is an input parameter defined in a given scheme. Using this technique, ATLAS and CMS have reported a precision of 1 GeV for the pole mass [84, 85].

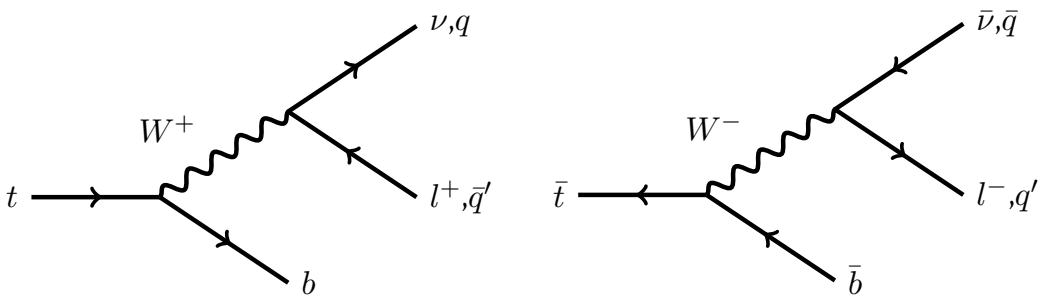

Figure 3.2: Top (left) and antitop (right) decay.

3.1.2 Top-quark decay

The top-quark decay width is measured to be $\Gamma_t = 1.42^{+0.19}_{-0.15}$ GeV (measurements making different assumptions enter in this combination [7]) while the SM predicts $\Gamma_t = (1.32 \pm 0.01)$ GeV [86]. Prediction and measurement are in good agreement. With the width we can estimate the top-quark lifetime as $\tau = 1/\Gamma \approx 5 \times 10^{-25}$s that is much smaller than the time for formation of QCD bound state hadrons ($\tau_{QCD} \approx 1/\Lambda_{QCD} \approx 3 \times 10^{-24}$s). This is the reason why hadrons formed by tops do not exist.

Due to the large value of the CKM matrix element V_{tb}, the top quark mostly decays into a bottom quark and a W boson with a probability of $\sim 100\%$, as represented in Figure 3.2.

In $t\bar{t}$ production, we can distinguish between three different scenarios depending on the final state: we could have a *dileptonic* final state channel if both W's decay into leptons, a *semileptonic* or *lepton+jets* final state channel when one W decays into leptons and the other into quarks, or a *fully-hadronic* final state channel when both decay into quarks. The fractions of events in the three cases are predicted to be [7]:

fully-hadronic	$t\bar{t} \to b\bar{b}q\bar{q}'q''\bar{q}'''$	45.7%
semileptonic	$t\bar{t} \to b\bar{b}q\bar{q}'l^-\bar{\nu}_l + b\bar{b}q''\bar{q}'''l^+\nu_l$	43.8%
dileptonic	$t\bar{t} \to b\bar{b}l^-\bar{\nu}_l l^{+'}\nu_{l'}$	10.5%

3.2 Top-quark production at hadron colliders

In hadron colliders, top quarks are mainly produced in pairs through the QCD processes $q\bar{q} \to g \to t\bar{t}$ and $gg \to t\bar{t}$ (see Figure 3.3), at leading order in QCD. At Tevatron energies, 85% of the $t\bar{t}$ production cross-section is from $q\bar{q}$ annihilation, while at the LHC energies, 80-90% of the production is from gluon-gluon fusion channel. Figure 3.4 summarizes the $t\bar{t}$ production cross-section measurements in LHC and Tevatron. The cross-section at 13 TeV is predicted to be $831.8^{+19.8}_{-29.2} \pm 35.1$ pb [7], in good agreement with the measurements by ATLAS and CMS.

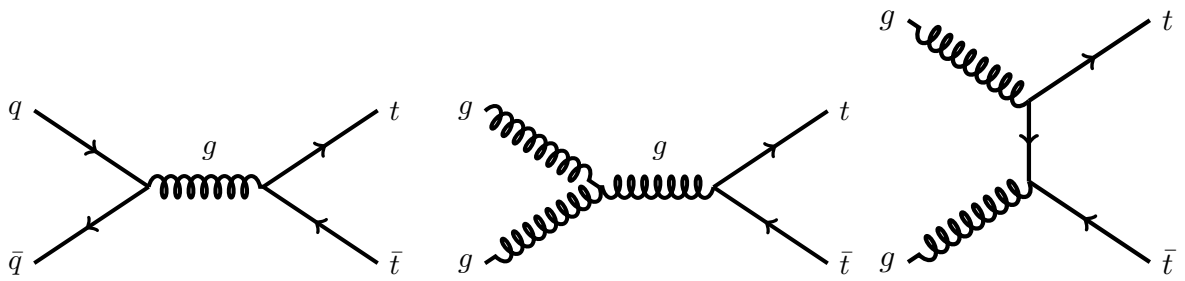

Figure 3.3: Feynman diagrams for $t\bar{t}$ production at hadron colliders. The first diagram corresponds to $q\bar{q}$ annihilation, predominant at Tevatron. The second and third diagrams correspond to gluon-gluon fusion, process dominant at LHC energies.

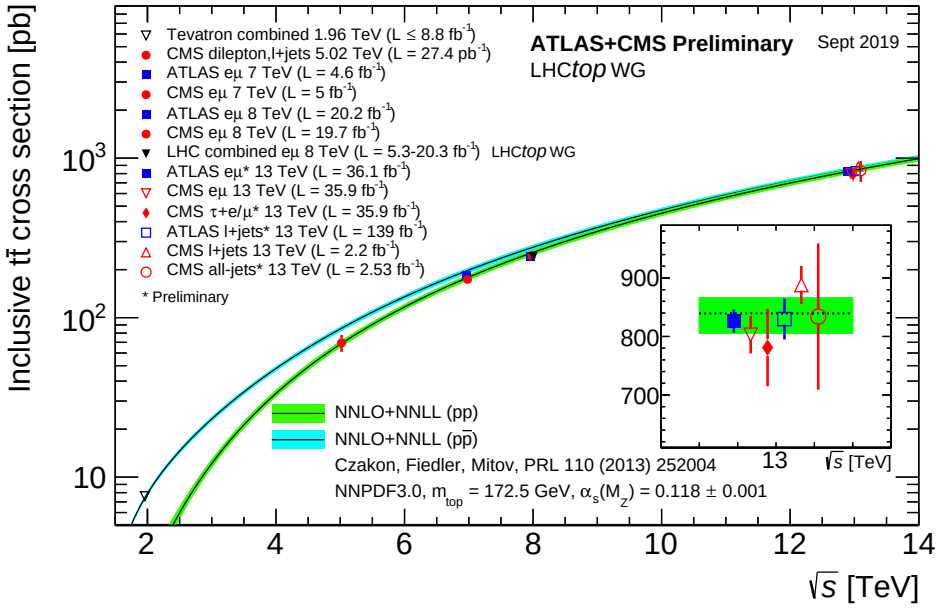

Figure 3.4: Measured and predicted $t\bar{t}$ production cross-section from Tevatron energies in $p\bar{p}$ collisions to LHC energies in pp collisions [83].

3.2.1 Forward-backward asymmetry

The forward-backward asymmetry in $t\bar{t}$ production is defined as:

$$A^{\mathrm{FB}} = \frac{N(\theta_t > 0) - N(\theta_t < 0)}{N(\theta_t > 0) + N(\theta_t < 0)}, \tag{3.1}$$

where θ_t is the polar angle of the top quark.

The first measurements at CDF and D0 experiments gave an asymmetry in excess of the prediction in the SM giving rise to speculation about exotic production mechanisms. With the acquisition of more data the experimental uncertainties have been reduced. The CDF and D0 combined result at $\sqrt{s} = 1.96$ TeV is $A^{\mathrm{FB}} = 0.128 \pm 0.021 \pm 0.014$, the first uncertainty being statistical and the second systematic.

On the other hand, the most recent calculations at α_s^4 gives a value of $A^{\text{FB}}= 0.095 \pm 0.007$ so the discrepancy is no longer statistically significant [87].

3.2.2 Charge asymmetry

At the LHC the dominant $t\bar{t}$ production is through gluon-gluon fusion which is a charge-symmetric mechanism. In this case the pp collision does not define a forward-backward asymmetry. Instead, a charge asymmetry, A_C, is defined in terms of a positive versus a negative $t - \bar{t}$ rapidity difference:

$$A_C^{t\bar{t}} = \frac{N\left(\Delta|y| > 0\right) - N\left(\Delta|y| < 0\right)}{N\left(\Delta|y| > 0\right) + N\left(\Delta|y| < 0\right)}. \tag{3.2}$$

The prediction in the SM for the charge asymmetry is $A_C^{t\bar{t}} = 1.23 \pm 0.05\%$ at $\sqrt{s} = 7$ TeV and $A_C^{t\bar{t}} = 1.11 \pm 0.04\%$ at $\sqrt{s} = 8$ TeV [88]. The ATLAS and CMS experiments have measured A_C using the lepton+jets and dilepton channels at both $\sqrt{s} = 7$ and 8 TeV. All the measurements are in agreement with the predictions in the SM.

ATLAS has provided the first measurement of the charge asymmetry at $\sqrt{s} = 13$ TeV. The inclusive $t\bar{t}$ charge asymmetry is measured as $A_C = 0.0060 \pm 0.0015$ (stat+syst.), which differs from zero by 4 standard deviations. The measurements is consistent with the predictions in the SM [89].

ATLAS and CMS have also provided differential measurements of the charge asymmetry as a function of $M_{t\bar{t}}$, the transverse momentum p_T and the rapidity y of the $t\bar{t}$ system. To study specifically the dependence of A_C with $M_{t\bar{t}}$, ATLAS has performed an analysis in boosted $t\bar{t}$ events [90]. The higher bin, $M_{t\bar{t}} > 0.75$ TeV, reports an asymmetry of $A_C^{t\bar{t}} = 4.2 \pm 3.2\%$, which is in agreement with the prediction in the SM, $A_C^{t\bar{t}} = 1.60 \pm 0.04\%$. This measurement is interesting to study contact interactions in $t\bar{t}$ collisions at the LHC as pointed out in Ref. [91] and developed in section 5.1.

3.2.3 Single-top production

At hadron colliders single-top production proceeds mainly through the exchange of a W boson (upper diagrams of Figure 3.5) or with an associated W boson (bottom diagrams of Figure 3.5). Although certain regions of the bW energies and invariant masses are enriched in double- and single-resonant processes [92], a clean separation between $t\bar{t}$ and Wt production is difficult to achieve. The fiducial cross-sections help to solve this problem. The measurement of Wt defines a fiducial region optimized for Wt and the same for $t\bar{t}$.

The production cross-sections for both processes are summarized in Figure 3.6 for Tevatron and LHC.

At Tevatron, the single-top production process with a higher cross-section is through the exchange of a W boson. Associated production with a W boson has a cross-section that is too small to be observed at Tevatron. At LHC energies the dominant process is the exchange of a W boson through the t-channel followed by the associated Wt production.

Top-quark decay and single-top production are good processes to characterize the Wtb coupling.

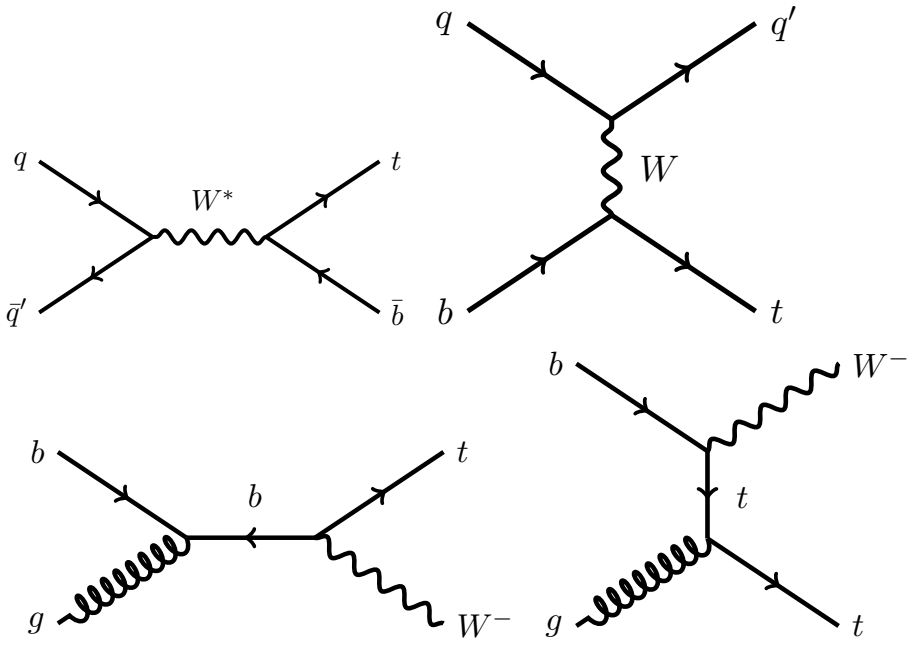

Figure 3.5: Single top production in hadron colliders in the s-channel with a virtual W^* mediator (upper left diagram), t-channel (upper right diagram) and with associated W boson (lower diagrams).

3.2.4 Associated production processes

The LHC has observed a number of processes where a top quark or top-quark pair is produced in association with a photon, a Z boson or a W boson.

In $t\bar{t}$ production the pairs are produced through the exchange of a gluon. In $q\bar{q} \to t\bar{t}$ production the mediator can be a gluon, a Z boson or a photon. In practice gluon initial-state dominates to such an extent that the EW couplings are not probed in $pp \to t\bar{t}$.

The processes shown in Figure 3.7 are very useful for the study of top-quark EW couplings. They provide direct constraints of the couplings of the top quark with the different gauge bosons. The processes $pp \to t\bar{t}X$ $(X = Z, \gamma, H)$ are produced through the exchange of a gluon and the X is radiated off the top quark or the initial state. The process $pp \to t\bar{t}W^{\pm}$ is produced through the exchange of a $W^{\pm}$ boson with $q\bar{q}$ initial state.

In single top production we also find the associated process $pp \to tZq$ represented in Figure 3.8. This process is possible through the exchange of a W boson in $q\bar{q}$ annihilation.

3.2.5 Four top-quark and two-top-two-bottom-quark production

The production of $t\bar{t}$ in association with a boson can produce a final state with four top quarks or two top and two bottom quarks (see Figure 3.9).

Four top-quark production is a rare process in the SM. The predicted cross-section in pp collisions for a centre-of-mass energy of 13 TeV is $12.0^{+2.2}_{-2.5}$ fb [93]. CMS has determined this cross-section to be $12.6^{+5.8}_{-5.2}$ fb, in good agreement with the prediction in the SM [94]. This process has been used

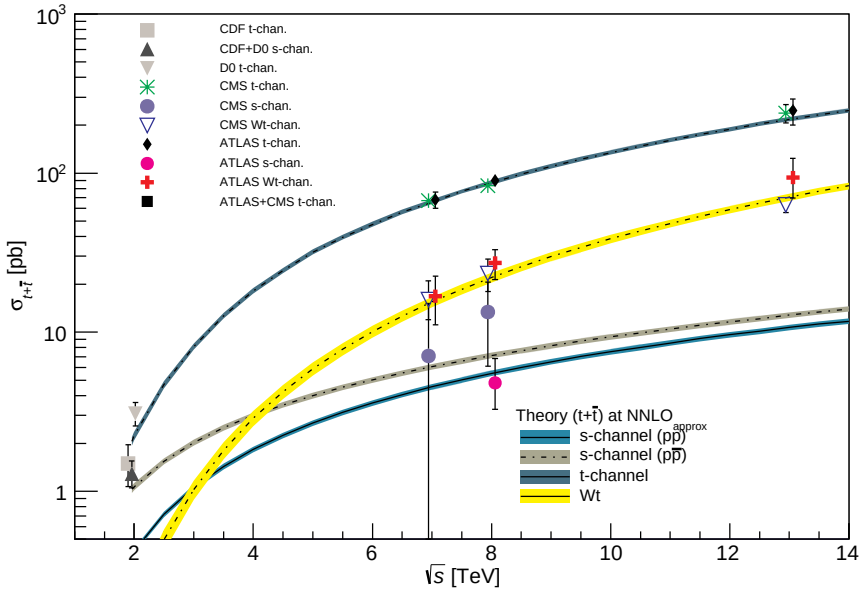

Figure 3.6: Measured and predicted single-top production cross-section from Tevatron energies in $p\bar{p}$ collisions to LHC energies in pp collisions [7].

for studying the top-Yukawa coupling due to a direct access to the $Ht\bar{t}$ vertex [95, 96] (see the middle diagram in Figure 3.9).

In the case of $t\bar{t}b\bar{b}$ production, CMS has published a recent measurement at 13 TeV with a cross-section of $5.5 \pm 0.3(\text{stat.})^{+1.6}_{-1.3}(\text{syst.})$ pb [97].

3.3 Top-quark production at electron-positron colliders

In the SM, electron-positron colliders primarily produce top quarks in pairs through the interchange of a Z boson or a photon in the *s*-channel, as illustrated in the left diagram of Figure 3.10. A number of other processes, including single-top production (right diagram of Figure 3.10) produce the same final state, $bW^+\bar{b}W^-$. As in pp collisions, it is difficult to distinguish between $t\bar{t}$ and single-top production, it is therefore preferable for $t\bar{t}$ production studies to consider the inclusive process $e^+e^- \to bW^+\bar{b}W^-$ [98].

In Figure 3.11 we show the production cross-section for the $e^+e^- \to t\bar{t}$ and $e^+e^- \to bW^+\bar{b}W^-$ processes as a functions of the centre-of-mass energy. The left-handed polarized electron beam leads to a significantly larger $t\bar{t}$ production cross-section. The enhancement is even more pronounced for single-top production, as the neutrino exchange diagram (right diagram of Figure 3.10) is absent for a right-handed electron. The pair production process is seen to provide the dominant contribution to $e^+e^- \to bW^+\bar{b}W^-$ production for centre-of-mass energies below 1 TeV. At higher energies, single-top production overtakes the *s*-channel pair production whose rate approximately falls off as $1/s$. Single and pair production contributions have comparable magnitudes at about $\sqrt{s} \approx 3$ TeV. On the other hand,

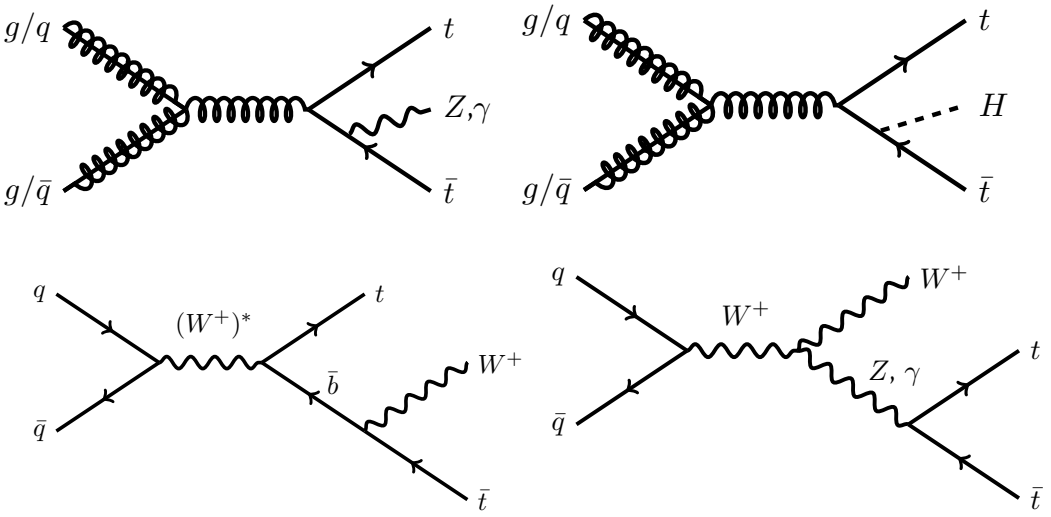

Figure 3.7: Feynman diagrams for $t\bar{t}$ production in association with a boson. In the upper diagrams one of the top quarks radiates a Z boson, a γ or a Higgs boson through s-channel $t\bar{t}$ production in a gluon exchange. In the bottom diagrams two different processes for $t\bar{t}$ final state in association with a W boson are represented.

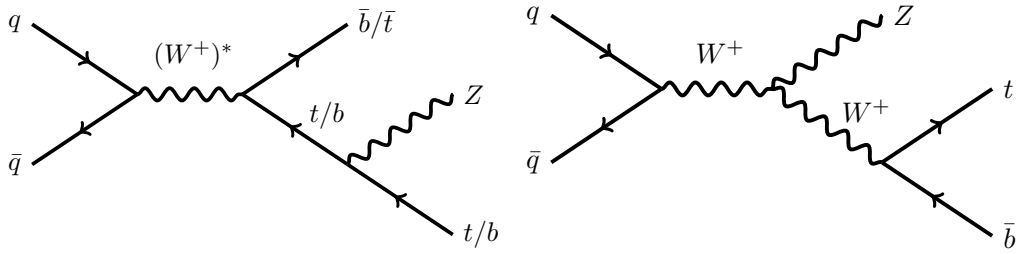

Figure 3.8: Feynman diagrams for single-top production together with a Z boson.

$bW^+\bar{b}W^-$ production remains measurable below the pair production threshold down to $\sqrt{s} \approx 300$ GeV with a production cross-section of $\approx 10^{-2}$ pb.

3.4 EFT analysis of top-quark couplings

In this work we study deviations from the SM in top-quark physics using dimension-six operators of the EFT described in section 1.6. We will work through a broad set of effective operators that affect top and bottom-quark interactions. We rely on the so-called Warsaw basis [45]. In Refs. [100–102] a complete and minimal list of top-quark operators is presented.

The electroweak couplings of the top quark are some of the least precisely constrained quantities in the SM. At the Tevatron and LHC, the process $q\bar{q} \to Z^*/\gamma^* \to t\bar{t}$ is inaccessible but $t\bar{t}$ production is mainly produced through gluon exchange (see Figure 3.3). The hadron collider experiments can probe the charged-current interactions of the top quark in its decay and single-top production (Figures 3.2 and 3.5) or in associated production with a photon or a Z boson (Figures 3.7 and 3.8). We also can probe the neutral current $t\bar{t}Z$ and $t\bar{t}\gamma$ through the associated process shown in the bottom diagrams of Figure 3.7.

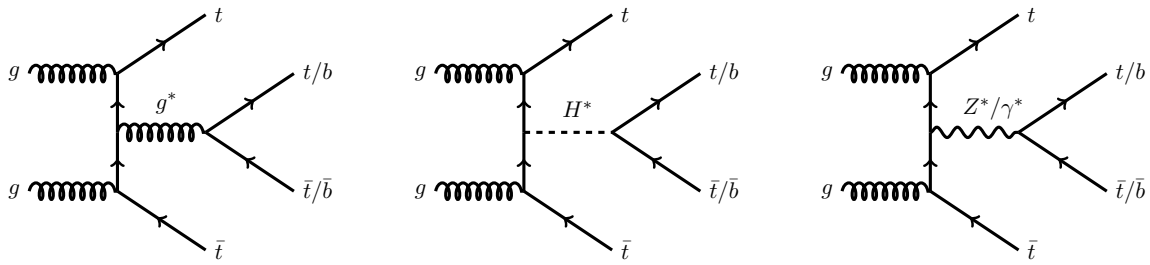

Figure 3.9: Feynman diagrams for $t\bar{t}t\bar{t}$ and $t\bar{t}b\bar{b}$ production at hadron colliders.

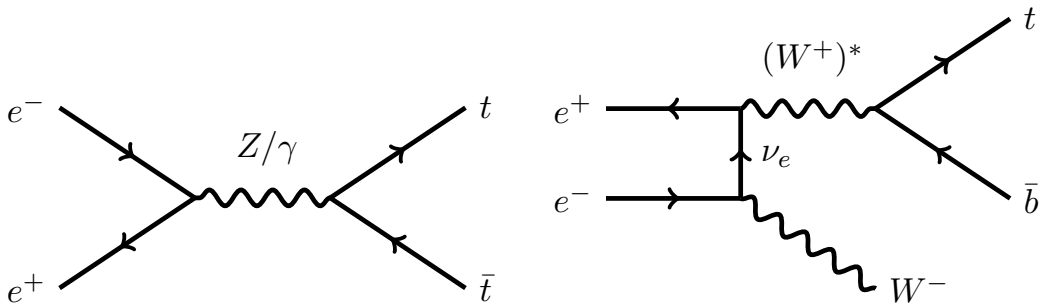

Figure 3.10: Feynman diagram for the $t\bar{t}$ production in an electron-positron collider.

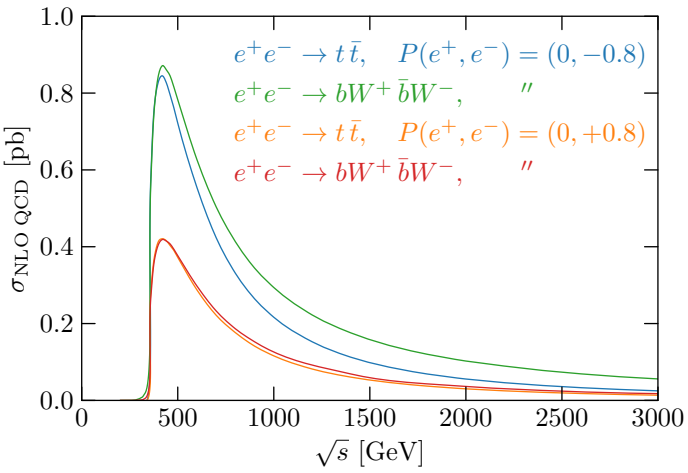

Figure 3.11: The production cross-section for the $e^+e^- \to t\bar{t}$ and $e^+e^- \to bW^+\bar{b}W^-$processes, at NLO in QCD, as functions of the centre-of-mass energy for two choices of electron beam polarization. Bound-state effects that significantly enhance the cross-section in the threshold region are not included. This plot is generated using `MG5_aMC@NLO` [99]. Figure reproduced from Ref. [49].

In section 5.2 we perfom a global fit to the electroweak couplings of the top and bottom quarks using LHC measurements based on single-top and associated production.

On the other hand lepton colliders can probe top-quark couplings with neutral electroweak gauge bosons directly in the $e^+e^- \to t\bar{t}$ process. ILC studies [103,104] relying on a full simulation of the detector response and on estimates for the main systematic uncertainties have shown that cross-section and forward-backward asymmetry measurements would yield percent-level determinations of the anomalous couplings of the top quark to the photon and the Z boson.

3.4.1 Two-quark operators

In this section we present the set of dimension-six operators formed by two quarks which involve the top quark. As the top and bottom quarks are partners of the same doublet, we also include operators that affect the bottom quark. We divide these operators into EW couplings (subsection 3.4.2), or QCD couplings (subsection 3.4.3). The top-quark EFT conventions adopted here are slightly different from the standard established by the LHC TOP Working Group in Ref. [105]. In the appendix of Ref. [106] a conversion to these standards is provided.

3.4.2 Bottom- and top-quark EW couplings

The two-fermion operators that affect top and bottom-quark interactions with vector, tensor, or scalar Lorentz structures are listed in Equation 3.3:

$$
\begin{array}{lll}
O^1_{\varphi Q} & \equiv \frac{y_t^2}{2} & \bar{q}\gamma^\mu q \quad \varphi^\dagger i\overleftrightarrow{D}_\mu \varphi, \\
O^3_{\varphi Q} & \equiv \frac{y_t^2}{2} & \bar{q}\tau^I\gamma^\mu q \quad \varphi^\dagger i\overleftrightarrow{D}^I_\mu \varphi, \\
O_{\varphi u} & \equiv \frac{y_t^2}{2} & \bar{u}\gamma^\mu u \quad \varphi^\dagger i\overleftrightarrow{D}_\mu \varphi, \\
O_{\varphi d} & \equiv \frac{y_t^2}{2} & \bar{d}\gamma^\mu d \quad \varphi^\dagger i\overleftrightarrow{D}_\mu \varphi, \\
O_{\varphi ud} & \equiv \frac{y_t^2}{2} & \bar{u}\gamma^\mu d \quad \varphi^T \epsilon i D_\mu \varphi, \\
O_{uW} & \equiv y_t g_W & \bar{q}\tau^I\sigma^{\mu\nu} u \quad \epsilon\varphi^* W^I_{\mu\nu}, \\
O_{dW} & \equiv y_t g_W & \bar{q}\tau^I\sigma^{\mu\nu} d \quad \epsilon\varphi^* W^I_{\mu\nu}, \\
O_{uB} & \equiv y_t g_Y & \bar{q}\sigma^{\mu\nu} u \quad \epsilon\varphi^* B_{\mu\nu}, \\
O_{dB} & \equiv y_t g_Y & \bar{q}\sigma^{\mu\nu} d \quad \epsilon\varphi^* B_{\mu\nu}, \\
O_{u\varphi} & \equiv & \bar{q}u \quad \epsilon\varphi^* \ \varphi^\dagger\varphi, \\
O_{d\varphi} & \equiv & \bar{q}d \quad \epsilon\varphi^* \ \varphi^\dagger\varphi,
\end{array}
\tag{3.3}
$$

where we have defined $q \equiv (u_L, V_{\text{CKM}} d_L)^T$, $u \equiv u_R$, $d \equiv d_R$, and V_{CKM} the Cabibbo, Kobayashi, Maskawa [23,24] matrix. $\epsilon \equiv \left(\begin{smallmatrix} 0 & 1 \\ -1 & 0 \end{smallmatrix}\right)$ acts on $SU(2)_L$ indices.

The operators $O^1_{\varphi Q}$ and $O^3_{\varphi Q}$ modify the left-handed couplings of the Z boson to down-type and up-type quarks. At leading order, the effect on the left-handed coupling of the top quark is proportional to the difference of the Wilson coefficients, $\delta g^t_L = -(C^1_{\varphi Q} - C^3_{\varphi Q}) m_t^2/\Lambda^2$, that on the left-handed coupling of the bottom quark depends on the sum: $\delta g^b_L = -(C^1_{\varphi Q} + C^3_{\varphi Q}) m_t^2/\Lambda^2$. The simultaneous fit of the coefficients $C^1_{\varphi Q}$ and $C^3_{\varphi Q}$ offers a rationale to combine the bottom- and top-quark operators in a fit.

Two further operators $O_{\varphi u}$ and $O_{\varphi d}$ modify the right-handed couplings of the top and bottom quarks to the Z boson, respectively, $\delta g^t_R = -C_{\varphi u}\, m_t^2/\Lambda^2$ and $\delta g^b_R = -C_{\varphi d}\, m_t^2/\Lambda^2$.

The operators labeled O_{uW}, O_{dW}, O_{uB} and O_{dB} in Equation 3.3 are EW dipole operators. The O_{uW} and O_{uB} give rise to tensor couplings of the photon and Z boson to the up-type quarks. Non-zero values of the Wilson coefficients C_{uW} and C_{uB} induce an anomalous dipole moment of the top quark. Similarly, the operators O_{dW} and O_{dB} give rise to tensor couplings of down-type quark to the photon and Z boson and induce an anomalous dipole moment in the bottom quark.

The $O^3_{\varphi Q}$ and O_{uW} operators also modify the charged-current interactions of the top quark with a W boson and left-handed bottom quark. The $O_{\varphi ud}$ and O_{dW} operators, give rise to interactions between the top quark, the right-handed bottom quark, and the W boson.

Finally, the last two operators, $O_{u\varphi}$ and $O_{d\varphi}$, lead to a shift in the Yukawa couplings of up-type and down-type quarks. The operator $O_{u\varphi}$ affects several observables at colliders. We discuss their potential to constrain $C_{u\varphi}$ in subsection 5.2.7 and subsection 7.2.5. A truly global treatment of this operator must take advantage of the measurements of the Higgs boson production and decay rates. The observables included in the analysis are not sensitive to $O_{d\varphi}$, so this operator is ignored in the following.

The Wilson coefficients are normalized to the TeV scale. By convention, our effective Lagrangian includes the Hermitian conjugate of all operators, even though the flavour-diagonal component of some of them are already Hermitian: $\mathcal{L}_{\text{EFT}} = \sum_i \left(\frac{C_i}{\Lambda^2} O_i + \text{h.c.}\right)$.

In the context of the fit to top and bottom-quark data we use the notation O_{tW}, O_{tB} and O_{bW}, O_{bB} for the dipole operators. We will use the notation $O_{\varphi t}$, $O_{\varphi b}$, and $O_{\varphi tb}$ when referring to the operators that modify the right-handed couplings of the top and bottom quark and the notation $O_{t\varphi}$ for the operator that modifies the top-Yukawa coupling.

The different parity transformation properties and sensitivities of operator combinations featuring vector and axial-vector quark currents motivate us to define:

$$\begin{aligned} C_{uA}^{R,I} &= \text{Re}, \text{Im}\{C_{uA}\} = \text{Re}, \text{Im}\{C_{uW} + C_{uB}\}, & C^V_{\varphi q} &\equiv C_{\varphi u} + C^-_{\varphi q}, \\ C_{uZ}^{R,I} &= \text{Re}, \text{Im}\{C_{uZ}\} = \text{Re}, \text{Im}\{c^2_W C_{uW} - s^2_W C_{uB}\}/s_W c_W. & C^A_{\varphi q} &\equiv C_{\varphi u} - C^-_{\varphi q}, \end{aligned} \tag{3.4}$$

where for convenience, we distinguish the real and imaginary parts of the weak dipole operator coefficients as two different real degrees of freedom. This notation is also helpful to easily transform the EFT scheme on the study of the EW couplings into the form-factors scheme used for instance in Refs. [103,104,107].

In Table 3.1 we summarize the contribution of the different two-fermion operators to the vertices of the SM. In the same table we also provide references to studies where these operators have been studied. In chapter 6 we study the sensitivity and complementarity of different observable to these operators.

3.4.3 Chromo-magnetic dipole operators

We treat the two-fermion operators that involve the $t\bar{t}g$ and $b\bar{b}g$ vertices separately. These are the chromo-magnetic dipole operators:

$$\begin{aligned} O_{uG} &\equiv \bar{q}\sigma^{\mu\nu} u \epsilon \varphi^* G_{\mu\nu}, \\ O_{dG} &\equiv \bar{q}\sigma^{\mu\nu} d \epsilon \varphi^* G_{\mu\nu}. \end{aligned} \tag{3.5}$$

They affect measurements of the $pp \to t\bar{t}/b\bar{b}$ cross-section. There are several studies and analysis that include the chromo-magnetic dipole top-quark operator in different fit scenarios, see for instance Refs. [108,109,112–115,117,118,120,125,132–136].

	$t\bar{t}Z$	$t\bar{t}\gamma$	$t\bar{t}g$	$t\bar{t}H$	tWb	$b\bar{b}Z$	$b\bar{b}\gamma$	$b\bar{b}g$	$b\bar{b}H$	Refs.
$C^1_{\varphi Q}$	✓		✓			✓		✓		[49,108–116]
$C^3_{\varphi Q}$	✓		✓		✓	✓		✓		[49,108–123]
$C_{\varphi t}$	✓		✓							[49,108–110,112–115]
$C_{\varphi b}$						✓		✓		[111,113,116]
$C_{\varphi tb}$					✓					[112,114,115,119,121,123]
C_{tW}	✓	✓			✓					[49,108–110,112,114,115,117–125]
C_{bW}					✓	✓	✓			[111,114–116,119,121,123,124]
C_{tB}	✓	✓								[49,108–110,112,114,115,124,125]
C_{bB}						✓	✓			[111,116]
$C_{t\varphi}$				✓						[112,114,126–129]
$C_{b\varphi}$									✓	[113,130,131]

Table 3.1: Relation between EW vertices involving top and bottom quarks and dimension-six operators coefficients. The ✓ symbol indicates a dependence at tree-level.

3.4.4 Four-quark operators

In this section we present the operators that consist of four quarks. This kind of operators is important in $t\bar{t}$ production at hadron colliders, where both the initial and final state is formed by quarks.

The set of four-quark operators we consider in this thesis is listed in Equation 3.6.

$$
\begin{aligned}
O_{qq}^{(1,3)} &\equiv \left(\bar{q}^i\gamma_\mu\tau^I q^j\right)\left(\bar{q}\gamma^\mu\tau^I q\right), \\
O_{qq}^{(8,1)} &\equiv \frac{1}{4}\left(\bar{q}^i\gamma_\mu\lambda^A q^j\right)\left(\bar{q}\gamma^\mu\lambda^A q\right), \\
O_{qq}^{(8,3)} &\equiv \frac{1}{4}\left(\bar{q}^i\gamma_\mu\tau^I\lambda^A q^j\right)\left(\bar{q}\gamma^\mu\tau^I\lambda^A q\right), \\
O_{ut}^{(8)} &\equiv \frac{1}{4}\left(\bar{u}^i\gamma_\mu\lambda^A u^j\right)\left(\bar{t}\gamma^\mu\lambda^A t\right), \\
O_{dt}^{(8)} &\equiv \frac{1}{4}\left(\bar{d}^i\gamma_\mu\lambda^A d^j\right)\left(\bar{t}\gamma^\mu\lambda^A t\right), \\
O_{qu}^{(1)} &\equiv \left(\bar{q}u^i\right)\left(\bar{u}^j q\right), \\
O_{qd}^{(1)} &\equiv \left(\bar{q}d^i\right)\left(\bar{d}^j q\right), \\
O_{qt}^{(1)} &\equiv \left(\bar{q}^i t\right)\left(\bar{t}q^j\right).
\end{aligned}
\tag{3.6}
$$

In Refs. [117,132] the role of these operators in top-quark studies at hadron colliders is discussed in detail. The first operator, $O_{qq}^{(1,3)}$, appears in single-top production and in top-quark decay studies, but it is not present in $t\bar{t}$ production. For a review of this operator, one can consult Refs. [108,112,120,122]. All other operators contribute to the processes $u\bar{u}/d\bar{d} \to t\bar{t}$.

This set of operators is widely studied in the literature, and there are several authors that have analysed their contributions to different observables and have put bounds in global fits [108, 112, 114, 115, 118, 134, 135, 137].

3.4.5 Two-lepton-two-quark operators

In this section we present the operators formed by two leptons and two quarks. The two-lepton-two-quark operators are important in $t\bar{t}$ production in electron-positron colliders.

In Equation 3.7 we present the set of two-lepton-two-quark operators that affect $t\bar{t}$ production observables at lepton colliders.

$$\begin{aligned}
O_{lq}^{1} &\equiv \bar{q}\gamma_\mu q \bar{l}\gamma^\mu l, \\
O_{lq}^{3} &\equiv \bar{q}\tau^I\gamma_\mu q \bar{l}\tau^I\gamma^\mu l, \\
O_{lu} &\equiv \bar{u}\gamma_\mu u \bar{l}\gamma^\mu l, \\
O_{ld} &\equiv \bar{d}\gamma_\mu d \bar{l}\gamma^\mu l, \\
O_{eq} &\equiv \bar{q}\gamma_\mu q \bar{e}\gamma^\mu e, \\
O_{eu} &\equiv \bar{u}\gamma_\mu u \bar{e}\gamma^\mu e, \\
O_{ed} &\equiv \bar{d}\gamma_\mu d \bar{e}\gamma^\mu e, \\
O_{lequ}^{T} &\equiv \bar{q}\sigma^{\mu\nu} u \epsilon \bar{l}\sigma_{\mu\nu} e, \\
O_{lequ}^{S} &\equiv \bar{q} u \epsilon\, \bar{l} e, \\
O_{ledq} &\equiv \bar{d} q \bar{l} e.
\end{aligned} \tag{3.7}$$

We have defined $l \equiv (V_{\text{PMNS}}\nu_L, e_L)^T$, $e \equiv e_R$, and V_{PMNS} is the Pontecorvo-Maki-Nakagawa-Sakata matrix. As for the two-quark operators, we define the combinations $O_{lq}^{\pm} \equiv (O_{lq}^{1} \pm O_{lq}^{3})/2$ and $C_{lq}^{\pm} = C_{lq}^{1} \pm C_{lq}^{3}$.

The first seven operators of Equation 3.7 have vector Lorentz structures similar to the gauge interactions of the SM. Three further scalar and tensor operators, the last three, have non-standard Lorentz structures and can effectively be constrained with specialized observables, see section 6.5.

As in the case of the two-quark operators, we can define the following linear combination:

$$\begin{aligned}
C_{lq}^{V} &\equiv C_{lu} + C_{lq}^{-}, & C_{eq}^{V} &\equiv C_{eu} + C_{eq}, \\
C_{lq}^{A} &\equiv C_{lu} - C_{lq}^{-}, & C_{eq}^{A} &\equiv C_{eu} - C_{eq},
\end{aligned} \tag{3.8}$$

3.4.6 CP-violating operators

We treat the coefficients of tensor, scalar and $O_{\varphi ud}$ operators as complex. These imaginary parts have no interference with the SM and are probed with observables sensitive to CP-violating effects. In this thesis we do not include the imaginary parts of the coefficients in the global fits. We however study some specific observables in chapter 6.

An example of specific observables are spin correlation observables in $t\bar{t}$ production. They are for instance discussed in Ref. [138] for the LHC and in [107] for the ILC. We can construct angular distributions which could reveal CP violation due to these operators. In section 6.3 we examine this case for the electroweak dipole operators at the ILC.

Also for the imaginary part of the top-Yukawa coupling there exist studies in which asymmetries based on angular distributions are analyzed. See for instance Ref. [139] for a study at the LHC at $\sqrt{s} = 14$ TeV or Ref. [140] for an electron-positron collider study.

3.4.7 The top quark in flavour changing neutral currents (FCNC)

As seen in chapter 1, in the SM this neutral currents do not change the flavour of the interacting particles in the process. Searches of FCNC interactions are performed in several BSM scenarios. Searches for top-quark decays into an up quark or a charm quark plus a Z boson are a good example. We can parameterize these interactions in terms of effective operators with the same structure of the ones presented in this chapter, but changing the indices of the quarks. In Ref. [141] the authors present a global approach to this kind of studies. CLIC projections on FCNC operators are presented in Ref. [51] for the process $e^+e^- \to tj$. One can also consult Refs. [142–147].

In this thesis we do not consider this kind of processes further.

3.4.8 Specific models

The EFT can be matched to specific new-physics models. Effective-operator coefficients then become functions of the underlying model parameters which therefore inherit their constraints. Different patterns of correlations between operator coefficients are produced depending on the model. Any evidence for non-vanishing operator coefficients can thus also point at particular extensions of the standard model.

For instance two-quark operators like $O_{\varphi q}^{1,3}$ and $O_{\varphi u}$ can be generated at tree level by mixing of SM particles with new fields of identical quantum numbers: W', Z', or heavy quarks. The O_{uW} and O_{uB} operators are in general generated at the loop level in scenarios like two-Higgs-doublet or supersymmetric models.

Two-quark–two-lepton operators of vector Lorentz structure (like $O_{lq}^{1,3}$, O_{lu}, O_{eq}, or O_{eu}) could for instance be generated in models featuring new heavy gauge bosons, such as a Z'. In Ref. [49] we find more examples for models involving two-quark and two-lepton-two-quark operators.

In Ref. [50] composite Higgs (CH) models where large mixings between the top quark and the new strongly interacting sector through the top-Yukawa coupling is studied. Precise measurements involving top as well as left-handed bottom quarks offer an interesting opportunity to probe such new physics scenarios. They translate prospective EFT sensitivities into the CH parameter space.

Axigluons are colored heavy neutral gauge bosons that couple to quarks through an axial vector current and the same strong coupling as gluons. Axigluon interactions with top quarks are introduced in Ref. [48]. The most important model independent manifestation of axigluons is the generation of a forward–backward asymmetry in top-antitop quark production at $p\bar{p}$ collisions which originates from the charge asymmetry. We transform limits from the four-quark operators to the axigluon mass in subsection 5.1.6.

4 Simulation and event reconstruction in ILC and CLIC

The prospects for future collider projects are based on a detailed MonteCarlo simulation of the physical processes and experimental response. In this chapter we will summarize the simulation infrastructure developed by the ILC and CLIC projects. We present the work done on top-quark physics in [104,148] and extend it with new results published in [149]. In section 4.1 we introduce the software for the generation and simulation of the $t\bar{t}$ samples analyzed in this thesis. In section 4.2 the different reconstruction steps are presented. Finally in section 4.3 we present the results of an analysis of the $t\bar{t}$ production process.

4.1 Software for event generation and full simulation

Event generation. The Monte Carlo event samples for the $e^+e^- \to 6f$ processes including $t\bar{t}$ production and backgrounds are generated using `WHIZARD 1.95` [150]. The parton shower, hadronization and fragmentation is performed using `PYTHIA` [151]. The luminosity spectrum of ILC and CLIC is generated using `GUINEAPIG` [152], that is interfaced to WHIZARD. Due to the 0.5 ns bunch spacing at CLIC, there exists a high level of beam-induced background. The background events from $\gamma\gamma \to$ hadrons are overlaid on the signal events in order to study the detector performance under the most realistic conditions.

Full simulation. The detector concepts for ILC and CLIC presented in subsection 2.3.3 use the `ILCSOFT` [153] software framework which provides the tools `LCIO` for the data model; `GEAR` for the detector geometry simulation; and `MOKKA` [154], included in the `GEANT4` interface, which produces a list of generated particles and detector hits. This framework has been used for a massive MonteCarlo production for studies under realistic conditions at the ILC and CLIC [155,156]. For the CLIC case, the results presented in this chapter are based on a full simulation of the CLIC_ILD detector concept [68].

4.2 Event reconstruction

The `MARLIN` [157] framework is used for the digitization, reconstruction, and analysis of events simulated with the ILD detector. It includes the algorithms needed for the track reconstruction, the particle flow technique, the jet reconstruction and the flavour tagging.

4.2.1 Track reconstruction

The reconstruction of charged particles is done with a set of C++ packages included in MARLIN. They include TPC recognition based on algorithms developed at LEP and track finding in the silicon detectors and merging of the silicon tracks with the TPC tracks. The tracking software is optimized to face the $\gamma\gamma \rightarrow$ hadrons background included for all generated events.

4.2.2 Particle flow technique

The particle-flow reconstruction is performed using the PandoraPFA [158] event reconstruction package, producing a list of reconstructed Particle Flow Objects (PFOs).

Traditionally, jet energies have been measured by taking the sum of the energies deposited in the hadronic and electromagnetic calorimeters. The hadronic calorimeter, having a relatively poor energy resolution, was the limiting factor in the precision of the jet energy measurements. At ILD, a highly granular calorimetry system will be used in conjunction with the tracking devices to measure the energy and momentum of every visible particle inside the detector. The energy of charged hadrons is measured by the tracking detectors; the energy of photons is measured by the electromagnetic calorimeter. The hadronic calorimeter is used only to measure the energy of neutral hadrons. The reduced dependence on the hadronic calorimeter leads to an unprecedented jet energy resolution.

MarlinPandora is a MARLIN package that converts the calorimeter hit and the track objects into corresponding data structures used in PandoraPFA, augmented with relevant information from the detector geometry and with suitable track quality cuts applied. The resulting list of particle flow objects is then converted back into a list of reconstructed particles which is used for further analysis.

4.2.3 Vertex finding, jet flavour tagging and lepton isolation

LCFIVertex [159] is a package for vertex finding and for jet flavour tagging. A complementary package, LCFIPlus [160], provides improved flavour tagging as well as new jet clustering algorithms for multi-jet final states. For lepton identification we use the package IsolatedLeptonFinder [161].

4.2.4 Jet reconstruction algorithms

Jet reconstruction algorithms are used in particle collider experiments to cluster the collimated sprays of particles that form in processes with asymptotically free quarks and gluons in the final state.

Modern collider experiments use sequential recombination algorithms. The clustering sequence is governed by the definition of the distance between two particles. In popular algorithms used at electron-positron colliders the distance is defined using information about the angle between the particles and the energy of particles.

Durham algorithm [162]. The Durham or e^+e^- k_t algorithm was used extensively at LEP and SLC. The distance between particles i and j is defined as follows:

$$d_{ij} = 2\min\left(E_i, E_j\right)\left(1-\cos\theta_{ij}\right). \tag{4.1}$$

Longitudinally invariant algotithms [163,164]. The distance criterion for hadron colliders is based on quantities that are invariant under boosts along the beam axis. The energy is replaced by the transverse momentum p_t and the angle by the quantity $\Delta R_{ij} = (\Delta\varphi))^2 + (\Delta y)^2$, being y the rapidity of the particles.

The generic distance is rewritten as follows:

$$d_{ij} = 2\min\left(p_{t_i}^{2n}, p_{t_j}^{2n}\right)\frac{\Delta R_{ij}^2}{R^2}, \tag{4.2}$$

where R is the radius parameter. Beam jets are introduced to absorb the radiation from the incoming beams. The beam distance is defined as $d_{iB} = p_{T_i}^{2n}$. Any particle with d_{iB} smaller than any d_{ij} is not merged with any other particle, but forms part of the beam jet.

We can choose different values for n. The algorithm with $n = 1$ is called longitudinally invariant kt algorithm, $n = 0$ yields the Cambridge-Aachen (C/A) algorithm and $n = -1$ the anti-kt algorithm, the default jet reconstruction algorithm at the LHC.

Generic e^+e^- k_t algorithm [162,164]. We can add the beam distance condition to the k_t algorithm for electron-positron colliders:

$$\begin{aligned} d_{ij} &= \min\left(E_i^2, E_j^2\right)\frac{1-\cos\theta_{ij}}{1-\cos R}, \\ d_{iB} &= E_i^2. \end{aligned} \tag{4.3}$$

The VLC algorithm [165]. LEP and SLD colliders presented an environment with essentially negligible background. While far from the background levels of the LHC, detailed studies of the $\gamma\gamma \to$ hadrons background at the ILC or CLIC have shown a non-negligible impact on the jet reconstruction performance.

The VLC algorithm maintains a Durham-like distance based on energy and polar angle and can compete with the longitudinally invariant k_t algorithm in background rejection. The distances in the VLC algorithm are defined as:

$$\begin{aligned} d_{ij} &= \min\left(E_i^{2\beta}, E_j^{2\beta}\right)\frac{1-\cos\theta_{ij}}{R^2}, \\ d_{iB} &= E^{2\beta}\sin^{2\gamma}\theta_{iB}. \end{aligned} \tag{4.4}$$

In Figure 4.1 we show the relation of the VLC algorithm with the other jet reconstruction algorithms in terms the different choices we can adopt for the parameters β and γ. The parameter γ governs the evolution of the jet area with polar angle and is therefore a crucial parameter for the resilience to the

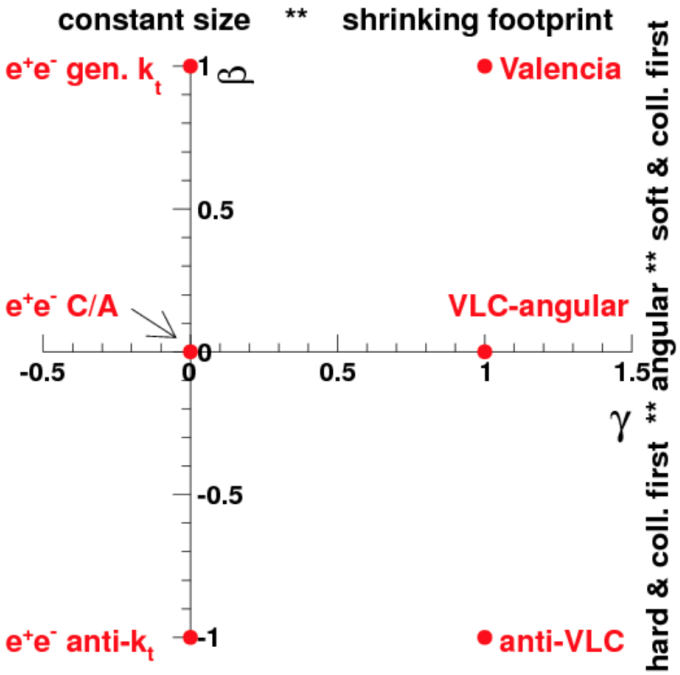

Figure 4.1: Diagram of the parameter space spanned by exponents β and γ of the VLC algorithm. Figure from Ref. [148].

forward-peaked $\gamma\gamma \to$ hadrons background. For a detailed characterization of the performance of the algorithm one can consult Refs. [148,165,166].

4.3 Analysis of $t\bar{t}$ events

In this section we present the selection and reconstruction of the $b\bar{b}$ final state published in Refs. [111, 116] for ILC and $t\bar{t}$ final states for linear collider scenarios published in Refs. [148, 149] for CLIC, and Refs. [104, 148] for ILC at $\sqrt{s} = 500$ GeV. The studies are focused on the reconstruction of the cross-section, forward-backward asymmetry and the optimal observables introduced in section 6.6.

4.3.1 Bottom-quark pair reconstruction at ILC scenario

The results of this section are based on Refs. [111, 116]. We summarize here the work done by the authors for reconstructing the $b\bar{b}$ final state in the ILC scenario. They study the differential cross-section as a function of the polar angle of the $e^+e^- \to b\bar{b}$ process at $\sqrt{s} = 250$ GeV. The study is performed with an integrated luminosity of 250 fb^{-1}. The results are later scaled using an integrated luminosity of 2 ab^{-1}.

Generated samples. The analyzed samples include $q\bar{q}$ final state ($q = u, d, s, c, b$). The experimental studies are made for 100% beam polarization but final results are scaled to the realistic beam polarization $P(e^-, e^+) = (\pm 0.8, \mp 0.3)$.

Pre-selection. Events are reconstructed with two jets using the Durham algorithm. These events have to satisfy the following conditions:

- The two jet system must have an invariant mass larger than 180 GeV and/or that if a photon is reconstructed inside of the detector, it must have an energy lower than 40 GeV in order to remove events with a visible ISR photon.
- If the sum of the two jet masses is greater than 120 GeV, the event is rejected. This cut helps to reduce the impact of QCD final state radiation that dilutes the back-to-back configuration of the two jets and also helps suppressing the remaining background from WW and ZZ events.
- To reduce the $e^-e^+ \to q\bar{q}$ $(q = u, d, s, c)$ background, a large b-tag value (b-tag> 0.9) is required for one jet and at least b-tag> 0.2 for the other.

Charge measurement. The jet charge is determined to reconstruct the angular distribution. The bottom quark hadronize in 40% percent of cases in charged $B^{\pm}$ mesons, 40% in neutral B mesons, 10% in strange B mesons and 10% into B baryons. Around 80% of the B mesons yield charged Kaons in the final state. The charge of the originating bottom quark can be identified by measuring the charge of the hadrons created in the bottom-quark hadronization process. There are two methods to do this: using the charge of the secondary vertex reconstructed with the vertex detector (Vtx-method) or using the charged kaons identified in the TPC (K-method). There are two jets, b and $\bar{b}$, and two methods, so with this information one can work out the mistag rate in the charge measurement. For the details of this process consult Refs. [111, 116].

Results. The angular distributions for the two polarizations are shown in Figure 4.2. The polar angle distributions are fitted to the following equation:

$$\frac{\mathrm{d}\sigma}{\mathrm{d}\cos\theta^*} = \sigma_1 \left(1 + \cos\theta^*\right)^2 + \sigma_2 \left(1 - \cos\theta^*\right)^2 + \sigma_3 \left(1 - \cos^2\theta^*\right). \tag{4.5}$$

At tree level the three terms can be related to the bottom-quark pair production cross-sections for different helicity combinations in the final state. The forward and backward cross-sections, σ_F and σ_B, can be obtained by integrating the differential cross-section over the bottom-quark polar angle ranges, $0 < \theta^* < \pi/2$ and $\pi/2 < \theta^* < \pi$, respectively. The total production cross-section, can be expressed as

$$\sigma = \sigma_F + \sigma_B = \frac{4}{3}\left(2\sigma_1 + 2\sigma_2 + \sigma_3\right), \tag{4.6}$$

while the top-quark forward-backward asymmetry is defined as

$$A^{\mathrm{FB}} = \frac{\sigma_F - \sigma_B}{\sigma_F + \sigma_B} = \frac{1}{\sigma} 2\left(\sigma_1 - \sigma_2\right). \tag{4.7}$$

The fit is performed to both distributions in Figure 4.2 in the region $|\cos\theta_b| < 0.8$ to avoid the regions with large drops of efficiency. In Table 4.1 the results on the expected precision for the cross-section and A^{FB} are summarized. Both the cross-section and the asymmetry can be determined with sub-percent precision.

$P\,(e^+, e^-)$	$(-0.8, +0.3)$	$(+0.8, -0.3)$
$(\delta\sigma/\sigma)_{\text{stat.}}$ [%]	0.10	0.18
$\left(\delta A^{\text{FB}}/A^{\text{FB}}\right)_{\text{stat.}}$ [%]	0.09	0.34

Table 4.1: Estimation of the achievable precision on the cross-section and forward-backward asymmetry for the $e^+e^- \to b\bar{b}$ process at $\sqrt{s} = 250$ GeV [116]. The fit from Figure 4.2 using Equation 4.5 is for 250 fb^{-1} and for fully-polarized beams. In this table we show the converted results for a total integrated luminosity of 2 ab^{-1} split following Table 2.2 at the correct beam polarizations.

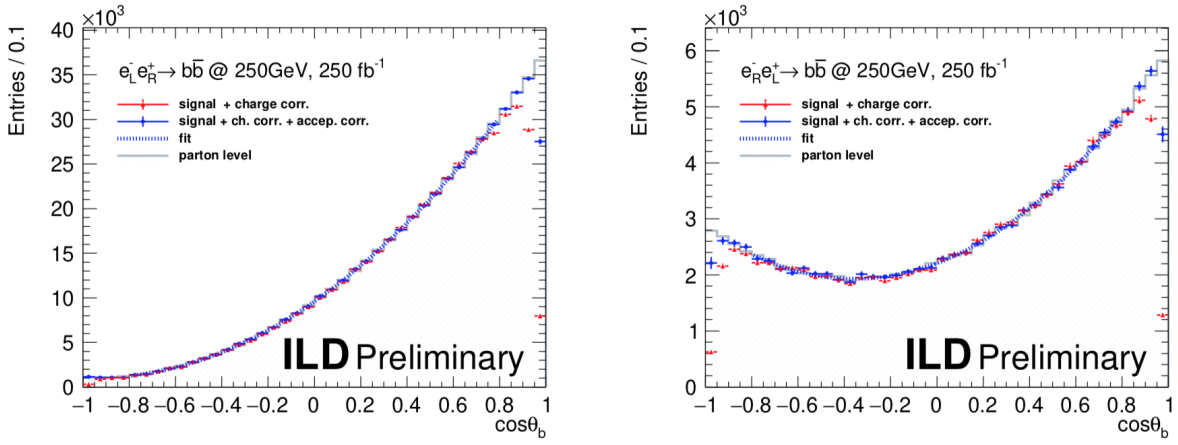

Figure 4.2: Preliminary results for the bottom-quark polar angle distribution at a centre-of-mass energy of 250 GeV for full polarized beams [116].

For the 500 and 1000 GeV runs a complete analysis does not yet exist. We adopt the acceptance times efficiency estimate of 25% based on full simulation by the same authors[1]. The statistical uncertainties for the cross-section and forward-backward asymmetry for the left-right and right-left beam polarizations are estimated assuming a total integrated luminosity of 4 ab^{-1}at $\sqrt{s} = 500$ GeV and 8 ab^{-1}at $\sqrt{s} =$ 1 TeV.

Systematic errors. The main systematic uncertainties affecting the measurements are the background subtraction, the errors due to beam polarization estimation and the b-tagging efficiency. It is assumed that the background will be known at the $\sim 1\%$ level and that the errors in the polarization will be as the ones described in Ref. [167]. Current studies show that the uncertainty on the b-tagging efficiency can be measured at the 0.1% precision. At this level systematic uncertainties are subdominant.

4.3.2 Top-quark pair reconstruction at CLIC380

Generated samples. Samples for CLIC are a six-fermion final state which includes also the fully-hadronic and fully-leptonic $t\bar{t}$ pair decays, thus a selection of the lepton+jets $t\bar{t}$ final state is

[1]Note that $b\bar{b}$ production at 1 TeV is extremely forward peaked, so assuming the same efficiency as at 500 GeV might not be a good choice. However we will use this approximation until a full analysis is completed.

required in CLIC studies. Only the electron beam is polarized for CLIC, $P(e^+, e^-) = (0, \mp 80\%)$. We use the relevant luminosity spectrum for all generated events.

Event selection. The PFOs are clustered into exactly four jets using the VLC algorithm with a radius of 1.6 and $\beta = \gamma = 0.8$. The use of such a large jet radius is made possible by the low level of beam-induced background at 380 GeV. Two of these jets must be identified as being produced by the bottom quarks of the top-quark decay. We also require an isolated charged lepton (electron or muon, we remove events with a tau lepton). More specifically, the following criteria are applied:

- An isolated charged lepton (electron or muon) with $p_T > 10$ GeV.
- We require a big b-tag for at least one of the jets (b-tag > 0.8) and a less restrictive b-tag for other of the jets (b-tag > 0.3).
- Kinematic cuts. $180 < m_{had.} < 420$ GeV for the invariant masses of the hadronic final state and $50 < m_W < 250$ GeV and $120 < m_t < 270$ GeV for the reconstructed W boson and top quark respectively.

The selection efficiency for semi-leptonic events for CLIC samples is 69% for left-handed polarized electron and 72% for right-handed electron beam.

Reconstruction. One top-quark candidate is reconstructed from the hadronically decaying W which is combined with one of the bottom-quark jets. The two remaining jets are associated with the decay products of the W boson. The charged lepton allows for the determination of the top-quark charge. As there are two b-tagged jets and two W-boson candidates there is a two-fold ambiguity in the reconstruction. The $t\bar{t}$ system is reconstructed by choosing the combination of b quark jet and W boson that minimises the following equation:

$$\begin{aligned} \chi^2 &= \left(\frac{m_{cand} - m_t}{\sigma_{m_t}}\right)^2 + \left(\frac{E_{cand} - E_{beam}}{\sigma_{E_{cand}}}\right)^2 \\ &+ \left(\frac{p_b^* - 68\text{GeV}}{\sigma_{p_b^*}}\right)^2 + \left(\frac{\cos\theta_{Wb} - \langle\cos\theta_{Wb}\rangle}{\sigma_{\cos\theta_{Wb}}}\right)^2, \end{aligned} \tag{4.8}$$

where m_{cand} and E_{cand} are invariant mass and energy of the top-quark candidate decaying hadronically, respectively, and m_t and E_{beam} (190 GeV for CLIC380) are the input top-quark mass and the beam energy. It also takes into account the momentum of the bottom-quark jet in the centre-of-mass frame of the top quark, p_b^*, and the angle between the bottom quark and the W boson. The expected value for the angle is $\langle\cos\theta_{Wb}\rangle = -0.67$. The measured values are compared with the expected ones and the denominator is the width of the measured distributions.

The top-quark direction measurement depends very strongly on the correct association of the bottom quarks to the jets of the hadronic W-boson decays. This jet pairing constitutes a source of mis-reconstruction that can lead to severe effects predominantly for the $P(e^-) = -80\%$ sample. For top quarks with left-handed helicity, the W boson is emitted opposite to the flight-direction of the top

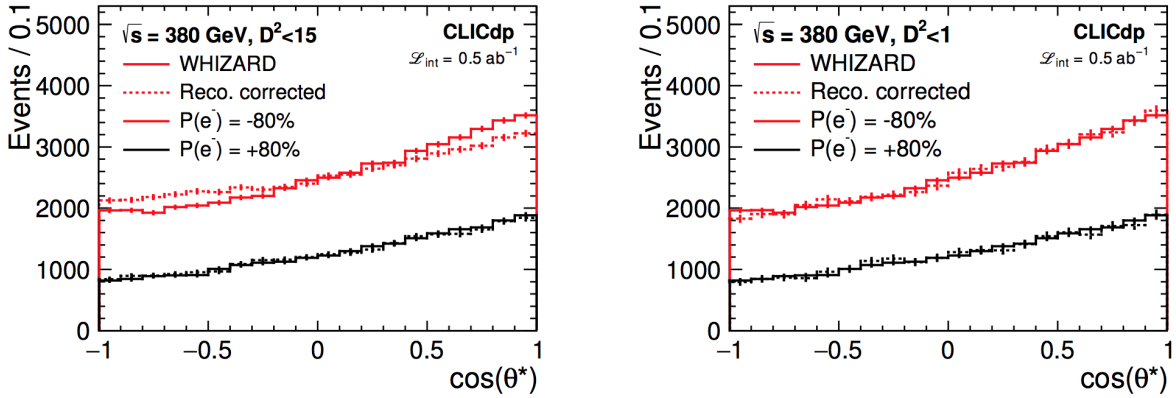

Figure 4.3: Top-quark polar angle distributions for operation at $\sqrt{s} = 380\text{GeV}$ after the application of a quality cut based on the kinematic variable D^2. A cut of $D^2 < 15(1)$ was applied for the left (right) figure. The solid lines show the reconstructed distributions including the effects of detector modelling, event reconstruction and candidate selection, while the dashed lines show the WHIZARD parton-level distributions, for the two beam polarization configurations considered. Note that efficiency corrections have been applied, corresponding to the parton-level expectation for $D^2 < 15$ [148,149].

quark and decays nearly at rest. The resulting final state has two hard jets from the bottom quarks and soft jets from the hadronically decaying W boson; a configuration that leads to substantial migrations in the top-quark polar angle distribution when paired wrongly.

A quality cut, D^2, is defined that compares the measured values of the Lorentz factor of the top quark, the momentum of the bottom quark in the rest frame of the top quark and the angle, $\cos\theta_{bW}$, between the bottom quark and the W boson. The correct association of the of jets from bottom quarks to that from W bosons is checked with the MonteCarlo truth information.

$$D^2 = \left(\frac{\gamma_t - \langle\gamma_t\rangle}{\sigma_{\gamma_t}}\right)^2 + \left(\frac{E_b^* - 68\text{GeV}}{\sigma_{E_b^*}}\right)^2 + \left(\frac{\cos\theta_{Wb} - \langle\cos\theta_{Wb}\rangle}{\sigma_{\cos\theta_{Wb}}}\right)^2, \tag{4.9}$$

where $\langle\gamma_t\rangle = \sqrt{s}/2m_t \sim 1.09$ and σ_{γ_t} are the mean and RMS, respectively, of the observed distribution of the top-quark Lorentz factor obtained from studies using full simulation.

The final step of the analysis is carried out separately for the two polarization states with stricter quality cuts applied for the extraction of A_{FB} and the statistically optimal observables (introduced in section 6.6) for the $P(e^-) = -80\%$ sample. For the $P(e-) = +80\%$ polarization we apply a cut of $D^2 < 15$, which reduces the efficiency from 72% to 67%. This value for the quality cut is not enough for correcting migrations for $P(e-) = -80\%$ as shown in the left plot of Figure 4.3. For this polarization a tighter cut is needed, $D^2 < 1$, giving rise to a selection efficiency that drops to 23% (right plot of Figure 4.3).

The statistically optimal observables are somewhat more robust than the forward-backward asymmetry against migrations. Consequently, a looser quality cut is applied in their construction. We apply $D^2 < 8$ for $P(e-) = -80\%$. This reduces the efficiency to 40%.

Results. We fit the polar distributions from Figure 4.3 to Equation 4.5. The results obtained for the fit at $\sqrt{s} = 380$ GeV are presented in Table 4.2.

4.3.3 Top-quark pair reconstruction at ILC500

The reconstruction of $t\bar{t}$ events at ILC500 was performed before the study at CLIC380. This study was published in Refs. [104, 148] and was the baseline for the reconstruction at CLIC380 presented previously. In this section we summarize the work done by the authors of Refs. [104,148].

Generated samples. Samples generated for ILC correspond to the semi-leptonic final state $l^{\pm}\nu b\bar{b}q'\bar{q}$ of the $t\bar{t}$ pair decay. Beams are fully polarized, $P(e^+, e^-) = (\pm 100\%, \mp 100\%)$.

Event selection. The selection criteria are very similar to those used for CLIC380. We look for an isolated charged lepton and two b-tagged jets. Contrary to CLIC380, in ILC500 we include the number of events with a tau lepton in the denominator when calculating the efficiency [148]. We also apply the same kinematic cuts for the hadronic mass and the W-boson and top-quark masses. The total selection efficiency for ILC is about 55% for $P(e^+, e^-) = (+100\%, -100\%)$ and 56% for $P(e^+, e^-) = (-100\%, +100\%)$.

Reconstruction. The same D^2 from Equation 4.8 is used for pairing the W-bosons and the bottom-quark jets. In this case we have $E_{beam} = 250$ GeV and we find $\langle \cos\theta_{Wb} \rangle = 0.23$ from the measured distribution. As in CLIC380, in ILC500 we find migrations caused for an incorrect $W - b$ pairing. In the case of a right-handed electron beam the direction of the top quark can be precisely reconstructed. In this case the selection efficiency remains 56% and a quality cut is not needed (see the left plot of Figure 4.4).

In the case of a left-handed electron beam, we apply the same quality cut defined in Equation 4.9 with a value of $D^2 < 15$. For this value we obtain an excellent agreement between the generated and reconstructed polar angle distributions (see the right plot of Figure 4.4). The tight selection reduces the efficiency in case of $P(e^+, e^-) = (+100\%, -100\%)$ from 55% to 28%. In Table 4.2 we show the results obtained from the fit of the polar angle distribution from Figure 4.4.

This study preceeds the development of statistically optimal observables (see section 6.6). Therefore, no full simulation study is available for these observables at ILC500.

4.3.4 Top-quark pair reconstruction in the boosted regime

In operation at centre-of-mass energies above $\sim$ 1 TeV the top quarks will be produced with significant boosts. In particular, the event topology is very different from that of the analysis described previous section, where the top quarks are produced close to the threshold. Owing to the boost, the top-quark candidates are more easily distinguishable from each other and the relative effect of migrations, as discussed in the previous section, is therefore expected to be smaller. This section describes the event selection and results for an analysis for semi-leptonic $t\bar{t}$ events (electron or muon) at the collision energies of 1.4 TeV and 3 TeV in CLIC. A more exhaustive discussion is found in Ref. [149].

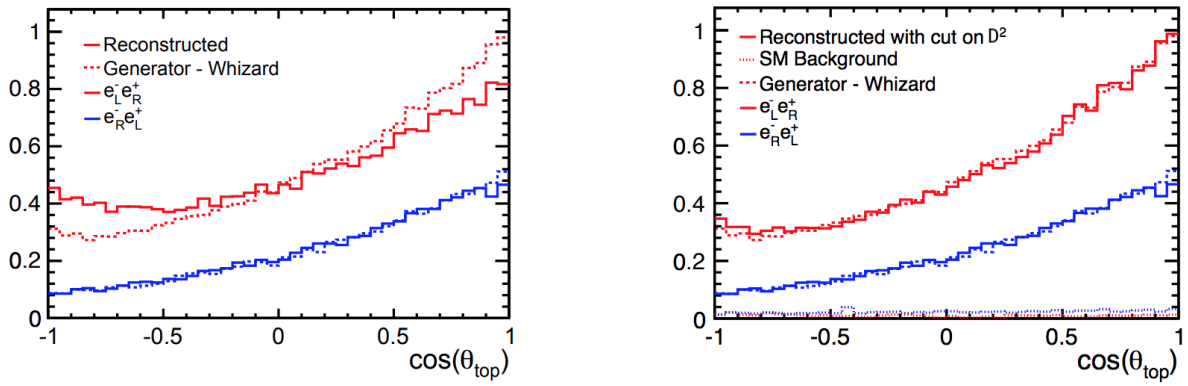

Figure 4.4: Left: Reconstructed forward-backward asymmetry compared with the prediction by the event generator WHIZARD [150] for two configurations of the beam polarizations at ILC 500 GeV. Right: the same but after the application of a cut on $D^2 < 15$ for the beam polarizations $P(e^+, e^-) = (+100\%, -100\%)$ as explained in the text. Note, that in both figures no correction is applied for the beam polarizations $P(e^+, e^-) = (-100\%, +100\%)$. The figure on the right shows also the residual background of the SM [148].

$\sqrt{s}$ [GeV]	500		380	
$P(e^+, e^-)$	$(+0.3, -0.8)$	$(-0.3, +0.8)$	$(0, -0.8)$	$(0, +0.8)$
$\mathcal{L}$ [fb^{-1}]	500	500	500	500
$(\delta\sigma/\sigma)_{\text{stat.}}$ [%]	0.43	0.67	0.48	0.68
$\left(\delta A^{\text{FB}}/A^{\text{FB}}\right)_{\text{stat.}}$ [%]	1.8	1.3	3.8	2.9

Table 4.2: The results at $\sqrt{s} = 380$ GeV for $P(e^-) = -80\%$ and $\sqrt{s} = 500$ GeV for $P(e^+, e^-) = (+30\%, -80\%)$ are obtained using the sample with a quality cut of $D^2 < 15$. For operation at $\sqrt{s} = 380$ GeV the A^{FB} for $P(e^-) = -80\%$ is extracted using the event sample defined by the quality cut $D^2 < 1$. No quality cut is needed for $\sqrt{s} = 500$ GeV for $P(e^+, e^-) = (-30\%, +80\%)$. For ILC500 the analysis is performed assuming a total integrated luminosity of 1ab^{-1}. These results are scaled for a total integrated luminosity of 4ab^{-1} in further studies.

Generated samples. As in the CLIC380 case, samples are a six-fermion final state which includes also the fully-hadronic and fully-leptonic $t\bar{t}$ pair decays. Only the electron beam is polarized for CLIC, $P(e^+, e^-) = (0, \mp 80\%)$. We use the relevant luminosity spectrum for all generated events. The signal events are restricted to the kinematic region defined as $\sqrt{s'} \geq 1.2$ TeV and $\sqrt{s'} \geq 2.6$ TeV, for 1.4 TeV and 3 TeV respectively. This cut is applied to the reconstructed collision energy as part of the pre-selection.

Top tagging algorithm. PFOs are clustered into exactly two jets using the VLC algorithm. A large-R jet radius of $R = 1.4$ and $R = 1.0$, each with $\beta = \gamma = 1.0$ is found to be optimal for operation at $\sqrt{s} = 1.4$ TeV and $\sqrt{s} = 3$ TeV, respectively.

The tagging of boosted top quarks at CLIC is based on the Johns Hopkins top tagger [168]. This tagger is explicitly designed for the identification of top quarks by recursively iterating through the clustering sequence to search for up to three or four hard subjets and then imposing mass constraints on these subjets. This procedure provides strong discrimination power for hadronically decaying top quarks against jets formed by light quarks or gluons.

Event selection. The event selection proceeds with the following conditions:

- Identification of one isolated charged lepton (electron or muon) with $p_T > 10$ GeV. In cases where several candidates exist, the candidate with the highest p_T is selected.
- The remaining PFOs are clustered in two exclusive large-R jets that are used as input to the top-quark tagging algorithm. One boosted top quark must be identified using the top-quark tagger algorithm.

Reconstruction of the effective centre-of-mass energy. We first assume that the missing transverse momentum, estimated by adding up the 4-vectors of the two large-R jets and the isolated charged lepton, can be used as an estimator for the neutrino transverse momentum components. Here we neglect the effect from unidentified ISR and beamstrahlung photons. The z-component of the neutrino momentum, $p_{\nu,z}$, is retrieved by solving the following equation:

$$M_W^2 = m_l^2 + 2\left(E_l E_\nu - \boldsymbol{p}_l \cdot \boldsymbol{p}_\nu\right), \tag{4.10}$$

where M_W is the mass of the leptonically decaying W boson and the indices l and ν denote the lepton and neutrino candidate quantities, respectively.

The equation is quadratic in $p_{\nu,z}$ and has no solution if the observed missing transverse energy fluctuates such that the invariant mass of the combined neutrino-lepton system is above M_W. In such cases the missing transverse energy is scaled to provide a real solution. The resulting neutrino-lepton system solutions are combined with each of the large-R jets and the final candidate is chosen as the one that yields a mass closest to the generated top-quark mass. This method yields an RMS on the centre-of-mass energy, $\sqrt{s'}$, of ∼140 GeV.

Event selection. The remaining events are analysed using multivariate classification algorithms (MVAs) based on Boosted Decision Trees (BDTs). In light of the large variety of the different backgrounds considered ($e^+e^- \to qqqqqq, qql\nu l\nu, qqqq, qql\nu, qqll, qq$), two initial MVAs are trained focussing on slightly different topologies. The first MVA is trained using backgrounds with two quarks and either 0, 1, or 2 leptons, while the second MVA focuses on fully-hadronic four-quark and six-quark jet topologies. The final MVA considers all relevant backgrounds and includes the score from the two initial MVAs.

Separate BDTs are applied for the 1.4 TeV and 3 TeV samples and for the two different polarizations considered. Each BDT uses 21 variables based on the kinematics of the hadronically decaying top quark, lepton and b-jet, the substructure of both large-R jets, the number of lepton candidates with energy > 30GeV, b-quark tagging information, and event shapes. The cut applied on the classification score is

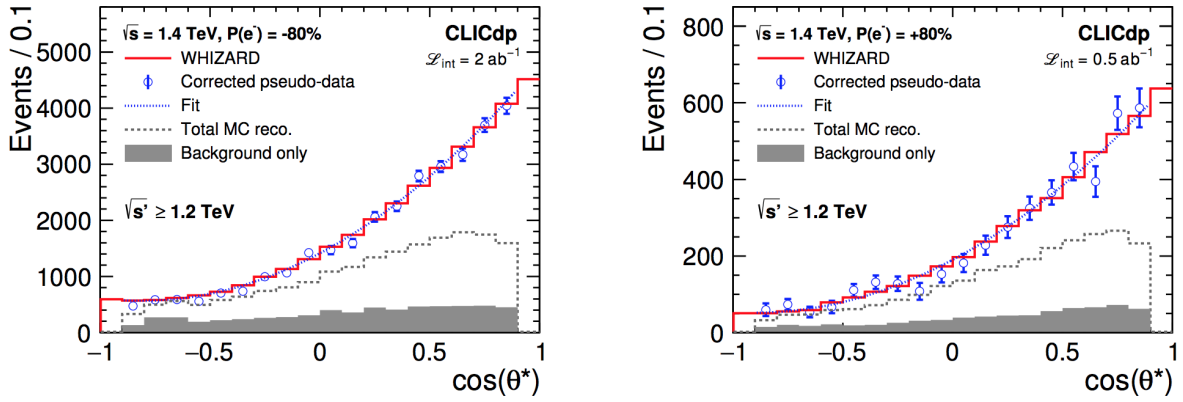

Figure 4.5: Top-quark polar angle distributions from the analysis of boosted semi-leptonic tt events, at a nominal collision energy of 1.4 TeV for $P(e^-) = -80\%$ (left) and $P(e^-) = +80\%$ (right), and an integrated luminosity of 2.0 ab^{-1} and 0.5 ab^{-1} , respectively. The dashed black curve shows the reconstructed total MC distribution, while the grey area indicates the level of background only. The blue data points and dotted line represent one pseudo-experiment after subtraction of background and correction for finite selection efficiencies, and the corresponding fit, respectively. The red solid line represents the simulated parton-level distribution [149].

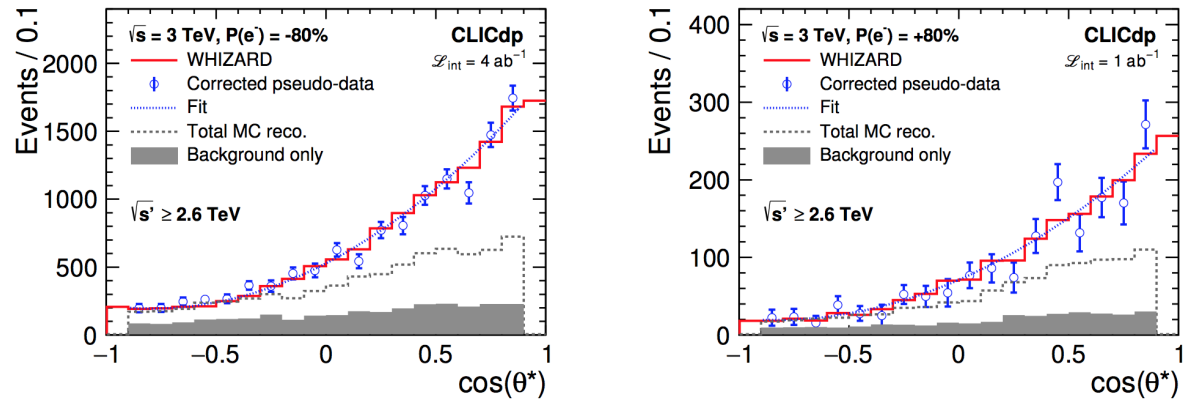

Figure 4.6: Top-quark polar angle distributions from the analysis of boosted semi-leptonic tt events, at a nominal collision energy of 3 TeV for $P(e^-) = -80\%$ (left) and $P(e^-) = +80\%$ (right), and an integrated luminosity of 4.0 ab^{-1} and 1.0 ab^{-1}, respectively. See further details in Figure 4.5 [149].

chosen to minimise the statistical uncertainty on the two extracted observables A_{FB} and $\sigma_{t\bar{t}}$. For the reconstruction of the optimal observables we use the same efficiency.

Results. The polar-angle distributions of the hadronically decaying top-quark candidates are shown in Figure 4.5 and Figure 4.6. The selection efficiency in the region $-0.7 \leq \cos\theta^* \leq 0.7$ is generally flat with a central value of about 50% for both analyses, at $\sqrt{s} = 1.4$ TeV and $\sqrt{s} = 3$ TeV. In the forward regions the efficiency drops to 30%.

$\sqrt{s}$ [TeV]	1.4		3.0	
$P(e^-)$	-0.8	$+0.8$	-0.8	$+0.8$
$\mathcal{L}$ [fb^{-1}]	2000	500	4000	1000
$(\delta\sigma/\sigma)_{\text{stat.}}$ [%]	1.14	2.95	1.99	4.71
$\left(\delta A^{\text{FB}}/A^{\text{FB}}\right)_{\text{stat.}}$ [%]	1.41	3.23	2.35	5.27

Table 4.3: Results from the analysis of semi-leptonically decaying top quarks at the boosted regime stages of CLIC. Note that the cross-section, $\sigma_{t\bar{t}}$, and A^{FB} are defined in the kinematic region of $\sqrt{s'} \geq 1.2(2.6)$ TeV for operation at $\sqrt{s} = 1.4(3)$ TeV [149].

$\sqrt{s}$ [GeV]	380		500	1000	1400		3000	
$P(e^+, e^-)$	$0-$	$0+$	$+-$ $-+$	$+-$ $-+$	$0-$	$0+$	$0-$	$0+$
cross-section	12.9	12.1	10.0	6.0	6.0	5.8	4.6	4.7
A^{FB}	4.7	12.1	10.0	6.0	6.0	5.8	4.6	4.7
Stat. Optimal Obs.	7.8	12.1	10.0	6.0	6.0	5.8	4.6	4.7

Table 4.4: Equivalent fractions of the theoretical $e^+e^- \to t\bar{t}$ rate at the nominal centre-of-mass energies that are assumed in the EFT fit. When multiplied by the inclusive $e^+e^- \to t\bar{t}$ cross-section, excluding the energy loss from ISR or beamstrahlung, and by the corresponding integrated luminosity, these fractions yield the numbers of events at final level of the analyses of semi-leptonic final states, as studied in full simulation.

As in the case of lower energies, the polar-angle distributions are fitted to Equation 4.5. In Table 4.3 we show the relative uncertainties for the forward-backward asymmetry and the cross-section obtained for the fit

4.3.5 Summary of top-quark pair reconstruction efficiencies

We calculate the equivalent fractions of the theoretical $e^+e^- \to t\bar{t}$ rate that is available for analysis, after accounting for efficiency, acceptance, branching ratios and the effect of the luminosity spectrum. These numbers, presented in the final row of Table 4.4, are used to determine the statistical uncertainty affecting observable measurements in the following chapters.

For a centre-of-mass energy of 500 GeV a complete full-simulation study for the statistically optimal observables has not been done, in that case we adopt an average of the equivalent $t\bar{t}$ fraction obtained at CLIC at $\sqrt{s} = 380$ GeV. Something similar occurs at ILC at $\sqrt{s} = 1$ TeV where a complete full-simulation study is still missing. In this case we adopt an average of the equivalent $t\bar{t}$ fraction obtained at CLIC at $\sqrt{s} = 1.4$ TeV.

Systematic uncertainties have been evaluated to some extent in Refs. [104,107,149]. It is plausible that theoretical and experimental systematics can be controlled to the level of the statistical uncertainties assumed here.

5.- Constraints on top-quark operators from existing collider data

In this chapter we present two fits of top-quark effective operators using Tevatron, LEP and LHC data. In section 5.1 we derive constraints on the four-quark operators introduced in subsection 3.4.4 using the charge asymmetry measurement at the LHC. This study is published in Ref. [91]. In section 5.2 we perform a global fit for the two-fermion operators introduced in subsection 3.4.1. This study is pusblished in Ref. [106].

5.1 Constraints on four-quark operators from the $t\bar{t}$ charge asymmetry

In $t\bar{t}$ production at hadron colliders several operators can contribute to the process amplitude. In Ref. [117] these amplitudes are calculated taking into account the operators C_G, $C_{\varphi G}$, C_{tG} and all the four-quark operators from Equation 3.6. If one only considers the term Λ^{-2} in the EFT Lagrangian expansion, the effects of the four-quark operators can be expressed in terms of the following linear combination of operator coefficients:

$$\begin{aligned} C_1^u &= C_{qq}^{(8,1)} + C_{qq}^{(8,3)} + C_{ut}^{(8)} \\ C_2^u &= C_{qu}^{(1)} + C_{qt}^{(1)} \\ C_1^d &= C_{qq}^{(8,1)} - C_{qq}^{(8,3)} + C_{dt}^{(8)} \\ C_2^d &= C_{qd}^{(1)} + C_{qt}^{(1)}. \end{aligned} \tag{5.1}$$

In Ref. [117] the authors make this assumption and discuss that other contributions at Λ^{-4} are negligible. In other studies, like [137], the authors also consider the Λ^{-4} terms, so in this case the basis from Equation 3.6 cannot be reduced into Equation 5.1 and other assumptions need to be considered to perform the fit. Following Ref. [117], in this work we only consider Λ^{-2} terms with the objective of deriving constraints on the operators C_1^u, C_2^u, C_1^d and C_2^d. We discuss the validity of this assumption in subsection 5.1.2. Other studies that use the same procedure are published in Refs. [108,118,132].

A further reduction of the basis for four-fermion operators to two effective operators is achieved by assuming $C_1^u = C_1^d = C_1$ and $C_2^u = C_2^d = C_2$. This reduction is valid in models where the new massive states couple to up-type and down-type quarks with the same strength. Among the models that satisfy this requirement the axigluon [48] has received most attention in the context of the $t\bar{t}$ charge

	SM prediction	Measurement
Tevatron, 1.96 TeV $p\bar{p}$, CDF+D0, cross-section	7.16 ± 0.26 pb [171]	7.60 ± 0.41 pb [172]
Tevatron, 1.96 1.96 TeV $p\bar{p}$, CDF+D0, A^{FB}	$9.5 \pm 0.7\%$ [87]	$13 \pm 2.3\%$ [173,174]
LHC, 8 TeV pp, CMS+ATLAS inclusive σ	245.80 ± 10.56 pb [171]	241.50 ± 8.54 pb [175]
ATLAS 8 TeV pp, inclusive A_C	$1.11 \pm 0.04\%$ [88]	$0.9 \pm 0.5\%$ [176]
CMS 8 TeV pp, inclusive A_C	$1.11 \pm 0.04\%$ [88]	$0.3 \pm 0.4\%$ [177]
ATLAS 8 TeVpp, differential A_C ($m_{t\bar{t}} > 0.75$ TeV)	$1.60 \pm 0.04\%$ [178]	$4.2 \pm 3.2\%$ [90]

Table 5.1: Datasets used in the fit. The Tevatron A^{FB} measurement corresponds to a naive approximation between D0 and CDF experiments [179]. A combination of the ATLAS and CMS measurements of the inclusive asymmetry at 8 TeV is not yet available, so both measurement are kept as independent constraints. Measured values include systematic and statistical uncertainties. Correlations between different systematic uncertainties are not considered.

asymmetry measurements at the Tevatron and the LHC. We note that the assumption is also valid for models that are not strictly flavour-universal, such as the axigluon with an opposite-sign coupling to top quarks ($g_t = -g_q$), that can give rise to positive contributions to the asymmetry, and the Kaluza Klein gluon as realized in Randall-Sundrum models with warped extra-dimensions in Refs. [169,170], the main benchmark for direct searches for resonant signals in $t\bar{t}$ production. One further consideration is that we only take into account four-quark operators in this fit, so we assume that the top-quark chromomagnetic dipole operator C_{tG} and the gluon self-interaction operators C_G and $C_{\varphi G}$ are constrained in other studies (see for instance Ref. [108]).

5.1.1 Measurements

To constrain the four-fermion effective operator coefficients simultaneously we need at least four independent measurements with good sensitivity to these operators. We choose the inclusive forward-backward asymmetry measured at Tevatron, and the charge asymmetry measured at the LHC at $\sqrt{s} = 8$ TeV and the inclusive $t\bar{t}$ production cross-section at the Tevatron and at the LHC at $\sqrt{s} = 8$ TeV. The data sets are summarized in Table 5.1.

The selection of Table Table 5.1 emphasizes inclusive measurements that integrate over all kinematic regimes. The use of differential measurements, especially of the production of high-mass $t\bar{t}$ pairs, may offer greater sensitivity to high-scale physics beyond the SM [180]. We therefore include an ATLAS result for the charge asymmetry in events where the top-quark pair is produced with a large invariant mass [90], which we take as a proxy for a large set of measurements in boosted top-quark pair production that become available at the LHC.

5.1.2 Sensitivity to effective operators

We generate $t\bar{t}$ samples at parton-level with the MonteCarlo generator `MG5_aMC@NLO` [181,182] using the UFO model `TopEffTh` [132] to calculate the impact of the effective operators on the cross-section and charge asymmetry.

The dependence of the top-quark pair production cross-section and the charge asymmetry on the four-fermion operator coefficients is parameterized using the linear dependence of Equations 5.2:

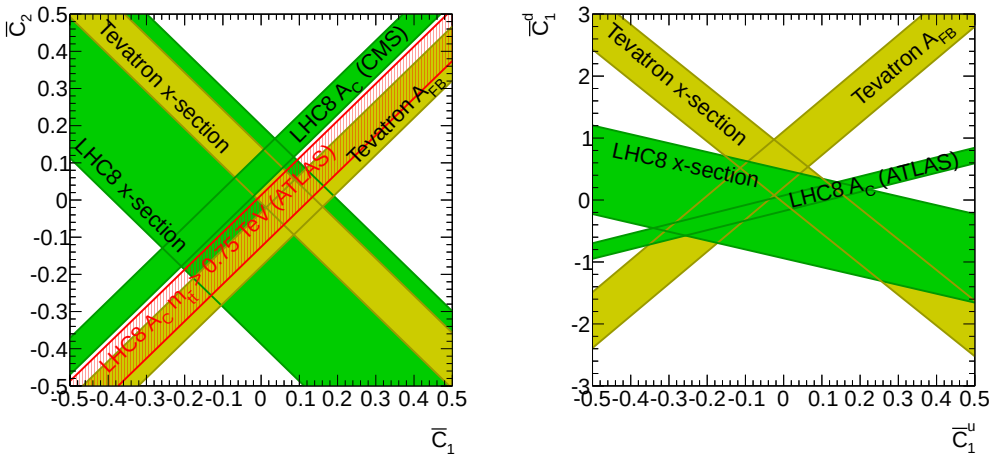

Figure 5.1: The constraints on pairs of effective operators from several cross-section and charge asymmetry measurements at 95% C.L. The bands in (a) represent the constraints on C_1 and C_2 (assuming $C_1^u = C_1^d = C_1$ and $C_2^u = C_2^d = C_2$). The bands in (b) represent the constraints on C_1^u and C_1^d. We have defined in both cases $\bar{C}_i = C_i v^2/\Lambda^2$.

$$\frac{(\sigma - \sigma^{\mathrm{SM}})}{\sigma^{SM}} = [\alpha_u(C_1^u + C_2^u) + \alpha_d(C_1^d + C_2^d)](\frac{1\ \mathrm{TeV}}{\Lambda})^2, \tag{5.2}$$

and 5.3:

$$(A_C - A_C^{\mathrm{SM}}) = [\beta_u(C_1^u - C_2^u) + \beta_d(C_1^d - C_2^d)](\frac{1\ \mathrm{TeV}}{\Lambda})^2. \tag{5.3}$$

As we use a leading order calculation for the SM contribution, σ^{SM} in Equation 5.2 corresponds to the tree-level result. The charge asymmetry appears only at next-to-leading order in the SM, so the leading-order asymmetry in Equation 5.3 vanishes; $A_C^{\mathrm{SM}} = 0$. For the comparison with data, NNLO+NNLL predictions are used for the pure SM contribution, while the charge asymmetry A_C at the LHC was only available to NLO precision at the time of writing.

Equation 5.2 shows that the cross-section is proportional to $C_1 + C_2$, while the asymmetry in Equation 5.3 is proportional to $C_1 - C_2$. Therefore, the combination of the two measurements provides a very powerful constraint on both the C_1 and C_2 operator coefficients. The complementarity is illustrated in the left plot of Figure 5.1, where the bands representing the constraint from the asymmetry measurement cross the cross-section bands at a straight angle.

The results for the coefficients of Equation 5.2 and Equation 5.3 are presented in Table 5.2. The coefficients α_u and α_d are defined such that they are proportional to the contribution of new interactions to the cross-section divided by the SM cross-section. As such, the size of $\alpha_{u/d}$ in different measurements

	α_u [%]	α_d [%]	β_u [%]	β_d [%]
Tevatron 1.96 TeV $p\bar{p}$ inclusive	5.19 ± 0.02	1.05 ± 0.02	1.66 ± 0.09	0.32 ± 0.09
LHC 8 TeV pp inclusive	1.02 ± 0.02	0.71 ± 0.02	0.37 ± 0.09	0.24 ± 0.09
LHC 8 TeV pp ($m_{t\bar{t}} > 0.75$ TeV)	3.03 ± 0.09	1.56 ± 0.09	2.16 ± 0.09	0.6 ± 0.09
LHC 13 TeV inclusive	0.73 ± 0.02	0.48 ± 0.02	0.26 ± 0.09	0.27 ± 0.09
LHC 13 TeV ($m_{t\bar{t}} > 1.2$ TeV)	6.61 ± 0.02	3.60 ± 0.02	6.09 ± 0.09	2.78 ± 0.09

Table 5.2: Parameterization of the coefficients of Eq. 5.2 and 5.3. The α and β coefficients govern the impact of non-zero effective operators on the cross-section and the charge asymmetry, respectively. The u/d subscripts indicate whether the coefficients correspond to $u-$type or $d-$type quarks.

offers a good indication of the sensitivity of the measurements (assuming the relative precision of all measurements is equal, condition that is approximately met for the measurements in the Table). The $\beta_{u/d}$ coefficients indicate the strength of the constraint for charge asymmetry measurements of the same absolute precision.

For all measurements the coefficients α_u and β_u for the up-type operators are larger than α_d and β_d, that apply to down-type operators. The ratios α_u/α_d and β_u/β_d are largest at the Tevatron, where a naive estimate based on the valence quark content of the proton and anti-proton would yield a factor of four. Tevatron measurements are powerful to derive simultaneous constraints on up-type and down-type operators. The Tevatron bands in C_1^u and C_1^d space in the right plot of Figure 5.1 cross at more favourable angles than the LHC bands. At the LHC (where the naive estimate would yield a ratio of two) the up-type and down-type operator coefficients are much closer.

Among the inclusive measurements, the Tevatron clearly offers a much greater sensitivity to four-fermion operators than the LHC at 8 TeV, reflecting the much larger dilution by gluon-initiated processes at the LHC. The impact of the dilution is most clearly observed in the cross-section bands in the left plot of Figure 5.1. Even if ATLAS and CMS have managed to reduce the uncertainty on the pair production cross-section measurement to approximately 4%, the constraint from the LHC 8 TeV cross-section data is quite weak. The gluon-gluon contribution to the cross-section reaches nearly 90% at 13 TeV, reducing the sensitivity even further.

Table 5.2 suggests a way to restore the sensitivity of the LHC to the level of the Tevatron and beyond. The differential measurements listed in the table correspond to the cross-section and charge asymmetry for boosted top-quark production. For 8 TeV operation the phase space is limited to events with an invariant mass of the $t\bar{t}$ system $m_{t\bar{t}} > 750$ GeV. For 13 TeV the cut on $m_{t\bar{t}}$ is raised to 1.2 TeV. We see that the α and β coefficients of these differential measurements are indeed an order of magnitude larger than those of the inclusive measurements at the same centre-of-mass energy. Therefore, the measurement of the charge asymmetry at high mass can provide a competitive constraint, even with an uncertainty that is an order of magnitude larger than that of the inclusive charge asymmetry measurement. The results for the boosted regime are becoming considerably more precise [89].

5.1.3 Validity of the effective operator approach

The charge asymmetry is reported by several authors (see for instance Ref. [138]) to receive relatively large contributions from terms that are proportional to Λ^{-4}. A full treatment of all these terms (including the contribution of the interference between dimension-eight operators with the SM and the interference between two dimension-six operators vertices and the SM) is beyond the scope this study, so this poor convergence may risk the effective operator paradigm in this area. In this section we estimate the size of the Λ^{-4} contributions by calculating the contribution of the dimension-six operator squared. We then have:

$$\left(O_i - O_i^{\mathrm{SM}}\right) = AC_i \left(\frac{1\ \mathrm{TeV}}{\Lambda}\right)^2 + A'C_i^2 \left(\frac{1\ \mathrm{TeV}}{\Lambda}\right)^4. \tag{5.4}$$

For each measurement and each operator from Equation 5.1 we determine the ratio A/A'. The results we obtain for the different operators depend on the observable we consider. We therefore present a unique interval for each measurement which corresponds to the stricter one obtained from the different operators. Following Ref. [138] the region of validity is given by the interval of the coefficient C_i where the Λ^{-2} linear term is at least twice as large as the quadratic Λ^{-4} term (i.e. $A/A' > 2C_i \left(\frac{1\ \mathrm{TeV}}{\Lambda}\right)^2$).

In Figure 5.2 the range of validity for each measurement is compared to the 95% C.L. constraint on C_1^u and C_1^d derived from that measurement (assuming vanishing contributions from all other operators). To guarantee valid results we require that the 95% C.L. interval is fully contained in the $A/A' > 1$ $C_i \left(\frac{1\ \mathrm{TeV}}{\Lambda}\right)^2$ band [1].

The interval of validity shrinks with the increase in centre-of-mass energy: at the 8 TeV LHC it is typically a factor two smaller than at the Tevatron. In combination with the reduced sensitivity to four-fermion operators of the LHC data there is a risk that adding a measurement may reduce the interval of validity more than the 95% C.L. interval. The differential measurements can see a very strong reduction of the interval of validity, in particular once we enter the regime of boosted top-quark pair production. However, in this case the sensitivity grows to compensate the reduced interval of validity. Therefore, a differential measurement of sufficient precision may prove to be useful in the fit.

The same trend towards smaller interval of validity for increasing centre-of-mass energy is observed for the cross-section and the charge asymmetry. The interval of validity of the charge asymmetry is generally somewhat smaller than that of the cross-section, but the difference is small compared to that between the Tevatron and the LHC, or between inclusive and differential measurements. For the inclusive measurements at the 8 TeV LHC the tension between interval of validity and the 95% C.L. interval on individual coefficients is much more pronounced for the cross-section measurement than for the charge asymmetry.

5.1.4 Multi-parameter fit

So far we have evaluated constraints on one coefficient at the time, assuming all others have a vanishing contribution. In this section we generalize the fit to all four-fermion operators (but still keep the

[1] This requirement ensures that the χ^2 evaluation on the 68% C.L. interval is within the $A/A' > 2\ C_i \left(\frac{1\ \mathrm{TeV}}{\Lambda}\right)^2$ interval where the Λ^{-4} is of minor importance. This is therefore equivalent to the criterion of Ref. [138].

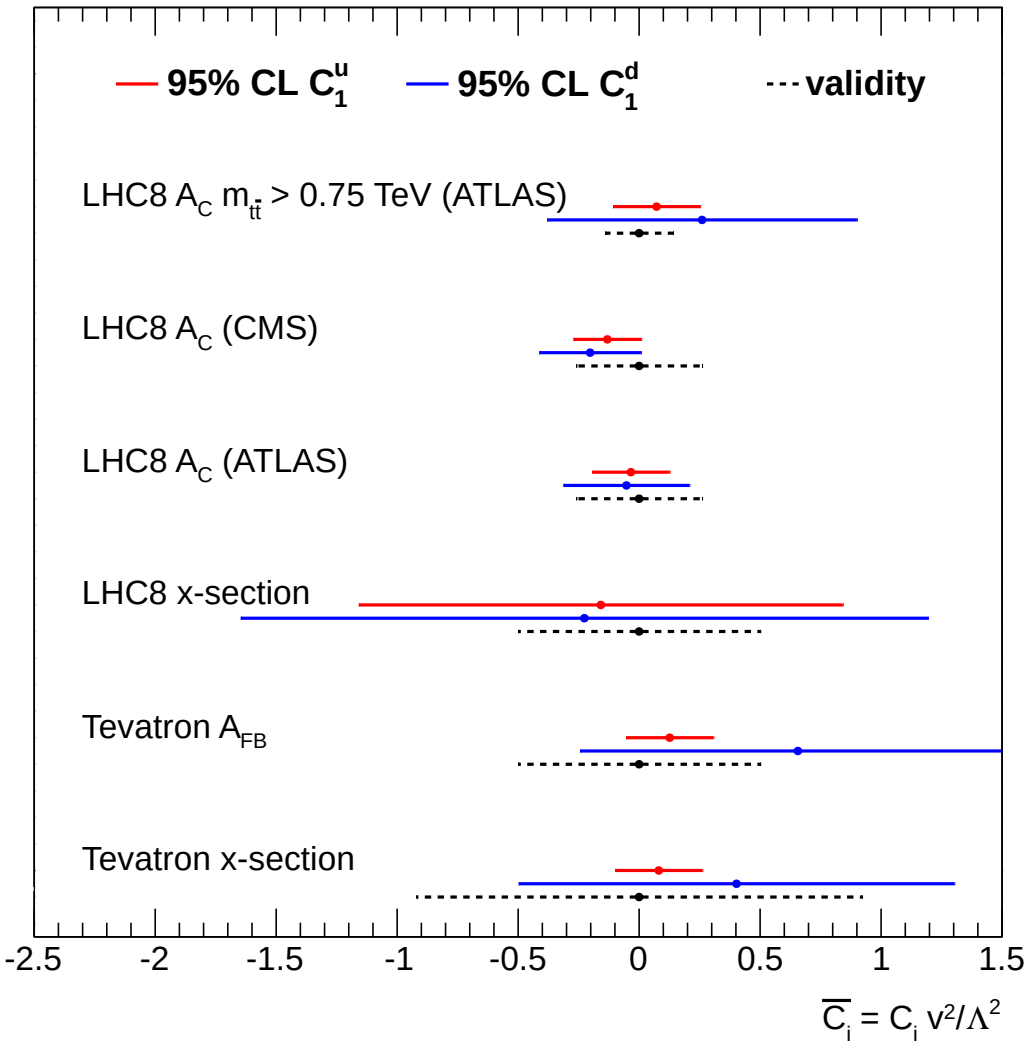

Figure 5.2: The interval of validity and 95% C.L. limits of cross-section and charge asymmetry measurements at hadron colliders. The interval of validity is given as a black dashed line. For each measurement the 95% C.L. limits on the coefficients of the effective operators involving up-type and down-type quarks are indicated as error bars. Operators are fit one by one, with all other dimension-six operators are set to 0.

remaining effective operators related to two-fermion interactions equal to 0). Using the parameterization of Equation 5.2 and Equation 5.3, and the datasets from Table 5.1, we construct an overall χ^2 function:

$$\chi^2 = \sum_i \left(\frac{O_i\left(\{C_i\}\right) - O_i^{exp}}{\Delta_i^{exp}} \right)^2 , \tag{5.5}$$

where $O_i\left(\{C_i\}\right)$ correponds to the parameterization of Equation 5.2 or Equation 5.3 and O_i^{exp} and Δ_i^{exp} to the experimental measurement and uncertainty. The sum runs over all measurements i defined in Table 5.1.

We minimize the χ^2 function using the root package MINUIT [183] in order to extract the parameters C_i.

The simultaneous fit of the four effective operators C_1^u, C_2^u, C_1^d and C_2^d using all data in Table 5.1 yields tight constraints on the former two, that correspond to interactions initiated by up-type quarks. The 95% C.L. limits are contained within the interval of validity. As we anticipated in subsection 5.1.2 the constraint on operators corresponding to down-type quarks is much weaker, where the marginalized 95% C.L. constraints from the four-parameter fit on C_1^d and C_2^d are 3-5 times weaker than the limits on single operators. The marginalized 95% C.L. intervals extend beyond the interval of validity. The exact level of tension between range of validity and limits depends somewhat on which measurements are included in the fit, but the qualitative conclusion remains true for all combinations of the data in Table 5.1: None of the combinations of the cross-section and charge asymmetry data yields meaningful marginalized limits on C_1^d and C_2^d. A similar observation was made in Ref. [118] for C_2^d.

Much stronger constraints are obtained when we assume $C_1^u = C_1^d = C_1$ and $C_2^u = C_2^d = C_2$. In this case, the interval is within the tightest interval of validity of the measurements used in the fit. We therefore present the constraints obtained with the two-parameter fit as the main result of this study.

5.1.5 Constraints on four-fermion operators

The result of the two-parameter fit of the coefficients $C_1 = C_1^u = C_1^d$ and $C_2 = C_2^u = C_2^d$ of the four-fermion operators to $t\bar{t}$ production cross-section and charge asymmetry measurments at hadron colliders is presented in Figure 5.3. All other dimension-six effective operators are assumed to have negligible impact. The allowed intervals at 95% confidence level are -0.06 $< \bar{C}_1 <$ 0.1 and -0.04 $< \bar{C}_2 <$ 0.11, where $\bar{C}_i = C_i \times v^2/\Lambda^2$, with $v = 246$ GeV the Higgs vacuum expectation value. The allowed intervals are contained within the region where the Λ^{-2} contribution of the dimension-six operators dominates over an estimate of the Λ^{-4} contribution (indicated as a dashed black line labelled *validity*).

The allowed bands in the C_1-C_2 plane of charge asymmetry and cross-section measurements cross at a straight angle, yielding tight constraints on both parameters (see left plot of Figure 5.1). Indeed, the simultaneous fit of C_1 and C_2 yields very similar results to the limits obtained when a single operator is floated in the fit.

A fit of the two linear combinations $\bar{C}_+ = \bar{C}_1 + \bar{C}_2$ and $\bar{C}_- = \bar{C}_1 - \bar{C}_2$ yields limits -0.09 $< \bar{C}_+ <$ 0.2 and -0.07 $< \bar{C}_- <$ 0.04 with a correlation of 0.75. In this case the results are readily related to the measurements. We see that the $\bar{C}_-$ constraint, driven by the charge asymmetry, is nearly three times stronger than the constraint on $\bar{C}_+$, that is dominated by the cross-section measurements. The central value of C_+ is 0.06, due to the Tevatron cross-section of Refs. [173,174] that slightly exceeds the prediction in the SM. The C_- fit is pulled towards negative values by the CMS measurement in Ref. [177]. This measurement 2σ below the SM value is able to compensate the positive pull from the Tevatron experiments.

The limits on the four-fermion operators presented in this paper are stronger than those of the global fit to the top-quark sector presented in Ref. [108, 118]. The prize to pay for this gain in precision is a loss of generality: the limits we derive are valid only under the assumption of equal coefficients for the four-fermion operators involving up-type and down-type quarks: $C_1 = C_1^u = C_1^d$ and $C_2 = C_2^u = C_2^d$.

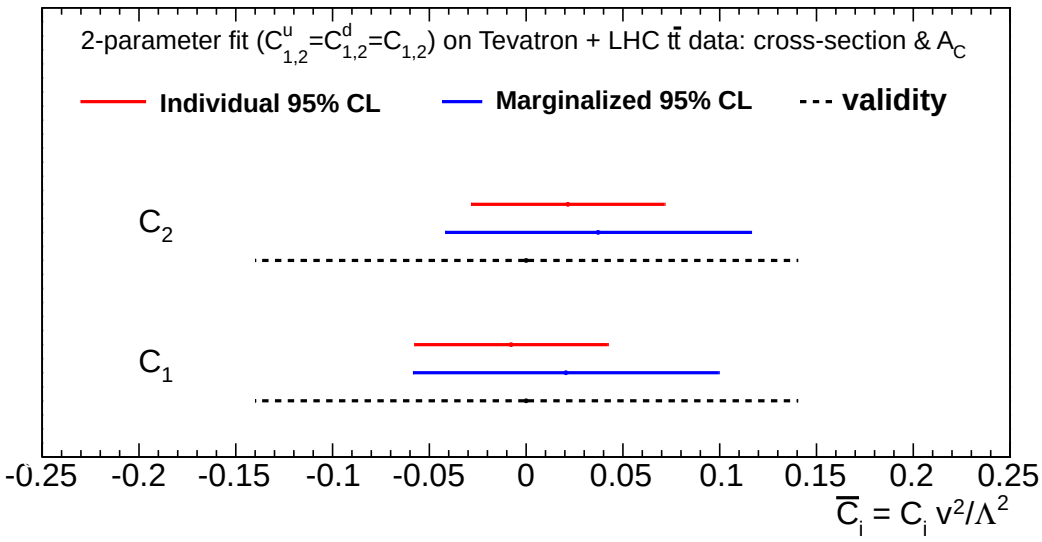

Figure 5.3: The 95% C.L. limits on the four-fermion operators C_1 and C_2 extracted from cross-section and charge asymmetry measurements at hadron colliders. The *individual* limits are obtained assuming all other dimension-six operators are 0, while the *marginalized* limits are obtained from a two-parameter fit that floats both operator coefficients simultaneously.

We believe, however, that this may be the most practical way to guarantee the validity of the effective operator approach with the current data sets. In the long run more precise data from LHC Run 2 should allow to constrain the separate four-fermion operators of up-type and down-type quarks to safe intervals.

5.1.6 Comparison to a concrete new physics model

The limits on C_- can be recast into limits on the mass of a flavour-universal axigluon [48] (with equal couplings to all quarks) using the relation $(C_1 - C_2)/\Lambda^2 = -4g_s^2/m_A^2$ from Ref. [132]. The 95% C.L. lower limit on the axigluon mass is 2.0 TeV. The axigluon with opposite-sign couplings to light and top quarks ($g_t = -g_q$), that makes a positive contribution to the charge asymmetry, is even more strongly constrained: $m > 2.8$ TeV. These limits extend the exclusion of earlier studies [184] considerably.

Both limits are well in excess of the 1.5 TeV that Ref. [132] quotes as the lower limit for application of the effective-operator analysis.

With LHC Run 1 the sensitivity for observation of a narrow signal on the SM $t\bar{t}$ background has entered the sub-pb regime for a multi-TeV resonance. The ATLAS and CMS searches [185, 186] yield a 95% C.L. lower limit on the axigluon mass of order 2 TeV. Limits from di-jet resonance searches at 13 TeV provide even stronger limits on this particular model [187].

5.1.7 First results at LHC Run 2

During the realization of this work in 2015 the analysis of LHC Run 2 data was in full swing. In the mean time, preliminary results have appeared on 13 TeV data [89]. These include an inclusive and a differential measurement on the charge asymmetry that extend well into the boosted regime.

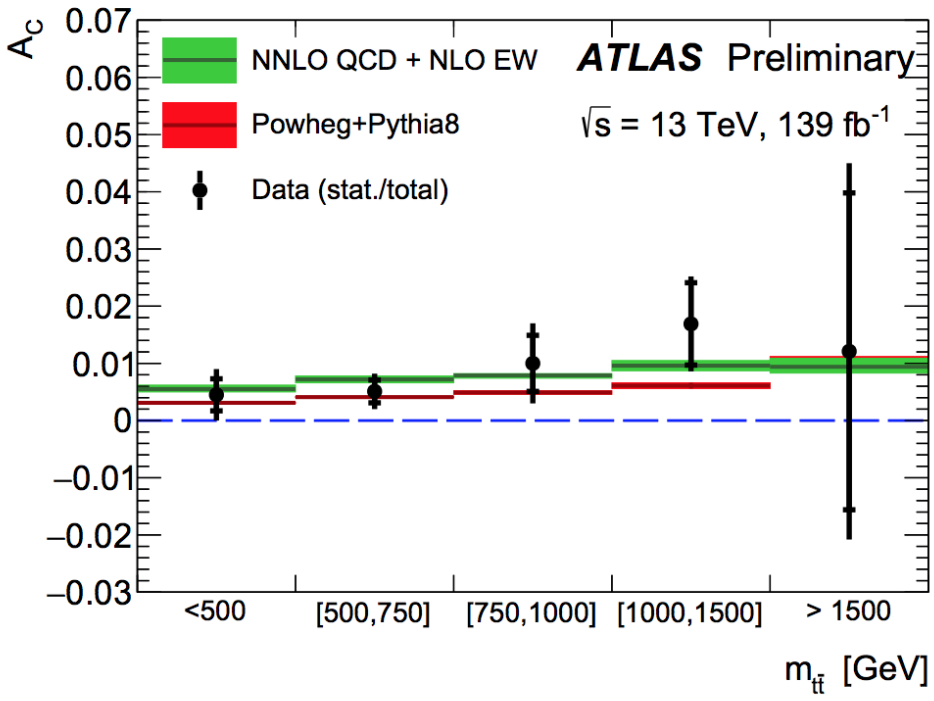

Figure 5.4: The unfolded differential charge asymmetry as a function of the top pair system in data (resolved and boosted topologies are combined). Green hatched regions show predictions in the SM calculated at NNLO in QCD and NLO in electroweak theory. Red hatched regions show parton-level truth asymmetry with its uncertainty extracted from the full phase space using nominal $t\bar{t}$ signal sample. Vertical bars correspond to the total uncertainties. Figure reproduced from Ref. [89].

In pp collisions at $\sqrt{s} = 13$ TeV, the $q\bar{q} \to t\bar{t}$ process is further diluted by the increase in gluon-gluon-initiated $t\bar{t}$ production. Therefore, the sensitivity of inclusive measurements to four-fermion operators is limited.

We already signalled in subsection 5.1.2 that the excellent sensivity to four-fermion operators of differential measurements, in particular measurements in the regime of boosted $t\bar{t}$ pair production, compensates for their (current) relatively poor precision.

ATLAS has published in 2019 the first measurement of the $t\bar{t}$ charge asymmetry with an integrated luminosity of 139 fb^{-1}. The inclusive $t\bar{t}$ charge asymmetry ATLAS is measured to be 0.0060 ± 0.0015 (stat.+syst.) [89] which differs from zero by 4 standard deviations. This is the first evidence for the subtle SM asymmetry at the LHC.

ATLAS also performed differential measurements as a function of the invariant mass and longitudinal boost of the $t\bar{t}$ system. In Figure 5.4 we show the differential measurement in terms of $m_{t\bar{t}}$.

Following our study, ATLAS interprets the results in terms of C_-. In Figure 5.5 the bounds on C_- for the different bins depending on $m_{t\bar{t}}$. They also study the impact of the quadratic term, proportional to Λ^{-4}, in red in the plot. The results they obtain compared with the parameterization with only the Λ^{-2} term are very similar.

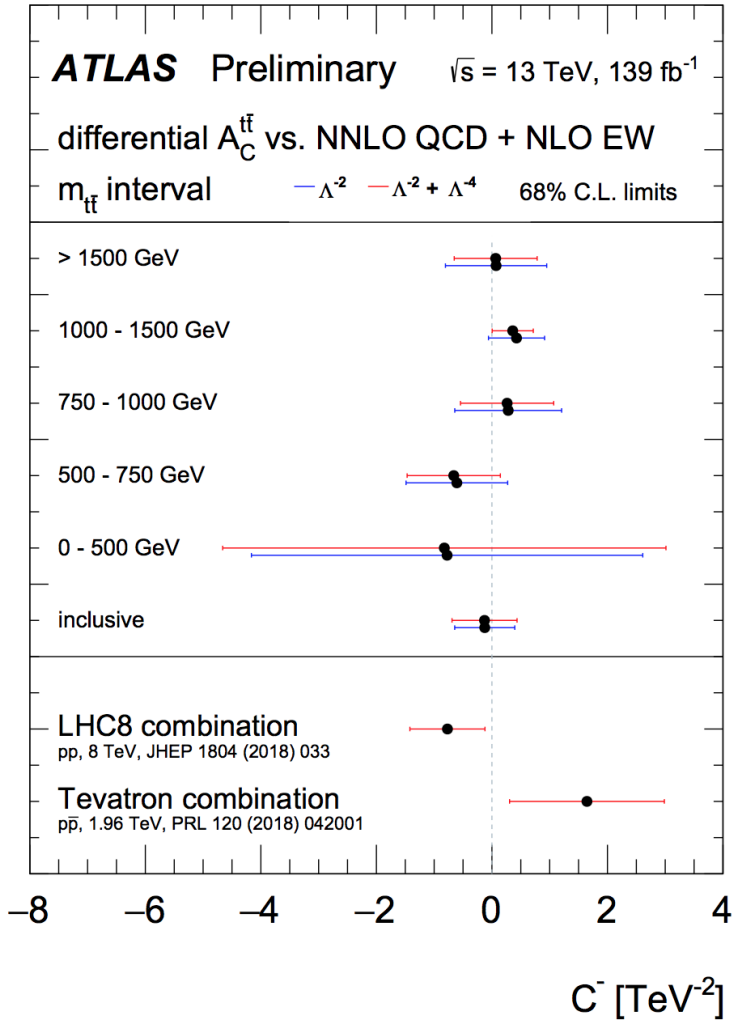

Figure 5.5: The 68% C.L. limits on the linear combination C_-/Λ^2 of Wilson coefficients of dimension-six operators. The bounds are derived from a comparison of the charge asymmetry measurements with the predictions in the SM of the NNLO QCD + NLO EW calculation [188]. The impact of dimension-six operators is parameterized [91]. Bounds are also shown from the forward-backward asymmetry measurements in $p\bar{p}$ collisions at $\sqrt{s} = 1.96$ TeV at the Tevatron and the charge asymmetry measurements in pp collisions at a centre-of-mass energy of 8 TeV in LHC Run 1. Figure reproduced from Ref. [89].

Thanks to the total uncertainty of 0.15%, the inclusive measurement yields a very tight bound. The sensitivity to C_- increases strongly with increasing invariant mass of the $t\bar{t}$ system. Therefore, the measurement of the asymmetry in the mass range of 1000-1500 GeV, with a precision of 0.83%, yields an equally tight bound. Transforming to our parameterization, $\bar{C}_- = C^- v^2/\Lambda^2$, the best bound is $0 < \bar{C}_- < 0.06$. The bound from 13 TeV data from ATLAS alone exceeds the bounds from the Tevatron and LHC Run 1 combinations.

Compared to the projections in Ref. [91] we find that the inclusive measurement has a much improved precision. Still, thanks to the greatly enhanced sensitivity of the boosted measurement the bound from the differential analysis is stronger than that from the inclusive measurement even if the boosted measurement is somewhat less precise than envisaged.

5.2 Constraints on top and bottom-quark EW couplings

In this section we evaluate the implications of LHC and LEP/SLC measurements for the EW couplings of the top and bottom quarks. We derive global bounds on the Wilson coefficients of the relevant two-fermion operators. This global fit is based on Ref. [106].

5.2.1 Fit setup

The dependence of the observables included in the fit of the Wilson coefficients is calculated at leading order with the MonteCarlo generator `MG5_aMC@NLO` [99]. The `TEFT_EW` UFO model [109] is used for most of the operators. Exceptions are $C_{t\varphi}$ for which the `dim6top` UFO model [105] is used, and C_{bW} and C_{bB} for which we use the `SMEFTsim` UFO model [189]. The following values of the input parameters are used in the calculation:

$$\begin{aligned} \alpha &= 1/127.9\,, & m_Z &= 91.1876\text{ GeV}\,, & m_b &= 0\text{ GeV}\,, \\ G_F &= 1.16637\times 10^{-5}\text{ GeV}^{-2}\,, & m_H &= 125\text{ GeV}\,, & m_t &= 172.5\text{ GeV}\,. \end{aligned}$$

The dependence of observables on the Wilson coefficients is parameterized using the following expansion:

$$o = o_{SM} + \frac{1}{\Lambda^2}\sum_i C_i o_i + \frac{1}{\Lambda^4}\sum_j\sum_k C_j C_k o_{jk} + \mathcal{O}(\Lambda^{-4}). \tag{5.6}$$

The leading EFT term proportional to Λ^{-2} reflects the interference of SM amplitudes with those featuring one dimension-six operator insertion. The terms proportional to Λ^{-4} stem from the square of the amplitudes involving one insertion of dimension-six operators, or from amplitudes involving two such insertions in interference with SM ones. Terms of order Λ^{-4} due to dimension-eight operators are ignored.

For several combinations of operators and observables the term proportional to Λ^{-2} in Equation 5.6 is suppressed. The Λ^{-4} terms then plays an important role and the EFT expansion is not valid in full generality. A well-known example is the dependence of the associated production processes $pp \to t\bar{t}X$ on the top-quark dipole operators. The $\sigma^{\mu\nu}q_\nu$ structure involves the momentum of the Z boson or photon, which leads to a suppression because the radiated Z boson or photon tends to be soft [109]. In

this case, other processes can be found, where the Λ^{-2} term dominates the sensitivity: the inclusion of charged-current interactions, and $e^+e^- \to t\,\bar{t}$ production at a future facility, restores the validity of the fit for C_{tW} and C_{tB}.

Several operators affecting the bottom-quark EW couplings lead to amplitudes whose interference with SM ones is suppressed by the small bottom-quark mass. The O_{bW} and $O_{\varphi tb}$ operators induce a $t\bar{b}W$ interaction involving a right-handed bottom quark. The O_{bB} operator also generate a chirality flipping in $b\bar{b}Z$ dipolar interactions. The interferences of the amplitudes they generate with SM ones thus vanish in the $m_b \to 0$ approximation adopted in this study. These interferences would remain suppressed even with a bottom-quark mass different from 0 at the centre-of-mass energies we work, so the impact of the $m_b \to 0$ approximation is not significant in our study and help to simplify the calculus.

5.2.2 Implementation of the fit

The fit to data is performed using the open source `HEPfit` package [190]. `HEPfit` is a general tool designed to combine direct and indirect constraints, in EFTs or particular SM extensions. Its flexibility allows to easily implement any BSM model or observable. `HEPfit` is available under the GNU General Public License. The developers' version can be downloaded at [191].

The fit is performed as a Bayesian statistical analysis of the model. `HEPfit` includes a Markov-Chain MonteCarlo implementation provided by the Bayesian Analysis Toolkit [192] to explore the parameter space. Similar fits using the `HEPfit` package have been performed for different models [193,194] and for EFT analysis [195,196].

The results in this work were verified with an independent fitting code based on the MINUIT minimization package in ROOT [197]. The results for individual limits agree to 1%. For the comparison of the global limits we perform an ad-hoc fit in which we reduce the number of parameters and observables. In this case the results agree to 10%. In general we find `HEPfit` is more robust when dealing with several local minima, so all final results in this section are obtained using `HEPfit`.

The fit is based on the Bayesian approach of statistics and the interpretation differs slightly from the frequentist interpretation. The fit results are given as intervals on the operator coefficients with a given posterior probability, typically 68%.

5.2.3 Measurements

The measurements that form the input to the fit are presented in this section.

Top-quark neutral-current interactions.

- $pp \to t\bar{t}h$ production. The production of a Higgs boson in association with a top-quark pair was observed by ATLAS and CMS in 2018 [198,199]. The production rate is sensitive to the coefficient $C_{t\varphi}$ of the operator that shifts the value of the top-Yukawa coupling.

- $pp \to t\bar{t}Z/W$ production. The associated production of top quarks with a Z boson gives access to all operators that modify the coupling of the top quark with neutral EW gauge bosons and

is therefore a key channel in a combined fit [109]. The ATLAS and CMS measurements of the inclusive cross-section using 36 fb^{-1} of data at 13 TeV have reached a precision of approximately 15-20% [200, 201]. The results on $pp \to t\bar{t}W$ production are also included in the fit.

- $pp \to t\bar{t}\gamma$ production. The rate of the $pp \to t\bar{t}\gamma$ process depends on the C_{tW} and C_{tB} coefficients of the EW dipole operators. ATLAS has published a measurement of the $pp \to t\bar{t}\gamma$ fiducial cross-section [202] at $\sqrt{s} = 13$ TeVwith 36.1 fb^{-1}.

- Single-top production in association with a Z boson has been observed by ATLAS and CMS. For the $pp \to tZq$ process the first cross-section measurements have reached a precision of approximately 15-35% [203, 204].

- $pp \to \gamma^*/Z^* \to t\bar{t}$ production. The neutral-current pair production process $q\bar{q} \to Z/\gamma \to t\bar{t}$ is overwhelmed by the QCD process and has not been isolated. This contribution to the inclusive $pp \to t\bar{t}$ process leads to a dependence of the rate on the EW operators considered, but in practice this contribution can be ignored.

Top-quark charged-current interactions.

- Top-quark decay, $t \to Wb$. The charged-current $t\bar{b}W$ vertex is accessible at hadron colliders in top-quark decay. The helicity fractions of the W boson produced in top-quark decay can be predicted to excellent precision [205]. The measurements by ATLAS and CMS [206–209] at $\sqrt{s} = 7$ and 8 TeV reach a precision of several percent. The combination of precise predictions and measurements converts these measurements in true hadron collider precision measurements and in sensitive probes to new physics affecting the $t\bar{b}W$ vertex [119]. We include the 8 TeV measurements of F_L and F_0, that yield a tight limit on C_{tW}.

- Single-top production. A second handle on the $t\bar{b}W$ vertex is found in charged-current single top-quark production. The t-channel process has a sizeable cross-section, which has been measured to better than 10% precision [210, 211] at $\sqrt{s} = 13$ TeV. ATLAS and CMS have also published precise measurements of the rate for the Wt associated production channel [212, 213].

Measurements in bottom-quark production.

- $e^+e^- \to b\bar{b}$ production. The LEP and SLC measurements of bottom-quark pair production provide a powerful, complementary handle on the operator coefficients $C^1_{\varphi Q}$ and $C^3_{\varphi Q}$. Combining measurements of bottom-quark production at LEP/SLC with measurements in top-quark production yield solid constraints on both operator coefficients in a global fit [49]. We consider the measurements of R_b and A^{bb}_{FBLR} at the Z pole [57].

- $pp \to b\bar{b}Z$ production. The associated production processes $pp \to b\bar{b}Z$ and $pp \to b\bar{b}\gamma$ at the Tevatron and LHC probe the $b\bar{b}Z$ and $b\bar{b}\gamma$ vertices. The ATLAS and CMS experiments have measured the cross-section for the associated production of a Z boson and at least one bottom quark [214, 215] in early LHC runs. The constraints derived from these measurements are not

Process	observable	$\sqrt{s}$	$\int \mathcal{L}$	SM	Ref.
$pp \to t\bar{t}H$	cross-section	13 TeV	36 fb^{-1}	[198]	[198]
$pp \to t\bar{t}Z/W$	cross-section	13 TeV	36 fb^{-1}	[109]	[200]
$pp \to t\bar{t}\gamma$	fid. x-sec.	13 TeV	36 fb^{-1}	[109]	[202]
single-top (t-ch)	cross-section	13 TeV	36 fb^{-1}	[210]	[210]
single-top (Wt)	cross-section	13 TeV	36 fb^{-1}	[212]	[212]
single-top (tZq)	cross-section	13 TeV	36 fb^{-1}	[216]	[216]
$t \to W^+b$	F_0, F_L	8 TeV	20 fb^{-1}	[205]	[206]
$e^-e^+ \to b\bar{b}$	R_b , A_{FBLR}^{bb}	$\sim$ 91 GeV	202.1 pb^{-1}	[57]	[57]

Table 5.3: Measurements included in the EFT fit of the top and bottom-quark EW sector. For each measurement, the process, the measured observable, the centre-of-mass energy and the integrated luminosity are listed. The last columns list the references for the SM prediction and the measurement that is included in the fit.

currently competitive with the LEP and SLC measurements. We therefore ignore them in the following.

Summary of measurements. The selected measurements that are included in our fit are summarized in Table 5.3. For all LHC observables, ATLAS and CMS measurements are available at $\sqrt{s} = 13$ TeV for an integrated luminosity of 36 fb^{-1}. As the measurements have not yet been combined, and a proper correlation of uncertainties requires harmonization of the definitions of the systematics, we include only one measurement for each observable. We select the most precise measurement among the 13 TeV measurements. The measurements of the same quantities at 8 TeV are not included except for the measurement of the W-boson helicity fractions in top-quark decay, that is only available at 8 TeV.

The LEP and SLC measurements of R_b and A_{FBLR}^{bb} at the Z pole have been combined in the EW fit of Ref. [57]. The fit correlates the measurements of several quantities and reports a complete covariance matrix.

Even with a single measurement for each observable included in the fit, the systematic uncertainties are expected to lead to correlations among the measurements. Also the theory predictions are correlated, through the parton density functions and the similarity of the matrix elements of the several associated production processes. We have cross-checked the effect of correlated systematics on the fit results explicitly. The full covariance matrix of the LEP/SLC EW fit is taken into account. These correlations have a negligible effect on our results. Also the introduction of an ad-hoc correlation of 50% between the results for associated top-quark production has a minor effect on the fit. We therefore expect that a full treatment of all correlations, once the combinations of ATLAS and CMS measurements are made available, will lead to only a slight improvement of the limits.

5.2.4 Sensitivity to operator coefficients

The set of measurements in Table 5.3 provides sensitivity to all operators listed in Equation 3.3. Associated production of top quarks with a Z boson at the LHC alone is sensitive to all five top-quark operators in our basis. Associated production with a photon gives access to the dipole operators C_{tB} and C_{tW}. Charged-current processes, such as $t\bar{t}W$ production, EW single-top production and top-quark

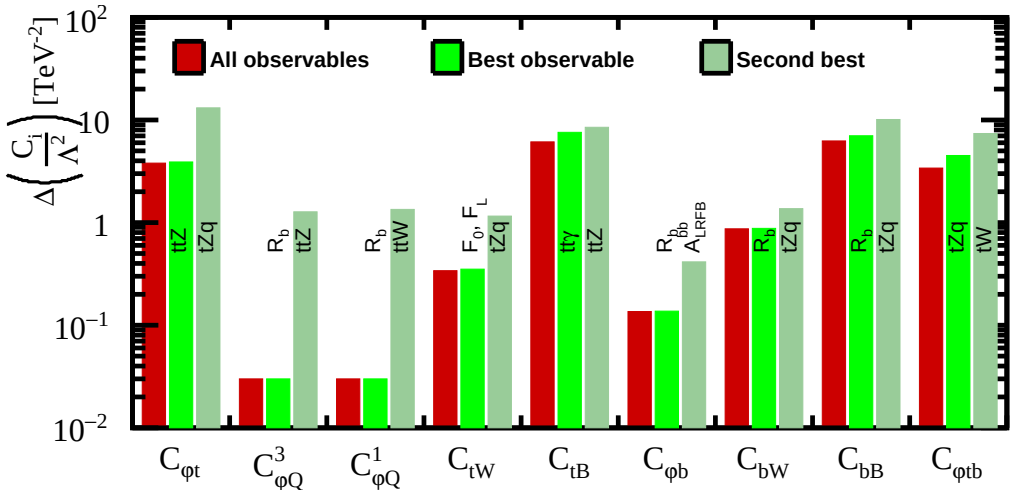

Figure 5.6: Results of single-parameter individual fits to the Wilson coefficients of the dimension-six operators introduced in Equation 3.3. For each operator the 1σ uncertainty is shown. The three bars respectively correspond to the result of the combined fit using all data (red), to the constraint obtained from the most sensitive single measurement (light green), and to that of the second-best measurement (greyish green). The operator $O_{t\varphi}$ only contributes to the $t\bar{t}H$ production, for this reason it is not included in the plot.

decay are sensitive to C_{tW}, $C^3_{\varphi Q}$, C_{bW} and $C_{\varphi tb}$. Results on $e^+e^- \to b\bar{b}$ production are sensitive to $C^1_{\varphi Q}$ and $C^3_{\varphi Q}$ and the pure bottom-quark operators included in the fit.

To explore the relative sensitivity of the existing measurements, the results of single-parameter fits are shown in Figure 5.6. For each of the operators, the first column displays the individual limit on the Wilson coefficients of the complete data set presented in Table 5.3. The second column shows the result of the most constraining measurement. The third column displays the second-best constraint.

For most operators, there is a strong hierarchy in the sensitivity of the measurements. For a majority of operator coefficients a single measurement drives the individual sensitivity. Typically, the limit of the most sensitive measurement is a factor 2-5 better than that of the second-best measurement for most operators. For $C^1_{\varphi Q}$ and $C^3_{\varphi Q}$ the precise LEP/SLC measurement of R_b yields a constraint 30 times better than that of the associated production processes at the LHC. For C_{tB}, the associated $t\bar{t}\gamma$ and $t\bar{t}Z$ production modes provide similar sensitivity and the combined results is significantly stronger than the limit derived from a single observable. Also in the case of $C_{\varphi tb}$, the different single top-quark measurements provide similar sensitivity.

A few observables are sensitive to a large number of operators: the measurement of R_b at LEP yields the best individual limits on five different operators. The $t\bar{t}Z$ and tZq cross-sections are also sensitive to several operators: they score among the two most sensitive measurements for six operators. The most specific observables are the helicity fractions of the W bosons in top-quark decay. They provide a stringent limit on C_{tW} and are not strongly affected by the other operators.

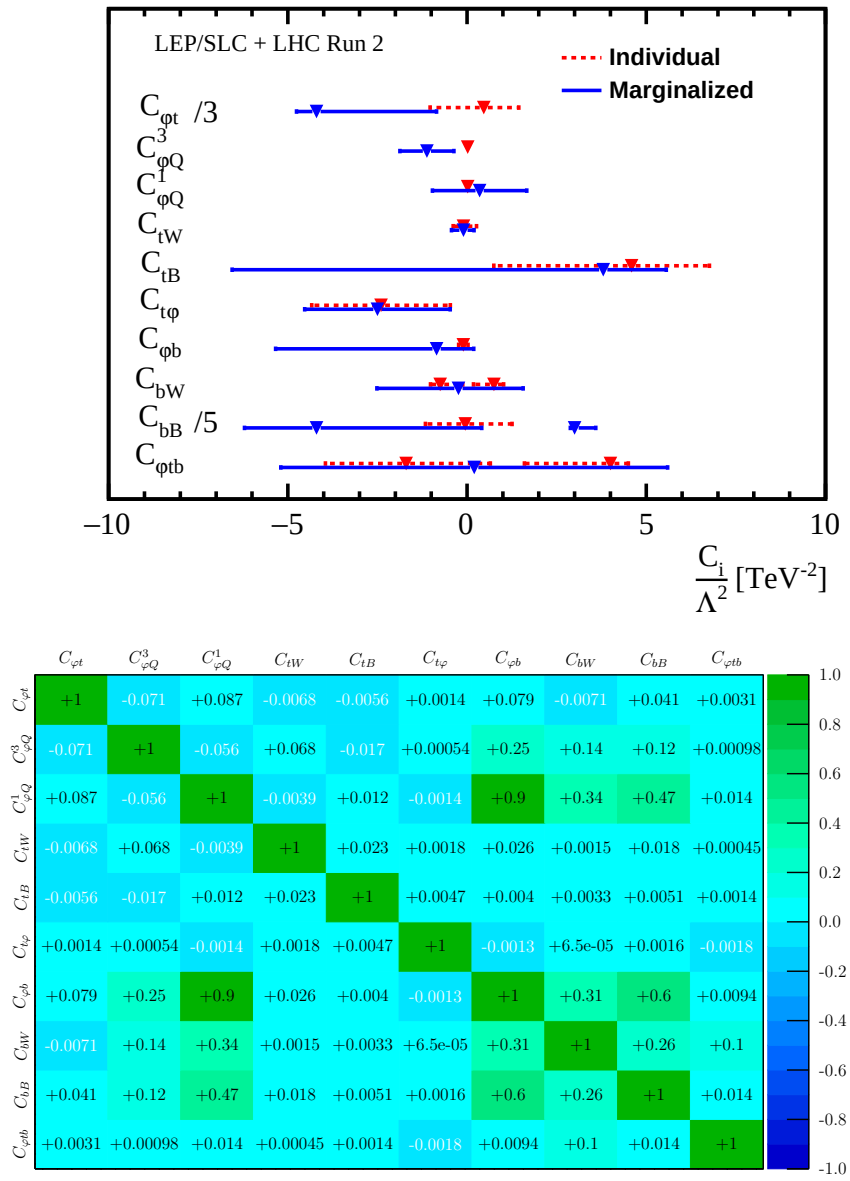

Figure 5.7: The 68% C.L. limits (upper plot) and correlation matrix (lower plot) for the Wilson coefficients of the ten effective operators that modify the EW couplings of top and bottom quarks derived from a fit of the data included in Table 5.3. The correlation matrix in `HEPfit` is calculated following Ref. [192]. Global (marginalized) limits obtained in the fit are shown as blue bars, the individual limits from single-parameter fit in red. The (local) minimum of the χ^2 are shown as triangles.

5.2.5 Fit to LHC and LEP/SLC data

A ten-parameter fit to the LHC and LEP/SLC measurements is presented in Table 5.4. The 68% probability bounds on the Wilson coefficients are also sown in Figure 5.7. Global or marginalized limits are obtained when all coefficients are varied simultaneously. These are shown as blue continuous lines. The individual limits from a single-parameter fit are presented as red dashed lines.

	Λ^{-2} and Λ^{-4} terms	Λ^{-2} term only
$C_{\varphi t}/\Lambda^2$	$(-16, -2.4)$	$(-2.1, +4.5)$
$C^3_{\varphi Q}/\Lambda^2$	$(-1.9, -0.4)$	$(-0.7, +0.5)$
$C^1_{\varphi Q}/\Lambda^2$	$(-1, +1.7)$	$(-0.6, +0.7)$
C_{tW}/Λ^2	$(-0.4, +0.2)$	$(-0.42, +0.24)$
C_{tB}/Λ^2	$(-6.8, +5.6)$	$(-9.6, +38.4)$
$C_{t\varphi}/\Lambda^2$	$(-4.6, -0.4)$	$(-4.42, 0)$
$C_{\varphi b}/\Lambda^2$	$(-5.4, +0.2)$	$(-0.6, +0.2)$
C_{bW}/Λ^2	$(-2.6, +2.1)$	—
C_{bB}/Λ^2	$(-31.2, +2.4)$, $(+14.4, +18)$	—
$C_{\varphi tb}/\Lambda^2$	$(-5.2, 5.6)$	—

Table 5.4: The 68% probability intervals on the dimension-six operator coefficients in units of TeV^{-2}. These results are obtained with a fit to LHC and LEP/SLC data for two parameterizations of the dependence of the observables on dimension-six operator coefficients. The first column lists the results from the fit based on the nominal parameterization, which includes terms proportional to Λ^{-2} and Λ^{-4} terms. The second column is obtained with a fit based on a parameterization that only includes Λ^{-2} terms.

Generally, the fit yields good results even when all operator coefficients are varied simultaneously. The individual limit on C_{tW}/Λ^2 is very tight and the constraints remain very strong in the ten-parameter fit. Several observables also have similar sensitivity to C_{tB}/Λ^2 and $C_{\varphi t}/\Lambda^2$. The global limits are therefore not degraded too much compared to the individual limits.

For the operators that affect bottom-quark production in e^+e^- collisions, the individual limits from the Z-pole measurements are very tight. To disentangle the contributions of different operators, the fit must use several observables. Given the large hierarchy in sensitivities observed in Figure 5.6, the global limits are typically much weaker than the individual ones. Even so, tight constraints of order $1\ \text{TeV}^{-2}$ are obtained for $C^1_{\varphi Q}/\Lambda^2$ and $C^3_{\varphi Q}/\Lambda^2$ and $C_{\varphi b}/\Lambda^2$.

Comparing these limits to those obtained by other groups, we find that our fit yields better results. In particular, the inclusion of the Z-pole data leads to considerably tighter limits on $C^3_{\varphi Q}$, compared to Ref. [114].

5.2.6 Impact of Λ^{-4} terms

The results of the nominal fit are based on a parameterization according to Equation 5.6, that includes Λ^{-2} and Λ^{-4} terms. The fit finds multiple allowed regions for several operator coefficients. These local minima are a result of the Λ^{-4} terms in the parameterization. Two regions, roughly equidistant from the prediction in the SM, are found for C_{bW}/Λ^2, C_{bB}/Λ^2 and $C_{\varphi tb}/\Lambda^2$.

In Table 5.4 the nominal results are compared to a fit based on a parameterization that includes only the Λ^{-2} terms.

For several operator coefficients the inclusion of Λ^{-4} terms is expected to have a profound impact on the result. In the dependence of the $t\bar{t}X$ rates on C_{tB}, the Λ^{-2} term is suppressed, and the Λ^{-4} terms dominate the sensitivity when limits are saturated. The bound on C_{tB} is therefore severely degraded when the Λ^{-4} terms are dropped. This is not the case for C_{tW}, for which the bound is dominated by the measurements of the helicity fractions in top-quark decay and of the single-top production cross-section.

For the bottom-quark dipole operators C_{bW}, C_{bB} as well as for $C_{\varphi tb}$, the interferences with SM amplitudes vanish in the $m_b = 0$ approximation. The fit based only on Λ^{-2} terms can therefore not bound these operators.

The correlations between the different operator coefficients propagate the effect of the Λ^{-4} terms to other operators. If the fit is repeated excluding O_{bW}, O_{bB} and $O_{\varphi tb}$ the results obtained with the two parameterizations are very similar for all operators except O_{tB} and $O_{\varphi t}$. In the appendices of Ref. [106] we find the covariance matrices we obtain from the global fits.

The importance of Λ^{-4} terms indicates that the validity of the EFT expansion should be carefully verified. When recasting these results in a concrete BSM scenario, one must verify that the dimension-eight operators that are ignored here are subdominant in comparison with dimension-six ones.

5.2.7 Current constraints on the top-Yukawa coupling

Indirect and direct bounds. The top-Yukawa coupling is one of the most intriguing parameters in the SM. With a value close to 1 it is the largest of all Yukawa couplings. New physics scenarios such as two-Higgs-doublet models, supersymmetric scenarios with small $\tan\beta$, and composite Higgs models [217] could lead to sizeable shifts from the prediction in the SM. A precise and robust measurement is therefore one of the main targets of high-energy physics experiments in the next decades.

The measurements of the Higgs boson decays and production rates other than $t\bar{t}H$ yield indirect constraints on the top-Yukawa coupling. A model-dependent bound can be derived from the loop-induced $gg \to H$, $H \to Z\gamma$ and $H \to \gamma\gamma$ rates. In the SM, the top-quark loop is the dominant contribution to these rates, but the effective couplings to the photon and the gluon could also receive contributions from new particles. In the κ fit framework employed in early Higgs coupling fits, these BSM contributions are assumed to be absent and the $gg \to H$ and $H \to \gamma\gamma$ rates yield a tight constraint on the factor $\kappa_t = \kappa_c = \kappa_u$ that multiplies the Yukawa couplings of the up-type quarks. The legacy result of LHC Run 1 is $\kappa_t = 1.40^{+0.24}_{-0.21}$ [218]. Significantly sharper results are available from Run 2 measurements [219, 220]. These indirect bounds tend to weaken considerably in a global fit.

Several attempts have been made to disentangle the contributions of different operators that contribute to the $gg \to H$ (and $H \to \gamma\gamma$) rates (see Ref. [221] and references therein) with additional probes, such as boosted Higgs+jet production, di-Higgs boson production, off-shell Higgs production. None of these seem sufficiently sensitive to lift the degeneracy between the operator that modifies the top-Yukawa coupling and operators representing Hgg (or $H\gamma\gamma$) contact interactions.

Therefore, we focus on the direct bound from $t\bar{t}H$ production in this section.

Associated $t\bar{t}H$ production at the LHC. The observation of the associated production process of a top-quark pair with a Higgs boson [198] provides a direct demonstration of the interaction of the Higgs boson with the top quark. The ratio $\mu_{t\bar{t}H}$ of the measured cross-section and the prediction in the SM is determined with a precision approaching 20%. With an uncertainty of 8%, the NLO QCD prediction in the SM is also relatively precise. The extraction of the top-Yukawa coupling from the $pp \to t\bar{t}H$ rate could thus yield a competitive and robust result, provided all other EFT contributions are sufficiently well constrained.

The fit presented in subsection 5.2.5 includes the ATLAS measurement of the $pp \to t\bar{t}H$ production cross-section. A single-parameter fit yields an individual 68% probability bound on the operator coefficient $C_{t\varphi}$ that shifts the value of the top-Yukawa coupling:

$$C_{t\varphi}/\Lambda^2 \in [-4.4, 0]\ \text{TeV}^{-2} \qquad \text{(individual)}.$$

Due to a small quadratic term in the dependence of the $t\bar{t}H$ cross-section on $C_{t\varphi}$, the fit finds a second minimum very far from the SM value. Here we only treat the minimum which is closer to the SM value. The bound becomes only slightly weaker in the ten-parameter fit:

$$C_{t\varphi}/\Lambda^2 \in [-4.6, -0.4]\ \text{TeV}^{-2} \qquad \text{(marginalized)}.$$

The individual and marginalized results are very close to each other, an indication that the constraint from the $t\bar{t}H$ rate is very robust against the effect of the operators that modify top-quark EW couplings. The dependence of $pp \to t\bar{t}H$ on other top-quark EW operators arises mainly from $q\bar{q}$-initiated production which is subdominant compared to the gg-initiated process. The correlation of $C_{t\varphi}/\Lambda^2$ with C_{tW}/Λ^2, $C^3_{\varphi Q}/\Lambda^2$, C_{tB}/Λ^2 and C_{bW}/Λ^2 is small, below 0.1%. We note, however, that including four-fermion $q\bar{q}t\bar{t}$ operators can have a significant impact on the extraction of the top-Yukawa coupling from $pp \to t\bar{t}H$ measurement. Other studies that have included the top-Yukawa and $q\bar{q}t\bar{t}$ operators in a global fit obtain much looser bounds [114].

5.2.8 Indirect constraints

For reference, we collect in this section several observables that can be used to derive indirect constraints on top-quark couplings. A more complete discussion can be found in appendix A of Ref. [105].

- Data from B-factories can provide stringent bounds. For instance, the rare meson decays $B_s \to \mu^+\mu^-$ and $K \to \pi\nu\bar{\nu}$ give access to the $t\bar{t}Z$ vertex [222] and yield constraints on the coefficients of the $O^3_{\varphi Q}$, $O^1_{\varphi Q}$ and $O_{\varphi t}$ operators. The $b \to s\gamma$ decays give access to the $t\bar{t}\gamma$ vertex [223] and bounds on C_{tW} and C_{tB} are derived from the $\bar{B} \to X_s\gamma$ decay rate measured by the BaBar, Belle and CLEO experiments. B-meson decays are used in Ref. [224, 225] to access the Wtb vertex and FCNC interactions in Ref. [226]. Dimension-six operators involving the top quark are also studied in the Standard-Model Effective-Field-Theory (SMEFT) matching onto weak effective theory (WET) for $\Delta F = 1$ [227], $\Delta F = 0$ [228], $\Delta F = 2$ [229].

- EW precision measurements also provide indirect sensitivity to top-quark operators through loop effects [230,231]. The impact of top-quark operators in Higgs production and decay at both hadron and lepton colliders was examined in Ref. [127, 232]. Including also the dependence of diboson production at future lepton colliders, a combined analysis of the electroweak, Higgs, and top-quark effective field theories was performed in Ref. [233].

- Measurements of electric dipole moments offer a complementary constraint on the top-quark EW couplings. In particular the CP-violating operators, that are not included in this work, receive stringent individual limits [234]. The inclusion of these bounds in a fully global analysis remains to be done.

Indirect bounds on a single coefficient, or small systems of a few coefficients, are often competitive in comparison with the direct bounds from LHC data that we present in subsection 5.2.5. With the inclusion of prospects for top-quark pair production at future electron-positron colliders of chapter 7, the bounds become less relevant. A global fit including the discussed measurements requires consideration of an extended set of operator coefficients and is beyond the scope of this thesis.

5.3 Summary of constraints

The couplings of the third-generation quarks form one of the uncharted corners of the SM. These couplings are a sensitive probe of broad classes of extensions of the SM. It is therefore very exciting to see meaningful bounds in a multi-parameter fit on LEP/SLC and LHC data.

Four-quark operators. Top-quark pair production data at hadron colliders allow to constrain four-quark interactions. Analyzing the relative sensitivities of pair production measurements at the Tevatron and the LHC we find that the cross-section and charge asymmetry measurements provide complementary constraints, where the latter are more powerful at the LHC. The sensitivity to four-quark operators is strongly enhanced for measurements in the boosted regime.

Several authors [108, 132, 138] have signalled the importance of higher-dimension contributions of order Λ^{-4} to high-energy collision data. We have ensured explicitly that these contributions, whose size is estimated as the contribution of the dimension-six operator squared, are subdominant in our fit.

We have extracted limits on the dimension-six operators C_1 and C_2, under the assumption of that the coupling strengths to up- and down-type quarks are identical (i.e. $C_1 = C_1^u = C_1^d$ and $C_2 = C_2^u = C_2^d$). The allowed intervals at 95% C.L., -0.06 $< C_1 \times v^2/\Lambda^2 <$ 0.10 and -0.04 $< C_2 \times v^2/\Lambda^2 <$ 0.11, are in good agreement with the prediction in the SM, $C_1 = C_2 = 0$. These form stricter limits than those obtained from a global fit that includes the same data [108] (at what we believe is an acceptable loss of generality).

For an explicit UV completion such as the axigluon model these limits correspond to a lower limit on the mass in excess of 2 TeV, which is a competitive constraint when compared to direct limits from resonance searches.

New preliminary results from ATLAS at 13 TeV provide even stricter bounds. ATLAS best measurement using differential analysis derives a bound of $0 < \bar{C}_- < 0.06$.

Two-quark EW operators. We have performed a fit to existing data of the dimension-six two-fermion operator coefficients affecting the EW couplings of the bottom and top quarks. We combine LEP/SLC data on bottom-quark production at the Z pole with LHC data on top-quark pair production in association with bosons, on single top-quark production and on W-boson helicity fraction in top-quark decay.

The results of the fit are given in Table 5.4. All 68% probability intervals include the prediction in the SM. The bound is well below 1 TeV^{-2} for the coefficient of the top-quark EW dipole operator C_{tW}/Λ^2 that is constrained by charged-current interactions. Very tight bounds are also obtained for the coefficients $C^1_{\varphi Q}/\Lambda^2$ and $C^3_{\varphi Q}/\Lambda^2$ that modify the left-handed couplings of the bottom and top quark to the Z boson. The combination of LHC data with that of LEP and SLC is very powerful to disentangle these operator coefficients that affect both top and bottom-quark physics. We are therefore able to present the tightest constraints on these operators to date.

The LHC has limited sensitivity to the operator coefficient $C_{\varphi t}$ that modifies the right-handed coupling of the top quark to the Z boson and coefficients of order 10^1 are still allowed. The same is true for the EW dipole operators C_{tB}/Λ^2 and C_{bB}/Λ^2. Inclusion of measurements of the $B_s \to \mu^+\mu^-$ and $b \to s\gamma$ decay rates may help to improve those bounds.

We also present results for the extraction of the top-Yukawa operator $C_{t\varphi}/\Lambda^2$ from the associated production processes $pp \to t\bar{t}H$.

For some operator coefficients, the fit results depends strongly on the presence of the terms proportional to Λ^{-4} (due to the contribution of dimension-six operators squared). Care is therefore required to re-interpret these bounds in terms of concrete extensions of the SM.

6.- Top-quark physics at electron-positron colliders

We examine in this chapter the sensitivity of several observables to the dimension-six operators affecting top-quark physics. The complementarity between different observables is examined, together with the impact of the possible beam polarization in electron-positron colliders and the centre-of-mass energy. We define the sensitivity of an observable o to an operator coefficient C_i as its normalized variation in that direction, around the SM point:

$$S_i^o = \frac{1}{o}\frac{\partial o}{\partial C_i}\bigg|_{C_i=0,\,\forall i} = \frac{o_i}{o_{\text{SM}}} \qquad \text{with} \quad o = o_{\text{SM}} + C_i o_i + C_i C_j o_{ij} + \ldots \quad . \tag{6.1}$$

The scale Λ is absorbed into the definition of o_i, o_{ij}, etc.

6.1 Cross-section and forward-backward asymmetry

The simplest observables one can define in the $e^+e^- \to t\bar{t}$ process are the total cross-section production, σ, and the forward-backward asymmetry A^{FB} (see Equation 3.1).

We can also define the A^{FB} asymmetry in terms of the forward-backward cross-section as:

$$A^{\text{FB}} \equiv \frac{\sigma^{\text{FB}}}{\sigma} \qquad \text{with } \sigma^{\text{FB}} \equiv \int_{-1}^{+1} \mathrm{d}\cos\theta_t \quad \text{sign}\{\cos\theta_t\} \quad \frac{\mathrm{d}\sigma}{\mathrm{d}\cos\theta_t}, \tag{6.2}$$

where θ_t is the angle between the positron and top-quark momenta in the centre-of-mass frame.

The forward-backward asymmetry has been studied in full simulation and interpreted in terms of an EFT for different scenarios in ILC [104] and CLIC [149]. Here we present the study developed in [49] where the SM, linear, and quadratic dependences of the total and forward-backward cross-sections are computed both analytically at leading order, and using `MG5_aMC@NLO` [99] at next-to-leading order in QCD, for the various initial-state helicities.

The left plot of Figure 6.1 shows the sensitivity of the cross-section to operator coefficients, as a function of the centre-of-mass energy, for a mostly left-handed electron beam polarization $P(e^+, e^-) = (+30\%, -80\%)$. It tends to a constant value at high energies for the two-quark operators: $C^A_{\varphi q}$, $C^V_{\varphi q}$, C^R_{uZ} and C^R_{uA}. This behaviour can be understood given that the φq operators induce $t\bar{t}Z$ couplings which scale as v^2/Λ^2 once the two Higgs fields they contain condense to their vacuum expectation value. The sensitivity of the cross-section to the $O^V_{\varphi q}$ operator actually slightly decreases with energy, as

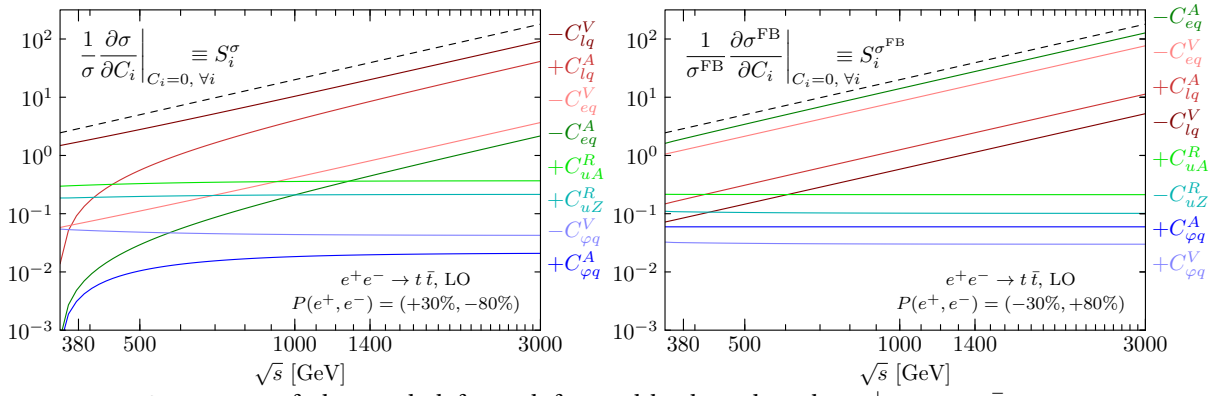

Figure 6.1: Sensitivity of the total (left) and forward-backward (right) $e^+e^- \to t\bar{t}$ cross-sections to various operator coefficients, as a function of the centre-of-mass energy, for a mostly left-handed (left) and right-handed (right) electron beam polarization. The dashed black line indicates the slope of a sensitivity scaling as the centre-of-mass energy squared. Figure reproduced from Ref. [49].

$1 + 2m_t^2/s$. On the other hand, the two uA and uZ electroweak dipole operators generate three-point interactions scaling as Ev/Λ^2, where E is an energy scale characteristic of the momentum transfer in the associated vertex. Their interference with SM amplitudes of identical top-quark helicities however requires a flip of chirality along the quark line, and thus a top-quark mass insertion. The resulting linear EFT contributions therefore scale with energy exactly as the SM cross-section and the sensitivity tends to a constant. The sensitivity to the dipole operators that grows with energy can be recovered through the interference of different helicity amplitudes once the angular distributions of the top-quark decay products are considered. The sensitivity of the cross-section to four-fermion operator coefficients C_{lq}^V, C_{lq}^A, C_{eq}^V, C_{eq}^A shows the naive s/Λ^2 increase with energy expected from dimensional analysis (see dashed black line). The constraints on those operators therefore benefit from increased centre-of-mass energies.

The right plot of Figure 6.1 shows the sensitivity of the forward-backward cross-section, for a mostly right-handed electron beam polarization $P(e^+, e^-) = (-30\%, +80\%)$. The sensitivity of the forward-backward asymmetry is simply given by $S_i^{A^{\mathrm{FB}}} = S_i^{\sigma^{\mathrm{FB}}} - S_i^{\sigma}$ and is qualitatively similar to that of σ^{FB}. The mostly right-handed electron polarization enhances the sensitivity to O_{eq} operators compared to the O_{lq} one, whereas the opposite is true for the mostly left-handed electron polarization. Interestingly also, the change of polarization reverts the sign of the O_{uZ} and $O_{\varphi q}^V$ interferences with SM amplitudes. The SM couplings of the Z to left- and right-handed electrons, $\frac{e}{2s_W c_W}(-1 + 2s_W^2)$ and $\frac{e}{2s_W c_W}(2s_W^2)$ respectively, indeed have different signs. A combination of the two polarizations therefore provides complementary information on different combinations of operators. The forward-backward cross-section also has an enhanced sensitivity to the axial-vector combinations of operators,[1] while the total cross-section is more sensitive to vector operators. This is especially true at lower energies where the sensitivity of the total cross-section to the $O_{\varphi q}^A$, O_{eq}^A, and C_{lq}^A operators suffers from a so-called *p-wave* suppression and falls off as $\beta \equiv (1 - 4m_t^2/s)^{1/2}$. In the forward-backward asymmetry, both the SM and linear EFT dependences are proportional to β so that this suppression drops out in their ratio.

[1] From $t\bar{t}$ helicity amplitudes in Eq. (4) of Ref. [235], the forward-backward cross-section is proportional to the $|{+}{-}|^2 - |{-}{+}|^2$ difference which is in turn proportional to $\beta\,\mathrm{Re}\{\mathcal{F}_{1A}(\mathcal{F}_{1V} + \mathcal{F}_{2V})^*\}$ combination of couplings.

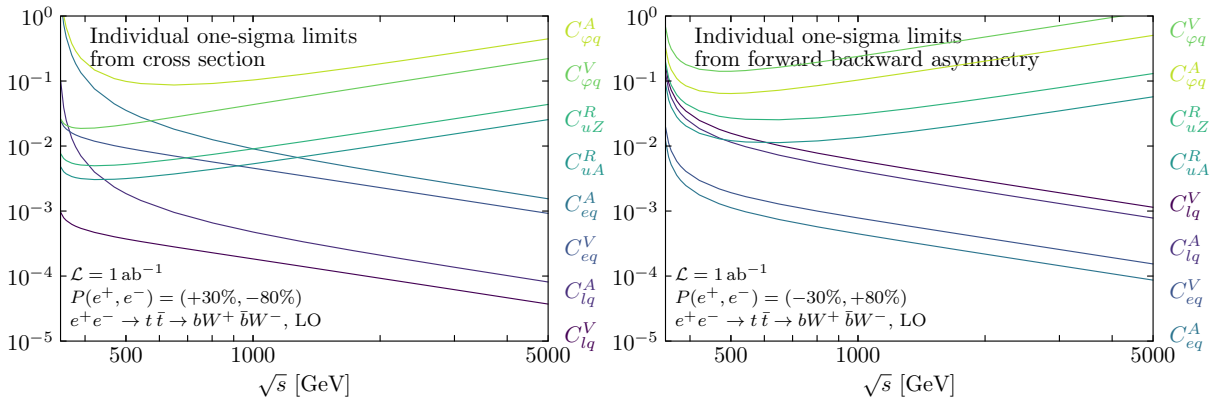

Figure 6.2: Individual one-sigma limits on operator coefficients as functions of the centre-of-mass energy, with either mostly left-handed (left) and mostly right-handed (right) electron beam polarizations, from either cross-section (left) or forward-backward asymmetry (right) measurements, for a fixed integrated luminosity times efficiency of $1\,\mathrm{ab}^{-1}$. Different integrated luminosities are trivially obtained through a $1/\sqrt{\mathcal{L}\,[\mathrm{ab}^{-1}]}$ rescaling. Only statistical uncertainty is taken into account. Figure reproduced from Ref. [49].

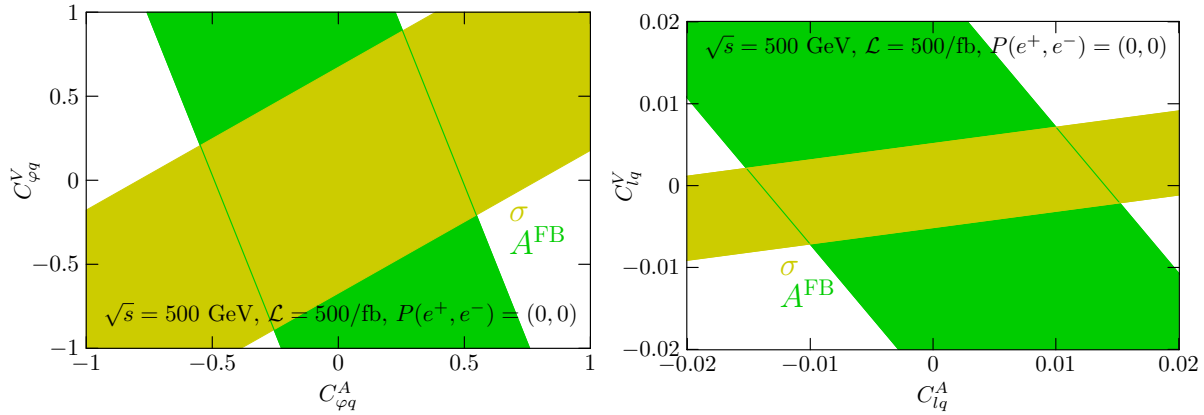

Figure 6.3: The 68% C.L. regions allowed by measurements of the cross-section and forward-backward asymmetry in $e^+e^- \to t\bar{t}$ production. An integrated luminosity of $500\,\mathrm{fb}^{-1}$ at a centre-of-mass energy of 500 GeV is considered, with unpolarized beams. Central values are assumed to confirm the SM.

Individual statistical constraints from the measurements of cross-sections and forward-backward asymmetries are displayed in Figure 6.2 as functions of the centre-of-mass energy. In these fits only statistical uncertainties are taken into account and the reconstruction efficiencies discussed in subsection 4.3.5 are not considered at this point. The constraints are arbitrarily normalized to an integrated luminosity times efficiency of $1\,\mathrm{ab}^{-1}$. Note however that, at linear colliders, the instantaneous luminosity which can be achieved scales approximately linearly with the centre-of-mass energy, while it falls off as the fourth power with the centre-of-mass energy at circular lepton colliders for a constant power of synchrotron radiation emission. Unlike the sensitivity, these idealised individual limits also account for the statistical precision to which cross-sections and forward-backward asymmetries can be measured. Quite naturally, the operators whose sensitivity does not grow with energy are more efficiently constrained at lower centre-of-mass energies, where the top-quark pair production cross-section is larger. For those, the optimal centre-of-mass energy lies roughly between 400 and 600 GeV.

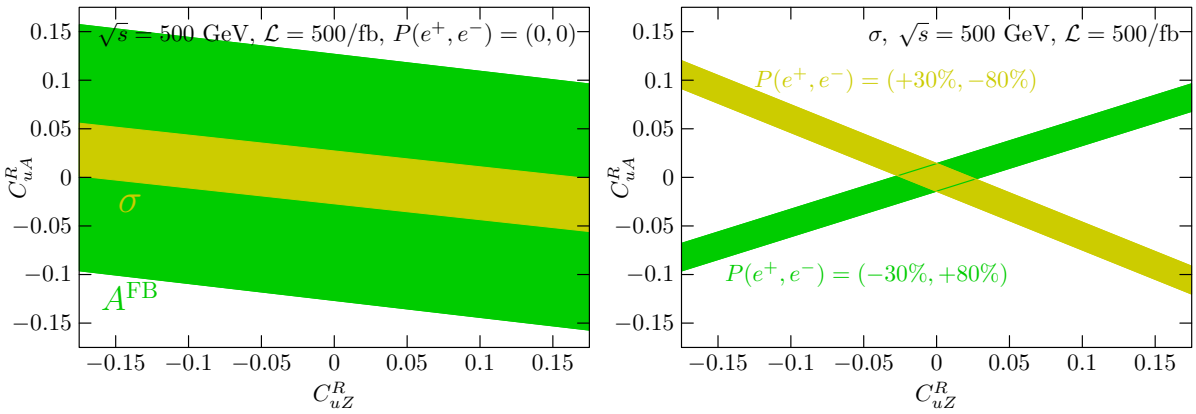

Figure 6.4: The 68% C.L. regions allowed by measurements of the cross-section and forward-backward asymmetry in $e^+e^- \to t\bar{t}$ production with unpolarized beams (left) and that of the cross-sections with two different configurations of the beam polarization (right). A total luminosity of $500\,\text{fb}^{-1}$ collected at 500 GeV is split evenly among two beam polarization configurations. The central values of measurements are assumed to match the predictions in the SM.

With unpolarized beams, the combination of cross-section and forward-backward asymmetry measurements allows to simultaneously constrain pairs of operator coefficients, as illustrated in Figure 6.3. Runs with two different beam polarizations effectively double the number of observables. Polarization was shown to effectively provide separate sensitivity to the photon and Z-boson form factors in Refs. [103, 104]. Similarly, in an EFT, dipole operator coefficients C^R_{uZ} and C^R_{uA} can be disentangled very effectively by taking data in two different beam polarization configurations. The combination of the cross-section and A^{FB} measurements with unpolarized beams are largely degenerate in this two-dimensional parameter subspace, see left plot in Figure 6.4. The combination of measurements with different beam polarizations, on the other hand, yields the tight constraint shown in the right plot in Figure 6.4.

The combination of total cross-section and angular distributions with different beam polarizations and at different centre-of-mass energies provides a set of complemetary constraints in top-quark dimension-six operators.

6.2 Top-quark polarization

We have seen in section 6.1 that the sensitivity to the EW dipole operator coefficients C_{uA}, C_{uZ} of the cross-section and forward-backward asymmetry in electron-positron colliders is approximately constant as a function of centre-of-mass energy. To achieve a sensitivity that grows with energy we must consider the interference between amplitudes with top quarks of different helicities. This can therefore only be observed through observables incorporating top-quark decay product distributions.

The top-quark decays before its spin could be flipped by the strong interaction, so the top-quark polarization is directly measurable via the angular distribution of its decay products. One could study the polarization of the top quark along its direction of motion in the centre-of-mass frame, by examining the angular distribution between one of the top-quark decay products in its rest frame. This so-called

helicity angle distribution takes the form

$$\frac{1}{\sigma}\frac{\mathrm{d}\sigma}{\mathrm{d}\cos\theta_i} = \frac{1}{2}(1+\alpha_i P\cos\theta_i), \tag{6.3}$$

where

$$P = \frac{N_\uparrow - N_\downarrow}{N_\uparrow - N_\downarrow}, \tag{6.4}$$

is the top-quark polarization, and α_i is the *spin analysing power* of the decay product i ($i = l, \nu, q, \bar{q}, W, b$). In the SM we find $\alpha_{l^+} = \alpha_{\bar{q}'} = 1$, $\alpha_\nu = \alpha_q = -0.32$ and $\alpha_b = -\alpha_{W^+} = -0.41$ (q and q' are the up- and down-type quarks, respectively, resulting from the W-boson decay). At leading order and in the absence of $C^I_{uZ,uA}$ and the scalar and tensor four-fermion, $C^{S,T}_{lequ}$, operator coefficients, P is degenerate with the forward-backward production asymmetry. In terms of $t\bar{t}$ helicity amplitudes (see e.g. Refs. [235, 236]), the forward-backward asymmetry is sensitive to the $|{+}{-}|^2 - |{-}{+}|^2$ combination[2], while P involves $|{+}{-}|^2 - |{-}{+}|^2 + |{+}{+}|^2 - |{-}{-}|^2$. In the SM, however, $|{+}{+}|^2 = |{-}{-}|^2$. This remains true when introducing CP-conserving dipole operators, or two- and four-fermion operators having (axial) vector Lorentz structures. Thus, adding both, A^{FB} and the top-quark polarization to the fit do not provide any advantage.

We can explore if further information from the top-quark polarization is useful. Generalizations of the W-boson helicity fractions (see section 6.4) have been proposed in Ref. [121]. They are based on the definition of two additional axes in the top-quark rest frame —besides the direction of motion of the W boson— with respect to which the angle of the charged lepton momentum in the W-boson rest frame could be measured. For this purpose, it is prescribed to use a reference direction along which most of the top-quark polarization lies. Ref. [236] demonstrated that a convenient choice of direction is that of the incoming positron for the top and that of the incoming electron for the anti-top (in the respective top and anti-top rest frames). One can then define two new axes, $\hat{e}\times\hat{W}$ and $\hat{W}\times(\hat{e}\times\hat{W})$, from the directions of the W boson and electron (positron) beam in the top (anti-top) rest frame. One can for instance construct asymmetries based on the sign of the cosine of the angle between either of these directions and the direction of the charged lepton arising from the leptonic W-boson decay measured in the W-boson rest frame.

Inspired by this proposal but aiming to obtain sensitivity to the top-quark polarization instead of that of the W, we define *normal* and *transverse* axes in the centre-of-mass frame as:

$$\hat{N} \equiv \hat{t}\times\hat{e} \quad \text{and} \quad \hat{T} \equiv \hat{t}\times\hat{N}$$

from the direction of motion of the (anti-)top $\hat{t}$ and that of the electron (positron) beam $\hat{e}$. Being orthogonal to $\hat{t}$, those vectors are not affected by a subsequent boost in the (anti-)top rest frame. Observables generalizing P can then be constructed from the distribution of the angles between $\hat{N}$ or $\hat{T}$ and one of the top-quark decay products, in the top-quark rest frame. The direction of the charged lepton arising from a semi-leptonic top-quark decay will be employed in the following. Asymmetries

[2]The notation refers to the sign of the top-quark helicity, e.g. $|{+}{-}|^2$ is the amplitude with one top quark with positive helicity and the other with negative helicity.

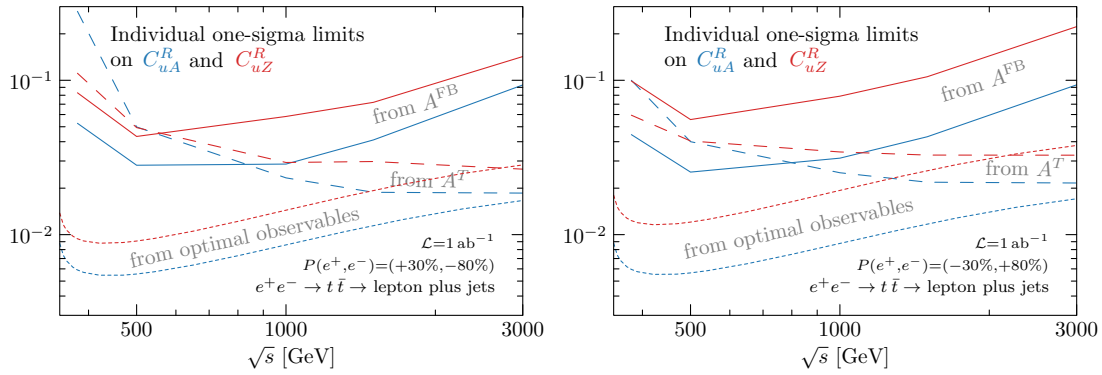

Figure 6.5: Individual one-sigma limits on the coefficients of the dipole operators O_{uA} and O_{uZ} obtained from measurements of the forward-backward production asymmetry A^{FB} (solid lines), transverse polarization asymmetry (dashed lines), and statistically optimal observables of section 6.6 (dotted lines), with beam polarization $P(e^+, e^-) = (+30\%, -80\%)$ in the left plot and $(-30\%, +80\%)$ in the right plot. A data sample of $1\mathrm{ab}^{-1}$ is assumed at centre-of-mass energies between the top-quark pair production threshold and 3 TeV.

based on the sign of the cosine of either of these angles will be named *normal* and *transverse polarization asymmetries*, A^N and A^T:

$$A^{(N,T)} = \frac{N\left(\cos\theta^{(N,T)} > 0\right) - N\left(\cos\theta^{(N,T)} < 0\right)}{N\left(\cos\theta^{(N,T)} > 0\right) + N\left(\cos\theta^{(N,T)} < 0\right)}. \tag{6.5}$$

In the same format as Figure 6.2, we compare in Figure 6.5 the one-sigma limits obtained from measurements of the forward-backward production asymmetry (solid line), the transverse polarization asymmetry (dashed line), and the statistically optimal observables[3] (dotted line) on the coefficients of the dipole operators C_{uA}^R and C_{uZ}^R. As mentioned earlier, the standard helicity angle asymmetry is fully degenerate with the forward-backward production asymmetry A^{FB}. Here again, a constant integrated luminosity times efficiency of $1\,\mathrm{ab}^{-1}$ is assumed at any given centre-of-mass energy. The left and right plots respectively assume mostly left-handed and mostly right-handed electron beam polarizations. The EFT dependences of the top-quark width and of its decay amplitudes have been included. At low energy, the transverse polarization asymmetry yields similar limits as A^{FB}, but its added value becomes clear at high energy. The sensitivity of A^{FB} is approximately constant over the $\sqrt{s}$ range considered here (see right plot of Figure 6.1). Therefore, with the cross-section falling as $1/s$ and the luminosity assumed constant, the limits deteriorate strongly with increasing centre-of-mass energy. The sensitivity of the transverse asymmetry to dipole operators, on the other hand, increases with centre-of-mass energy. At high energies, both the sensitivity and the statistical uncertainty increase as $\sqrt{s}$ and balance each other. The individual limits thus become independent of $\sqrt{s}$. For centre-of-mass energies above 1 TeV, the constraints derived from the transverse asymmetry are significantly stronger than those implied by A^{FB}. At 3 TeV, they are an order of magnitude better. The optimal observables that will be introduced in section 6.6 present a similar high-energy behaviour but perform better than the transverse polarization asymmetry at low energies.

[3]We define the statistically optimal observables based on the $e^+e^- \to t\bar{t} \to bW^+\bar{b}W^-$kinematics in section 6.6.

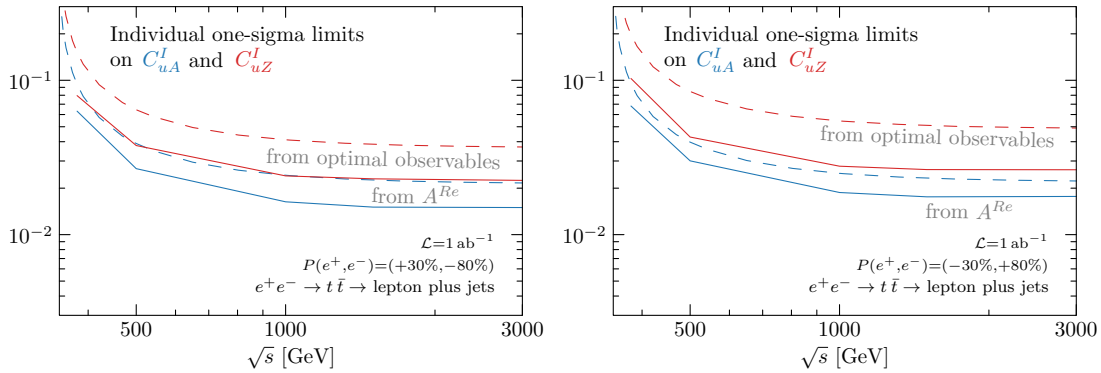

Figure 6.6: Individual limits on the imaginary parts of the dipole operator coefficients C^I_{uA} and C^I_{uZ} from measurements with $P(e^+, e^-) = (-30\%, +80\%)$ and $(-30\%, +80\%)$ beam polarizations (left and right plots, respectively). The limits deriving from A^{Re} measurements (solid lines) are compared to that of optimal observables defined in section 6.6. A data sample of 1ab^{-1} is assumed at centre-of-mass energies ranging between the top-quark pair production threshold and 3 TeV.

Measurements of the transverse polarization asymmetry may add valuable information in a global fit of top-quark EW couplings. The information contained in the usual helicity angle asymmetry overlaps with that of the forward-backward asymmetry. The sensitivity of the transverse polarization asymmetry grows with the centre-of-mass energy and yields significantly tighter constraints for $\sqrt{s}$ above about 1 TeV. As seen in Figure 6.5, the transverse polarization asymmetry gives better results than the optimal observables at high energies. This gain may arise from the higher top-quark spin analysing power of the charged lepton compared to that of the W boson (or bottom quark) that is accessible to statistically optimal observables defined on the $bW^+\bar{b}W^-$kinematics.

6.3 CP-odd observables

Imaginary coefficients for the electroweak dipole operators O_{uZ} and O_{uA} (or O_{uW} and O_{uB}) violate the combination of charge conjugation and parity symmetries (CP). Close-to-optimal observables specifically designed to test CP conservation [237] provide very precise constraints on these parameters [107].

Following Ref. [237], one defines first

$$\mathcal{O}^{Re}_{+} \equiv (\hat{\bar{t}} \times \hat{l}_{+}) \cdot \hat{e}_{+} \quad \text{and} \quad \mathcal{O}^{Re}_{-} \equiv (\hat{t} \times \hat{l}_{-}) \cdot \hat{e}_{+}\,,$$

where $\hat{t}$ ($\hat{\bar{t}}$) and $\hat{e}_+$ are unit vectors pointing in the direction of the top (anti-top) and incoming positron beam momenta in the centre-of-mass frame. The unit vectors $\hat{l}_\pm$ point in the direction of the charge lepton momenta arising from the W decay in the top and anti-top rest frames. The $\mathcal{O}^{Re}_{\pm}$ observables are CP conjugate of each other. While non-vanishing expectation values for $\mathcal{O}^{Re}_{+}$ and $\mathcal{O}^{Re}_{-}$ could be generated by absorptive parts in amplitudes, their difference $A^{Re} \equiv \mathcal{O}^{Re}_{+} - \mathcal{O}^{Re}_{-}$ is only sensitive to genuine CP-violation [107].

The limits extracted from the A^{Re} asymmetry are very similar to the limits obtained from the top and anti-top normal polarization asymmetries defined in section 6.2, with a slight advantage for the A^{Re}

asymmetry. Both observables are indeed based on the same $\mathcal{O}_{\pm}^{Re}$ kinematic functions. We therefore only discuss the A^{Re} asymmetry.

The one-sigma individual limits on the imaginary parts of the dipole operator coefficients C_{uA}^{I} and C_{uZ}^{I} are presented as functions of the centre-of-mass energy in Figure 6.6. As before, the integrated luminosity is fixed to 1ab^{-1} to facilitate comparisons. The limits extracted from the A^{Re} asymmetry are displayed together with those obtained with the optimal observables that will be defined in section 6.6. Optimal observables provide constraints a factor of two better than A^{Re}. As in the transverse polarization asymmetry, this difference may come from the higher top-quark spin analysing power of the charged lepton compared to that of the W boson (or bottom quark) that is accessible to statistically optimal observables defined on the $bW^{+}\bar{b}W^{-}$kinematics. In both cases, the sensitivity grows with the centre-of-mass energy. At large energies and for a fixed integrated luminosity, the individual limits saturate to constants. These observables are quite specific to the imaginary part of the O_{uA} and O_{uZ} operators and the constraints they imply have little correlations with that of the CP-conserving operator coefficients.

6.4 Top-quark decay and single production

Some of the dimension-six operators that affect the top-quark couplings to the photon and Z boson also modify the tbW vertex. Among those, O_{tW} and $O_{\varphi q}^{3}$ interfere with SM amplitudes in the vanishing bottom-quark mass limit.

In $e^{+}e^{-}$ collisions, the O_{tW} and $O_{\varphi q}^{3}$ operators affect top-quark pair production, single production, and decay. We compare in this section the sensitivity of the production and decay processes to the C_{tW} operator coefficient. In the narrow top-quark width approximation[4], the dependence on $O_{\varphi q}^{3}$ drops out from the differential $t \to bW$ branching fraction. The $e^{+}e^{-} \to t\bar{t}$ process is only sensitive to the difference of $O_{\varphi q}^{1}$ and $O_{\varphi q}^{3}$ (which we denote $O_{\varphi q}^{-}$). We explore several ways to disentangle the contributions of $O_{\varphi q}^{1}$ and $O_{\varphi q}^{3}$.

Transverse polarization asymmetry The transverse polarization asymmetry of the top quark A^{T}, introduced in section 6.2, is sensitive to new physics in top-quark production. It may also be affected by new physics in top-quark decay since it relies on the distribution of the charged lepton produced in the $t \to Wb, W \to l\nu_{l}$ decay chain.

W-boson helicity fractions The helicity fractions of the W boson are classical observables measured in top-quark decay. We denote θ_{l}^{*} the angle between the charged lepton momentum in the W-boson rest frame and the W-boson momentum in the top-quark rest frame. Its distribution,

$$\frac{1}{\Gamma}\frac{\mathrm{d}\Gamma}{\mathrm{d}\cos\theta_{l}^{*}} = \frac{3}{8}F_{+}\left(1+\cos\theta_{l}^{*}\right)^{2} + \frac{3}{4}F_{0}\sin^{2}\theta_{l}^{*} + \frac{3}{8}F_{-}\left(1-\cos\theta_{l}^{*}\right)^{2}, \tag{6.6}$$

[4]The narrow width approximation (NWA) sets the intermediate particles on-shell and allows to drop off-shell contributions, ultimately writing the NWA cross-section as a product of the production cross-section and relevant branching ratios only. It is an approximation used when the total decay width of the resonant particle is much smaller than its mass.

$P(e^+, e^-)$	$(+30\%, -80\%)$		$(-30\%, +80\%)$	
observables	A^T	A^W_{FB}	A^T	A^W_{FB}
SM predictions	-0.6	-0.17	0.57	-0.29
sensitivity to C_{tW} [%]				
in production	38 ± 1	9 ± 2	-25 ± 1	—
in decay	—	16 ± 2	—	11 ± 3
in prod. & decay	37 ± 1	26 ± 2	-24 ± 1	10 ± 3

Table 6.1: Sensitivities to the real part of C_{tW} operator coefficient, artificially decomposed into *production* and *decay* components, and quoted in percent. The sensitivity of an observable o is simply defined as $o(C = 1)/o(C = 0) - 1$. A centre-of-mass energy of 500 GeV and the two $P(e^+, e^-) = (\pm 30\%, \mp 80\%)$ beam polarizations are considered. The uncertainties displayed are due to limited MonteCarlo statistics. A sensitivity compatible with zero, within uncertainties, is replaced by a dash.

serves to define the positive, negative and longitudinal W-boson helicity fractions of unit sum: $F_+ + F_- + F_0 = 1$. In the following, we consider the asymmetry formed by positive and negative helicity fractions $A^W_{FB} \equiv \frac{3}{4}(F_+ - F_-)$ extracted from a fit to the $\cos\theta^*_l$ distribution.

Leading-order SM estimates for A^T and A^W_{FB} are presented in the first row of Table 6.1 for a centre-of-mass energy of 500 GeV and the two $P(e^+, e^-) = (\pm 30\%, \mp 80\%)$ beam polarizations. The remaining rows present the sensitivity of these observables to C_{tW}, artificially decomposed into components arising from top-quark production and decay, in the narrow width approximation. For the purpose of this table, the sensitivity of an observable o is simply defined as $o(C = 1)/o(C = 0) - 1$ and quoted in percent. The transverse polarization asymmetry has a remarkable sensitivity to C_{tW}. It arises dominantly from production. On the other hand, the sensitivity of the W-boson helicity fractions to C_{tW} mostly arises from top-quark decay. For the centre-of-mass energy considered, it is smaller than the one achieved with the transverse polarization asymmetry.

Total width Measurements of the top-quark decay width are sensitive to dimension-six operators. Computing its linear dependence at NLO in QCD using `MG5_aMC@NLO` [99], we obtain:

$$\Gamma_t = \underset{0.914}{1.36}\,{}^{+1.2\%}_{\pm 0.043\%}{}_{-1.4\%} + \left(\underset{0.914}{0.161}\,{}^{+1.2\%}_{\pm 0.027\%}{}_{-1.4\%} C^3_{\varphi q} + \underset{0.923}{0.147}\,{}^{+1.1\%}_{\pm 0.03\%}{}_{-1.3\%} C_{tW} \right) \left(\frac{1\,\text{TeV}}{\Lambda} \right)^2 + O(\Lambda^{-4}).$$

Central values, k-factors ($\Gamma_{\text{NLO}}/\Gamma_{\text{LO}}$) and uncertainties are displayed in the following format:

$$\underset{\text{k-factor}}{\text{central value}}\,{}^{+\text{scale up}\%}_{\pm\text{Monte Carlo}\%}{}_{-\text{scale down}\%}.$$

The scale uncertainty is computed from the running of $\alpha_S(\mu)$ between $\mu = m_t/2$ and $2m_t$.

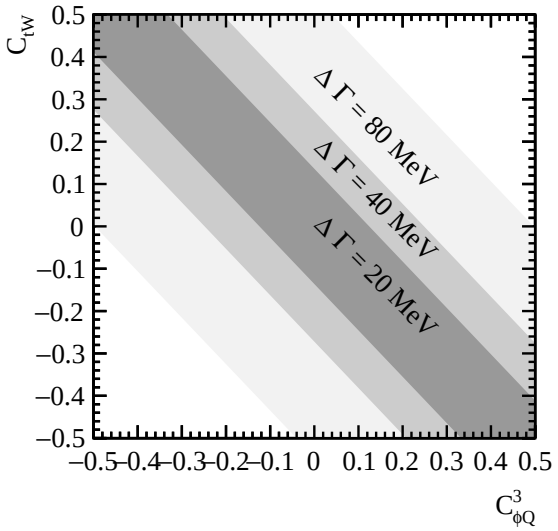

Figure 6.7: One-sigma constraints on the C_{tW} and $C^3_{\varphi q}$ operator coefficients that would derive from a measurement of the top-quark width with 20, 40, or 80 MeV precision. The central value of the measurement is assumed to coincide with the prediction in the SM.

The top-quark width has only a leading-order linear dependence on $C^3_{\varphi q}$ and C_{tW} operator coefficients. A small dependence on C_{tG} also arises at next-to-leading order in QCD. Tight constraints on this operator coefficient can however be obtained at the LHC, or from the associated production of a top-quark pair with a hard jet at a linear collider [238]. We therefore ignore this dependence. For constraints achievable at lepton colliders, the quadratic dependences on the coefficients which appear already at the linear order are subleading. Operators inducing a right-handed current or CP-violation only start contributing a the quadratic level.

A precise measurement of the top-quark width is possible at an e^+e^- collider by scanning the centre-of-mass energy through the top-quark pair production threshold.[5] Ref. [240] demonstrated that a precise determination, simultaneous to that of the top-quark mass and strong coupling constant, can be obtained from a fit of the threshold line shape. The analysis of Ref. [241] estimates a statistical uncertainty for the total width of 21 MeV with an integrated luminosity of 100fb^{-1}. Theory uncertainties are however likely to dominate. For uncertainties of 20, 40, and 80 MeV and a SM central value, the regions of the parameter space spanned by the operator coefficients C_{tW} and $C^3_{\varphi q}$ allowed at the 68% C.L. are presented in Figure 6.7. The constraint imposed by the width measurement effectively disentangles the coefficients of the $O^1_{\varphi q}$ and $O^3_{\varphi q}$ operators (see also Ref. [242]).

6.5 Observables for scalar and tensor two-lepton-two-quark operators

The scalar and tensor four-fermion operators O^S_{lequ} and O^T_{lequ} present a distinctive Lorentz structure. They do not interfere with SM amplitudes in the limit of vanishing lepton masses. For the range of energy and initial state polarizations we consider, we find the difference $A_{pol} = P_t - P_{\bar{t}}$ of the polarization of the top and anti-top quark (see section 6.2) is sensitive to both operators. In a lepton-plus-jets sample,

[5] A determination of the total width is also possible immediately below the $t\bar{t}$ threshold [239] or in the continuum well above the threshold [92].

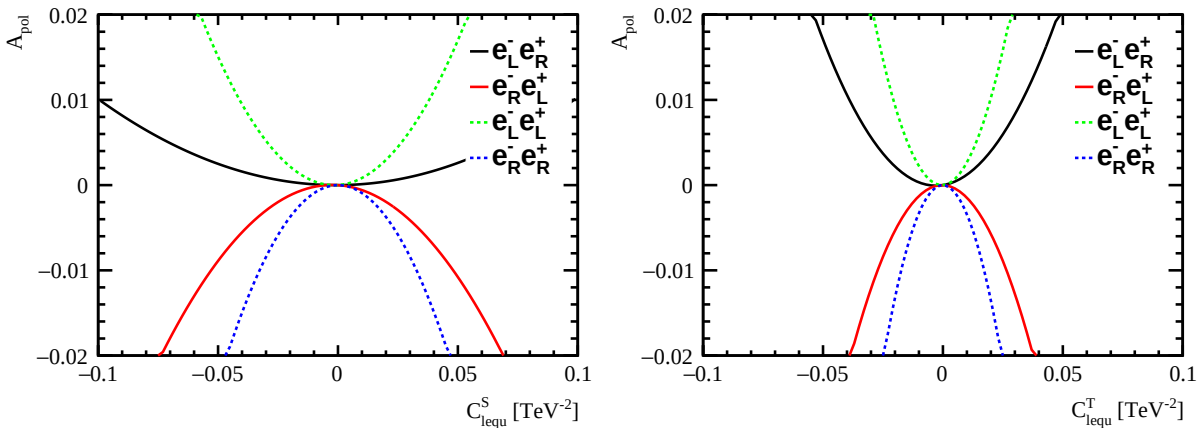

Figure 6.8: The dependence of $A_{pol} = P_t - P_{\bar{t}}$ on the scalar and tensor operator coefficients C^S_{lequ} (left) and C^T_{lequ} (right) for $\sqrt{s} = 500$ GeV. The electron and positron beams are 80% and 30% polarized, as envisaged in the ILC design. The four curves represent four different configurations: two standard configurations with opposite electron and polarization ($e^-_L e^+_R$ in black, $e^-_R e^+_L$ in red), and two same-sign configurations ($e^-_L e^+_L$ in green, $e^-_R e^+_R$ in blue.)

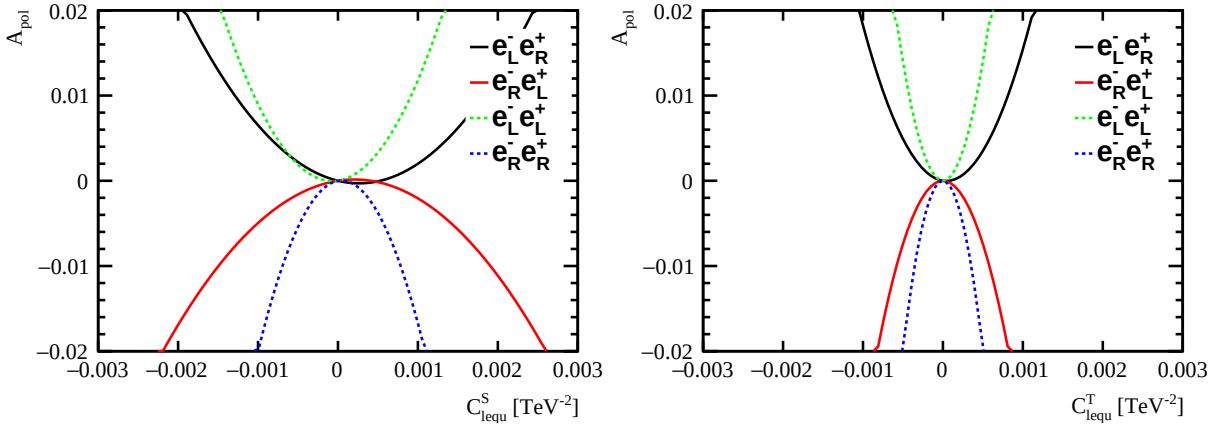

Figure 6.9: The dependence of $A_{pol} = P_t - P_{\bar{t}}$ on the scalar and tensor operator coefficients C^S_{lequ} (left) and C^T_{lequ} (right) for $\sqrt{s} = 3$ TeV. The electron is 80% polarized, as envisaged in the CLIC design. For the positron beam a 30% polarization is assumed for comparison with Figure 6.8, even if positron polarization is not part of the CLIC baseline design. The four curves represent four different configurations: two standard configurations with opposite electron and polarization ($e^-_L e^+_R$ in black, $e^-_R e^+_L$ in red), and two same-sign configurations ($e^-_L e^+_L$ in green, $e^-_R e^+_R$ in blue.)

both polarizations are measured in a straightforward fashion through Equation 6.3. The observable A_{pol} vanishes in the SM and is *specific* to the scalar and tensor operators: it has little or no sensitivity to any of the other operators considered in this thesis.

The sensitivity to the scalar and tensor operator moreover increases in runs with electron and positron beam polarizations of the same sign. In Figure 6.8, the sensitivity of A_{pol} to the O^S_{lequ} and O^T_{lequ} operators at a centre-of-mass energy of 500GeV is represented for four different initial-state polarization configurations. The curves labelled $e^-_L e^+_R$ and $e^-_R e^+_L$ represent the opposite-sign configurations that are usually considered, with $P(e^+, e^-) = (+30\%, -80\%)$ and $P(e^+, e^-) = (-30\%, +80\%)$. Two further curves, labelled as $e^-_L e^+_L$ and $e^-_R e^+_R$ represent same-sign configurations with $P(e^+, e^-) =$

$P(e^+, e^-)$	A_{pol} uncert. [%]	$\lvert C^S_{lequ}\rvert^2$	$\lvert C^T_{lequ}\rvert^2$
$(+30\%, -80\%)$	1.0	3×10^{-3}	1×10^{-3}
$(-30\%, +80\%)$	1.4	5×10^{-3}	9×10^{-4}
$(-30\%, -80\%)$	2.6	1×10^{-2}	9×10^{-4}
$(+30\%, +80\%)$	3.4	4×10^{-3}	9×10^{-4}

Table 6.2: Individual 68% C.L. limits on the scalar and tensor four-fermion operator coefficients obtained with an integrated luminosity of $500\,\text{fb}^{-1}$ collected at $\sqrt{s} = 500$ GeV. Following the ILC scenarios of Table 2.2, respectively 40% and 10% of the total luminosity is devoted to runs with each of the $P(e^+, e^-) = (-30\%, +80\%)$, $(+30\%, -80\%)$ and $P(e^+, e^-) = (-30\%, -80\%)$, $(+30\%, +80\%)$ polarization configurations. We assume A_{pol} is measured in lepton-plus-jets events. A total efficiency to 20% is applied, including top-quark branching fractions and an estimate of the selection efficiency. The scale Λ is fixed to 1 TeV.

$P(e^+, e^-)$	A_{pol} uncert. [%]	$\lvert C^S_{lequ}\rvert^2$	$\lvert C^T_{lequ}\rvert^2$
$(+30\%, -80\%)$	2.2	4×10^{-5}	2×10^{-6}
$(-30\%, +80\%)$	3.0	1×10^{-5}	1×10^{-6}
$(-30\%, -80\%)$	5.7	4×10^{-6}	10^{-6}
$(+30\%, +80\%)$	7.3	5×10^{-6}	8×10^{-7}

Table 6.3: Individual limits on the square of the Wilson coefficients of the scalar and tensor operator coefficients at $\sqrt{s} = 3$ TeV. A_{pol} is measured in lepton+jets events in a data sample with an integrated luminosity of $\mathcal{L} = 3\,\text{ab}^{-1}$. A selection efficiency of 20% is applied. For comparison to the ILC scenario, a 30% positron polarization is assumed and the sample is divided among the four configurations as in Table 6.2

$(-30\%, -80\%)$ and $P(e^+, e^-) = (-30\%, -80\%)$. Clearly, the same-sign configurations $e^-_L e^+_L$ and $e^-_R e^+_R$ enhance the sensitivity to these operators significantly. The tensor operator has a larger impact on A_{pol} for all scenarios considered here.

To get a grasp of the $\sqrt{s}$ dependence of the sensitivity we consider 3 TeV operation under the same conditions. The CLIC baseline design does not envisage positron polarization. There is however no technical impediment to positron polarization at high energy. We therefore present the sensitivity plots at $\sqrt{s} = 3$ TeV under the same conditions as the ILC in Figure 6.9. As already observed for the other four-fermion operators, the sensitivity increases strongly with centre-of-mass energy (note the different range on the x-axes between Figs. 6.8 and 6.9).

Operations with same-sign polarizations help constraining the scalar and tensor four-fermion operator coefficients. The ILC operating scenarios envisage a fraction of the integrated luminosity to be collected in the same-sign configurations (see Table 2.2). We provide individual 68% C.L. limits on the scalar and tensor operator coefficients, in Table 6.2, assuming a total integrated luminosity of $500\,\text{fb}^{-1}$. Statistical uncertainties are based on 20% of the $t\bar{t}$ sample, to take into account the branching fraction of the lepton-plus-jets final state and an estimate of the selection efficiency.

The results in Table 6.2 indicate that the same-sign configurations can indeed offer quite powerful constraints. The higher sensitivity compensates for the smaller integrated luminosity. Individual limits on $|C^S_{lequ}|^2$ and $|C^T_{lequ}|^2$ approximately reach the 10^{-3} level for all configurations. As for the other four-fermion operators, the sensitivity dramatically improves with the centre-of-mass energy. Individual constraints obtained with $3\,\text{ab}^{-1}$ of integrated luminosity collected at a centre-of-mass energy of 3 TeV are displayed in Table 6.3 and reach the 10^{-6} level.

6.6 Statistically optimal observables

Statistically optimal observables [243, 244] are constructed to maximally exploit the available differential information and extract the tightest constraints on parameters whose dependence is expanded to linear order only. For a differential distribution across the phase space Φ given by

$$\frac{\mathrm{d}\sigma}{\mathrm{d}\Phi} = \frac{\mathrm{d}\sigma_{\text{SM}}}{\mathrm{d}\Phi} + \sum_i C_i \frac{\mathrm{d}\sigma_i}{\mathrm{d}\Phi},$$

the observables maximizing the constraints on the $\{C_i\}$ parameter space are shown to be the average values of $O_i = n \, \frac{\mathrm{d}\sigma_i}{\mathrm{d}\Phi} \Big/ \frac{\mathrm{d}\sigma_{\text{SM}}}{\mathrm{d}\Phi}$ where n is the number of events observed. They can be computed as

$$\bar{O}_i = \epsilon \, \mathcal{L} \int \mathrm{d}\Phi \, \left(\frac{\mathrm{d}\sigma_i}{\mathrm{d}\Phi} \Big/ \frac{\mathrm{d}\sigma_{\text{SM}}}{\mathrm{d}\Phi} \right) \frac{\mathrm{d}\sigma}{\mathrm{d}\Phi},$$

where $\mathcal{L}$ is the total integrated luminosity and an ϵ can be introduced to effectively account for finite efficiencies. Defining

$$\sigma_i \equiv \int \mathrm{d}\Phi \frac{\mathrm{d}\sigma_i}{\mathrm{d}\Phi}, \qquad \text{and} \quad d_{ij} \equiv \int \mathrm{d}\Phi \left(\frac{\mathrm{d}\sigma_i}{\mathrm{d}\Phi} \frac{\mathrm{d}\sigma_j}{\mathrm{d}\Phi} \Big/ \frac{\mathrm{d}\sigma_{\text{SM}}}{\mathrm{d}\Phi} \right),$$

their sensitivity to operator coefficients and the covariance matrix on the extracted C_i are given by

$$S_j^{O_i} \equiv \frac{1}{\bar{O}_i} \frac{\partial \bar{O}_i}{\partial C_j}\bigg|_{C_k=0,\forall k} = \frac{d_{ij}}{\sigma_i} + \mathcal{O}(C_k), \qquad \text{and} \qquad V^{-1}\big|_{ij} = \epsilon \, \mathcal{L} \, d_{ij} + \mathcal{O}(C_k).$$

Their analytical construction is based on the decomposition of the differential $e^+e^- \to t\bar{t} \to bW^+\bar{b}W^-$ cross-section in terms of helicity amplitudes, carried out for instance in Ref. [235]. It has been extended to include the dependence on four-fermion operators.

In Figure 6.10 the $S_i^{O_i}$ sensitivities for both mostly right-handed and mostly left-handed polarized electron beams are shown. In contrast to that of the total and forward-backward cross-sections (see Figure 6.1), note the sensitivities of the statistically optimal observables to dipole operators slowly grow with $\sqrt{s}$ in the range shown. Beyond the energies displayed, they actually start growing quadratically with the centre-of-mass energy, like the four-fermion operators. Consult Ref. [49] for further discussion.

In section 7.1 we explore the capability of the optimal observables for constraining the top-quark EW two-fermion operators in different future scenarios.

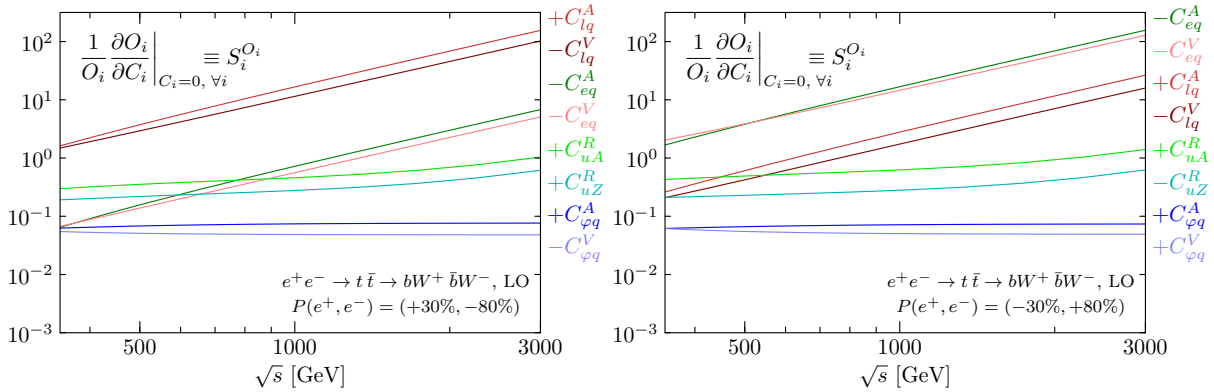

Figure 6.10: Sensitivity of each statistically optimal observable to the corresponding operator coefficient. Note that these observables do not necessarily have maximal sensitivities but rather, as a set, induce minimal statistical uncertainties on the coefficient determination. Figure reproduced from Ref. [49].

7.- Global top-quark EFT fit on prospects

In this chapter we study future scenarios for improving the bounds obtained in the global fits of the top and bottom-quark EW couplings in section 5.2. In section 7.1 we explore different scenarios for future electron-positron colliders using the optimal observables for top-quark operators introduced in section 6.6. In section 7.2 we extend the global fit from section 5.2 including future stages of the LHC and the official operating ILC scenarios. Finally in section 7.3 we study the possibility of extend the top-quark couplings fit into a combined top-Higgs couplings fit.

This work is published in Refs. [49, 106] and included in the CLIC top-quark paper [149] and BSM report [51].

7.1 Exploring different scenarios for the future

In this section we explore global fits in three different scenarios for future colliders we have introduced in chapter 2. At an electron-positron collider bottom and top-quark pair production through the exchange of a photon or Z boson are among the dominant processes. A future high-energy e^+e^- collider thus provides an ideal laboratory to characterize the $Z/\gamma^* \, b\bar{b}$ and $Z/\gamma^* \, t\bar{t}$ vertices. Single-top production could also bring valuable constraining power [98] but no quantitative prospect is currently available. So we do not consider this process.

The uncertainties and assumptions for each scenario are motivated in chapter 4, however some scenarios have revised their parameters since the realization of this work. The global reach is rather sensitive to the operating scenario, especially to the centre-of-mass range covered by the machine and to the polarization of the electron and positron beams. We adopt the following benchmark scenarios:

Circular collider-like scenario As introduced in subsection 2.3.4, we consider the possibility that a circular lepton collider (CC, for short) would collect 200fb^{-1} and 1.5ab^{-1} at centre-of-mass energies of 350 and 365 GeV respectively, without beam polarization.

ILC-like scenario We consider an integrated luminosity of 500fb^{-1} at a centre-of-mass energy of 500 GeV and of 1ab^{-1} at $\sqrt{s} = 1$ TeV[1]. The luminosity is shared equally between the mostly left-handed $P(e^+, e^-) = (+30\%, -80\%)$ and mostly right-handed $(-30\%, +80\%)$ beam polarization configurations. Compared to the stages introduced in subsection 2.3.1 from Ref. [66], we ignore in this study the possibility (discussed in section 6.5) of colliding electrons and positrons

[1]Although the planned integrated luminosity is 8ab^{-1}, we considered in this study a more conservative scenario.

of like-sign helicities. We also give priority to a 1 TeV run over a luminosity upgrade, which could enhance the integrated luminosity at $\sqrt{s} = 500$ GeV to 4ab^{-1}.

CLIC-like scenario Following the staging scheme presented in Ref. [245][2], we consider an integrated luminosity of 500fb^{-1} at $\sqrt{s} = 380$ GeV, of 1.5ab^{-1} at $\sqrt{s} = 1.4$ TeV[3] and of 3ab^{-1} at $\sqrt{s} = 3$ TeV in a CLIC-like run scenario. These integrated luminosities are equally shared between left-handed $P(e^+, e^-) = (0, -80\%)$ and right-handed $(0, +80\%)$ beam polarization configurations. Positron polarization is not foreseen in the baseline operating scenario.

We present, in this section, the global reach offered by statistically optimal observable measurements in the scenarios specified above with the overall $t\bar{t}$ reconstruction efficiencies quoted in Table 4.4. We derive constraints in top-quark EW couplings in the vector-axial basis (see Equation 3.4).

A convenient metric to globally quantify the strength of the constraints in the n-dimensional parameter space of effective-operator coefficient is the so-called *global determinant parameter* defined as the $2n$ root of the Gaussian covariance matrix determinant [246]:

$$\text{GDP} \equiv \sqrt[2n]{\det V}. \tag{7.1}$$

It evaluates to the geometric average of the semiaxes of the one-sigma ellipsoid of constraints. Interestingly, ratios of such quantities are independent of the operator basis used to capture departure from the SM. Indeed, they are invariant under rotations and rescalings in the space of operator coefficients.

GDP ratios between CC, ILC and CLIC constraints are $30 : 2.2 : 1$. To match the CLIC level of constraints, the corresponding overall increase in luminosity required at the ILC and CC are respectively of 4.8 and 990 for all centre-of-mass energies (given our inclusion of statistical uncertainties only, GDPs scale as $1/\sqrt{\mathcal{L}}$). Note that the current official luminosity for both ILC and CLIC is higher that the one we have considered.

We show in Figs. 7.1, 7.2 and 7.3 the global limits for each scenario. Individual constraints on $C_{\varphi q}^V$ and $C_{\varphi q}^A$ operator coefficients, that affect the left-handed coupling of the top quark, are comparable in all three scenarios. The sensitivity to these operators does not grow with energy and arises mostly at low centre-of-mass energies where the top-quark pair production cross-section is maximal.

Similar observations can be made for the dipole operator coefficients C_{uA}^R and C_{uZ}^R whose sensitivity grows only mildly with energy (see Figure 6.10). They are most efficiently constrained at lower centre-of-mass energies. Their CP-violating counterparts are, on the contrary, easier to constrain at higher energies. They are thus somewhat better bounded in ILC- and CLIC-like scenarios. In those two cases, C_{uA}^I and C_{uZ}^I are also completely uncorrelated with the eight other CP-conserving coefficients. No difference is then observed between their individual and global limits. Present direct individual constraints on CP-conserving dipole operators are two to three orders of magnitude looser than the prospects we obtain at future lepton colliders.

[2] At the time of the realization of this work, this reference from 2016 had more conservative scenarios that the current ones from 2018 presented in subsection 2.3.2.

[3] At the first CLIC reports, the second stage was planned to be at $\sqrt{s} = 1.4$ TeV instead of the current $\sqrt{s} = 1.5$ TeV.

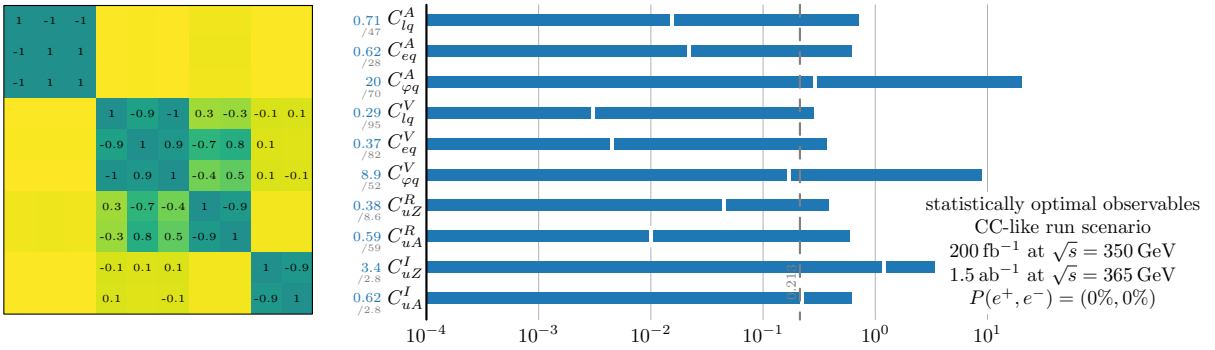

Figure 7.1: Global one-sigma constraints in a (CC-)like benchmark run scenario. The white marks indicate the constraints that are individually obtained when all other operator coefficients are set to zero. The dashed lines provides the *global determinant parameter* of the constraints on all ten operator coefficients. Numerical values for the marginalized constraints and their ratio to individual ones are provided on the left-hand side. $\Lambda = 1$ TeV is assumed.

Four-fermion operator coefficients benefit greatly from increase in centre-of-mass energy. A clear improvement is therefore seen from CC- to ILC- and CLIC-like scenarios. Four-fermion operators drive the reduction in GDP between ILC- and CLIC-like scenarios, as the constraints obtained on other operator coefficients are similar in these two cases.

The limits on $C_{\varphi q}^{V}$ and $C_{\varphi q}^{A}$ and on four-fermion operators of identical Lorentz structures are correlated. Beam polarization or angular distributions are unable to disentangle these two types of contributions. Only runs at different energies can effectively separate them. These correlations are therefore reduced in the ILC-like and, even further, in the CLIC-like scenario. Global constraints come close to individual ones in these cases. The best individual limits on $C_{\varphi q}^{V}$ and $C_{\varphi q}^{A}$ are obtained in the ILC-like scenario which features the highest degree of polarization and runs closest to ideal energies. The CLIC-like scenario however provides slightly stronger global constraints thanks to reduced correlations with four-fermion operators. Individual constraints on two-fermion operators are one to two orders of magnitude stronger than present ones (see Figure 5.7) and at least a factor of three better than the most optimistic HL-LHC prospects (see section 7.2 for a fit extension adding HL-LHC prospects).

Although a direct comparison between the two-lepton-two-quark operators of interest here and the four-quark operators probed in top-quark pair production at the LHC in section 5.1 is not strictly speaking possible, ILC- or CLIC-like scenarios would derive constraints on four-fermion operators two to four orders of magnitude smaller than the current LHC ones at $\sqrt{s} = 13$ TeV (see Figure 5.5).

7.2 Prospects for top and bottom-quark EW couplings

In this section we present a global fit on prospects on the top and bottom-quark EW couplings exploring the high-luminosity phase of the LHC and also adding the ILC-like scenario. This fit extends the global fit performed in section 5.2 using HL-LHC and ILC prospects. This work is published in [106].

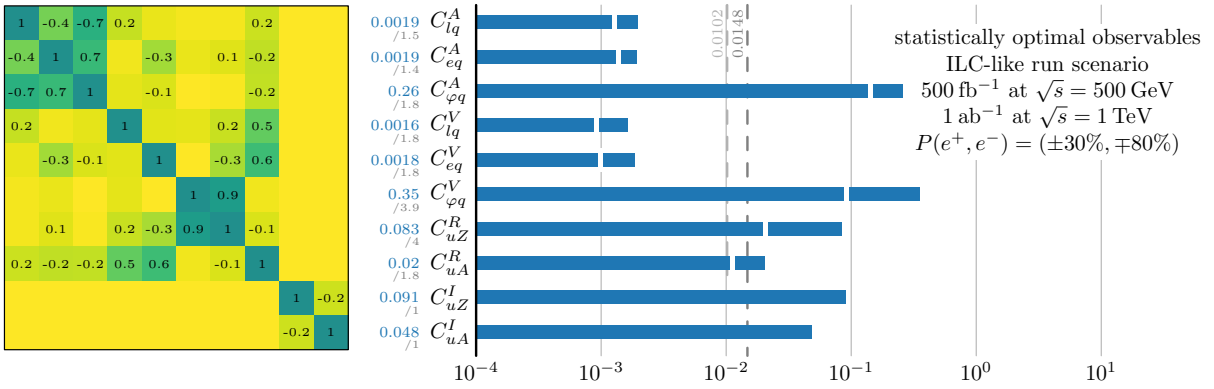

Figure 7.2: Global one-sigma constraints in an ILC-like benchmark run scenario. The dashed lines provides the GDP of the constraints on all ten operator coefficients, or on CP-conserving ones only. See further details in Figure 7.1.

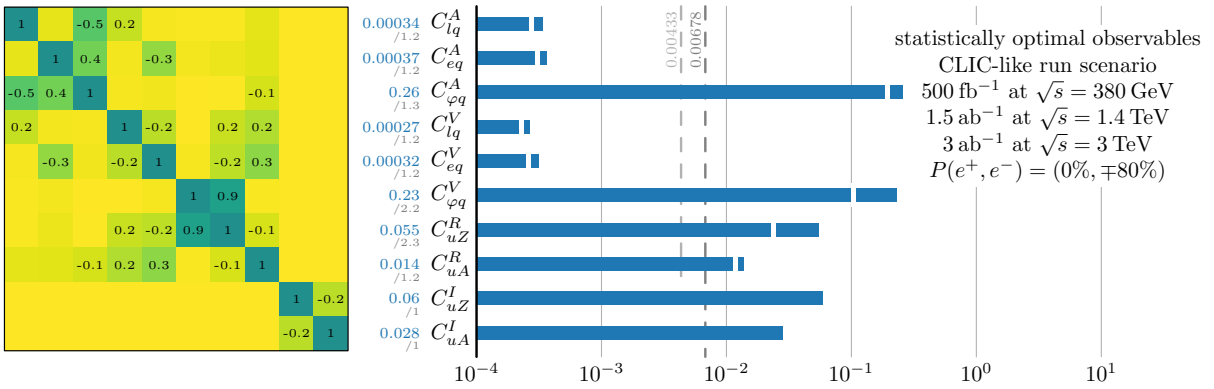

Figure 7.3: Global one-sigma constraints and correlation matrix in a CLIC-like benchmark run scenario. The dashed lines provides the GDP of the constraints on all ten operator coefficients, or on CP-conserving ones only. See further details in Figure 7.1.

7.2.1 High-luminosity phase of the LHC

At the time of writing ATLAS and CMS have collected approximately 140 fb^{-1} of pp collisions at a centre-of-mass energy of 13 TeV in Run 2. After a long shutdown (LS2), LHC Run 3 is expected to deliver a total of 300 fb^{-1} per experiment at the nominal energy ($\sqrt{s} = 14$ TeV). Between 2023 and 2026, an upgrade of the LHC accelerator complex [247] and detectors will allow operation at five to seven times the nominal LHC luminosity. The HL-LHC phase will bring the total integrated luminosity to 3 ab^{-1} by 2037.

The expected precision for SM measurements after the full 3 ab^{-1} is presented in a series of Yellow Reports. The chapter on top-quark physics [248] does not provide a quantitative basis for all measurements included in our study. We therefore adopt two simple scenarios to project the existing measurements from Table 5.3, that are loosely inspired by the scenarios prepared for the Higgs chapter of the HL-LHC Yellow Report [249]. The "S1" scenario envisages that the statistical uncertainty scales with the inverse square root of the integrated luminosity. The systematic uncertainties, in measurements and predictions, do not change. The "S2" scenario envisages an improvement of a factor two for the theory uncertainty, while the statistical uncertainty and the experimental systematic uncertainty scale with the

inverse square root of the integrated luminosity. For the measurements included in the fit, this scenario thus implies a reduction of the experimental uncertainty by a factor 6-10. At that point, the comparison with the SM is generally limited by the theory uncertainty, that has the more modest improvement.

It is instructive to compare the S2 scenario to more detailed projections. ATLAS and CMS have provided detailed prospect studies for some analyses [250]. Other groups have published independent prospect studies, see in particular Ref. [124] for $t\bar{t}Z$ production and Ref. [119] for top-quark decay.

The production of a top-quark pair in association with a gauge boson plays an important role in the fit. In the ATLAS and CMS measurements we consider, the theory uncertainty (typically of the order of 10%) is similar in size to the experimental uncertainty. In the S2 scenario, the experimental uncertainties are improved very substantially. The theory uncertainties are then expected to be limiting by the end of the HL-LHC. This indeed seems the most likely scenario. The factor two improvement in the theory uncertainty envisaged in the S2 scenario could well be achieved by improving the description from the current NLO to NNLO in QCD, which seems feasible on the time scale of the HL-LHC programme.

A promising avenue for many of the associated production processes is a differential analysis. In the current data set, the precision is still very limited for rare processes. However, with a hundred-fold increase in the data sample, differential analyses at the HL-LHC are expected to provide powerful constraints [124, 251]. This is particularly relevant for the dipole operators. In Figure 7.4, the sensitivity of the differential $pp \to t\bar{t}\gamma$ cross-section is seen to increase strongly with the transverse momentum of the photon. A shape analysis of the spectrum may yield a powerful constraint, possibly even exceeding the prospects of the S2 scenario.

The case of the W-boson helicity fraction measurement in top-quark decays is an example where the S2 scenario is probably overly optimistic. The theory uncertainty is currently significantly below the experimental precision, so that it does not limit the precision for this projection. The strong improvement in the precision envisaged by the S2 scenario is optimistic in comparison with the outlook in Ref. [119]. In practice, the impact on the overall prospects is limited. The measurements in top-quark decay are most relevant for the constraint on C_{tW}/Λ^2, that is probed by several other measurements. In case the measurements in top-quark decay should fail to improve as expected in S2, other measurements (such as single top-quark production with a Z boson) can take over its role in the global fit. We expect, therefore, that the overall results presented in this section are not affected too much, even if the top-quark decay measurements improve less than envisaged.

7.2.2 Global fit on prospects

In Figure 7.5, we present the global fit results adding the HL-LHC and the ILC-like scenarios prospects. For $b\bar{b}$ production we have added the cross-section and forward-backward asymmetry at $\sqrt{s} = 250, 500$ GeV. In the case of $t\bar{t}$ production, we use the statistically optimal observables. The uncertainties for each case are motivated in chapter 4.

The complete covariance matrices for all the fits are provided in [106]. In Figure 7.5 the uncertainty ΔC_i on the operator coefficients is shown. This uncertainty is estimated as half of the 68% probability interval. In order to compare all projects on an equal footing, the central value of all measurements,

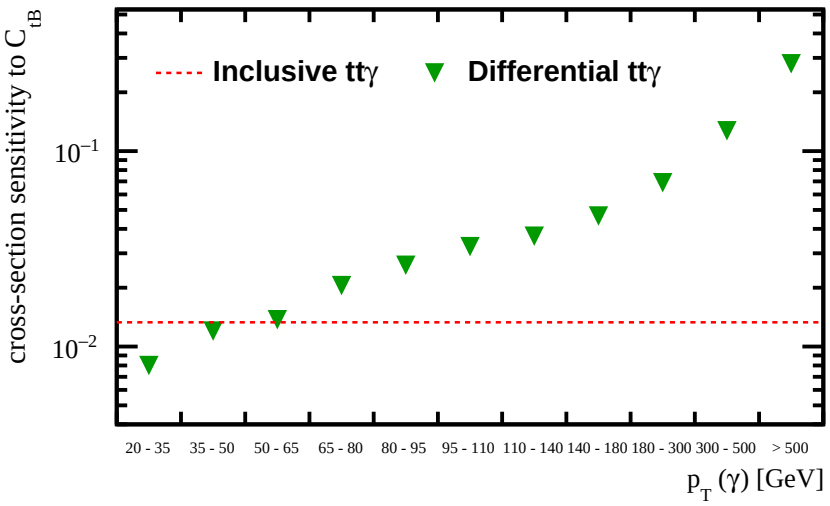

Figure 7.4: The sensitivity of the differential $pp \to t\bar{t}\gamma$ cross-section to the operator coefficient C_{tB}/Λ^2. The sensitivity is defined as the relative change in the cross-section due to a unit change in C_{tB}/Λ^2.

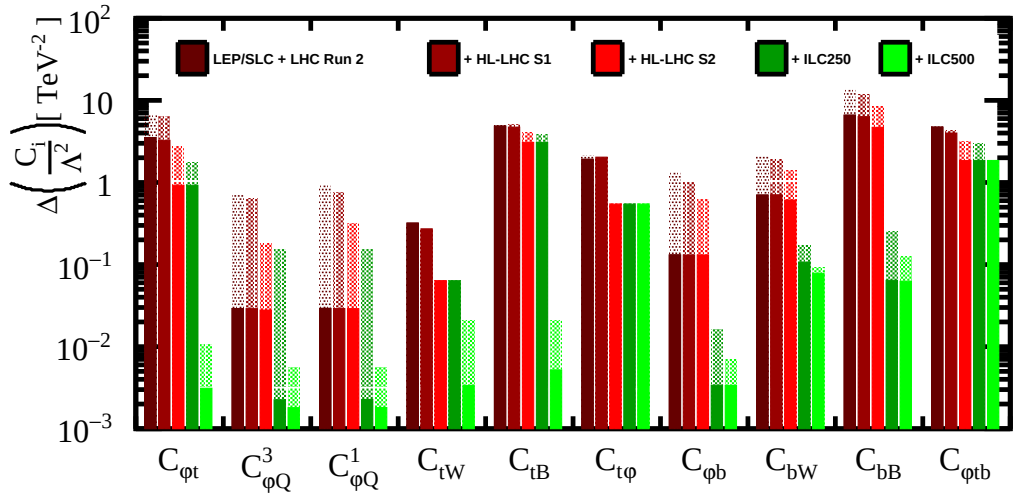

Figure 7.5: Prospects for the precision of the Wilson coefficients in future high-luminosity operation of the LHC and at a high-energy e^+e^- collider. Assumptions on the operating scenarios and details of the uncertainty estimates are given in text. The solid section of the bars represents the individual constraints, where each parameter is fitted in isolation, the full length indicates the marginalized constraint in a ten-parameter fit. The complete covariance matrices of the fits that are presented in this figure are available in Ref. [106].

including the existing LHC and LEP/SLC results, is set to the SM value[4]. For each Wilson coefficient, the first vertical bar represents the current data. In the second and third bars, the measurements envisaged in the S1 or S2 scenario for the HL-LHC are added. The fourth bar includes the LEP/SLC data, the data

[4]The "LEP/SLC + LHC Run2" bar in Figure 7.5 use the same data explained in section 5.2, but in this case the central values are taken to be the predictions in the SM, and in Figure 5.7 the values are taken from the measurements.

of the HL-LHC S2 scenario and the ILC run at $\sqrt{s} = 250$ GeV. The fifth bar adds also the 500 GeV run at the ILC.

For the first HL-LHC scenario, S1, we find that, due the conservative assumptions on systematic uncertainties, the bounds on the Wilson coefficient improve only marginally. In the S2 scenario, almost all limits are considerably tighter. For the dipole operator O_{tB} the constraint remains very poor due the limited sensitivity of the LHC observables. This could be improved by the addition of the differential $t\bar{t}\gamma$ measurement, as discussed in subsection 7.2.1.

The individual and marginalized limits for the operators that affect only the top-quark sector are very similar. Most operators are constrained from several angles, by different LHC observables (see Figure 5.6). This limits the correlation in the global fit. In the bottom-quark sector, the sensitivity is dominated by the R_b measurement, giving rise to a strong correlation and considerably larger differences between individual and marginalized limits.

Adding the $e^+e^- \to b\,\bar{b}$ data at $\sqrt{s} = 250$ GeV provides an improvement for the pure bottom-quark operators by an order of magnitude. The top-quark operators improve somewhat as well, due to a reduction of the correlation with the bottom-quark operators.

Finally, we consider the ILC500 scenario. At this energy, the sensitivity to the bottom-quark operators is very similar to that at $\sqrt{s} = 250$ GeV. As the $b\bar{b}$ production cross-section decreases with the centre-of-mass energy, the addition of the 500 GeV data does not provide an important improvement on the bottom-quark coefficients limits.

For $e^-e^+ \to t\,\bar{t}$, the optimal observables place bounds on a subset of operators that affect the top-quark EW couplings; $C_{\varphi t}$, $C^-_{\varphi Q}$, C_{tW} and C_{tB}. The addition of the $e^+e^- \to t\,\bar{t}$ data leads to a very pronounced improvement of the constraints on the top-quark operator coefficients, by one or two orders of magnitude. The direct access to the $Z/\gamma\, t\bar{t}$ vertex provides very tight constraints. Also the bounds on $C^1_{\varphi Q}/\Lambda^2$ and $C^3_{\varphi Q}/\Lambda^2$ are expected to improve by an order of magnitude. The combination of high-precision constraints on the two linear combinations ($C^1_{\varphi Q} + C^3_{\varphi Q}$, that affects bottom-quark pair production, and the difference, $C^1_{\varphi Q} - C^3_{\varphi Q}$, that affects top-quark pair production) finally lift the degeneracy that affects the LHC/LEP/SLC fit of subsection 5.2.5.

7.2.3 Validity of the EFT framework

In subsection 5.2.6, the terms of order Λ^{-4} were found to have a considerable impact on the fit to current LHC and LEP/SLC data. This limits the generality of the interpretation to extensions of the SM where the contribution of the dimension-eight terms we have ignored is less important than that of the dimension-six operators we have included. With the increasing precision of the measurements at the LHC and at future facilities, this tension in the EFT description is expected to decrease.

In the second HL-LHC scenario, S2, the difference between the nominal fit and a fit based on a parameterization that only considers the Λ^{-2} terms is indeed reduced significantly. In fact, for most of the observables the former gives better constraints (by a factor 3 at most) due to the fact that the observables depend on less parameters because of the vanishing Λ^{-2} terms for C_{bW}, C_{bB} and $C_{\varphi tb}$ in the $m_b \to 0$ limit. However, the Λ^{-4} term still plays an important role for C_{tB} due to the suppression of the linear term explained in subsection 5.2.3.

The high-precision measurements in e^+e^- collisions improve the bounds by at least an order of magnitude and bring most operator coefficients safely into the range where the EFT expansion is valid in full generality. The difference between the nominal fit and the fit based on only Λ^{-2} terms is reduced to less than 20%.

7.2.4 Addition of two-lepton-two-quark operators to the global fit

We discuss here the perspective for an extension of the fit to the complete set of CP-conserving dimension-six operators that affect the bottom- and top-quark EW couplings.

The two-lepton-two-quark operators contributing to $e^+e^-t\bar{t}$ and $e^+e^-b\bar{b}$ (as well as $\nu e^-t\bar{b}$) interactions are listed in Equation 3.7. The scalar and tensor operators, $\{C^S_{lequ}, C^T_{lequ}, C_{ledq}\}$, can effectively be constrained with specialized observables as explained in section 6.5 and in runs with left-left or right-right beam polarization [66]. These kind of observables and scenarios are not considered in this work, so in the following, we therefore focus on the seven vector operators, $\{C^+_{lq}, C^-_{lq}, C_{lu}, C_{ld}, C_{lu}, C_{eq}, C_{eu}, C_{eu}\}$.

The primary handle to constrain the two-fermion and four-fermion operators in a global fit is the energy dependence. The sensitivity to four-fermion operators grows very strongly with energy, while that to the two-fermion operators is essentially flat (see Figure 6.1).

At hadron colliders, the four-fermion operators of $e^+e^-t\bar{t}$ form can, at least in principle, be constrained by a differential analysis of the cross-section of the $pp \to t\bar{t}e^+e^-$ process versus the invariant mass and transverse momentum of the e^+e^- system [109]. The fit can then disentangle the photon, Z boson, and the contact interaction contributions. No such analysis has been made public, so far.

A future e^+e^- collider with multiple energy stages is expected to provide a powerful bound on the four-fermion operator coefficients. In section 7.1, we find that a ten-parameter fit of the two-fermion and four-fermion operator coefficients that affect the EW couplings of the top quark is shown to provide stringent bounds when at least two well-separated energy stages are available.

To estimate the effect of the inclusion of the four-fermion operators, we extend the fit with seven additional degrees of freedom. At the same time, the prospects for measurements at $\sqrt{s} = 1$ TeV, with an integrated luminosity of 8 ab^{-1}, are added to the HL-LHC+ILC250+ILC500 scenario. For the top-quark operators we again adopt the projections of the statistically optimal observables. For bottom-quark operators, statistical uncertainties on the cross-section and A_{FB} are propagated, assuming a conservative acceptance times selection efficiency of 10%.

The results of this extended fit are shown in Table 7.1. The marginalized 68% probability bounds are compared to those obtained in the ten-parameter fit (i.e. the results labeled ILC500 in Figure 7.5).

This seventeen-parameter fit yields excellent limits on the four-fermion operators, below 10^{-3} TeV^{-2}. The bounds agree with those of section 7.1 when the larger integrated luminosity in the 1 TeV scenario is accounted for.

The bounds on the dipole operators are similar to those of the ten-parameter fit: the bounds on the coefficients C_{tW}/Λ^2 and C_{tB}/Λ^2 of the top-quark dipole operators improve somewhat, as the sensitivity of the optimal observables grows with increasing centre-of-mass energy. The bound on C_{bW}/Λ^2 derives

	10-parameter fit ILC250 + ILC500	17-parameter fit + ILC1000
$C_{\varphi t}/\Lambda^2$	0.01	0.09
$C^3_{\varphi Q}/\Lambda^2$	0.005	0.04
$C^1_{\varphi Q}/\Lambda^2$	0.005	0.04
C_{tW}/Λ^2	0.02	0.014
C_{tB}/Λ^2	0.02	0.015
$C_{t\varphi}/\Lambda^2$	0.54	0.54
$C_{\varphi b}/\Lambda^2$	0.007	0.008
C_{bW}/Λ^2	0.09	0.17
C_{bB}/Λ^2	0.13	0.17
$C_{\varphi tb}/\Lambda^2$	1.9	1.9
C_{eu}/Λ^2	—	0.0006
C_{ed}/Λ^2	—	0.0005
C_{eq}/Λ^2	—	0.0004
C_{lu}/Λ^2	—	0.0006
C_{ld}/Λ^2	—	0.0009
C^-_{lq}/Λ^2	—	0.0006
C^+_{lq}/Λ^2	—	0.0005

Table 7.1: The marginalized 68% probability bounds on the dimension-six operator coefficients in units of TeV^{-2}. The results in the first column are based on a ten-parameter fit on pseudo-data from two ILC runs, with an integrated luminosity of 2 ab^{-1} at 250 GeV and 4 ab^{-1} at $\sqrt{s} = 500$ GeV. These results are identical to those of the ILC500 entry in Figure 7.5. The second column presents the results of the seventeen-parameter fit. It includes an additional run, with an integrated luminosity of 8 ab^{-1} at $\sqrt{s} = 1$ TeV and seven additional degrees of freedom corresponding to two-lepton-two-third-generation-quark operators.

from cross-section and A^{FB} in $e^+e^- \to b\bar{b}$ measurements. It does therefore not improve at higher centre-of-mass energies and moreover suffers somewhat from the introduction of additional $e^+e^-b\bar{b}$ degrees of freedom.

The largest difference between the two fits is found for the two-fermion operators that modify the left-handed couplings of the top and bottom quark to the Z boson or the right-handed coupling of the top quark to the Z boson. The presence of the four-fermion operators degrades the excellent limits on $C_{\varphi t}/\Lambda^2$ and $C^{1,3}_{\varphi Q}/\Lambda^2$ by a factor eight.

We conclude, therefore, that a global EFT fit, including all dimension-six operators that affect the top and bottom-quark EW interactions, is feasible provided data is collected at two sufficiently distinct centre-of-mass energies above the top-quark pair production threshold.

7.2.5 Prospects on top-Yukawa coupling

In this section, we extract the top-Yukawa coupling from LHC data and the prospects for measurements at the HL-LHC and ILC.

An e^+e^- collider also offers several handles on the top-Yukawa coupling. The same indirect methods introduced in subsection 5.2.7 are available at centre-of-mass energies below the $t\bar{t}H$ production threshold in an e^+e^- collider. The top-Yukawa coupling be extracted indirectly from the measurement

of the Hgg and $H\gamma\gamma$ couplings, with 1% precision after 2 ab^{-1} at $\sqrt{s} = 250$ GeV [127]. A global EFT analysis of the indirect sensitivity of Higgs and diboson measurements to EW top-quark couplings, including the top-Yukawa coupling, is performed in Ref. [233] and discussed in section 7.3. It is found that differential measurements are crucial to simultaneously disentangle all tree and loop-level contributions.

HL-LHC prospects. The fit in subsection 5.2.5 is repeated on projections to assess the expected precision after the complete data set collected during the high-luminosity phase of the LHC. As before, we focus on the S2 scenario, based on an integrated luminosity of 3 ab^{-1} at $\sqrt{s} = 14$ TeV. In this scenario, the statistical uncertainty on the $t\bar{t}H$ cross-section becomes negligible and the precision is primarily limited by the precision of the theory prediction (currently 8% and assumed to improve to 4%). The precision of the global fit improves considerably, reducing the 68% probability interval to $[-0.55, +0.55]$. This result agrees with the S2 prospects in Ref. [249].

ILC prospects. The direct measurement of the top-Yukawa coupling in $e^+e^- \to t\bar{t}H$ production requires operation at a centre-of-mass energy above the $t\bar{t}H$ production threshold. The cross-section turns on sharply at around $\sqrt{s} = 500$ GeV. The unpolarized cross-section reaches a maximum of 2 fb at a centre-of-mass energy of approximately 800 GeV. The $t\bar{t}H$ production rate is two orders of magnitude lower than that for top-quark pair production rate, which forms the most important background for the $H \to b\bar{b}$ analysis. The cross-section of the irreducible $t\bar{t}b\bar{b}$ background, either from associated $t\bar{t}Z$ production or a hard gluon splitting to a $b\bar{b}$ pair, is similar to that of the signal.

Full-simulation studies of the potential of the linear collider [149, 252–255] have been performed at centre-of-mass energies from 500 GeV to several TeVs. They include realistic descriptions of the $t\bar{t}$ and $t\bar{t}Z$ backgrounds, of the detector response, flavour tagging and jet clustering.

Projections for the nominal ILC programme [66], with 4 ab^{-1} of integrated luminosity collected at 500 GeV are presented in Ref. [256]. An uncertainty of 13% is expected on the $t\bar{t}H$ cross-section, limited by statistics. As the nominal ILC energy is very close to the $t\bar{t}H$ production threshold, operation at a slightly higher energy improves the precision considerably. Increase of the centre-of-mass energy by 10% (i.e. to $\sqrt{s} = 550$ GeV) enhances the cross-section by a factor of four and the precision on the Yukawa coupling by a factor two, for the same integrated luminosity [256].

We base our projection for 1 TeV operation on the analysis of Ref. [252] of $t\bar{t}H$ production followed by $H \to b\bar{b}$ decay. The expected uncertainty on the $t\bar{t}H$ cross-section for an integrated luminosity of 8 ab^{-1} is of 3.2%, obtained by scaling the signal and background yields with a flat luminosity factor.

To match the statistical precision, the systematic uncertainties must be controlled to a challenging level. At 1 TeV the signal efficiency and background yield must be known to approximately 1%, which seems feasible with data-driven estimation in control regions. The theory uncertainty in the cross-section at $\sqrt{s} = 1$ TeV must be reduced to the level of 1-2%, a factor two with respect to currently available calculations [257]. On the other hand, it is likely that the analysis can be further improved, by reoptimizing the selection, with the inclusion of other Higgs decay channels and of the τ-lepton plus jets final state. Significant additional improvements are possible with improved jet clustering algorithms and the use of kinematic fits.

scenario	LHC Run 2 +LEP/SLC	HL-LHC S2 +LEP/SLC	ILC500	ILC550	ILC500 +ILC1000
$\sqrt{s}$, $\int \mathcal{L}$	13TeV, 36 fb^{-1}	14TeV, 3 ab^{-1}	500 GeV, 4 ab^{-1}	550 GeV, 4 ab^{-1}	+1 TeV, +8 ab^{-1}
68% probability interval for effective operator coefficient $C_{t\varphi}/\Lambda^2$ [TeV^{-2}]					
individual	$[-4.4, +0.0]$	$[-0.55, +0.55]$	$[-1.06, +1.06]$	$[-0.50, 0.50]$	$[-0.27, +0.27]$
marginalized	$[-4.6, -0.2]$	$[-0.55, +0.55]$	$[-1.07, +1.07]$	$[-0.52, +0.52]$	$[-0.32, +0.32]$
corresponding relative uncertainty on top-Yukawa coupling $\Delta y_t/y_t$ *[%]*					
individual	13.2	3.3	6.4	3.0	1.62
marginalized	13.2	3.3	6.4	3.1	1.96

Table 7.2: The 68% probability intervals for $C_{t\varphi}/\Lambda^2$ and the corresponding precision on the top-Yukawa coupling. The results of the first four columns correspond to the ten-parameter fit that we used to obtain the results of Figure 7.5. The results for the scenario with ILC runs at two different centre-of-mass energies in the last column were obtained with the extended seventeen-parameter fit presented in subsection 7.2.4.

Summary of results. In Table 7.2, we present the individual and marginalized 68% probability bounds on $C_{t\varphi}/\Lambda^2$ from the fits to LEP/SLC+LHC data and to the future collider scenarios. For comparison to the literature, the same results are also provided in terms of the precision with which the Yukawa coupling can be extracted, using the simple relation:

$$\delta y_t = -\frac{C_{t\varphi} v^2}{\Lambda^2}. \tag{7.2}$$

The results of the first four columns correspond to the ten-parameter fit that we used to obtain the results of Figure 7.5. The results for the scenario with ILC runs at two different centre-of-mass energies in the last column were obtained with the extended seventeen-parameter fit presented in subsection 7.2.4.

Before turning to a discussion of the global fit results, we compare the individual limits to the literature. The HL-LHC result in Table 7.2 agrees with the HL-LHC projection of Ref. [249]. The ILC results at 500 GeV agree —by construction— with the summary of the Higgs/EW group for the 2020 update of the European strategy for particle physics in Ref. [258]. The results for operation at 550 GeV and 1 TeV extend the study to higher energy.

We find that in nearly all cases the individual and marginalized results agree very closely. This implies that the operators that modify the top-quark EW couplings do not affect the extraction of the top-Yukawa coupling.

In the LHC and HL-LHC fits, despite the relatively poor constraints on the EW couplings of the top quark, the bounds on $C_{t\varphi}/\Lambda^2$ are not affected by the presence of the additional degrees of freedom. In this case, it is important to note, however, that the operators that affect the QCD interactions of the top quark, such as C_{tG}/Λ^2 and four-fermion operators of the form $q\bar{q}t\bar{t}$, are not included in the fit. These can in principle be constrained using precise measurements of the differential $t\bar{t}$ cross-section. A recent global fit of the top-quark sector on LHC data [114] finds, however, that the marginalized limit on $C_{t\varphi}$ is approximately a factor 10 weaker than the individual limit, due to strong correlations between operator coefficients. The addition of Tevatron results or future differential measurements could help to reduce this degeneracy. It is nevertheless likely that a combination of $pp \to t\bar{t}$ and $pp \to t\bar{t}X$ measurements

could be needed to constrain simultaneously all $q\bar{q}t\bar{t}$ operators. In this respect, the extraction of the top-Yukawa coupling at future lepton colliders seems more robust.

At a future e^+e^- collider, we indeed find that the contamination of both four-fermion and two-fermion operators in $e^-e^+ \to t\bar{t}H$ is limited due to the very tight constraints on these coefficients deriving from $e^-e^+ \to t\bar{t}$ production. Even in the most challenging case, the ILC scenario at 1 TeV with a precision on the top-quark Yukawa coupling of 1.6% and sixteen competing operator coefficients, the marginalized bound is only about 20% weaker than the individual bound. The extraction of the top-Yukawa is then very clean in this case. We also note that the measurement of $e^-e^+ \to t\bar{t}H$ in addition to $e^-e^+ \to t\bar{t}$ does not improve significantly the constraints on operators other than the top-Yukawa coupling. Only a 14% improvement is observed on C_{tW}.

The results in Table 7.2 demonstrate that the bounds on the Wilson coefficient $C_{t\varphi}/\Lambda^2$ that shifts the top-Yukawa coupling from measurements of the $t\bar{t}H$ production are robust in the presence of the operators that affect the top and bottom-quark EW couplings. A precise measurement of this rate is therefore an ideal complement to more indirect bounds from $gg \to H$ production and $H \to \gamma\gamma$, $H \to gg$ and $H \to Z\gamma$ decay.

7.3 Outlook to a combined top-quark and Higgs-boson fit

In an ongoing study we assess the interplay between Higgs-boson and top-quark sectors. The study of the top-Yukawa coupling from the indirect constraints using $H \to gg$, $H \to Z\gamma$ and $H \to \gamma\gamma$ processes requires to disentangle the contribution of different operators to these processes.

In Ref. [127] the authors demonstrate that the top-Yukawa coupling can be measured with a precision of 1.2% in the ILC250 scenario from an individual fit from the process $H \to gg$. When one includes Higgs operators that affect the same vertex this precision is lost. The current most robust extraction of the top-Yukawa coupling is then using $t\bar{t}H$ production, as seen in previous section.

A complete study of the dimension-six operators that affect Higgs-boson physics is found in Refs. [259, 260] using LEP and LHC processes. The same is done in Refs. [130, 131] for prospescts in the ILC scenario. These studies use precise measurements of the electroweak precision observables (EWPOs), and Higgs production and decay at different energies.

In Refs. [232, 233] the authors study the impact of the dimension-six top-quark operators in the Higgs processes. They study the next-to-leading order electroweak corrections to Higgs processes from dimension-six top-quark operators. They consider WH, ZH, and VBF production at the LHC, and ZH, VBF production at future lepton colliders, and Higgs-boson decays, $H \to \gamma\gamma$, γZ, $Wl\nu$, Zll, $\bar{b}b$, $\mu\mu$, $\tau\tau$. The results show that with the current constraints, top-quark operators shift the signal strength of the loop-induced processes by factors of $\sim O(1) - O(10)$, and that of the tree-level processes, i.e. all remaining production and decay channels, by $\sim 5 - 10\%$ at the LHC, and up to $\sim 15\%$ at future lepton colliders. This means that all Higgs channels are sensitive to top-quark couplings.

We combine the dimension-six Higgs operators used in Refs. [130, 131] with our top-quark fit from section 5.2. We also study the impact of the top-quark operators to the Higgs boson observables described in Refs. [130, 131]. In Figure 7.6 we show preliminary results of the fit for the Higgs boson

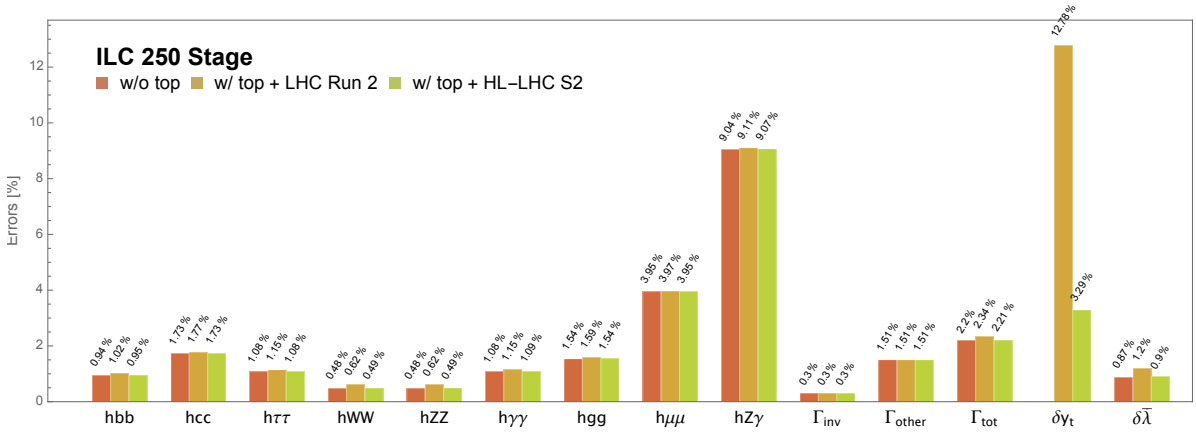

Figure 7.6: Results on the physical Higgs couplings of the fit for the ILC250 scenario. The first column in red corresponds to a 22-parameter fit without top operators [130]. The second column in orange represents the result that is obtained when the basis is extended with the seven top-quark EW operator coefficients: $C^3_{\varphi Q}$, $C^1_{\varphi Q}$, $C_{\varphi t}$, C_{tW}, C_{tB}, $C_{\varphi tb}$ and $C_{t\varphi}$ and LHC Run 2 data is added. The last column in green repeats the same fit with the expectations of the S2 scenario for the measurement of the top-quark EW operators. Figure reproduced from [261].

couplings. The parameters δy_t and $\delta\bar{\lambda}$ represent the top-Yukawa coupling and the Higgs self-coupling respectively.

At the ILC250 scenario, the inclusion of the current dimension-six top operator bounds from the fit in Table 5.4 does not have a significant impact on the physical Higgs couplings limits. With the addition of the prospects on the top-quark couplings for the HL-HLC S2 scenario we recover the original value in the reference fit without top-quark operators. However, the impact of the inclusion of the top-quark operators on the Higgs-boson dimension-six operator basis has an important effect. Even if the physical couplings of the Higgs boson may be well constrained, strong degeneracies may remain in the operator basis. This study is under developement and will be public soon [261].

7.4 Summary of prospects

We have evaluated the potential of future lepton colliders to reveal new physics effects in precision measurements of top-quark pair production. We studied the sensitivity of a large number of observables, as well as the impact of the centre-of-mass energy and beam polarization. Combining measurements of the top-quark polarization and of CP-odd observables with that of the cross-section and forward-backward asymmetry increases the sensitivity to the real and imaginary parts of the dipole operators, respectively. We also examined the power of additional constraints, such as the measurement of the top-quark width in a threshold scan or of bottom-quark pair production.

We observed that even with an extended set of observables, control over the beam polarization remains an important handle to simultaneously constrain the contributions of vector and axial-vector operators. Operation at high centre-of-mass energy provides tight bounds on four-fermion operators

whose contributions grow quadratically with the energy. The inclusion of data acquired at two centre-of-mass energies is crucial in a global fit of two-fermion and four-fermion operators.

To effectively and simultaneously cover all considered directions of the EFT parameter space, we considered a set of statistically optimal observables that maximally exploits the information contained in the fully differential $bW^+\bar{b}W^-$distribution. A combination of statistically optimal observable measurements at two different centre-of-mass energies is sufficient to simultaneously constrain the operator coefficients considered. Larger separations between the two centre-of-mass energies resolve approximate degeneracies and bring global limits closer to individual ones. Beam polarization helps to increase individual sensitivities and reduces global correlations.

We assess the potential of future measurements to improve the current bounds on the dimension-six top-quark operators. The main result is presented in Figure 7.5. The remaining LHC program, including the high-luminosity phase, can sharpen most bounds by a factor two to three, provided the uncertainties on the predictions in the SM are improved by a factor two and experimental systematics evolve with luminosity in the same way as the statistical uncertainties. An electron-positron collider with a centre-of-mass energy that exceeds the top-quark pair production threshold, can greatly improve the bounds. The nominal ILC operating scenario with runs at $\sqrt{s} = 250$ GeV and 500 GeV is expected to improve on the HL-LHC bounds by one or two orders of magnitude.

The precision measurements at a future lepton collider also reduce the importance of terms of order Λ^{-4} and brings the EFT expansion into the regime where the bounds are valid in full generality. We show that with a further run at higher energy the ILC can constrain the coefficients of the four-fermion operators that are not included in our baseline fit.

Finally, we present prospects for the extraction of the top-Yukawa coupling from the associated production processes $pp \to t\bar{t}H$ and $e^+e^- \to t\bar{t}H$ in Table 7.2. The current precision of order 10% is expected to improve by more than a factor three in the HL-LHC S2 scenario. The ILC can achieve a similar precision when operated at 550 GeV and can exceed this precision by a further factor two for a 1 TeV energy upgrade with 8 ab^{-1}. These results are found to be robust in a multi-parameter fit that includes the degrees of freedom corresponding to operators that modify the EW couplings of the bottom and top quark.

8.- Conclusions

The Standard Model is a very robust and predictive theory that describes the elementary particles and their interactions, but there are evidences that it is not a complete theory. Many have proposed extensions of the SM that address its shortcomings.

The top quark is a great candidate to reveal signals of new physics. In this thesis we have used an EFT approach in which we characterize BSM contributions to the top-quark couplings through dimension-six operators.

We have performed a fit to four-quark operators using measurements of the cross-sections and charge asymmetries from the Tevatron and LHC data. We have seen that the sensitivity to these operators is increased in the boosted regime. The fit yields very competitive bounds if we use differential measurements of the charge asymmetry at very large invariant mass of the $t\bar{t}$ system.

We have also studied the EW couplings of the top quark. Deviations in the left-handed couplings of the top and bottom quarks to the Z boson are generated by the same operators $O^3_{\varphi Q}$ and $O^1_{\varphi Q}$. For this reason we perform a combined fit of the bottom and top-quark couplings. We use LEP, SLC and LHC Run 2 data to constrain a total of 10 parameters. We obtain a robust fit which yields to the best bounds to date on the EW operators.

We have also studied the potential of future electron-positron colliders for improving our fit on the dimension-six top-quark operators. We have studied different scenarios, especially for the ILC and CLIC projects. The existing bounds on the EW operators improve by two orders of magnitude if we add to the fit the stages of the ILC at $\sqrt{s} = 250$ GeV and $\sqrt{s} = 500$ Gev.

An electron-positron collider also allows to constrain two-lepton-two-quark operators. The sensitivity to these operators grows with the energy, so a high energy point is needed to constrain the complete set of operators. We have studied that adding a run of the ILC at $\sqrt{s} = 1$ TeV to the previous fit allows us to contrain a total of 17 dimension-six operators of the top and bottom quarks.

All the measurements used in the fits are sensitive to the dimension-six operators at tree level. We have started to study the impact of top-quark operators in the Higgs sector through the renormalization group equations.

In conclusions, we have made several important contributions to the developement of a global EFT fit on the top-quark sector. Our final goal would be to perform a fit which includes all the measurements to date with all the effective operators affecting the top quark. Even, more ambitiously, in the long run one can envisage to constrain the full set of dimension-six operators in the SM Lagrangian using all available precision measurements at hadron colliders and future lepton colliders.

Bibliography

[1] MissMJ, "Standard Model of Elementary Particles." https://commons.wikimedia.org/wiki/File:Standard_Model_of_Elementary_Particles.svg, 27 June 2006.

[2] A. Pich, *The Standard Model of Electroweak Interactions*, in *Proceedings, High-energy Physics. Proceedings, 18th European School (ESHEP 2010): Raseborg, Finland, June 20 - July 3, 2010*, pp. 1–50, 2012, 1201.0537.

[3] P. A. M. Dirac, *Quantum theory of emission and absorption of radiation*, *Proc. Roy. Soc. Lond.* **A114** (1927) 243.

[4] S. Tomonaga, *On a relativistically invariant formulation of the quantum theory of wave fields*, *Prog. Theor. Phys.* **1** (1946) 27.

[5] J. S. Schwinger, *Quantum electrodynamics. I A covariant formulation*, *Phys. Rev.* **74** (1948) 1439.

[6] R. P. Feynman, *Space - time approach to quantum electrodynamics*, *Phys. Rev.* **76** (1949) 769.

[7] Particle Data Group collaboration, *Review of particle physics*, *Phys. Rev. D* **98** (2018) 030001.

[8] M. Gell-Mann, *The Eightfold Way: A Theory of strong interaction symmetry*, .

[9] M. Gell-Mann, *Symmetries of baryons and mesons*, *Phys. Rev.* **125** (1962) 1067.

[10] D. J. Gross and F. Wilczek, *Ultraviolet Behavior of Nonabelian Gauge Theories*, *Phys. Rev. Lett.* **30** (1973) 1343.

[11] H. D. Politzer, *Reliable Perturbative Results for Strong Interactions?*, *Phys. Rev. Lett.* **30** (1973) 1346.

[12] C. S. Wu, E. Ambler, R. W. Hayward, D. D. Hoppes and R. P. Hudson, *Experimental Test of Parity Conservation in Beta Decay*, *Phys. Rev.* **105** (1957) 1413.

[13] S. L. Glashow, *Partial Symmetries of Weak Interactions*, *Nucl. Phys.* **22** (1961) 579.

[14] J. Goldstone, A. Salam and S. Weinberg, *Broken Symmetries*, *Phys. Rev.* **127** (1962) 965.

[15] A. Salam and J. C. Ward, *Electromagnetic and weak interactions*, *Phys. Lett.* **13** (1964) 168.

[16] S. Weinberg, *A Model of Leptons*, *Phys. Rev. Lett.* **19** (1967) 1264.

[17] G. 't Hooft, *Renormalizable Lagrangians for Massive Yang-Mills Fields*, *Nucl. Phys.* **B35** (1971) 167.

[18] G. 't Hooft and M. J. G. Veltman, *Regularization and Renormalization of Gauge Fields*, *Nucl. Phys.* **B44** (1972) 189.

[19] UA1 collaboration, *Experimental Observation of Isolated Large Transverse Energy Electrons with Associated Missing Energy at s**(1/2) = 540-GeV*, *Phys. Lett.* **122B** (1983) 103.

[20] UA2 collaboration, *Observation of Single Isolated Electrons of High Transverse Momentum in Events with Missing Transverse Energy at the CERN anti-p p Collider*, *Phys. Lett.* **122B** (1983) 476.

[21] UA1 collaboration, *Experimental Observation of Lepton Pairs of Invariant Mass Around 95-GeV/c**2 at the CERN SPS Collider*, *Phys. Lett.* **126B** (1983) 398.

[22] UA2 collaboration, *Evidence for Z0 —> e+ e- at the CERN anti-p p Collider*, *Phys. Lett.* **129B** (1983) 130.

[23] N. Cabibbo, *Unitary Symmetry and Leptonic Decays*, *Phys. Rev. Lett.* **10** (1963) 531.

[24] M. Kobayashi and T. Maskawa, *CP Violation in the Renormalizable Theory of Weak Interaction*, *Prog. Theor. Phys.* **49** (1973) 652.

[25] B. Pontecorvo, *Mesonium and anti-mesonium*, *Sov. Phys. JETP* **6** (1957) 429.

[26] Z. Maki, M. Nakagawa and S. Sakata, *Remarks on the unified model of elementary particles*, *Prog. Theor. Phys.* **28** (1962) 870.

[27] B. Pontecorvo, *Neutrino Experiments and the Problem of Conservation of Leptonic Charge*, *Sov. Phys. JETP* **26** (1968) 984.

[28] KTeV collaboration, *Observation of direct CP violation in $K_{S,L} \to \pi\pi$ decays*, *Phys. Rev. Lett.* **83** (1999) 22 [hep-ex/9905060].

[29] NA48 collaboration, *A New measurement of direct CP violation in two pion decays of the neutral kaon*, *Phys. Lett.* **B465** (1999) 335 [hep-ex/9909022].

[30] J. Beyer, R. Karl and J. List, *Precision measurements of Triple Gauge Couplings at future electron-positron colliders*, in *International Workshop on Future Linear Colliders*, 2, 2020, 2002.02777.

[31] J. Beyer and J. List, *ILD benchmark: Quartic Gauge Couplings*, 2002.10830.

[32] Y. Nambu, *Quasi-particles and gauge invariance in the theory of superconductivity*, *Phys. Rev.* **117** (1960) 648.

[33] J. Goldstone, A. Salam and S. Weinberg, *Broken symmetries*, *Phys. Rev.* **127** (1962) 965.

[34] Y. Nambu, *Quasiparticles and Gauge Invariance in the Theory of Superconductivity*, *Phys. Rev.* **117** (1960) 648.

[35] J. Goldstone, *Field Theories with Superconductor Solutions*, *Nuovo Cim.* **19** (1961) 154.

[36] F. Englert and R. Brout, *Broken Symmetry and the Mass of Gauge Vector Mesons*, *Phys. Rev. Lett.* **13** (1964) 321.

[37] P. W. Higgs, *Spontaneous symmetry breakdown without massless bosons*, *Phys. Rev.* **145** (1966) 1156.

[38] G. S. Guralnik, C. R. Hagen and T. W. B. Kibble, *Global conservation laws and massless particles*, *Phys. Rev. Lett.* **13** (1964) 585.

[39] T. W. B. Kibble, *Symmetry breaking in non-abelian gauge theories*, *Phys. Rev.* **155** (1967) 1554.

[40] ATLAS collaboration, *Observation of a new particle in the search for the Standard Model Higgs boson with the ATLAS detector at the LHC*, *Phys. Lett.* **B716** (2012) 1 [1207.7214].

[41] CMS collaboration, *Observation of a new boson at a mass of 125 GeV with the CMS experiment at the LHC*, *Phys. Lett.* **B716** (2012) 30 [1207.7235].

[42] C. Murgui, A. Peñuelas, M. Jung and A. Pich, *Global fit to $b \to c\tau\nu$ transitions*, *JHEP* **09** (2019) 103 [1904.09311].

[43] A. Pich, *Effective field theory: Course*, in *Probing the standard model of particle interactions. Proceedings, Summer School in Theoretical Physics, NATO Advanced Study Institute, 68th session, Les Houches, France, July 28-September 5, 1997. Pt. 1, 2*, pp. 949–1049, 1998, hep-ph/9806303.

[44] A. V. Manohar, *Introduction to Effective Field Theories*, in *Les Houches summer school: EFT in Particle Physics and Cosmology Les Houches, Chamonix Valley, France, July 3-28, 2017*, 2018, 1804.05863.

[45] B. Grzadkowski, M. Iskrzynski, M. Misiak and J. Rosiek, *Dimension-Six Terms in the Standard Model Lagrangian*, *JHEP* **10** (2010) 085 [1008.4884].

[46] A. Azatov, R. Contino, C. S. Machado and F. Riva, *Helicity selection rules and noninterference for BSM amplitudes*, *Phys. Rev.* **D95** (2017) 065014 [1607.05236].

[47] T. Appelquist and J. Carazzone, *Infrared Singularities and Massive Fields*, *Phys. Rev.* **D11** (1975) 2856.

[48] O. Antunano, J. H. Kuhn and G. Rodrigo, *Top quarks, axigluons and charge asymmetries at hadron colliders*, *Phys. Rev.* **D77** (2008) 014003 [0709.1652].

[49] G. Durieux, M. Perelló, M. Vos and C. Zhang, *Global and optimal probes for the top-quark effective field theory at future lepton colliders*, *JHEP* **10** (2018) 168 [1807.02121].

[50] G. Durieux and O. Matsedonskyi, *The top-quark window on compositeness at future lepton colliders*, 1807.10273.

[51] J. de Blas et al., *The CLIC Potential for New Physics*, 1812.02093.

[52] A. W. Chao, K. H. Mess, M. Tigner and F. Zimmermann, eds., *Handbook of accelerator physics and engineering*. World Scientific, Hackensack, USA, 2013, 10.1142/8543.

[53] B. Richter, *THE SLAC ELECTRON - POSITRON COLLIDERS: PRESENT AND FUTURE*, in *Proceedings, 13th International Conference on High-Energy Accelerators (HEACC 1986): Novosibirsk, Soviet Union, August 07-11, 1986*, 9, 1986.

[54] D0 collaboration, *Observation of the top quark*, *Phys. Rev. Lett.* **74** (1995) 2632 [hep-ex/9503003].

[55] CDF collaboration, *Observation of top quark production in $\bar{p}p$ collisions*, *Phys. Rev. Lett.* **74** (1995) 2626 [hep-ex/9503002].

[56] *LEP design report*. CERN, Geneva, 1984.

[57] ALEPH, DELPHI, L3, OPAL, SLD, LEP Electroweak Working Group, SLD Electroweak Group, SLD Heavy Flavour Group collaboration, *Precision electroweak measurements on the Z resonance*, *Phys. Rept.* **427** (2006) 257 [hep-ex/0509008].

[58] LEP Working Group for Higgs boson searches, ALEPH, DELPHI, L3, OPAL collaboration, *Search for the standard model Higgs boson at LEP*, *Phys. Lett.* **B565** (2003) 61 [hep-ex/0306033].

[59] O. S. Brüning, P. Collier, P. Lebrun, S. Myers, R. Ostojic, J. Poole et al., *LHC Design Report*, CERN Yellow Reports: Monographs. CERN, Geneva, 2004, 10.5170/CERN-2004-003-V-1.

[60] https://www.lhc-closer.es/taking_a_closer_look_at_lhc/1.home.

[61] CLICdp, "Interesting processes at CLIC." https://clicdp.web.cern.ch/content/analysis, 2020.

[62] H. Baer, T. Barklow, K. Fujii, Y. Gao, A. Hoang, S. Kanemura et al., *The International Linear Collider Technical Design Report - Volume 2: Physics*, 1306.6352.

[63] H. Abramowicz et al., *The International Linear Collider Technical Design Report - Volume 4: Detectors*, 1306.6329.

[64] P. Bambade et al., *The International Linear Collider: A Global Project*, 1903.01629.

[65] K. Yokoya, K. Kubo and T. Okugi, *Operation of ILC250 at the Z-pole*, 1908.08212.

[66] T. Barklow, J. Brau, K. Fujii, J. Gao, J. List, N. Walker et al., *ILC Operating Scenarios*, 1506.07830.

[67] M. Aicheler, P. Burrows, M. Draper, T. Garvey, P. Lebrun, K. Peach et al., *A Multi-TeV Linear Collider Based on CLIC Technology: CLIC Conceptual Design Report*, CERN Yellow Reports: Monographs. CERN, Geneva, 2012, 10.5170/CERN-2012-007.

[68] L. Linssen, A. Miyamoto, M. Stanitzki and H. Weerts, *Physics and Detectors at CLIC: CLIC Conceptual Design Report*, 1202.5940.

[69] P. Lebrun, L. Linssen, A. Lucaci-Timoce, D. Schulte, F. Simon, S. Stapnes et al., *The CLIC Programme: Towards a Staged e+e- Linear Collider Exploring the Terascale : CLIC Conceptual Design Report*, 1209.2543.

[70] CLICdp, CLIC collaboration, *The Compact Linear Collider (CLIC) - 2018 Summary Report*, *CERN Yellow Rep. Monogr.* **1802** (2018) 1 [1812.06018].

[71] CLIC accelerator collaboration, *The Compact Linear Collider (CLIC) - Project Implementation Plan*, 1903.08655.

[72] A. C. Abusleme Hoffman et al., *Detector Technologies for CLIC*, 1905.02520.

[73] ILD collaboration, *The ILD detector at the ILC*, 1912.04601.

[74] FCC collaboration, *FCC Physics Opportunities*, *Eur. Phys. J.* **C79** (2019) 474.

[75] FCC collaboration, *FCC-ee: The Lepton Collider*, *Eur. Phys. J. ST* **228** (2019) 261.

[76] FCC collaboration, *FCC-hh: The Hadron Collider*, *Eur. Phys. J. ST* **228** (2019) 755.

[77] FCC collaboration, *HE-LHC: The High-Energy Large Hadron Collider Volume*, *Eur. Phys. J. ST* **228** (2019) 1109.

[78] CEPC Study Group collaboration, *CEPC Conceptual Design Report: Volume 1 - Accelerator*, 1809.00285.

[79] CEPC Study Group collaboration, *CEPC Conceptual Design Report: Volume 2 - Physics & Detector*, 1811.10545.

[80] ATLAS, CDF, CMS, D0 collaboration, *First combination of Tevatron and LHC measurements of the top-quark mass*, 1403.4427.

[81] A. H. Hoang, *The Top Mass: Interpretation and Theoretical Uncertainties*, in *Proceedings, 7th International Workshop on Top Quark Physics (TOP2014): Cannes, France, September 28-October 3, 2014*, 2014, 1412.3649.

[82] A. Juste, S. Mantry, A. Mitov, A. Penin, P. Skands, E. Varnes et al., *Determination of the top quark mass circa 2013: methods, subtleties, perspectives*, *Eur. Phys. J.* **C74** (2014) 3119 [1310.0799].

[83] LHCTopWG, "Standalone Summary Plots." https://twiki.cern.ch/twiki/bin/view/LHCPhysics/LHCTopWGSummaryPlots#Summary_Plots_in_Publications, 2019.

[84] ATLAS collaboration, *Measurement of lepton differential distributions and the top quark mass in $t\bar{t}$ production in pp collisions at $\sqrt{s} = 8$ TeV with the ATLAS detector*, *Eur. Phys. J.* **C77** (2017) 804 [1709.09407].

[85] CMS collaboration, *Measurement of $\mathrm{t\bar{t}}$ normalised multi-differential cross sections in pp collisions at $\sqrt{s} = 13$ TeV, and simultaneous determination of the strong coupling strength, top quark pole mass, and parton distribution functions*, *Submitted to: Eur. Phys. J.* (2019) [1904.05237].

[86] M. Jezabek and J. H. Kuhn, *The Top width: Theoretical update*, *Phys. Rev.* **D48** (1993) R1910 [hep-ph/9302295].

[87] M. Czakon, P. Fiedler and A. Mitov, *Resolving the Tevatron Top Quark Forward-Backward Asymmetry Puzzle: Fully Differential Next-to-Next-to-Leading-Order Calculation*, *Phys. Rev. Lett.* **115** (2015) 052001 [1411.3007].

[88] W. Bernreuther and Z.-G. Si, *Top quark and leptonic charge asymmetries for the Tevatron and LHC*, *Phys. Rev.* **D86** (2012) 034026 [1205.6580].

[89] ATLAS Collaboration collaboration, *Inclusive and differential measurement of the charge asymmetry in $t\bar{t}$ events at 13 TeV with the ATLAS detector*, Tech. Rep. ATLAS-CONF-2019-026, CERN, Geneva, Jul, 2019.

[90] ATLAS collaboration, *Measurement of the charge asymmetry in highly boosted top-quark pair production in $\sqrt{s} = 8$ TeV pp collision data collected by the ATLAS experiment*, 1512.06092.

[91] M. Perelló Roselló and M. Vos, *Constraints on four-fermion interactions from the $t\bar{t}$ charge asymmetry at hadron colliders*, *Eur. Phys. J.* **C76** (2016) 200 [1512.07542].

[92] S. Liebler, G. Moortgat-Pick and A. S. Papanastasiou, *Probing the top-quark width through ratios of resonance contributions of $e^+e^- \to W^+W^-b\bar{b}$*, *JHEP* **03** (2016) 099 [1511.02350].

[93] R. Frederix, D. Pagani and M. Zaro, *Large NLO corrections in $t\bar{t}W^{\pm}$ and $t\bar{t}t\bar{t}$ hadroproduction from supposedly subleading EW contributions*, *JHEP* **02** (2018) 031 [1711.02116].

[94] CMS collaboration, *Search for production of four top quarks in final states with same-sign or multiple leptons in proton-proton collisions at $\sqrt{s} = 13$ TeV*, 1908.06463.

[95] Q.-H. Cao, S.-L. Chen and Y. Liu, *Probing Higgs Width and Top Quark Yukawa Coupling from $t\bar{t}H$ and $t\bar{t}t\bar{t}$ Productions*, *Phys. Rev.* **D95** (2017) 053004 [1602.01934].

[96] Q.-H. Cao, S.-L. Chen, Y. Liu, R. Zhang and Y. Zhang, *Limiting top quark-Higgs boson interaction and Higgs-boson width from multitop productions*, *Phys. Rev.* **D99** (2019) 113003 [1901.04567].

[97] CMS collaboration, *Measurement of the $\mathrm{t\bar{t}b\bar{b}}$ production cross section in the all-jet final state in pp collisions at $\sqrt{s} = 13$ TeV*, 1909.05306.

[98] J. Fuster, I. García, P. Gomis, M. Perelló, E. Ros and M. Vos, *Study of single top production at high energy electron positron colliders*, *Eur. Phys. J.* **C75** (2015) 223 [1411.2355].

[99] J. Alwall, R. Frederix, S. Frixione, V. Hirschi, F. Maltoni, O. Mattelaer et al., *The automated computation of tree-level and next-to-leading order differential cross sections, and their matching to parton shower simulations*, *JHEP* **07** (2014) 079 [1405.0301].

[100] J. A. Aguilar-Saavedra, *A Minimal set of top anomalous couplings*, *Nucl. Phys.* **B812** (2009) 181 [0811.3842].

[101] J. A. Aguilar-Saavedra, *A Minimal set of top-Higgs anomalous couplings*, *Nucl. Phys.* **B821** (2009) 215 [0904.2387].

[102] J. A. Aguilar-Saavedra, *Effective four-fermion operators in top physics: A Roadmap*, *Nucl. Phys.* **B843** (2011) 638 [1008.3562].

[103] M. S. Amjad, M. Boronat, T. Frisson, I. Garcia, R. Poschl, E. Ros et al., *A precise determination of top quark electro-weak couplings at the ILC operating at* $\sqrt{s} = 500$ *GeV*, 1307.8102.

[104] M. S. Amjad et al., *A precise characterisation of the top quark electro-weak vertices at the ILC*, *Eur. Phys. J.* **C75** (2015) 512 [1505.06020].

[105] D. Barducci et al., *Interpreting top-quark LHC measurements in the standard-model effective field theory*, 1802.07237.

[106] G. Durieux, A. Irles, V. Miralles, A. Peñuelas, R. Pöschl, M. Perelló et al., *The electro-weak couplings of the top and bottom quarks - global fit and future prospects*, 1907.10619.

[107] W. Bernreuther, L. Chen, I. García, M. Perelló, R. Pöschl, F. Richard et al., *CP-violating top quark couplings at future linear* e^+e^- *colliders*, 1710.06737.

[108] A. Buckley, C. Englert, J. Ferrando, D. J. Miller, L. Moore, M. Russell et al., *Constraining top quark effective theory in the LHC Run II era*, *JHEP* **04** (2016) 015 [1512.03360].

[109] O. Bessidskaia Bylund, F. Maltoni, I. Tsinikos, E. Vryonidou and C. Zhang, *Probing top quark neutral couplings in the Standard Model Effective Field Theory at NLO in QCD*, *JHEP* **05** (2016) 052 [1601.08193].

[110] C. Englert and M. Russell, *Top quark electroweak couplings at future lepton colliders*, *Eur. Phys. J.* **C77** (2017) 535 [1704.01782].

[111] S. Bilokin, R. Pöschl and F. Richard, *Measurement of b quark EW couplings at ILC*, 1709.04289.

[112] C. Degrande, F. Maltoni, K. Mimasu, E. Vryonidou and C. Zhang, *Single-top associated production with a* Z *or* H *boson at the LHC: the SMEFT interpretation*, *JHEP* **10** (2018) 005 [1804.07773].

[113] J. Ellis, C. W. Murphy, V. Sanz and T. You, *Updated Global SMEFT Fit to Higgs, Diboson and Electroweak Data*, *JHEP* **06** (2018) 146 [1803.03252].

[114] N. P. Hartland, F. Maltoni, E. R. Nocera, J. Rojo, E. Slade, E. Vryonidou et al., *A Monte Carlo global analysis of the Standard Model Effective Field Theory: the top quark sector*, *JHEP* **04** (2019) 100 [1901.05965].

[115] I. Brivio, S. Bruggisser, F. Maltoni, R. Moutafis, T. Plehn, E. Vryonidou et al., *O new physics, where art thou? A global search in the top sector*, 1910.03606.

[116] S. Bilokin, A. Irles, R. Pöschl and F. Richard, *Measurement of b quark EW couplings at ILC250 with 2000* fb^{-1}, *In preparation* (2020) .

[117] C. Zhang and S. Willenbrock, *Effective-Field-Theory Approach to Top-Quark Production and Decay*, *Phys. Rev.* **D83** (2011) 034006 [1008.3869].

[118] A. Buckley, C. Englert, J. Ferrando, D. J. Miller, L. Moore, M. Russell et al., *Global fit of top quark effective theory to data*, *Phys. Rev.* **D92** (2015) 091501 [1506.08845].

[119] J. L. Birman, F. Déliot, M. C. N. Fiolhais, A. Onofre and C. M. Pease, *New limits on anomalous contributions to the Wtb vertex*, *Phys. Rev.* **D93** (2016) 113021 [1605.02679].

[120] C. Zhang, *Single Top Production at Next-to-Leading Order in the Standard Model Effective Field Theory*, *Phys. Rev. Lett.* **116** (2016) 162002 [1601.06163].

[121] J. A. Aguilar-Saavedra and J. Bernabeu, *W polarisation beyond helicity fractions in top quark decays*, *Nucl. Phys.* **B840** (2010) 349 [1005.5382].

[122] M. de Beurs, E. Laenen, M. Vreeswijk and E. Vryonidou, *Effective operators in t-channel single top production and decay*, *Eur. Phys. J.* **C78** (2018) 919 [1807.03576].

[123] E. Boos and V. Bunichev, *Symbolic expressions for fully differential single top quark production cross section and decay width of polarized top quark in presence of anomalous Wtb couplings*, 1910.00710.

[124] M. Schulze and Y. Soreq, *Pinning down electroweak dipole operators of the top quark*, *Eur. Phys. J.* **C76** (2016) 466 [1603.08911].

[125] S. M. Etesami, S. Khatibi and M. Mohammadi Najafabadi, *Study of top quark dipole interactions in $t\bar{t}$ production associated with two heavy gauge bosons at the LHC*, *Phys. Rev.* **D97** (2018) 075023 [1712.07184].

[126] K. Hagiwara, H. Yokoya and Y.-J. Zheng, *Probing the CP properties of top Yukawa coupling at an e^+e^- collider*, *JHEP* **02** (2018) 180 [1712.09953].

[127] S. Boselli, R. Hunter and A. Mitov, *Prospects for the determination of the top-quark Yukawa coupling at future e^+e^- colliders*, 1805.12027.

[128] A. Ferroglia, M. C. N. Fiolhais, E. Gouveia and A. Onofre, *The Role of the $t\bar{t}h$ Rest Frame in Direct Top-Quark Yukawa Coupling Measurements*, 1909.00490.

[129] D. A. Faroughy, J. F. Kamenik, N. Košnik and A. Smolkovič, *Probing the CP nature of the top quark Yukawa at hadron colliders*, 1909.00007.

[130] T. Barklow, K. Fujii, S. Jung, R. Karl, J. List, T. Ogawa et al., *Improved Formalism for Precision Higgs Coupling Fits*, *Phys. Rev.* **D97** (2018) 053003 [1708.08912].

[131] T. Barklow, K. Fujii, S. Jung, M. E. Peskin and J. Tian, *Model-Independent Determination of the Triple Higgs Coupling at e+e- Colliders*, *Phys. Rev.* **D97** (2018) 053004 [1708.09079].

[132] C. Degrande, J.-M. Gerard, C. Grojean, F. Maltoni and G. Servant, *Non-resonant New Physics in Top Pair Production at Hadron Colliders*, *JHEP* **03** (2011) 125 [1010.6304].

[133] J. A. Aguilar-Saavedra, B. Fuks and M. L. Mangano, *Pinning down top dipole moments with ultra-boosted tops*, *Phys. Rev.* **D91** (2015) 094021 [1412.6654].

[134] F. Maltoni, E. Vryonidou and C. Zhang, *Higgs production in association with a top-antitop pair in the Standard Model Effective Field Theory at NLO in QCD*, *JHEP* **10** (2016) 123 [1607.05330].

[135] C. Englert, K. Nordstrom, L. Moore and M. Russell, *Giving top quark effective operators a boost*, *Phys. Lett.* **B763** (2016) 9 [1607.04304].

[136] C. Englert, P. Galler and C. D. White, *Effective field theory and scalar extensions of the top quark sector*, 1908.05588.

[137] C. Zhang, *Constraining $qqtt$ operators from four-top production: a case for enhanced EFT sensitivity*, *Chin. Phys.* **C42** (2018) 023104 [1708.05928].

[138] W. Bernreuther, D. Heisler and Z.-G. Si, *A set of top quark spin correlation and polarization observables for the LHC: Standard Model predictions and new physics contributions*, *JHEP* **12** (2015) 026 [1508.05271].

[139] R. Patrick, A. Scaffidi and P. Sharma, *Top polarisation as a probe of CP-mixing top-Higgs coupling in tjh signals*, 1909.12772.

[140] K. Ma, *Enhancing CP Measurement of the Yukawa Interactions of Top-Quark at e^-e^+ Collider*, *Phys. Lett.* **B797** (2019) 134928 [1809.07127].

[141] G. Durieux, F. Maltoni and C. Zhang, *Global approach to top-quark flavor-changing interactions*, *Phys. Rev.* **D91** (2015) 074017 [1412.7166].

[142] M. Chala, J. Santiago and M. Spannowsky, *Constraining four-fermion operators using rare top decays*, *JHEP* **04** (2019) 014 [1809.09624].

[143] W. Liu and H. Sun, *Top FCNC interactions through dimension six four-fermion operators at the electron proton collider*, *Phys. Rev.* **D100** (2019) 015011 [1906.04884].

[144] Z. Hioki, K. Ohkuma and A. Uejima, *Correlations in flavor-changing tqZ couplings constrained via experimental data*, 1909.03383.

[145] H. Khanpour, *Probing top quark FCNC couplings in the triple-top signal at the high energy LHC and future circular collider*, 1909.03998.

[146] J. Alcaide, S. Banerjee, M. Chala and A. Titov, *Probes of the Standard Model effective field theory extended with a right-handed neutrino*, *JHEP* **08** (2019) 031 [1905.11375].

[147] L. Shi and C. Zhang, *Probing the top quark flavor-changing couplings at CEPC*, *Chin. Phys.* **C43** (2019) 113104 [1906.04573].

[148] I. Garcia Garcia, "Future Linear Colliders: Detector R&D, Jet Reconstruction and Top Physics Potential." https://cds.cern.ch/record/2239794, Nov, 2016.

[149] CLICdp collaboration, *Top-Quark Physics at the CLIC Electron-Positron Linear Collider*, 1807.02441.

[150] W. Kilian, T. Ohl and J. Reuter, *WHIZARD: Simulating Multi-Particle Processes at LHC and ILC*, *Eur. Phys. J.* **C71** (2011) 1742 [0708.4233].

[151] T. Sjostrand, S. Mrenna and P. Z. Skands, *PYTHIA 6.4 Physics and Manual*, *JHEP* **05** (2006) 026 [hep-ph/0603175].

[152] D. Schulte, "Beam-Beam Simulations with GUINEA-PIG." https://cds.cern.ch/record/382453, Mar, 1999.

[153] DESY, "ILCsoft." https://ilcsoft.desy.de/portal/, 2020.

[154] https://ilcsoft.desy.de/portal/software_packages/mokka/.

[155] https://ilcsoft.desy.de/portal/data_samples.

[156] https://twiki.cern.ch/twiki/bin/view/CLIC/MonteCarloSamplesForTopPhysics.

[157] https://ilcsoft.desy.de/portal/software_packages/marlin/.

[158] M. A. Thomson, *Particle Flow Calorimetry and the PandoraPFA Algorithm*, *Nucl. Instrum. Meth.* **A611** (2009) 25 [0907.3577].

[159] R. Walsh, *Flavour tag studies with the LCFIVertex package*, in *Linear colliders. Proceedings, International Linear Collider Workshop, LCWS08, and International Linear Collider Meeting, ILC08, Chicago, USA, Novermber 16-20, 2008*, 2009, 0901.4894.

[160] T. Suehara and T. Tanabe, *LCFIPlus: A Framework for Jet Analysis in Linear Collider Studies*, *Nucl. Instrum. Meth.* **A808** (2016) 109 [1506.08371].

[161] https://github.com/iLCSoft/MarlinReco/tree/master/Analysis/IsolatedLeptonFinder.

[162] S. Catani, Y. L. Dokshitzer, M. Olsson, G. Turnock and B. R. Webber, *New clustering algorithm for multi - jet cross-sections in e+ e- annihilation*, *Phys. Lett.* **B269** (1991) 432.

[163] S. Catani, Y. L. Dokshitzer, M. Seymour and B. Webber, *Longitudinally invariant K_t clustering algorithms for hadron hadron collisions*, *Nucl.Phys.* **B406** (1993) 187.

[164] M. Cacciari, G. P. Salam and G. Soyez, *FastJet User Manual*, *Eur.Phys.J.* **C72** (2012) 1896 [1111.6097].

[165] M. Boronat, J. Fuster, I. García, E. Ros and M. Vos, *A new jet reconstruction algorithm for lepton colliders*, *Nucl. Part. Phys. Proc.* **273-275** (2016) 2749.

[166] J. Aparisi, I. García, M. Perelló, P. Roloff, R. Simoniello and M. Vos, "Jet reconstruction algorithms in e^+e^- collisions." http://cds.cern.ch/record/2253123, Feb, 2017.

[167] C. Adolphsen, M. Barone, B. Barish, K. Buesser, P. Burrows, J. Carwardine et al., *The International Linear Collider Technical Design Report - Volume 3.I: Accelerator & in the Technical Design Phase*, 1306.6353.

[168] D. E. Kaplan, K. Rehermann, M. D. Schwartz and B. Tweedie, *Top Tagging: A Method for Identifying Boosted Hadronically Decaying Top Quarks*, *Phys. Rev. Lett.* **101** (2008) 142001.

[169] K. Agashe, A. Belyaev, T. Krupovnickas, G. Perez and J. Virzi, *LHC Signals from Warped Extra Dimensions*, *Phys. Rev.* **D77** (2008) 015003 [hep-ph/0612015].

[170] B. Lillie, L. Randall and L.-T. Wang, *The Bulk RS KK-gluon at the LHC*, *JHEP* **09** (2007) 074.

[171] M. Czakon, P. Fiedler and A. Mitov, *Total Top-Quark Pair-Production Cross Section at Hadron Colliders Through $O(\alpha_s^4)$*, *Phys. Rev. Lett.* **110** (2013) 252004 [1303.6254].

[172] CDF, D0 collaboration, *Combination of measurements of the top-quark pair production cross section from the Tevatron Collider*, *Phys. Rev.* **D89** (2014) 072001 [1309.7570].

[173] D0 collaboration, *Measurement of the forward-backward asymmetry in top quark-antiquark production in ppbar collisions using the lepton+jets channel*, *Phys. Rev.* **D90** (2014) 072011 [1405.0421].

[174] CDF collaboration, *Measurement of the top quark forward-backward production asymmetry and its dependence on event kinematic properties*, *Phys. Rev.* **D87** (2013) 092002 [1211.1003].

[175] CMS and ATLAS collaborations, *Combination of ATLAS and CMS top quark pair cross section measurements using proton-proton collisions at 8 TeV, CMS-PAS-TOP-14-016, ATLAS-CONF-2014-054*, http://cds.cern.ch/record/1951322 (2014) .

[176] ATLAS collaboration, *Measurement of the charge asymmetry in top-quark pair production in the lepton-plus-jets final state in pp collision data at $\sqrt{s} = 8$ TeV with the ATLAS detector*, 1509.02358.

[177] CMS collaboration, *Measurement of the Charge Asymmetry in Top Quark Pair Production in pp Collisions at $\sqrt{s}$ = 8 TeV using a Template Method*, 1508.03862.

[178] J. H. Kuhn and G. Rodrigo, *Charge asymmetries of top quarks at hadron colliders revisited*, *JHEP* **01** (2012) 063 [1109.6830].

[179] J. A. Aguilar-Saavedra, D. Amidei, A. Juste and M. Perez-Victoria, *Asymmetries in top quark pair production at hadron colliders*, *Rev. Mod. Phys.* **87** (2015) 421 [1406.1798].

[180] J. L. Hewett, J. Shelton, M. Spannowsky, T. M. P. Tait and M. Takeuchi, *A_{FB}^t Meets LHC*, *Phys. Rev.* **D84** (2011) 054005 [1103.4618].

[181] C. Degrande, C. Duhr, B. Fuks, D. Grellscheid, O. Mattelaer and T. Reiter, *UFO - The Universal FeynRules Output*, *Comput. Phys. Commun.* **183** (2012) 1201 [1108.2040].

[182] J. Alwall, M. Herquet, F. Maltoni, O. Mattelaer and T. Stelzer, *MadGraph 5 : Going Beyond*, *JHEP* **06** (2011) 128 [1106.0522].

[183] F. James and M. Winkler, "MINUIT User's Guide." http://seal.web.cern.ch/seal/documents/minuit/mnusersguide.pdf, June 16, 2014.

[184] P. Ferrario and G. Rodrigo, *Constraining heavy colored resonances from top-antitop quark events*, *Phys. Rev.* **D80** (2009) 051701 [0906.5541].

[185] ATLAS collaboration, *A search for $t\bar{t}$ resonances using lepton-plus-jets events in proton-proton collisions at $\sqrt{s} = 8$ TeV with the ATLAS detector*, *JHEP* **08** (2015) 148 [1505.07018].

[186] CMS collaboration, *Search for Resonant $\mathrm{t\bar{t}}$ Production in Proton-Proton Collisions at $\sqrt{s}$ = 8 TeV*, 1506.03062.

[187] CMS collaboration, *Search for narrow resonances decaying to dijets in proton-proton collisions at sqrt(s) = 13 TeV*, 1512.01224.

[188] M. Czakon, D. Heymes, A. Mitov, D. Pagani, I. Tsinikos and M. Zaro, *Top-quark charge asymmetry at the LHC and Tevatron through NNLO QCD and NLO EW*, *Phys. Rev.* **D98** (2018) 014003 [1711.03945].

[189] I. Brivio, Y. Jiang and M. Trott, *The SMEFTsim package, theory and tools*, *JHEP* **12** (2017) 070 [1709.06492].

[190] J. De Blas et al., *HEPfit: a Code for the Combination of Indirect and Direct Constraints on High Energy Physics Models*, 1910.14012.

[191] https://github.com/silvest/HEPfit/blob/master/NewPhysics/src/NPSMEFT6dtopquark.cpp.

[192] A. Caldwell, D. Kollar and K. Kroninger, *BAT: The Bayesian Analysis Toolkit*, *Comput. Phys. Commun.* **180** (2009) 2197 [0808.2552].

[193] O. Eberhardt, A. Peñuelas and A. Pich, *Global fits in the Aligned Two-Higgs-Doublet model*, *In preparation* (2020) .

[194] V. Miralles and A. Pich, *LHC bounds on colored scalars*, *Phys. Rev.* **D100** (2019) 115042 [1910.07947].

[195] J. de Blas, O. Eberhardt and C. Krause, *Current and Future Constraints on Higgs Couplings in the Nonlinear Effective Theory*, *JHEP* **07** (2018) 048 [1803.00939].

[196] M. Ciuchini, A. M. Coutinho, M. Fedele, E. Franco, A. Paul, L. Silvestrini et al., *New Physics in $b \to s\ell^+\ell^-$ confronts new data on Lepton Universality*, 1903.09632.

[197] F. James and M. Winkler, *MINUIT User's Guide*, *https://inspirehep.net/record/1258345* (2004) .

[198] ATLAS collaboration, *Observation of Higgs boson production in association with a top quark pair at the LHC with the ATLAS detector*, *Phys. Lett.* **B784** (2018) 173 [1806.00425].

[199] CMS collaboration, *Observation of $t\bar{t}H$ production*, *Phys. Rev. Lett.* **120** (2018) 231801 [1804.02610].

[200] ATLAS collaboration, *Measurement of the $t\bar{t}Z$ and $t\bar{t}W$ cross sections in proton-proton collisions at $\sqrt{s} = 13$ TeV with the ATLAS detector*, 1901.03584.

[201] CMS collaboration, *Measurement of top quark pair production in association with a Z boson in proton-proton collisions at $\sqrt{s} = 13$ TeV*, 1907.11270.

[202] ATLAS collaboration, *Measurements of inclusive and differential fiducial cross-sections of $t\bar{t}\gamma$ production in leptonic final states at $\sqrt{s} = 13$ TeV in ATLAS*, *Eur. Phys. J.* **C79** (2019) 382 [1812.01697].

[203] CMS collaboration, *Observation of Single Top Quark Production in Association with a Z Boson in Proton-Proton Collisions at $\sqrt{s}$ =13 TeV*, *Phys. Rev. Lett.* **122** (2019) 132003 [1812.05900].

[204] ATLAS collaboration, *Measurement of the production cross-section of a single top quark in association with a Z boson in proton?proton collisions at 13 TeV with the ATLAS detector*, *Phys. Lett.* **B780** (2018) 557 [1710.03659].

[205] A. Czarnecki, J. G. Korner and J. H. Piclum, *Helicity fractions of W bosons from top quark decays at NNLO in QCD*, *Phys. Rev.* **D81** (2010) 111503 [1005.2625].

[206] ATLAS collaboration, *Measurement of the W boson polarisation in $t\bar{t}$ events from pp collisions at $\sqrt{s}$ = 8 TeV in the lepton+jets channel with ATLAS*, 1612.02577.

[207] CMS collaboration, *Measurement of the W boson helicity fractions in the decays of top quark pairs to lepton + jets final states produced in pp collisions at $\sqrt{s} = 8$TeV*, *Phys. Lett.* **B762** (2016) 512 [1605.09047].

[208] CMS collaboration, *Measurement of the W-boson helicity in top-quark decays from $t\bar{t}$ production in lepton+jets events in pp collisions at $\sqrt{s} = 7$ TeV*, *JHEP* **10** (2013) 167 [1308.3879].

[209] ATLAS collaboration, *Measurement of the W boson polarization in top quark decays with the ATLAS detector*, *JHEP* **06** (2012) 088 [1205.2484].

[210] CMS collaboration, *Measurement of the single top quark and antiquark production cross sections in the t channel and their ratio in proton-proton collisions at $\sqrt{s} = 13$ TeV*, 1812.10514.

[211] ATLAS collaboration, *Measurement of the inclusive cross-sections of single top-quark and top-antiquark t-channel production in pp collisions at $\sqrt{s}$ = 13 TeV with the ATLAS detector*, *JHEP* **04** (2017) 086 [1609.03920].

[212] CMS collaboration, *Measurement of the production cross section for single top quarks in association with W bosons in proton-proton collisions at $\sqrt{s} = 13$ TeV*, *JHEP* **10** (2018) 117 [1805.07399].

[213] ATLAS collaboration, *Measurement of the cross-section for producing a W boson in association with a single top quark in pp collisions at $\sqrt{s} = 13$ TeV with ATLAS*, *JHEP* **01** (2018) 063 [1612.07231].

[214] ATLAS collaboration, *Measurement of differential production cross-sections for a Z boson in association with b-jets in 7 TeV proton-proton collisions with the ATLAS detector*, *JHEP* **10** (2014) 141 [1407.3643].

[215] CMS collaboration, *Measurement of the Z/γ*+b-jet cross section in pp collisions at $\sqrt{s}$ = 7 TeV*, *JHEP* **06** (2012) 126 [1204.1643].

[216] CMS collaboration, *Measurement of the associated production of a single top quark and a Z boson in pp collisions at $\sqrt{s} = 13$ TeV*, *Phys. Lett.* **B779** (2018) 358 [1712.02825].

[217] S. Dawson et al., *Working Group Report: Higgs Boson*, in *Community Summer Study 2013: Snowmass on the Mississippi (CSS2013) Minneapolis, MN, USA, July 29-August 6, 2013*, 2013, 1310.8361, http://inspirehep.net/record/1262795/files/arXiv:1310.8361.pdf.

[218] ATLAS, CMS collaboration, *Measurements of the Higgs boson production and decay rates and constraints on its couplings from a combined ATLAS and CMS analysis of the LHC pp collision data at $\sqrt{s} = 7$ and 8 TeV*, *JHEP* **08** (2016) 045 [1606.02266].

[219] ATLAS Collaboration collaboration, "Combined measurements of Higgs boson production and decay using up to 80 fb^{-1} of proton–proton collision data at $\sqrt{s} = 13$ TeV collected with the ATLAS experiment." http://cds.cern.ch/record/2668375, Mar, 2019.

[220] CMS collaboration, *Combined measurements of Higgs boson couplings in proton–proton collisions at $\sqrt{s} = 13$ TeV*, *Eur. Phys. J.* **C79** (2019) 421 [1809.10733].

[221] A. Azatov, C. Grojean, A. Paul and E. Salvioni, *Resolving gluon fusion loops at current and future hadron colliders*, *JHEP* **09** (2016) 123 [1608.00977].

[222] J. Brod, A. Greljo, E. Stamou and P. Uttayarat, *Probing anomalous $t\bar{t}Z$ interactions with rare meson decays*, *JHEP* **02** (2015) 141 [1408.0792].

[223] S. Bißmann, J. Erdmann, C. Grunwald, G. Hiller and K. Kröninger, *Constraining top-quark couplings combining top-quark and B decay observables*, 1909.13632.

[224] B. Grzadkowski and M. Misiak, *Anomalous Wtb coupling effects in the weak radiative B-meson decay*, *Phys. Rev.* **D78** (2008) 077501 [0802.1413].

[225] J. Drobnak, S. Fajfer and J. F. Kamenik, *Probing anomalous tWb interactions with rare B decays*, *Nucl. Phys.* **B855** (2012) 82 [1109.2357].

[226] P. J. Fox, Z. Ligeti, M. Papucci, G. Perez and M. D. Schwartz, *Deciphering top flavor violation at the LHC with B factories*, *Phys. Rev.* **D78** (2008) 054008 [0704.1482].

[227] J. Aebischer, A. Crivellin, M. Fael and C. Greub, *Matching of gauge invariant dimension-six operators for $b \to s$ and $b \to c$ transitions*, *JHEP* **05** (2016) 037 [1512.02830].

[228] F. Feruglio, P. Paradisi and O. Sumensari, *Implications of scalar and tensor explanations of $R_{D^{(*)}}$*, *JHEP* **11** (2018) 191 [1806.10155].

[229] M. Endo, T. Kitahara and D. Ueda, *SMEFT top-quark effects on $\Delta F = 2$ observables*, *JHEP* **07** (2019) 182 [1811.04961].

[230] N. Greiner, S. Willenbrock and C. Zhang, *Effective Field Theory for Nonstandard Top Quark Couplings*, *Phys. Lett.* **B704** (2011) 218 [1104.3122].

[231] C. Zhang, N. Greiner and S. Willenbrock, *Constraints on Non-standard Top Quark Couplings*, *Phys. Rev.* **D86** (2012) 014024 [1201.6670].

[232] E. Vryonidou and C. Zhang, *Dimension-six electroweak top-loop effects in Higgs production and decay*, *JHEP* **08** (2018) 036 [1804.09766].

[233] G. Durieux, J. Gu, E. Vryonidou and C. Zhang, *Probing top-quark couplings indirectly at Higgs factories*, *Chin. Phys.* **C42** (2018) 123107 [1809.03520].

[234] V. Cirigliano, W. Dekens, J. de Vries and E. Mereghetti, *Constraining the top-Higgs sector of the Standard Model Effective Field Theory*, *Phys. Rev.* **D94** (2016) 034031 [1605.04311].

[235] C. R. Schmidt, *Top quark production and decay at next-to-leading order in e+ e- annihilation*, *Phys. Rev.* **D54** (1996) 3250 [hep-ph/9504434].

[236] S. J. Parke and Y. Shadmi, *Spin correlations in top quark pair production at e^+e^- colliders*, *Phys. Lett.* **B387** (1996) 199 [hep-ph/9606419].

[237] W. Bernreuther and P. Overmann, *Probing Higgs boson and supersymmetry induced CP violation in top quark production by (un)polarized electron - positron collisions*, *Z. Phys.* **C72** (1996) 461 [hep-ph/9511256].

[238] T. G. Rizzo, *Anomalous chromoelectric and chromomagnetic moments of the top quark at the NLC*, in *1996 DPF / DPB Summer Study On New Directions For High-Energy Physics: Proceedings, Snowmass 1996*, 1996, hep-ph/9605361, http://www-public.slac.stanford.edu/sciDoc/docMeta.aspx?slacPubNumber=SLAC-PUB-7154.

[239] P. Batra and T. M. P. Tait, *Measuring the W-t-b Interaction at the ILC*, *Phys. Rev.* **D74** (2006) 054021 [hep-ph/0606068].

[240] M. Martinez and R. Miquel, *Multiparameter fits to the t anti-t threshold observables at a future e^+e^- linear collider*, *Eur. Phys. J.* **C27** (2003) 49 [hep-ph/0207315].

[241] T. Horiguchi, A. Ishikawa, T. Suehara, K. Fujii, Y. Sumino, Y. Kiyo et al., *Study of top quark pair production near threshold at the ILC*, 1310.0563.

[242] Q.-H. Cao and B. Yan, *Determining V_{tb} at Electron-Positron Colliders*, 1507.06204.

[243] D. Atwood and A. Soni, *Analysis for magnetic moment and electric dipole moment form-factors of the top quark via $e^+e^- \to t\bar{t}$*, *Phys. Rev.* **D45** (1992) 2405.

[244] M. Diehl and O. Nachtmann, *Optimal observables for the measurement of three gauge boson couplings in $e^+e^- \to W^+W^-$*, *Z. Phys.* **C62** (1994) 397.

[245] CLIC, CLICdp collaboration, *Updated baseline for a staged Compact Linear Collider*, 1608.07537.

[246] G. Durieux, C. Grojean, J. Gu and K. Wang, *The leptonic future of the Higgs*, *JHEP* **09** (2017) 014 [1704.02333].

[247] G. Apollinari, I. Béjar Alonso, O. Brüning, P. Fessia, M. Lamont, L. Rossi et al., *High-Luminosity Large Hadron Collider (HL-LHC)*, *CERN Yellow Rep. Monogr.* **4** (2017) 1.

[248] HL-LHC, HE-LHC Working Group collaboration, *Standard Model Physics at the HL-LHC and HE-LHC*, 1902.04070.

[249] Physics of the HL-LHC Working Group collaboration, *Higgs Physics at the HL-LHC and HE-LHC*, 1902.00134.

[250] CMS collaboration, *Observation of single top quark production in association with a Z boson in proton-proton collisions at $\sqrt{s} = 13$ TeV*, .

[251] R. Röntsch and M. Schulze, *Constraining couplings of top quarks to the Z boson in $t\bar{t}$ + Z production at the LHC*, *JHEP* **07** (2014) 091 [1404.1005].

[252] T. Price, P. Roloff, J. Strube and T. Tanabe, *Full simulation study of the top Yukawa coupling at the ILC at $\sqrt{s} = 1$ TeV*, *Eur. Phys. J.* **C75** (2015) 309 [1409.7157].

[253] R. Yonamine, K. Ikematsu, T. Tanabe, K. Fujii, Y. Kiyo, Y. Sumino et al., *Measuring the top Yukawa coupling at the ILC at $\sqrt{s} = 500$ GeV*, *Phys. Rev.* **D84** (2011) 014033 [1104.5132].

[254] A. Gay, *Measurement of the top-Higgs Yukawa coupling at a Linear e+ e- Collider*, *Eur. Phys. J.* **C49** (2007) 489 [hep-ph/0604034].

[255] A. Juste and G. Merino, *Top Higgs-Yukawa coupling measurement at a linear e^+e^- collider*, hep-ph/9910301.

[256] K. Fujii et al., *Physics Case for the International Linear Collider*, 1506.05992.

[257] B. C. Nejad, W. Kilian, J. M. Lindert, S. Pozzorini, J. Reuter and C. Weiss, *NLO QCD Predictions for off-shell $t\bar{t}$ and $t\bar{t}H$ Production and Decay at a Linear Collider*, 1609.03390.

[258] J. De Blas et al., *Higgs Boson Studies at Future Particle Colliders*, 1905.03764.

[259] A. Falkowski and F. Riva, *Model-independent precision constraints on dimension-6 operators*, *JHEP* **02** (2015) 039 [1411.0669].

[260] A. Falkowski, M. Gonzalez-Alonso, A. Greljo, D. Marzocca and M. Son, *Anomalous Triple Gauge Couplings in the Effective Field Theory Approach at the LHC*, *JHEP* **02** (2017) 115 [1609.06312].

[261] S. Jung, J. Lee, M. Perello, J. Tian and M. Vos, *Higgs and top precision at future e^+e^- colliders with renormalization group mixing, in preparation* (2019) .

Resum

El Model Estàndard. El progrés científic de l'inici del segle XX va canviar completament el paradigma de la física fonamental amb el descobriment dels electrons per J.J. Thomson, la quantització de l'energia per M. Planck i la postulació de l'efecte fotoelèctric i el fotó per A. Einstein.

Avui sabem que l'àtom està compost per partícules fonamentals, les interaccions de les quals està més enllà del que la gravetat i electromagnetisme clàssics poden explicar. Va ser necessari el desenvolupament de noves teories quàntiques per a explicar aquestes interaccions.

L'electrodinàmica quàntica (QED per les seues sigles en anglés) és el resultat d'unir l'electromagnetisme clàssic amb la teoria quàntica que explica la interacció entre el fotó i l'electró. Dues noves interaccions sorgeixen per a explicar el nucli atòmic i la radiació observada en alguns isòtops: la força nuclear forta (QCD per les seues sigles en anglés) i la força nuclear dèbil respectivament.

La unió de les noves interaccions i totes les partícules fonamentals s'anomena Model Estàndard. Aquest model ofereix la millor i més simple descripció de les partícules fonamentals que formen la matèria i les seues interaccions.

Les partícules responsables de mediar les interaccions s'anomenen bosons, partícules d'espín enter, i són: el fotó per a la interacció QED, el gluó per a QCD, els bosons W i Z per a la teoria electrodèbil, que naix d'unificar QED amb la força nuclear dèbil, i el recentment descobert bosó de Higgs que dona explicació sobre l'origen de la massa de les partícules. La gravitació no forma part del Model Estàndard, ja que no s'ha aconseguit desenvolupar una teoria quàntica de camps per a descriure-la.

Per altra banda, les partícules constituents de la matèria s'anomenen fermions, els quals són partícules d'espín 1/2. A cause de l'espín, els fermions poden tindre dues quiralitats: dextrogira i levogira. Hi ha dos tipus de fermions: els quarks, i els leptons, dels quals l'electró és la partícula més coneguda. Els quarks formen partícules compostes anomenades hadrons. Hi ha de dos tipus, els mesons, formats per un quark i un antiquark, i els barions, formats per tres quarks o tres antiquarks. Els barions més coneguts són el protó (format per dos quarks amunt i un avall) i el neutró (format per dos quarks avall i un amunt), els quals formen el nucli atòmic. Tant els quarks com els leptons s'organitzen en tres famílies:

$$\text{I}: \begin{bmatrix} \nu_e & u \\ e^- & d \end{bmatrix}, \quad \text{II}: \begin{bmatrix} \nu_\mu & c \\ \mu^- & s \end{bmatrix}, \quad \text{III}: \begin{bmatrix} \nu_\tau & t \\ \tau^- & b \end{bmatrix}.$$

En la Taula 1 trobem la massa i la càrrega elèctrica de totes les partícules fonamentals. Cada partícula tindria la seua corresponent antipartícula amb la càrrega oposada i mateixa massa.

		Massa[GeV]	Càrrega Q[e]
Bosons	fotó, γ	$< 1 \times 10^{-27}$	$< 1 \times 10^{-35}$
	gluó, g	0	0
	$W^{\pm}$	80.379 ± 0.012	± 1
	Z	91.1876 ± 0.0021	0
	higgs, H	125.18 ± 0.16	0
		Massa[MeV]	Càrrega Q[e]
Leptons	electró, e	$0.5109989461 \pm 0.0000000031$	-1
	neutrí electrònic, ν_e	-	0
	muó, μ	$105.6583745 \pm 0.0000024$	-1
	neutrí muònic, ν_μ	-	0
	tau, τ	1776.86 ± 0.12	-1
	neutrí taònic, ν_τ	-	0
		Massa[GeV]	Càrrega Q[e]
Quarks	avall, d	$\left(4.7^{+0.5}_{-0.3}\right) \cdot 10^{-3}$	-1/3
	amunt, u	$\left(2.2^{+0.5}_{-0.4}\right) \cdot 10^{-3}$	2/3
	estrany, s	$\left(95^{+9}_{-3}\right) \cdot 10^{-3}$	-1/3
	encant, c	$1.275^{+0.025}_{-0.035}$	2/3
	fons, b	$4.18^{+0.04}_{-0.03}$	-1/3
	cim, t	173.0 ± 0.4	2/3

Taula Resum 1: Propietats de les partícules fonamentals descrites pel Model Estàndard.

Propietats de les interaccions del Model Estàndard. El Model Estàndard és una teoria gauge quàntica de camps relativista basada en la simetria de grup $SU(3)_C \otimes SU(2)_L \otimes U(1)_Y$ que descriu la força nuclear forta, la dèbil i l'electromagnetisme. Aquesta simetria gauge es trenca a través de l'anomenat trencament espontani de simetria, donant lloc al mecanisme de Higgs i al corresponent bosó de Higgs, el qual donen explicació a l'origen de les masses de les partícules fonamentals.

Cada interacció del Model Estàndard està representada per diferents nombres quàntics:

- QED té la propietat de la càrrega elèctrica, Q, mediada pel fotó. Quan s'unifica amb la dèbil, es redefineix la càrrega elèctrica com a hipercàrrega, $Y = Q - T_3$, on T_3 és la matriu de Pauli present en la transformació $SU(2)_L$. La simetria és aleshores $U(1)_Y$.

- La interacció dèbil es va observar experimentalment que sols afectava els fermions levogirs o als antifermions dextrogirs, mentre que els fermions dextrogirs i els antifermions levogirs no la sentien. La simetria sota la qual es transforma és $SU(2)_L$. La teoria electrodèbil naix d'unificar la interacció dèbil amb QED, d'aquesta unificació naixen els dos bosons W i el bosó Z, i es conserva el fotó. Així, en aquesta teoria els fermions levogirs s'organitzen en doblets els quals interaccionen amb els bosons, mentre que els dextrogirs són singlets.

  Quan són els bosons W els que medien la interacció, obtenim els corrents carregats, ja que els bosons W tenen càrrega ± 1. Si són el bosó Z o el fotó els mediadors, tenim corrents neutres.

- QCD té la propietat de color, C, la qual sols posseeixen els quarks, però no els leptons. Açò significa que els gluons sols interaccionen amb els quarks. La simetria QCD és per tant $SU(3)_C$. La interacció QCD té dues propietats importants: confinament i la llibertat asimptòtica. El confinament ens diu que a baixes energies la força augmenta, el que fa als quarks estar junts, el que permet la creació dels nuclis. Per altra banda la llibertat asimptòtica ens diu que per a energies altes, els quarks es comporten com si foren lliures, permetent el càlcul de processos com si els quarks foren independents.

- El mecanisme de Higgs prediu una massa per als bosons gauge W i Z i per al mateix bosó de Higgs, així com prediu que el fotó i el gluó no tenen massa. A més, incorpora al lagrangià del Model Estàndard els termes anomenats Yukawa, els quals donen explicació a la massa dels fermions. Aquestes masses, no obstant, són paràmetres lliures que no prediu el Model Estàndard i han de ser determinats experimentalment.

Teoria Efectiva de Camps. Encara que el Model Estàndard descriu les partícules fonamentals i les seues interaccions amb molta precisió, hi ha evidències de què encara no és una teoria completa. Per exemple no inclou la gravitació com a una teoria quàntica de camps, ni dona una explicació clara sobre de què està constituïda la matèria fosca. A més els col·lisionadors de partícules han mesurat xicotetes desviacions respecte a les prediccions del Model Estàndard. Tot açò, conjuntament amb el desig d'una gran teoria d'unificació que unifique totes les interaccions en una sola, han portat als físics a treballar en diferents models més enllà del Model Estàndard.

Les Teories Efectives de Camps (EFT per les seues sigles en anglés) són àmpliament utilitzades en física d'altes energies per a parametritzar els efectes desconeguts de nova física a baixes energies. La idea bàsica és calcular la fenomenologia de la teoria més completa sense saber la teoria exacta que està darrere del Model Estàndard. Açò s'aconsegueix expandint sistemàticament el Model Estàndard amb tots els operadors que són compatibles amb l'estructura i simetries del Model Estàndard.

Així, el lagrangià d'una teoria efectiva de camps és una expansió dimensional de tots els operadors que podem construir amb simetries del Model Estàndard:

$$\mathcal{L}_{\text{EFT}} = \sum_{\mathcal{D}\geq 0,i} \frac{c_i^{(\mathcal{D})} O_i^{(\mathcal{D})}}{\Lambda^{\mathcal{D}-4}} = \sum_{\mathcal{D}\geq 0} \frac{\mathcal{L}_{\mathcal{D}}}{\Lambda^{\mathcal{D}-4}},$$

on $O_i^{(\mathcal{D})}$ són els operadors permesos de dimensió $\mathcal{D}$. Per a $D = 4$ obtenim el lagrangià del Model Estàndard. L'escala d'energia Λ ha sigut introduïda perquè els coeficients $c_i^{(\mathcal{D})}$ (anomenats coeficients de Wilson) siguen adimensionals.

A partir d'aquest lagrangià es poden construir els observables que descriuen la interacció que volem estudiar. En aquesta tesi estem interessats en els operadors que descriuen les interaccions del quark cim. Per a tal estudi tallarem l'expansió dimensional en els operadors de dimensió sis, amb la qual cosa els nostres observables tindran la forma:

$$o = o_{SM} + \frac{1}{\Lambda^2} \sum_i C_i o_i + \frac{1}{\Lambda^4} \sum_j \sum_k C_j C_k o_{jk} + \mathcal{O}(\Lambda^{-4}).$$

El terme proporcional a Λ^{-2} descriu la interferència del Model Estàndard amb els operadors de dimensió sis. Els termes proporcionals a Λ^{-4} provenen de l'amplitud al quadrat dels operadors de dimensió sis. Si haguérem considerat operadors de dimensió huit, aquests també contribuirien al terme Λ^{-4}, però aquests són ignorats als nostres estudis.

Col·lisionadors de partícules: passat, present i futur. Va ser a partir de 1960 quan van començar a desenvolupar-se els acceleradors de partícules. Aquests permeten accelerar feixos de partícules, electrons o protons, a grans energies per a després fer-les col·lidir contra altre feix de partícules. Trobem acceleradors de dos tipus: hadrònics, quan col·lideixen protons, o col·lisionadors electró-positró, els quals fan col·lidir electrons contra les seues antipartícules, els positrons.

Els col·lisionadors han evolucionat al llarg de la història augmentant l'energia de col·lisió de les partícules per a poder crear i estudiar cada vegada partícules amb masses més grans. En aquesta tesi ens centrem en els últims quatre acceleradors: el col·lisionador lineal d'Stanford (SLC), el Gran col·lisionador electró-positró (LEP), el Tevatró i el Gran col·lisionador d'Hadrons (LHC) al CERN.

La teoria electrodèbil va ser extensament provada als acceleradors electró-positró SLC i LEP. En aquests acceleradors els feixos s'acceleraven fins a una energia en centre de masses igual a la massa del bosó Z. Així, el bosó Z es va produir en grans quantitats de forma que les seues propietats van ser determinades amb gran precisió.

Al Tevatró es feien col·lidir protons contra antiprotons a energies en centre de masses de 1.8 i 1.96 TeV. En 1995 al Tevatró es va descobrir el quark cim. Per últim l'LHC és l'accelerador de partícules més gran mai construït. Fa col·lidir protons contra protons a energies en centre de masses de 7 i 8 TeV en la seua primera fase, i 13 i 14 TeV en la segona. Dos grans experiments, ATLAS i CMS, són els encarregats de detectar les partícules. En el 2012 es va descobrir el bosó de Higgs, última peça per descobrir del Model Estàndard.

Encara que l'LHC té un programa científic per als anys vinents, augmentant la seua lluminositat en el que s'anomena programa HL-LHC, hi ha certes propietats del bosó de Higgs i del quark cim que no són mesurades adequadament en un accelerador d'hadrons. Com que són les partícules amb més

massa, s'espera que tant el quark cim com el bosó de Higgs tinguen papers importants en models de nova física més enllà del Model Estàndard a través d'acoblaments a noves possibles partícules. És per això que existeixen projectes de futurs acceleradors pensats per a mesures de precisió de les propietats d'aquestes dues partícules.

Els projectes més avançats són el col·lisionador lineal internacional (ILC) al Japó i el col·lisionador lineal compacte (CLIC) al CERN. Aquests farien col·lidir electrons contra positrons a energies en centre de massa de 250, 500 i 1000 GeV en el cas de l'ILC i 380, 1400 i 3000 GeV en el cas de CLIC. A més, els dos col·lisionadors tenen la possibilitat de polaritzar els feixos de partícules en dues configuracions diferents: $P(e^+, e^-) = (\mp 30\%, \pm 80\%)$ per a l'ILC i $P(e^+, e^-) = (0, \pm 80\%)$ per a CLIC.

Hi ha altres futurs projectes d'acceleradors circulars electró-positró, com són Futur Col·lisionador Circular (FCCee) al CERN i el Col·lisionador Circular electró-positró a la Xina. No obstant en aquesta tesi ens centrem més en l'estudi de l'ILC i de CLIC.

El Quark Cim. El quark cim és la partícula fonamental coneguda més pesada. Va ser descoberta al col·lisionador Tevatró pels experiments CDF i D0 en 1995. El quark cim té càrrega elèctrica $Q_t = 2/3$ i com tots els fermions té espín 1/2. Forma doblet $SU(2)_L$ amb el quark fons. Al ser la partícula amb més massa del Model Estàndard, s'espera que tinga un paper important en teories de nova física més enllà del Model Estàndard. Si existeixen partícules amb més massa que el quark cim que no coneguem, s'espera que aquestes interaccionen amb el quark cim, de forma que conéixer les propietats del quark cim amb gran precisió és necessari.

El quark cim es produeix típicament per parells cim-anticim (anomenarem a aquest procés creació de parells cim), però també es pot produir amb un únic quark cim a través de diferents canals (anomenarem a aquest procés cim individual).

El quark cim decau a un bosó W i a un quark fons. Al mateix temps el bosó W pot decaure a un leptó i el seu corresponent neutrí o a dos quarks. En un estat final $t\bar{t}$ tindrem les següents configuracions possibles depenent del decaïment del bosó W:

$$\begin{aligned} \text{totalment hadrònic} \quad & t\bar{t} \to b\bar{b}q\bar{q}'q''\bar{q}''' && 45.7\% \\ \text{semileptònic} \quad & t\bar{t} \to b\bar{b}q\bar{q}'l^-\bar{\nu}_l + b\bar{b}q''\bar{q}'''l^+\nu_l && 43.8\% \\ \text{totalment leptònic} \quad & t\bar{t} \to b\bar{b}l^-\bar{\nu}_l l^{+'}\nu_{l'} && 10.5\%, \end{aligned}$$

on el nombre entre parèntesis representa la probabilitat de cada canal.

El quark cim mai ha sigut produït en col·lisionadors electró-positró, per tant els projectes futurs ILC i CLIC són una gran oportunitat per a estudiar les seues propietats electrodèbils. Més en concret, en aquesta tesi ens centrarem a estudiar els acoblaments del quark cim a través d'operadors efectius de dimensió sis. Per tal objectiu treballarem de dues formes:

- Interpretant mesures existents dels col·lisionadors SLC, LEP i l'LHC en termes d'aquests operadors efectius. Amb aquest estudi obtindrem unes cotes per als operadors efectius.
- Simulant futures mesures accessibles als col·lisionadors ILC i CLIC i interpretar-les en funció dels operadors efectius. Així podrem veure com milloren les cotes que obtenim per als operadors respecte als resultats existents.

Com estem interpretant els acoblaments del quark cim en funció d'una teoria efectiva, esperem que els resultats que obtinguem per a les cotes dels operadors siguen compatibles amb 0, el que significaria que les mesures són compatibles amb el Model Estàndard. Desviacions respecte de 0 significaria desviacions respecte del Model Estàndard, i podrien ser indicis de nova física.

Els operadors efectius que defineixes els acoblaments del quark cim són els següents:

- **Operadors de dos quarks.** Són operadors que medien la interacció del quark cim amb altre quark (que potser el quark fons o altre cim) amb un bosó. La llista d'operadors és: $O^1_{\varphi Q}$, $O^3_{\varphi Q}$, $O_{\varphi t}$ i $O_{\varphi b}$, que modifiquen els acoblaments levogirs i dextrogirs dels quarks cim i fons; $O_{\varphi tb}$, que modifica el corrent carregat d'interacció entre el quark cim i el fons; O_{tW}, O_{bW}, O_{tB} i O_{bB}, els quals representen els dipols electrodèbils dels quarks cim i fons; i finalment $O_{t\varphi}$, que representa el Yukawa del quark cim, és a dir, el terme que defineix la interacció del quark cim amb el bosó de Higgs per a generar la massa del quark cim.

  En aquesta llista no incloguem la interacció del quark cim amb gluons. A més, hem inclòs operadors que afecten el quark fons, ja que al ser el company de doblet del quark cim per a la simetria $SU(2)_L$, estan altament correlacionats.

  Aquests operadors s'estudien molt bé a col·lisionadors electró-positró, ja que el procés de producció de quarks cims és $e^+e^- \to Z/\gamma \to t\bar{t}$. Per tant l'acoblament dels quarks cim amb els bosons Z i fotó es poden estudiar directament al vèrtex de producció. A col·lisionadors hadrònics, com l'LHC, també es poden estudiar aquests operadors a través de producció associada, $p \to g \to t\bar{t} + X$, on $X = Z, \gamma, W, H$. Aquests processos són més difícils de veure a l'LHC. No obstant, a la seua segona fase, corrent a una energia de 13 TeV en centre de masses, s'ha aconseguit mesurar aquests processos amb una precisió suficient per a poder ficar cotes als operadors de dos quarks.

- **Operadors de quatre quarks.** Són operadors que descriuen les interaccions de contacte de quatre quarks (dos quarks lleugers amb dos quarks cim) sense un bosó mediador. Aquests són: $O^{(8,1)}_{qq}$, $O^{(8,3)}_{qq}$, $O^{(8)}_{ut}$, $O^{(8)}_{dt}$, $O^{(1)}_{qu}$, $O^{(1)}_{qd}$ i $O^{(1)}_{qt}$.

  Aquests operadors s'estudien molt bé en col·lisionadors hadrònics, ja que els protons que col·lideixen estan formats per quarks i per tant es donen processos del tipus $u/d\bar{u}/\bar{d} \to t\bar{t}$.

- **Operadors de dos quarks i dos leptons.** Són operadors que descriuen les interaccions de contacte de dos leptons (electró i positró) amb dos quarks (dos quarks cim o dos fons). Aquests són: O^1_{lq}, O^3_{lq}, O_{lu}, O_{ld}, O_{eq}, O_{eu}, O_{ed}.

  Aquests operadors s'estudien molt bé a col·lisionadors electró-positró a través del procés $e^+e^- \to t\bar{t}$. Una diferència entre aquests operadors és la quiralitat dels quarks i leptons. Alguns d'ells són més sensibles quan els leptons són levogirs, i altres quan són dextrogirs. Per això que els feixos es puguen polaritzar a l'ILC i CLIC jugarà un paper molt important a l'hora de ficar cotes sobres aquests operadors.

Simulació i reconstrucció d'esdeveniments basats en els acceleradors ILC i CLIC. Les perspectives que volem obtindre per als operadors del quark cim estan basades en simulacions completes dels futurs

col·lisionadors ILC i CLIC. Per tal objectiu s'utilitzen programes que inclouen tot el procés que ocorre a un col·lisionador de partícules: la col·lisió, la posterior creació de partícules, l'hadronització (quan els quarks es confinen en hadrons) i pluja de partícules a les diferents capes dels detectors i la resposta dels mateixos detectors al pas de les partícules. Aquesta simulació completa permet predir el comportament exacte dels futurs acceleradors, i per tant ens permet reconstruir esdeveniments i estudiar-los com si de processos reals es tractaren. Per a tal objectiu es disposa d'un programa especialitzat inclòs en la interfície `ILCsoft`.

Quan en una col·lisió es produeixen quarks, aquestes hadronitzen pel confinament present a la interacció QCD. A més les partícules creades poden decaure o radiar altres partícules que a la vegada podran tornar a hadronitzar. Per a reconstruir tot aquest procés totes aquestes partícules creades s'uneixen en el que s'anomena un doll de partícules. Cada doll provindrà d'una partícula mare d'on ha començat tot el procés. Per a reconstruir aquests dolls s'empren algoritmes de reconstrucció, els quals han anat evolucionant depenent de les energies i tipus de col·lisionadors en els quals es treballava. Nosaltres utilitzarem per a la reconstrucció de dolls l'algoritme VLC, optimitzat per a futurs col·lisionadors electró-positró amb un gran fons $\gamma\gamma \rightarrow$ hadrons.

El nostre senyal que volem estudiar i reconstruir és $e^+e^- \rightarrow t\bar{t}$ per a ILC a $\sqrt{s} = 500$ GeV (ILC500) i CLIC per a $\sqrt{s} = 380$ (CLIC380), $\sqrt{s} = 1.5$ TeV (CLICl500) i $\sqrt{s} = 3$ TeV (CLIC3000). Les eines de reconstrucció seran diferents depenent de l'energia en centre de masses. Per a 1.4 i 3 TeV ens trobem a una topologia on els quarks cim es produeixen a una energia molt alta, per tant les tècniques de reconstrucció seran diferents que per a 380 i 500 GeV on l'energia de producció dels quarks és més baixa.

Per a reconstruir el senyal, utilitzarem mostres de simulació completa on es produeix $e^+e^- \rightarrow$ 6 fermions on alguns dels esdeveniments vindran del decaïment de dos quarks cim, però altres provindran d'altres estats. Aquests últims s'anomenen fons, i hem d'eliminar-lo per a reconstruir el nostre senyal. A més, exigirem que l'estat final corresponga a un estat semileptònic, és a dir, un dels bosons W decaurà a leptons i l'altre a quarks. El procés serà el següent:

- Per a CLIC380 i ILC500 utilitzarem l'algoritme de reconstrucció per a reconstruir quatre dolls. Dos d'aquests dolls hauran de provindre dels quarks fons originats del decaïment del cim. Per tant exigirem que dos dels dolls reconstruïts passen per un algoritme d'etiquetatge de quarks fons. Els altres dos dolls vindran dels quarks del decaïment d'un dels bosons W. Per últim utilitzarem un algoritme per a trobar un leptó, que vindrà del bosó W que decau a leptons.

  Una vegada identificats els quatre dolls i el leptó, emparellem un dels dolls del quark fons amb els dos dolls que venen del W, així haurem reconstruït el quark cim que decau hadrònicament. Aquest pas pot donar lloc a migracions degudes a un emparellament erroni dels dolls. Per a corregir-ho s'apliquen talls cinemàtics més estrictes. Per últim identificarem que el quark cim reconstruït és un cim o un anticim identificant la càrrega del leptó.

- Per a CLICl500 i CLIC3000 s'ha desenvolupat una tècnica anomenada etiquetadora de quarks cim. Consisteix a reconstruir dos dolls grans, un que serà el quark que ha decaigut hadrònicament, i l'altre el que ha decaigut leptònicament. Una vegada reconstruït els dolls grans, s'identifiquen els

$\sqrt{s}$ [GeV]	380		500	1000	1400		3000	
Pol(e^-, e^+)	-0	$+0$	$-+$ $+-$	$-+$ $+-$	-0	$+0$	-0	$+0$
secció eficaç	12.9	12.1	10.0	6.0	6.0	5.8	4.6	4.7
A^{FB}	4.7	12.1	10.0	6.0	6.0	5.8	4.6	4.7
Obs. Estad. Òptims	7.8	12.1	10.0	6.0	6.0	5.8	4.6	4.7

Taula Resum 2: Fraccions equivalents de la taxa teòrica de producció del procés teòric $e^+e^- \to t\bar{t}$ per a diferents energies en centre de massa. Aquests nombres són utilitzats posteriorment en l'ajust global dels operadors efectius del quark cim. Quan multipliquem aquests nombres per la secció eficaç inclusiva del procés $e^+e^- \to t\bar{t}$ obtenim el nombre d'esdeveniments finals estudiats en simulació completa.

components que formen el doll. Per exemple, per al quark hadrònic, es buscarà dins del doll un bosó W que haja decaigut a dos quarks lleugers, i un quark fons. El procés de reconstrucció i optimització en aquest cas s'ha fet amb algoritmes d'aprenentatge automàtic.

Aquests mètodes ens donen una eficiència de reconstrucció que podem aplicar als nostres estudis per a reproduir les incerteses que tindrien els nostres observables en els futurs col·lisionadors. En la Taula 2 es mostra un resum de les eficiències obtingudes per a diferents observables que interpretarem en funció dels operadors efectius del quark cim. Els observables són:

- secció eficaç de producció del procés $e^+e^- \to t\bar{t}$ per a cada energia i polarització del feix.
- asimetria avant-arrere. Es calcula com

$$A^{\text{FB}} = \frac{N(\theta_t > 0) - N(\theta_t < 0)}{N(\theta_t > 0) + N(\theta_t < 0)},$$

  on θ_t és l'angle polar del quark cim.
- Els Observables Estadísticament Òptims (OEOs). Estan construïts per a utilitzar tota la informació diferencial disponible en el procés $e^+e^- \to t\bar{t} \to W^+bW^-\bar{b}$ i extraure les millors cotes possibles sobre els operadors del quark cim.

A més, s'han utilitzat dades existents per a la reconstrucció d'estats finals $b\bar{b}$ per a una energia en centre de masses de 250 GeV.

Ajust dels operadors de quatre quarks utilitzant dades del Tevatró i de l'LHC. La producció de pars de quarks cim en col·lisionadors hadrònics permet fer un ajust global als operadors de quatre quarks i així ficar cotes sobre els coeficients de Wilson. Les mesures utilitzades a l'ajust es mostren en la Taula 3.

Analitzant les sensibilitats relatives de la mesura de producció de pars al Tevatró i a l'LHC trobem que la secció eficaç i l'asimetria de càrrega, definida com

$$A_C^{t\bar{t}} = \frac{N(\Delta|y| > 0) - N(\Delta|y| < 0)}{N(\Delta|y| > 0) + N(\Delta|y| < 0)}.$$

	Predicció	Mesura
Tevatró, 1.96 TeV $p\bar{p}$, CDF+D0, secció eficaç	7.16 ± 0.26 pb	7.60 ± 0.41 pb
Tevatró, 1.96 1.96 TeV $p\bar{p}$, CDF+D0, A^{FB}	$9.5 \pm 0.7\%$	$13 \pm 2.3\%$
LHC, 8 TeV pp, CMS+ATLAS inclusiu σ	245.80 ± 10.56 pb	241.50 ± 8.54 pb
ATLAS 8 TeV pp, inclusiu A_C	$1.11 \pm 0.04\%$	$0.9 \pm 0.5\%$
CMS 8 TeV pp, inclusiu A_C	$1.11 \pm 0.04\%$	$0.3 \pm 0.4\%$
ATLAS 8 TeVpp, diferencial A_C ($m_{t\bar{t}} > 0.75$ TeV)	$1.60 \pm 0.04\%$	$4.2 \pm 3.2\%$

Taula Resum 3: Dades utilitzades a l'ajust dels operadors de quatre quarks.

proveeixen informació complementària per a l'ajust. La sensibilitat als operadors de quatre quarks s'incrementa molt quan anem a règims d'energia molt alts. Per aquest motiu utilitzem mesures diferencials en funció de la massa invariant del sistema $t\bar{t}$.

Per a l'ajust sols hem considerat la contribució Λ^{-2} als observables. Fent aquesta assumpció, podem reduir la quantitat d'operadors de quatre quarks de la següent forma:

$$\begin{aligned} C_1^u &= C_{qq}^{(8,1)} + C_{qq}^{(8,3)} + C_{ut}^{(8)} \\ C_2^u &= C_{qu}^{(1)} + C_{qt}^{(1)} \\ C_1^d &= C_{qq}^{(8,1)} - C_{qq}^{(8,3)} + C_{dt}^{(8)} \\ C_2^d &= C_{qd}^{(1)} + C_{qt}^{(1)}. \end{aligned}$$

A més, assumirem la següent reducció addicional: $C_1^u = C_1^d = C_1$ i $C_2^u = C_2^d = C_2$. Aquesta reducció és vàlida en models on les noves partícules acoblen als quarks amunt i avall amb la mateixa força.

Molts autors han senyalat la importància de les contribucions als observables dels termes Λ^{-4}. Nosaltres ens hem assegurat explícitament que aquestes contribucions són subdominants en l'ajust.

Hem extret cotes per a C_1 i C_2. Els intervals obtinguts al 95% de nivell de confiança són, -0.06 $< C_1 \times v^2/\Lambda^2 <$ 0.10 i -0.04 $< C_2 \times v^2/\Lambda^2 <$ 0.11. Aquests resultats són compatibles amb les prediccions del Model Estàndard, $C_1 = C_2 = 0$.

ATLAS ha publicat resultats preliminars utilitzant dades a 13 TeV. La millor mesura utilitzant un anàlisi diferencial en funció de la massa invariant del sistema $t\bar{t}$ és $0 < \bar{C}_- < 0.06$.

Ajust global dels operadors de dos fermions utilitzant dades de SLC, LEP i LHC. Hem realitzat un ajust global a mesures existents dels operadors de dimensió sis del quark cim que afecten les interaccions de la tercera família de quarks (cim i fons) amb els bosons W, Z, γ i Higgs. Les mesures utilitzades es resumeixen en la Taula 4.

Els resultats de l'ajust es mostren en la Figura 1. La combinació de mesures escollida permet un ajust global molt robust sobre els operadors efectius. Fins avui, aquests són els resultats amb la incertesa més baixa.

Procés	observable	$\sqrt{s}$	$\int \mathcal{L}$
$pp \to t\bar{t}H$	secció eficaç	13 TeV	36 fb^{-1}
$pp \to t\bar{t}Z/W$	secció eficaç	13 TeV	36 fb^{-1}
$pp \to t\bar{t}\gamma$	secció eficaç fid.	13 TeV	36 fb^{-1}
cim individual (canal t)	secció eficaç	13 TeV	36 fb^{-1}
cim individual (cabal Wt)	secció eficaç	13 TeV	36 fb^{-1}
cim individual (canal tZq)	secció eficaç	13 TeV	36 fb^{-1}
$t \to W^+b$	F_0, F_L	8 TeV	20 fb^{-1}
$e^-e^+ \to b\bar{b}$	R_b , A_{FBLR}^{bb}	$\sim$ 91 GeV	202.1 pb^{-1}

Taula Resum 4: Mesures incloses a l'ajust d'operadors efectius de dos quarks de dimensió sis del sector dels quarks cim i fons.

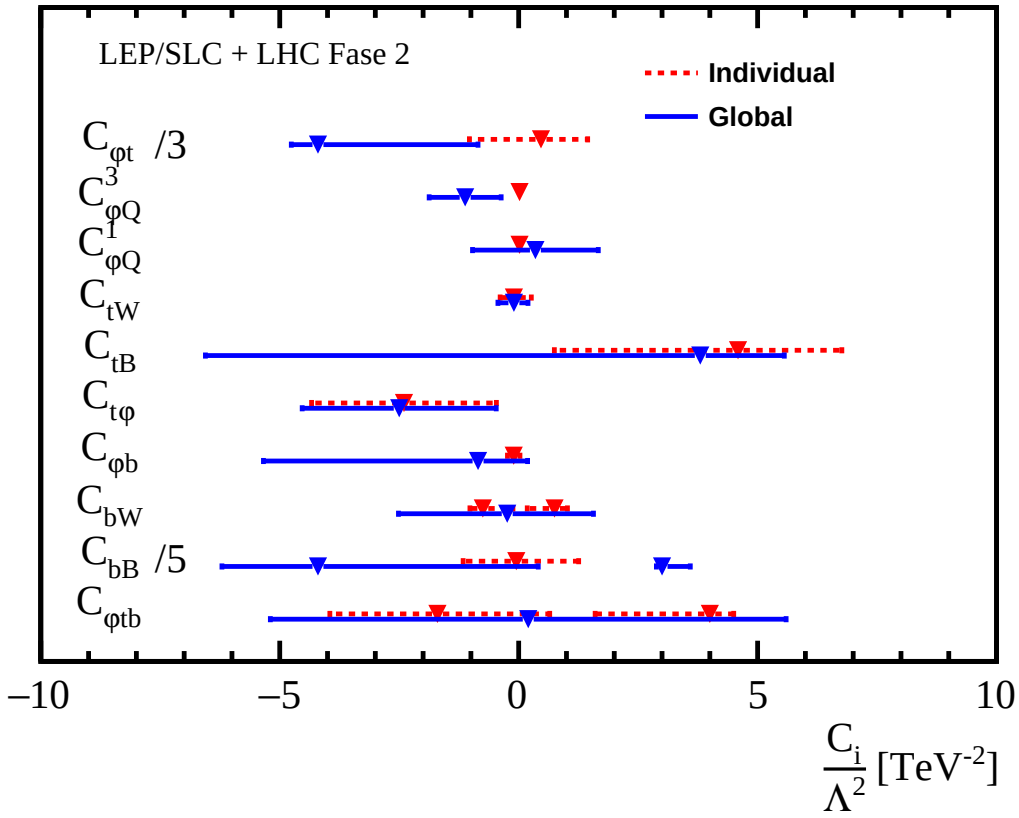

Figura Resum 1: Cotes obtingudes al 68% de probabilitat per als coeficients de Wilson dels operadors efectius que modifiquen els acoblaments electrodèbils dels quarks cim i fons. Les cotes globals es mostren en blau, mentre que les cotes individuals (quan sols un paràmetre pot variar a l'ajust) es mostren en roig. El mínim del χ^2 utilitzat a l'ajust es mostra com un triangle.

Ajust global sobre perspectives de futurs acceleradors electró-positró. Hem avaluat el potencial d'un col·lisionador electró-positró a l'hora de revelar efectes de nova física en mesures de precisió en la producció de pars del quark cim. Hem estudiat la sensibilitat d'un gran nombre d'observables als operadors efectius estudiats, així com l'impacte de l'energia en el centre de masses i de la polarització dels feixos.

També hem examinat la capacitat d'altres mesures a l'hora de ficar cotes als operadors del quark cim. Exemples serien la mesura de l'amplada de desintegració del quark cim en un escaneig en el llindar de producció de parells cim o en l'estudi de producció de parells del quark fons.

Hem observat que inclús amb un conjunt ampli d'observables, el control sobre la polarització dels feixos continua sent important a l'hora d'acotar les contribucions dels diferents operadors. A més, l'operació de l'accelerador a altes energies en centre de massa proveeix cotes molt estretes per als operadors de quatre fermions, les contribucions dels quals creixen quadràticament amb l'energia. Per tant la inclusió de dues energies de centre de massa és crucial en un ajust global que incloga operadors de dos i de quatre fermions.

Per a cobrir totes les direccions en l'espai d'operadors de forma eficaç i simultània, hem considerat un grup d'observables estadísticament òptims que aprofiten de forma màxima la informació continguda en la distribució diferencial sencera de l'estat final $bW^+\bar{b}W^-$.

Una combinació de mesures dels observables estadísticament òptims en dues energies diferents en centre de massa és suficient per a acotar simultàniament els coeficients dels operadors efectius de dimensió sis considerats al nostre ajust. Si considerem dos punts d'energia suficientment allunyats, aconseguim resoldre aproximadament les degeneracions en els coeficients i obtenim conseqüentment límits globals més propers als obtinguts en els ajustos individuals. La polarització dels feixos ajuda a augmentar les sensibilitats individuals, reduint les correlacions globals en l'ajust.

Hem investigat el potencial de futures mesures per a millorar les cotes actuals dels operadors de dimensió sis del quark cim. Els resultats principals es mostren en la figura Figura 7.5. El futur programa de l'LHC, incloent-hi la fase d'alta lluminositat, pot millorar moltes cotes per un factor dos o tres, a causa d'una millora en les incerteses de les prediccions teòriques del Model Estàndard per un factor dos i d'un decreixement de les incerteses sistemàtiques i estadístiques escalat amb la lluminositat. Hem considerat dos possibles escenaris per a la fase d'alta lluminositat: un més pessimista anomenat HL-LHC S1, on sols l'error estadístic de les mesures es redueix per l'augment de lluminositat; i un altre més optimista anomenat HL-LHC S1, on els errors estadístics i sistemàtics es redueixen a causa de l'augment de lluminositat, i el teòric es redueix un factor 2.

Un col·lisionador electró-positró amb una energia de centre de masses que estiga per damunt del llindar de producció de pars del quark cim pot millorar les cotes àmpliament. Amb les energies nominals de l'ILC, $\sqrt{s} = 250$ GeV i 500 GeV, s'espera millorar les cotes del programa de HL-LHC per un o dos ordres de magnitud.

Les mesures de precisió en un col·lisionador leptònic futur també redueix la importància dels termes d'ordre Λ^{-4}. Açò porta l'expansió EFT a un règim al qual els límits obtinguts són vàlids sense pèrdua de generalitat. Demostrem que per a poder ficar cotes als operadors de quatre fermions necessitem un punt d'energia alta en centre de masses.

Finalment hem presentat perspectives per a l'extracció de l'acoblament Yukawa del quark cim a partir del procés de producció associada $pp \to t\bar{t}H$ i $e^+e^- \to t\bar{t}H$. S'espera millorar la precisió actual de l'ordre del 10% en aproximadament un factor tres en el programa HL-LHC S2. L'ILC pot aconseguir una precisió similar quan opere a un centre de masses de 550 GeV, i pot arribar a millorar-lo un factor dos a 1 TeV per a una lluminositat integrada de 8 ab^{-1}. Aquests resultats són robustos quan són

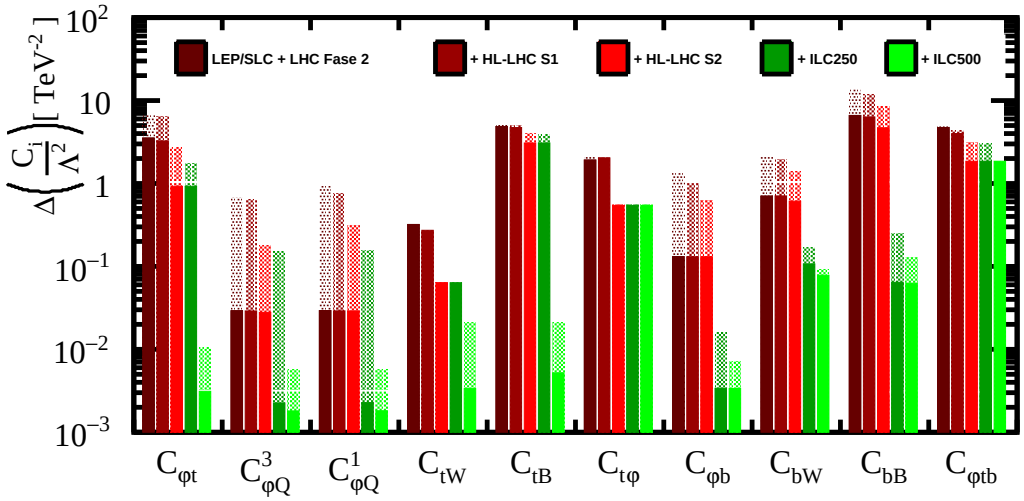

Figura Resum 2: Perspectives per a la precisió dels coeficients de Wilson basades el programa d'alta lluminositat de l'LHC i en un futur col·lisionador electró-positró. La part acolorida de les barres representa els límits individuals, mentre que la puntejada representa les cotes obtingudes de l'ajust global.

extrets dins d'un ajust multiparamètric que inclou tots els operadors electrodèbils que modifiquen els acoblaments dels quarks cim i fons.